Climate Impacts of Stratospheric Particle Injection

Simon Driscoll

Linacre College

University of Oxford

A thesis submitted for the degree of

Doctor of Philosophy

Michaelmas 2014

Acknowledgements

When embarking upon such a long project there can be too many people to thank who have been great friends, mentors and colleagues, so I decided to keep this short. I would like to thank in particular all those who gave me direct supervision and support throughout my thesis: Alessio Bozzo, Manoj Joshi, Don Grainger, Lesley Gray, Scott Osprey, Ray Pierrehumbert, Alan Robock and Georgiy Stenchikov, and all in the SPICE research group.

I would like to thank those at or affiliated with the Oxford Martin School's Oxford Geoengineering Project: Clare Heyward, Tim Kruger, Ed Pitt and Phil Renforth. I would like to thank all at the Future of Humanity Institute in the Oxford Martin School. The experience of being with and learning from you on all the various social, ethical, and science aspects of geoengineering has been invaluable.

I would like to thank all those who I have met at summer schools and elsewhere who have given me constantly interesting questions and discussions. I would like to thank all those who have given me time to raise the varied scientific and ethical questions around geoengineering in news, books and tv, and in particular Annalee Newitz, Filip Rogiers and all at VRT. I would like to thank those for fascinating discussions and those who I await to start many new directions with: Myles Allen, Michael Oppenheimer, Valerio Lucarini. Ray Pierrehumbert, Jordan Smith, Mikhael Vimont, Timo Goeschl and Tobias Pfrommer.

I would like to thank all my friends at Linacre (and the "SCR"). I would very much like to thank my family. The rest know who they are.

Abstract

Geoengineering has attracted large attention over recent years as to being a possible way to ameliorate some of the effects of climate change. One of these proposals, involving injecting sulphate aerosols into the stratosphere in order to cool Earth's temperature back to pre-industrial levels, has been assessed as one of the leading geoengineering proposals. Despite this, large uncertainties remain in both the physical and social sciences. Small scale trials of sulphate aerosol injection are not seen as ways to provide large amounts of useful data to inform on the climatic response to stratospheric sulphate aerosol loading (whilst also facing many social and ethical barriers). Large scale trials involving injecting amounts of aerosol more comparable to what would be required to cool the Earth's temperature back to pre-industrial levels are viewed as too risky.

Assessments of the climatic effects of sulphate aerosol geoengineering by the scientific community therefore have largely relied on climate modelling studies. The thesis begins by reviewing sulphate aerosol geoengineering and the modelling studies that have been conducted to date. In light of the need to verify modelling results with observations the thesis seeks to understand the effects of nature's analogue to sulphate aerosol geoengineering: large volcanic eruptions. When a volcano erupts it can inject large amounts of SO_2 gas into the stratosphere, which then undergo conversion to form sulphate aerosol, cooling the Earth in a way analogous to sulphate aerosol geoengineering.

The ability of the climate models submitted to the Coupled Model Intercomparison Project 5 (CMIP5) database is assessed, with a particular focus on dynamical changes in the Northern Hemisphere winter period. These models fail to capture

the observed NH dynamical response following eruptions, which is of concern for the accuracy of geoengineering modeling studies that assess the atmospheric response to sulphate aerosol geoengineering.

Simulations of volcanic eruptions are then performed with high-top and low-top configurations of the HadGEM2-CC climate model. The high-top version of HadGEM2-CC, with enhanced vertical resolution and model height, gives a markedly improved and statistically significant different post-volcanic winter dynamical simulation to its low-top counterpart. The post-winter dynamical simulation in the high-top model agrees with the observed response following volcanic eruptions. Accordingly, mechanisms involved in the dynamical changes are analysed and it is concluded that the HadGEM2-CC high-top model would give more confident simulations of sulphate aerosol geoengineering over its low-top counterpart.

Given the identification of a more suitable model for geoengineering simulations following extensive investigation, the final chapter analyses simulations of the HadGEM2-CC high-top model for asymmetries between the climate response to an immediate onset of geoengineering and a rapid cessation of geoengineering - known as a 'termination' of geoengineering. The project is summarised and discussed, and future work is proposed, involving a large host of projects.

Contents

1 Introduction - Geoengineering, Motivation and Our Understanding to Date **1**

1.1 The Climate Change Problem, Geoengineering and the Need for Constraining Climate Modelling Studies. 1

1.2 An Overview of the Climate Effects of Geoengineering from Modelling Studies 7

2 Volcanic Eruptions and Their Effect on Climate As Model Verification **18**

2.1 Literature Review 18

2.2 Ocean Response 29

2.3 Interactions with ENSO and the QBO 31

2.4 Simulations of Climate following Volcanic Eruptions 33

3 Coupled Model Intercomparison Project 5 (CMIP5) Simulations of Climate following Volcanic Eruptions **37**

3.1 Introduction 37

3.2 Models and Experiments 38

3.3 Results 47

3.3.1 Direct Radiative Effect of Volcanic Aerosol 47

3.3.2 Surface Temperature and Mean Sea Level Pressure - Multi-Model Averages 50

3.3.3 Surface Temperature and Mean Sea Level Pressure - Individual Models . . . 54
3.3.4 Geopotential Height . . . 60
3.3.5 NAO Index . . . 66
3.4 Discussion and Conclusions . . . 74

4 Simulations of NAO Changes following the 1991 Mount Pinatubo Eruption Using High-Top and Low-Top Configurations of HadGEM2 80
4.1 Pinatubo as a Case Study . . . 80
4.2 Experimental Set-Up and Purpose . . . 85
4.3 Results . . . 89
4.3.1 ERA40 Dataset . . . 89
4.3.2 Results from the L38 Pinatubo Simulations . . . 90
4.3.3 Results from the L60 Pinatubo Simulations . . . 94
4.3.4 L60 - First and Second Winter Responses . . . 97
4.3.5 Stratospheric Evolution . . . 101
4.4 Mechanisms - The Transformed Eulerian-Mean Framework . . . 106
4.4.1 Decompositions of Atmospheric Circulation . . . 107
4.4.2 The Primitive Equations and Transformed Eulerian Means . . . 108
4.5 Analysis of Stratospheric Dynamical Changes . . . 112
4.5.1 The Brewer-Dobson Circulation . . . 113
4.5.2 On EP Fluxes and Scaling . . . 114
4.5.3 Frequency of Negative Refractive Index Squared . . . 121
4.5.4 Summary of L60 and L38 Comparison . . . 124
4.5.5 Changed Aerosol Profile in the L60 . . . 126
4.5.6 Results from the L60 - First Winter Response . . . 128
4.6 Chapter Summary and Discussion . . . 139

5 Asymmetries Between the Onset and Termination of Geoengineering in the UM-CLASSIC Configuration of HadGEM2 **141**

5.1 Introduction 141

5.2 Experimental Set-Up 146

5.3 Results 147

5.3.1 RCP4.5 Scenarios 147

5.3.2 G4mod: Onset and Termination 150

5.3.3 Onset and Termination 156

5.3.4 Onset and Termination Acceleration Factors 157

5.3.5 Exploring Imbalances Between Sulphate Aerosol Amounts between Onset and Termination 160

5.4 Discussion and Conclusions 166

6 Conclusions and Further Work **169**

6.1 Summary 169

6.2 Further Work - Extension of the Thesis 172

6.3 Further Work - Geoengineering Studies 175

List of Figures

1.1 The Earth's Global Annual Mean Energy Budget (Trenberth et al., 2009) 3

2.1 Basic radiative and chemical impact of a volcanic eruption on the Atmosphere, from Robock (2000) 22
2.2 Schematic diagram illustrating the proposed volcanic mechanism from Stenchikov et al. (2002) 26
2.3 Some of the effects of a positive phase AO (left) and a negative phase (right) 27
2.4 Post Pinatubo 1991-1992 DJF Lower Troposphere Temperature Anomalies from the 1984-1990 average showing anomalous surface warming over North America and Eurasia, from Robock (2003) 27
2.5 (a) Precipitation and (b) Runoff Anomalies, and (c) Palmer Drought Severity Index following Pinatubo, from Trenberth and Dai (2007) . . 29
2.6 A schematic diagram representing the ability of waves to propagate into the tropical regions during a westerly QBO (left) and an inability to propagate into these regions, and thus disturb the vortex, during an easterly QBO 32

3.1 Leading EOF of the monthly winter (DJF) mean sea level pressure anomaly over the North Atlantic region (110° W-70° E) for each model ensemble mean and 20CRv2 over the period 1860-2000. EOF values are expressed as hPa. In the top right corner of each plot is indicated the percentage of variance explained by the first EOF. 46

3.2 3-months running average of global averaged de-trended and de-seasonalised TOA outgoing shortwave radiation anomalies for the 13 CMIP5 models listed in Table 3.1, over the period of 1860-2000. The gray shading shows the spread among the minimum and maximum of the means of each model ensemble. The lines show the multi-model mean (CMIP5-MM) and the multi model mean for the models using Sato et al. (1993) database and Ammann et al. (1993). The ensemble mean for MRI-CGCM3 is shown, which computes interactively the evolution of volcanic aerosol. The green line at the bottom shows the 30° S and 30° N volcanic aerosol optical depth (AOD) at 550 nm from Sato et al. (1993) and updates. The grey bars at the top of plots indicate the occurrence of the nine volcanic eruptions listed in Table 3.2. 48

3.3 As Fig. 3.2 but for the 50 hPa temperature anomalies averaged between 30° S and 30° N. In the bottom panel the corresponding 50 hPa temperature anomalies from ERA40 are included. 49

3.4 Comparison between reanalysis and multi-model mean. Composite anomaly averaged after 2 post-volcanic winters for (a,b) near-surface temperature (K), (c,d) mean sea level pressure (hPa), (e,f) and (g,h) respectively 200 and 50 hPa geopotential (m). The anomalies in (e,g) are computed for the last four volcanoes listed in Table 3.2. Hatching displays, for the left column areas at or over 95 % significance using a local two tailed t-test, for the right column where at least 90 % of models agree on the sign of the anomaly. Notice the different scale in (a,b) and (c,d) 52

3.5 Difference in the composite anomaly averaged after two post-volcanic winters between the multi-model mean and the reanalysis. a) near-surface temperature, b) mean sea level pressure, c) 200 hPa geopotential, d) 50 hPa geopotential. a) and b) refer to the nine eruptions listed in Table 3.2 and 20CRv2 is used , c) and d) are for the most recent four eruptions and ERA40 is used. Coloured areas are significant at the 99 % level using a 2-tailed one-sample t-test 53
3.6 Composite near-surface temperature anomalies (K) for the two following winters of the past nine most recent large tropical volcanic eruptions (Table 3.2) in all models and the 20th century reanalysis (20CRv2). Hatching displays areas at or over 95 % significance using a two tailed t-test. 56
3.6 **(continued)** 57
3.7 NH stereographic plot of composite MSLP anomalies (hPa) for the two following winters of the past nine most recent large tropical volcanic eruptions in all models and the 20th century reanalysis (20CRv2). Hatching displays areas at or over 95 % significance using a two tailed t-test. 58
3.7 **(continued)** 59
3.8 NH stereographic plot of composite 200 hPa Geopotential Height anomalies (m) for the two following winters of the past nine most recent large tropical volcanic eruptions in all models and ERA40 reanalysis. The anomalies in the reanalysis are computed for the four eruptions after 1960. Hatching displays areas at or over 95 % significance using a two tailed t-test. 62
3.8 **(continued)** 63

3.9 NH stereographic plot of composite 50 hPa Geopotential Height anomalies (m) for the two following winters of the past nine most recent large tropical volcanic eruptions in all models and ERA40 reanalysis. The anomalies in the reanalysis are computed for the four eruptions after 1960. Hatching displays areas at or over 95 % significance using a two tailed t-test. 64
3.9 **(continued)** 65
3.10 Superposed epoch analysis for the winter (DJF) NAO index for the 13 CMIP5 models and the 20th century reanalysis (20CRv2) for the nine eruptions listed in Table 3.2. The average over nine volcanic eruptions is shown at different lag time. Lag 0 indicates the first winter after a volcanic eruption. The horizontal lines show, from bottom to top, the 1st, 5th, 95th and 99th percentiles of the bootstrap distribution. For each plot is indicated the number of ensemble members (r), the ratio of total number of winters with positive NAO with respect to the total number of winters in each ensemble (σ) and the number of winters at lag 0 with positive NAO (N_0) with the relative p-value. 68
3.10 **(continued)** 69
3.11 As Fig 3.10 but using the convention adopted in Christiansen (2008) for the first winter after the eruptions of Santa María (1902-1903) and Fuego (1974-1975). 70
3.11 **(continued)** 71

4.1 Simple schematic diagram representing experimental set-up. 86

4.2 A diagram to represent the time evolution of volcanic stratospheric aerosol in HadGEM2. The aerosol is applied in four quarterspheres of approximately equal area: 90° N to 30° N, 30° N to 0°, 0° to 30° S, 30° S to 90° S. Shading corresponds to aerosol optical depth values at 0.55 μ m of 0-0.05 (white), 0.05-0.10 (light gray), 0.10-0.15 (dark gray) and 0.15-0.20 (dark black) and demonstrates how a volcano would be represented. 87

4.3 The aerosol lid of HadGEM2 when set to 30hPa (black line), which is currently implemented in all HadGEM2 simulations, and the modified lid as given in equations 4.1-4.7 (navy blue line). 89

4.4 Seasonally averaged anomalies of near-surface air temperature (K) from the ERA40 analysis for the winters (DJF) 1991/92 and 1992/93. Anomalies are calculated with respect to the mean for the years 1985-1990. As with Stenchikov et al. (2002) the hatching corresponds to the 90% confidence level using a two tailed t-test. A t-test compares the difference in the mean of two groups of normally distributed data. When one value is to be compared against another group of data, that single value is compared against the mean of the other group of data. Therefore, here the hatched areas areas represent differences significant at the 90% level according to the t-test between their 1991/92 and 1992/93 values and the mean of the pdf from the 1985-1990 climatology. 91

4.5 L38 anomalies of DJF temperature (K), wind (ms^{-1}), MSLP (hPa) and near surface temperature (K) for the two winters. Stippling corresponds to the 90% confidence level using a two tailed t-test. Unlike observations, for all model simulations hatching represents significant differences between the volcanically perturbed simulations and the control simulations with no volcanic perturbation (otherwise exactly alike). 92

4.6 L60 anomalies of DJF temperature (K), wind (ms^{-1}), MSLP (hPa) and near surface temperature (K) for the two winters. Stippling corresponds to the 90% confidence level using a two tailed t-test. 95
4.7 L60 anomalies of temperature (K), and MSLP (hPa) for DJ (left) and FM (right) for all the first post-Pinatubo winters. Hatching corresponds to the 95% confidence level using a t-test. 98
4.8 As figure 4.6 but for the second simulated winter. Hatching corresponds to the 95% confidence level using a t-test. 100
4.9 As figure 4.8, but here anomalies are the L60 from the L38 model instead of climatology. Hatching corresponds to the 95% confidence level using a t-test. 101
4.10 Monthly first winter temperature anomalies (K) for L60. Stippling corresponds to the 95% confidence level using a t-test. 102
4.11 Monthly first winter u wind anomalies (ms^{-1}) for L60. Stippling corresponds to the 95% confidence level using a t-test. 104
4.12 Left: A simplified diagram of the Brewer-Dobson circulation, showing rising at the tropics and descent at the poles, from Brewer (1949). Right: A schematic representation of the residual mean circulation showing the influence planetary waves and EP flux convergence in the tropics and subtropical stratosphere on driving the tropical rising and polar descent, from Salby (2008). 114

4.13 Schematic illustrations from Kodera and Kuroda (2002), showing a) a stronger jet due to the warming effect and temperature gradient of solar maximum compared to minimum deflecting planetary waves from the subtropical regions, which is represented by a large positive area of increased EP flux, and b) the change in wave forcing in this period implies an anomalous decrease in the Brewer-Dobson circulation. Both effects are seen in the L60 model simulations for a very similar situation where volcanic aerosol plays the role of the forcing that creates the stratospheric heating and temperature gradient. This is accompanied with an increase in the Brewer-Dobson circulation directly as a result of the tropical heating, also seen in other studies on volcanic eruptions and climate. 115

4.14 Top: December (left) and January (right) vertical and meridional EP flux anomalies and divergence ($\mathrm{ms^{-1}\,day^{-1}}$) for L60. Below, images from Kodera and Kuroda (2002), the contours show composite differences of zonal mean zonal wind (with interval is $2\mathrm{ms^{-1}}$) and the arrows show composite differences of EP flux vectors, both for the solar maximum minus solar minimum for December (left) and January (right) using the NCEP Reanalysis dataset over the period of 1979-1998. They do not show the anomalies for February. Note the differences in the latitude and height range presented between the images computed here and those used in Kodera and Kuroda (2002). 117

4.15 Monthly v^+ anomalies ($\mathrm{ms^{-1}}$) for L60. Stippling corresponds to the 95% confidence level using a t-test. 118

4.16 Monthly w^+ anomalies ($\mathrm{ms^{-1}}$) for L60. Stippling corresponds to the 95% confidence level using a t-test. 119

4.17 Anomalies of heat flux, $[\mathrm{v}^*\theta^*]$ ($\mathrm{K\,m\,s^{-1}}$), for L60 for December and January. Stippling corresponds to the 95% confidence level using a t-test. 120

4.18 December (left) and January (right) $(\rho a \cos\phi)^{-1}\nabla\cdot F$ anomalies ($\mathrm{ms}^{-1}\,\mathrm{day}^{-1}$) for L60. Stippling corresponds to the 95% confidence level using a t-test. 121
4.19 December (top left), January (top right) and February anomalies of frequency of negative refractive index squared, n^2. Stippling corresponds to the 95% confidence level using a t-test. 124
4.20 L60 anomalies of DJF temperature (K), wind (ms^{-1}), MSLP (hPa) and near surface temperature (K) for the two winters. Stippling corresponds to the 90% confidence level using a two tailed t-test. 128
4.21 L60 anomalies of temperature (K), and MSLP (hPa) for DJ (left) and FM (right) for all the first post-Pinatubo winters. Hatching corresponds to the 95% confidence level using a two tailed t-test. 129
4.22 As figure 4.6 but for the second model winter. Hatching corresponds to the 95% confidence level using a t-test. 130
4.23 Monthly first winter temperature anomalies (K) for L60. Stippling corresponds to the 95% confidence level using a t-test. 131
4.24 Monthly first winter u wind anomalies (ms^{-1}) for L60. Stippling corresponds to the 95% confidence level using a t-test. 133
4.25 Monthly vertical and meridional EP flux anomalies and divergence ($\mathrm{ms}^{-1}\,\mathrm{day}^{-1}$) for L60. 134
4.26 Anomalies of heat flux, $[v^*\theta^*]$ ($\mathrm{K\,m\,s}^{-1}$), for L60 for December and January. Stippling corresponds to the 95% confidence level using a t-test. 134
4.27 Monthly $(\rho a \cos\phi)^{-1}\nabla\cdot F$ anomalies ($\mathrm{ms}^{-1}\,\mathrm{day}^{-1}$) for L60. Stippling corresponds to the 95% confidence level using a t-test. 135
4.28 Monthly v^+ anomalies (ms^{-1}) for L60. Stippling corresponds to the 95% confidence level using a t-test. 136
4.29 Monthly w^+ anomalies (ms^{-1}) for L60. Stippling corresponds to the 95% confidence level using a t-test. 137

5.1 Schematic diagrams illustrating the four GeoMIP experiments, G1 (top left), G2 (top right), G3 (bottom left), G4 (bottom right), from Kravitz et al. (2011) 145
5.2 Global mean annual mean values of near-surface temperature, precipitation and fraction of global surface area covered in sea ice for the three RCP4.5 simulations. 149
5.3 Linearly fitted rate of change in temperature (top left), precipitation (top right), and per cent of area covered in sea ice for the Northern Hemisphere Sea Ice (bottom left) and the Southern Hemisphere (bottom right) over the RCP4.5 scenario. 151
5.4 Global averaged, yearly averaged anomalies of near-surface temperature, precipitation and fraction of global surface area covered in sea ice of G4mod from each respective RCP4.5 simulation. 153
5.5 Linearly fitted changes in temperature (top left), precipitation (top right), and per cent of area covered in sea ice for the Northern Hemisphere Sea Ice (bottom left) and the Southern Hemisphere (bottom right) over the ten years following the onset of geoengineering. 154
5.6 Linearly fitted rate of change in temperature (top left), precipitation (top right), and per cent of area covered in sea ice for the Northern Hemisphere Sea Ice (bottom left) and the Southern Hemisphere (bottom right) over the ten years following the termination of geoengineering. 155
5.7 RCP4.5 scenario at the 95% level. for temperature (top left), precipitation (top right) and and per cent of area covered in sea ice for the Northern Hemisphere (bottom left) and Southern Hemisphere (bottom right). Statistical significance represents where the onset period are statistically significantly different to the α_{Onset} 158

5.8 RCP4.5 scenario at the 95% level. for temperature (top left), precipiation (top right) and and per cent of area covered in sea ice for the Northern Hemisphere (bottom left) and Southern Hemisphere (bottom right). Statistical significance represents where the termination period are statistically significantly different to the $\alpha_{\text{Termination}}$ 160

5.9 α_{Ratio} for temperature (top left), precipiation (top right) and and per cent of area covered in sea ice for the Northern Hemisphere (bottom left) and Southern Hemisphere (bottom right). Statistical significance represents where the onset period are statistically significantly different to termination at the 95% level. 161

5.10 Globally averaged sulphate aerosol throughout the entire atmosphere during the onset and termination periods. 162

5.11 Globally averaged sulphate aerosol in the entire atmosphere during the onset and termination periods. 166

List of Tables

3.1 Models used in the study and their basic characteristics (horizontal resolution, vertical levels and model top), imposed aerosol forcing and number of ensemble members available. In the last column are listed the variables analysed for each model (T ≡ 1.5 m temperature, P ≡ mean sea level pressure, Z ≡ geopotential height). 44

3.2 Major low latitude eruptions from 1883 to present day. 45

3.3 Climatological indices 75

5.1 α values 162

Chapter 1

Introduction - Geoengineering, Motivation and Our Understanding to Date

1.1 The Climate Change Problem, Geoengineering and the Need for Constraining Climate Modelling Studies.

Geoengineering, defined as "the deliberate large scale intervention in the Earth's climate system in order to moderate global warming" (Shepherd et al., 2009), has attracted much attention over recent years as a possible solution to avert dangerous anthropogenic climate change (e.g. Wigley, 2006, Crutzen, 2006). Fossil fuel emissions have been rising at rates which suggest substantial impacts upon the climate system and society and these emissions are predicted to rise for at least a few decades (Stocker et al., 2013). The political will as well as other social and economical factors (such as the substantial benefits to developing countries to use fossil fuels) implies that the world is highly likely to miss a long standing target of avoiding 2 K global average temperature rise from pre-industrial climate (Anderson and Bows, 2011, Rogelj et al. 2012). The most important greenhouse gas is carbon dioxide (CO_2), of which 50% of the emitted CO_2 can remain in the atmosphere on the time scale of centuries to millennia, meaning that the Earth's temperature relative to pre-industrial will also stay high for centuries to millennia (Solomon et al., 2011).

Increased greenhouse gases in the atmosphere will cause not only global average temperature increases (e.g. Hansen et al., 1981, Lashof and Ahuja 1990, Crowley, 2000, Solomon et al., 2011), but precipitation increases (Allen and Ingram, 2002, Stocker et al., 2013), decreases in sea ice cover (e.g. Maslanik et al., 2007, Serreze et al. 2007), sea level rise (e.g. Gornitz et al., 1982, Rahmstorf 2007), ocean acidification (Orr et al., 2005, Doney et al., 2009), heat stress and other negative impacts upon crops (e.g. Rosenzweig, 2000, Lobell and Field, 2007, Battisti and Naylor, 2009), and likely increases in extreme weather (e.g. Rosenzweig et al., 2001), species extinction and other damages (Hansen et al., 2006) on top of existing flooding, droughts, and so on, causing a substantial increase in current economic and social damage (for a more exhaustive list of climate change impacts, see Stocker et al., 2013).

Despite this, Rasch et al. (2008) note that reducing fossil fuel emissions to avoid undesirable impacts from climate change requires transformation of technological systems on scales that are unprecedented, and moreover it has been noted it is substantially unclear to what extent scientific predictions have the ability to change social policy (Sarewitz and Pielke, 2000, Sarewitz et al., 2000). Therefore, with atmospheric greenhouse gas concentrations rising, substantial likely damages and little evidence of the changes that are necessary to avoid such potentially catastrophic climate change being implemented, alternative and novel ways outside of the traditional mitigation and adaptation to combat climate change known as geoengineering have been proposed (see Shepherd et al., 2009, and references therein for a more comprehensive overview of the different schemes). Geoengineering schemes can be fit into two categories: Solar Radiation Management (SRM) techniques and carbon dioxide Removal (CDR) techniques. However, there exists debate about the terminology to be used. For example, other categories are possible: such as Radiation Management (RM) which encompasses not only SRM technologies but also those proposals that seek to enhance outgoing longwave radiation, such as cirrus stripping (Klepper and Rickels, *in press*). Also there are those methods which seek to remove greenhouse gases out of the atmosphere other than CO_2 (Greenhouse Gas Removal, 'GHGR'), as well as debate on the term geoengineering itself which brings together many entirely separate

technologies with different climatic and social issues (e.g. Heyward, 2013). However, in this thesis the three most commonly used terms: geoengineering, CDR and SRM are used.

SRM techniques aim to reduce the global mean temperature of the Earth by changing the Earth's global annual mean energy budget (figure 1.1) - this is achieved by scattering a small fraction of the 341.3 W m^{-2} incoming solar radiation shown in figure 1.1 back to space. CDR techniques, on the other hand, aim to cool the atmosphere by actively removing carbon dioxide from the atmosphere and thus reducing the greenhouse gas radiative forcing. Examples of SRM techniques include increasing the surface reflectivity of the planet through painting roofs or placing reflective materials over large areas of desert, enhancement of marine cloud reflectivity, injecting sulphate aerosols into the lower stratosphere, and placing shields or deflectors in space, whilst examples of CDR techniques include afforestation, biomass/biofuels with carbon sequestration, biochar, enhanced weathering, and ocean fertilisation (Shepherd et al., 2009).

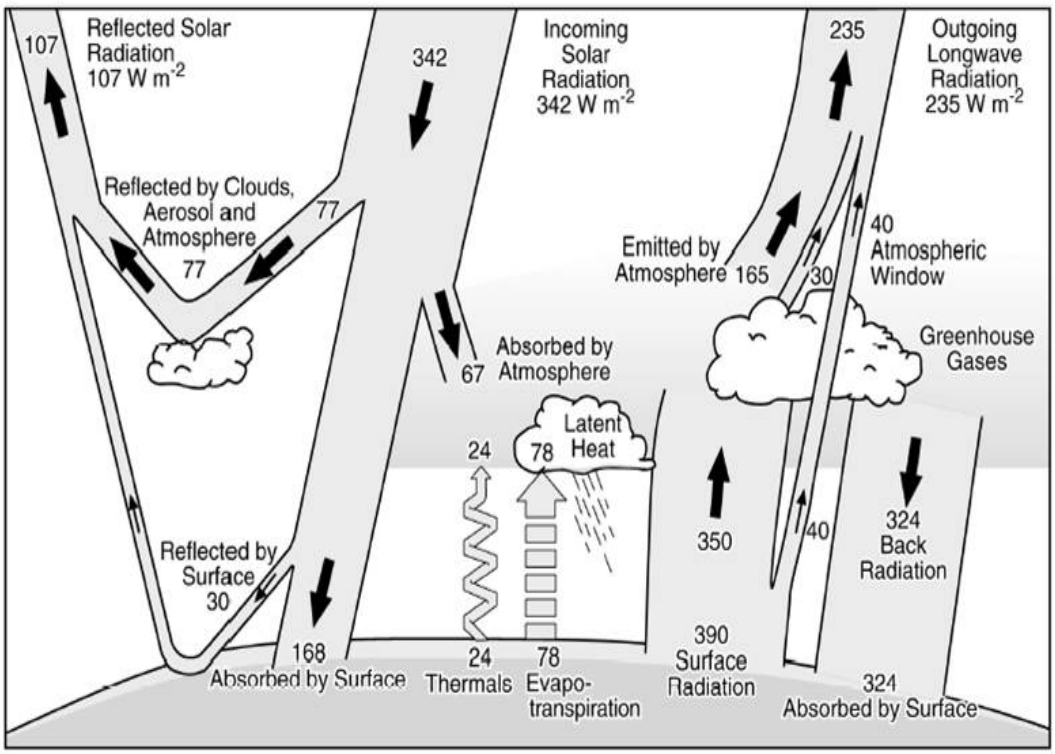

Figure 1.1: The Earth's Global Annual Mean Energy Budget (Trenberth et al., 2009)

As CDR methods reduce the amount of carbon dioxide in the atmosphere, they deal directly with the source of increased radiative forcing and climate change. Therefore, they address other effects of climate change, such as ocean acidity, which SRM techniques cannot address. CDR techniques may therefore seem to be the most appropriate, however, recent modelling research has suggested that rising SSTs are a greater threat for tropical coral reefs than ocean acidification, so SRM may help maintain coral reef habitats in the near-term (Couce et al. 2013). CDR techniques also act on much slower time-scales (Shepherd et al., 2009). The size of industry required, cost and problems with scalability from the laboratory to the world, mean that they are not ready for implementation as a viable alternative to mitigation and adaptation, and the time taken to develop these technologies may be very long, such that sufficient economic and ecological damage is likely to occur during their development (Shepherd et al., 2009).

SRM techniques have therefore generated a substantial amount of focus in the past five to ten years (Mercer et al., 2011) and are now being substantially investigated into (e.g. Robock, 2008, Robock et al., 2009, Kravitz et al., 2011, Ricke et al., 2010, Ricke et al., 2012, Irvine et al., 2011, Latham et al., 2012). Some SRM techniques, such as stratospheric aerosols, have some potential advantages over others, such as space mirrors, in that the scheme is operable from an engineering perspective within a few years (Shepherd et al., 2009, McCellan et al., 2011, McCellan et al., 2012). Other SRM schemes, such as roof painting, have been shown to have a negligible globally averaged climate effect (Akbari et al., 2012). There remain some fundamental physical questions about other the ability of other schemes to be able to reflect away substantial amounts of incoming solar radiation, such as marine cloud brightening (Christensen and Stephens, 2011, Chen et al., 2012, Christensen and Stephens, 2012). Due to its relative effectiveness of sulphate aerosol geoengineering over other SRM methods, sulphate aerosol injection is the focus of this thesis (from hereon, we often use the term geoengineering often as a short hand for sulphate aerosol geoengineering).

Upon implementation SRM techniques would have very quick impacts on the climate, being able to reduce global average temperature almost immediately (e.g. Schmidt

et al. 2012, Kravitz et al., 2013). Hence, they have been argued to possess a particular advantage over CDR methods in their ability to deal rapidly with climate emergencies (Shepherd et al., 2009). They are also much cheaper to implement than CDR technologies (e.g. Shepherd et al., 2009, Goes et al., 2010, Davidson et al., 2012, McCellan et al., 2011, McCellan et al., 2012) and have therefore been raised as a luring compliment or alternative to the more expensive and slower options of mitigation, adaptation and CDR. These benefits and the cheapness would indicate that SRM, at first, can appear as a 'no brainer', however, the uncertainties and lack of understanding surrounding unknown side-effects associated with such a scheme are so high as to warrant extreme caution on any type of global SRM programme currently (Klepper and Rickels, *in press*). Indeed, SRM methods and its research have been described as in their 'infancy' (Gadian et al., 2012). Research into geoengineering has been encouraged as part of the general portfolio of climate related research, competing with the full panoply of societal responses to climate change (Robock, 2012, Jamieson, 2013) as well as some policy researchers and ethicists considering some implementation of stratospheric aerosols as likely to highly likely (Gardiner, *personal communication*, Frame, *personal communication*). Therefore, there is a need to understand the climate impacts of these schemes before they are implemented on a full scale, and to understand their costs and benefits (Shepherd et al., 2009), and different options for decreasing uncertainty on these methods have been proposed.

Some have suggested performing global experiments in order to aid the understanding of the impacts of SRM are an issue of immediate importance (Victor et al., 2013). Parson and Keith (2013) have suggested a framework for global experiments such that there should be a moratorium of experiments that would produce an annual averaged change radiative forcing of greater than approximately $10^{-2}\,\mathrm{Wm}^{-2}$, whilst experiments below an annual averaged change radiative forcing of approximately 10^{-2} Wm^{-6} should be allowed to proceed. Others have questioned both the urgency of global experiments and have raised the political and social complications involved and that may arise from global experiments (e.g. Robock, 2008, Robock et al., 2010, Schäfer et al., 2013) as well as questions being raised as to what of value may be

learnt from such experiments (Rotman, 2013). Albeit substantial SRM and CDR experiments have already taken place in both the ocean and atmosphere (Russell et al., 2011, Tollefson, 2012, Nicoll and Delaney, 2012), whilst further plans are being made for both global marine cloud brightening and sulphate aerosol geoengineering experiments (Latham et al., 2012, Keith, 2013, Kintisch, 2013). A number of other social and ethical issues exist around doing global experiments (e.g. Hamilton et al., 2013).

As regards global experiments small perturbations to the climate system would likely require implementation for many years to understand the climate response to a sufficient degree of accuracy, whilst progressively larger experiments require less time in order to obtain a clear signal. For example, MacMynowski et al. (2011) perform simulated field tests where a radiative forcing of -1Wm^{-2} is implemented, represents approximately a quarter of that required for offsetting a doubling of atmospheric carbon concentration. They show that to detect the local-scale temperature signal with a 95 per cent confidence interval, such field tests would have to be maintained for durations in excess of 50 years, whilst understanding local-scale precipitation would take longer. Other simulations attempting to isolate the climate change signal upon precipitation demonstrate large differences in the season of the precipitation (Fowler and Wilby, 2010), implying that to understand all effects could take substantially longer. Understanding that any tests will need to be above a certain size and duration threshold implicitly blurs the boundaries between testing and implementation which possess, not least, important legal issues (MacMynowski et al., 2011, Klepper and Rickels, *in press*).

Assessments from past observations have been suggested. One example is Lunt et al. (2008) who note that the Cambrian period (approximately 540 to 485 million years ago) experienced a high CO_2 reduced solar forcing world. Therefore, they note that in terms of gross radiation balance, a geoengineered world could be broadly similar to the Cambrian World. Especially given that geoengineering efforts may have to be continued for hundreds, if not thousands, of years due to the long lifetime of CO_2 in the atmosphere the suggestion of Lunt et al. (2008) could be useful in

providing insight on the longer term response of the climate to a combination of high CO_2 and reduced incoming solar radiation. The reliability of such analysis on the scales required would likely not be sufficiently accurate to substantially constrain the climate response to geoengineering, however, Wunsch et al. (2013), for example, express reservations about understanding the impact of geoengineering due to having only ten years of well observed ocean data - which, due to the time-scales of the ocean, is not enough to be confident about oceans processes and their corresponding response to geoengineering. This uncertainty holds when attempting to make similarly detailed assessments of the oceanic response to increased CO_2 emissions. Therefore, climate modelling studies have naturally taken a role of central importance in assessing the impact of sulphate aerosol geoengineering.

1.2 An Overview of the Climate Effects of Geoengineering from Modelling Studies

Whilst only a few field trials have been conducted for CDR and SRM, there has been a vastly larger and increasing amount of solar radiation management modelling studies conducted over the past few years (Mercer et al., 2011). Early modelling results suggest a mixture of possible climatic benefits and damages from stratospheric aerosol geoengineering. Studies have demonstrated that sulphate aerosol geoengineering is an effective way at cooling global temperatures back to pre-industrial levels (e.g. Robock et al., 2008, Rasch et al., 2008, Jones et al., 2010, Ammann et al., 2010, McCusker et al., 2012, Kravitz et al., 2013). Modelling studies all demonstrate a decrease in precipitation following a reduction in solar constant (e.g. Irvine et al., 2010, Ricke et al., 2010, Jones et al., 2010, Ricke et al., 2012, Volodin et al., 2011, MacMynowski et al., 2011, Kravitz et al., 2013). Such results are understood independently of models from simple considerations of the surface energy budget analysis, and so are likely to be robust (Bala et al., 2008).

A reduction in incoming solar radiation has also been simulated to reduce sea level rise. Moore et al. (2010) point out that damage from sea level rise from climate

change could cost 10% of projected gross world product (GWP) in the 2070's and compare sea level rise in various emissions pathways (RCP3PD, RCP4.5 and RCP8.5) with and without geoengineering. They demonstrate that geoengineering on a level similar to experiencing one Mount Pinatubo eruption every 18 months (an injection that would deliver a constant 4 Wm^{-2} reduction in radiative forcing), could delay sea level rise by 40-80 years. They use a simple linear model incorporating effects such as radiative forcing and sea level, but neglecting possibly important feedbacks from ice sheets and atmospheric dynamics.

Whilst showing the ability to reduce some of the physical changes to the climate system from increased CO_2, sulphate aerosol geoengineering studies have also indicated that there would be undesirable impacts. Robock et al. (2009) note that geoengineering would cause a reduction of the ozone in the stratosphere. Whilst Wigley (2006) points out that if stratospheric chlorine levels were to drop as expected then this effect would be reduced relative to ozone loss from stratospheric aerosols today, Tilmes et al. (2008) performed simulations of doubling of atmospheric CO_2 with and without sulphate aerosol geoengineering using the Whole Atmosphere Chemistry Climate Model 3 using 'small' aerosols (injected at a rate of 1.5 Tg S per year - 1 Tg = 10^{12} g) and 'large' aerosols (injected at a rate of 5.3 Tg S per year) for future scenarios, incorporating changes in the potential for activation of chlorine. Both sets of simulations are designed to take the global average temperature approximately back to pre-industrial climate, but vary in aerosol mass loading because of the dependence of backscattering upon particle size. Whilst small aerosols possess this advantage, meaning that less would need to be injected for a given temperature target, small aerosols particles would cause more ozone depletion due to a higher surface area density allowing for more ozone destroying chemical reactions to take place. The simulations they perform reveal that between 2050 and 2100 that ozone loss from sulphate aerosol geoengineering could be around at least 60 to 80 Dobson Units (DU) for 75% of all winters, with loss being possibly as high as 150 DU assuming sulphate aerosols are used to balance a doubling of CO_2 that occurs during this period. Tilmes

et al. (2008) conclude by noting that sulphate aerosol geoengineering could delay the recovery of the Antarctic ozone hole by between 30 and 70 years.

Despite their study, ozone loss may not be a major issue for a smaller level of geoengineering. More 'practical' levels of geoengineering have been proposed. These involve only reflecting away a small fraction of the Earth's incoming solar radiation and do not aim to totally offset the CO_2 radiative forcing to avoid only the worst effects of climate change (e.g. Wigley, 2006, Crutzen, 2006). Further geoengineering studies aiming at exploring benefits of a lesser amount of aerosol than required to take global average temperatures back to preindustrial have been performed. Using the HadCM3L general circulation model MacMartin et al. (2012) explore the effects of a non-uniform reduction in solar constant on Northern Hemisphere September sea ice extent, precipitation and surface temperature. MacMartin et al. (2012) conclude from simulations that if sulphate aerosol profiles that varied in latitude and time were possible (represented by varying solar constant only as an approximation to sulphate aerosol geoengineering), it could be possible to help restore substantial amounts of Northern Hemisphere Arctic sea ice with a substantially lower amount of reduced incoming solar radiation than what has previously been implemented where uniform solar constant reductions were made which impacts upon other aspects of the climate more substantially.

The spatial heterogeneity of a given diagnostic, as well as different responses of diagnostics to specified levels of geoengineering in the climate system, is one of crucial importance. Not only does this raise extremely complicated social issues around who 'wins' and who 'loses', but it also raises the complexity of deciding which variable to choose as "the" important variable (e.g. Lucarini, 2013). Increased greenhouse gases alter the hydrological cycle essentially through two processes. The first is purely by increasing the temperature of the climate, whilst the second involves altering the ability of the atmosphere to lose heat via emitting radiation when condensation occurs. The first of these increases the intensity of the hydrological cycle, whilst the second acts as a damper on this effect by reducing the ability of a condensing atmosphere to lose heat as easily (and so reduces the rate of condensation and so rainfall, Allen and

Ingram, 2002, Bala, 2008). The net effect is an increase in precipitation for increases in greenhouse gases. Reducing the temperature of the Earth back to pre-industrial climate via sulphate aerosol geoengineering, however, only addresses the first of these physical effects and therefore causes a global average reduction in precipitation. The first study on optimisation of stratospheric geoengineering (to achieve optimal temperature and precipitation anomalies from pre-industrial climate) was Ban-Weiss and Caldeira (2010). Using the NCAR CAM3.1 model, they first perform a variety of geoengineering simulations with different aerosol profiles. Then they use an optimisation model to predict aerosol profiles most suited to reducing the root mean squared error in zonal average temperature and zonal average precipitation minus evaporation - and these predicted aerosol profiles give temperatures and precipitation anomalies close to zero. They conclude that aerosol profiles can be found that result in similar current climate conditions, however, as expected the aerosol profiles to minimise temperature and precipitation minus evaporation are different. Disparity between temperature and precipitation effects from sulphate aerosol geoengineering have been also noted by Rasch et al. (2008).

Ricke et al. (2010) show, using a large ensemble of simulations of HadCM3, substantial spatial anomalies in both temperature and precipitation (often in particularly politically powerful countries) in simulations of the A1B emissions scenario (see McCarthy et al., 2001, for more details on this and other scenarios) with sulphate aerosol geoengineering from the A1B scenario with no geoengineering used as a control. The amount of aerosol needed to return China to within one standard deviation of their pre-industrial temperature in 2070 would not be the same as that for India. Not only does this creates 'winners' and 'losers', but arguably creates a very strong tension between different countries.

The substantial difference in annual average incoming solar radiation according to latitude may be regarded as one of the most important drivers in producing many large scale features climate system, such as the Hadley Cell (Gill, 1982). The intensity of these convection cells is not only related to the vertical and meridional velocities, but are also intimately related to zonal wind due to the effects of rotation of the Earth

and atmosphere. The atmosphere is a thermo-hydrodynamical system which may be regarded as a heat engine, generally transporting heat from the warm sources (often around the equator) to the cold sinks (often around the poles) generating entropy by irreversible processes (Peixoto and Oort, 2007, Lucarini, 2012). Simulations of geoengineering have shown substantial reductions in the meridional (equator-to-pole) temperature gradient of the Earth (e.g. Schmidt et al., 2012, Kravitz et al., 2013), potentially having substantial regional effects on the climate system despite global average properties of the climate for a single chosen diagnostic, such as temperature or precipitation, being indistinguishable from the pre-industrial climate.

Irvine et al. (2012) point to tensions arising due to the different timescales for different aspects of the climate system to respond to geoengineering. Their simulations show that to keep sea level rise to a minimum would require aggressive geoengineering whilst to keep surface temperature change to a minimum would require much less geoengineering.

Whilst many studies of geoengineering have simply incorporated changes of a reduced solar constant as an approximation to injecting aerosols (e.g. Kravitz et al., 2011), some have incorporated a representation of sulphate aerosols and investigated certain chemical effects. One concern raised is the possible effect of increased acid rain (Robock, 2008). However, acid rain due to increased sulphate aerosols is not currently thought to be a major risk due to stratospheric aerosol geoengineering as they contribute a relatively small amount of aerosol to the total tropospheric and stratospheric sulphate aerosol budget (Rasch et al., 2008). Kravitz et al. (2009) tested this idea by performing climate model simulations. They concluded that the effects of increased acid rain were likely to be too small to negatively affect most ecosystems.

Another fundamental component of the climate system is the biosphere (Peixoto and Oort, 2007), for which the effect of geoengineering is also highly uncertain. Despite decreases in direct radiation, the increased levels of diffuse light from geoengineering (which will lead to whiter skies, Kravitz et al., 2012) have been suggested to be beneficial to plants as photosynthesis is more efficient under diffuse light. One

of the first experiments was Govindasamy et al. (2002), although they only reduced the solar constant. Coupled with a doubling of CO_2, reductions of incoming solar radiation have been simulated with the CCM3 atmospheric general circulation model which created almost a doubling of Net Primary Productivity (NPP) relative to the $1\,\mathrm{x}\,CO_2$ world, (Govindasamy et al., 2002). However, in their study, the large increase in NPP is attributable to the doubling of CO_2, with simulations of a CO_2 world without solar reductions showing NPP increases slightly larger than that with reductions in incoming solar radiation. More recent modelling research using the CAM3.5 model with a sulphate aerosol implementation, however, has shown that crop yields increase in a high-CO_2 geoengineered world largely due to the effects of heat stress being diminished whilst the effects of CO_2 fertilisation are retained (Pongratz et al., 2012) - possibly indicative of both the CCM3 model used in Govindasamy et al. (2002) underestimating the effects of heat stress on the biosphere as well as missing out important biosphere responses from enhanced diffuse light. There is a corresponding need to narrow the uncertainty in this area and the impact of changes to diffuse and direct radiation on the biosphere.

Biogeochemical coupling has been simulated to be of substantial importance in capturing the changes in precipitation following decreases in incoming solar radiation to offset the radiative forcing from elevated CO_2, in particular due to reductions in transpiration due to elevations in CO_2 (Fyfe et al., 2013). Climate models that do not incorporate such carbon coupling may therefore substantially underestimate reductions in precipitation, and as a result many important biosphere impacts (and the results from impact models), in a geoengineered world.

Uncertainty can be seen to remain high in all domains of study. Robock (*in prep/personal communication*) points out the need for better observations of volcanic eruptions in order to understand the full effects of geoengineering on the climate system. Wunsch et al. (2013) furthermore point out the necessity for more and better observations of the climate system, and in particular the oceans that have been sparsely observed. They present the view that geoengineering proposals must include an understanding of its influence on the climate system which retains memories of

disturbances for thousands of years, given the length of time that may be necessary to continue geoengineering, and that lack of sufficiently fine and long observations severely hinders the understanding of the impacts in a system that retains memories of induced disturbances for thousands of years.

If geoengineering were to be terminated before CO_2 levels have been stabilised and reduced, it would cause an abrupt perturbation to the climate system. Termination from geoengineering could be catastrophic (Baum et al., 2012). It can be argued to be likely that it would be very hard to sustain such a scheme for hundreds, if not thousands of years (Baum et al., 2012). The rapid loss of aerosols from the atmosphere is expected to lead to a rapid increase in the global average temperature back to the temperature of a non-geoengineered climate. Some modelling work has been conducted on the termination effect (Brovkin et al., 2009, McCusker et al., 2012, Jones et al., *submitted*). These show increases in global average temperature, precipitation and decreases in sea ice cover, although little effect upon NPP by geoengineering or its termination in these simulations.

A number of other possible benefits to SRM techniques have been suggested, such as possibly prevent the Earth's climate system from passing some tipping points (e.g. Shepherd et al., 2009). Simulations performed by Irvine et al. (2010) analyse one tipping point, namely the irreversible melting of the Greenland Ice Sheet. They deem that geoengineering can help prevent the climate system from passing this tipping point. However, Lenton (2013) suggests that the idea that geoengineering could be used as an emergency technology capable of avoiding tipping points to be seriously flawed, but that further research should be continued - to analyse what circumstances exist (if any) where geoengineering could successfully be employed to avoid a tipping point or reverse one which has been passed - to reduce this uncertainty. In particular, many climate models have insufficiently simulated the pace of continental ice disapearance at the end of the last ice age, and are missing potentially important processes for simulating the behaviour of the Greenland Ice Sheet (Lenton et al., 2008). Understanding their ability to reproduce the past changes to alterations in radiative forcing, therefore, is an important issue.

Some ways to increase confidence in the results of geoengineering modelling studies have been proposed. The Geoengineering Model Intercomparison Project (GeoMIP, Kravitz et al., 2011) was created in order to understand the variation of model responses to precisely the same experiments. Before its creation, many geoengineering studies being performed involved both different experiments and different models (Kravitz et al., 2011). Kravitz et al. (2011) suggest there is a need, therefore, to have a standardised set of experiments to compare model responses and help narrow uncertainty. Similarly, Jones et al. (2010) investigated the response of geoengineering in the HadGEM2 and GISS-ModelE. Despite good general agreement, there was still some disagreement, which led to a similar proposition that many different climate models performing the same experiments may help reduce uncertainty of the simulated climate response to geoengineering.

There are four GeoMIP experiments, called G1, G2, G3 and G4. They aim to understand the effects of sulphate aerosol geoengineering increasing the complexity of the experiment from a large solar constant reduction combined with a high amount of CO_2 designed to maximise the signal to noise (G1) to full implementation of stratospheric aerosol in a more realistic emissions pathway (G4). Modelling groups around the world have been invited to participate in conducting these experiments, and 12 state of the art models have been used to perform these simulations. GeoMIP may, therefore, be thought of as the most robust set of experiments and analysis for the general climate response to geoengineering to date.

Analysis of the GeoMIP scenarios has only recently began, with G1 being the most heavily analysed scenario to date. Simulations of the first experiment, 'G1', in which models simulate the climate response to an abrupt quadrupling of CO2 from preindustrial concentrations brought into radiative balance via uniform insolation reduction, show a reduction of the solar constant largely offsets the global average surface temperature increase forced by greenhouse gases but compared to the preindustrial climate leaves the tropical regions cooler and the poles warmer (Kravitz et al. 2013). The hydrological cycle is affected although there is no robust impact on summer monsoon precipitation over the Indian subcontinent. Whilst some regions

in the tropics experience notable impacts such as the reduction in precipitation due to suppression of convection, the annual mean precipitation minus evaporation (PE) anomalies for G1 are small over large regions (less than 0.2 mm day^{-1} over 92% of the globe). Similar to some other studies, global average NPP increases by 118% relative to the (simulated) preindustrial levels - mostly as a result of CO_2 fertilization, but reduced heat stress on the plants compared to a high CO_2 is shown to contribute.

Despite this, large uncertainty remains in the models themselves. Steinhaeuser and Tsonis (2013) analysed a large suite of Coupled Model Intercomparison Project (CMIP) 5 models have substantial differences in their ability to simulate the statistical properties of many fields, in particular temperature and precipitation, yielding large differences between not only the models themselves but also having large discrepancies between all models and observations. Villegas et al. (2013) also analyse a large suite of CMIP3 and and CMIP5 models primarily to understand their reliability for impact model research. Their analysis differs from that of Steinhaeuser and Tsonis (2013), but they show that there are substantial differences in temperature and precipitation in the models. They conclude with an estimate of 30-50 years for the models to have sufficiently good simulation of precipitation to be fed directly into an impacts model.

Moreover, in implementing approximations to a sulphate aerosol geoengineered world in implementing solar constant reductions, many GeoMIP scenarios do not consider the effects of important factors. The amount needed to counteract a certain level of SO_2 radiative forcing depends on factors such as refractive index, coagulation, and particle size (e.g. Niemeier et al., 2010, Pierce et al., 2010, Pope et al., 2012), meaning that aerosol microphysics can be important in the lifetime and position of aerosol in the stratosphere. Kravitz et al. (2011) simulated the effect of injection of black carbon into the stratosphere as a geoengineering method. They find that an injection rate of 1 Tg per year causes little surface cooling for large radii, whilst the same injection rate for small radii yields large surface cooling and also stratospheric warming of over 60 K. Simulations where injections of the same particles but in the lower and mid stratosphere, respectively, show substantial differences in the amount of aerosol that persists in the stratosphere and its lifetime. Therefore, whilst simulations

involving reductions in the solar constant or fixed aerosol optical depths can be useful, they are not capable of elucidating on the full climatic response to sulphate aerosol injection.

Large differences in estimates of the amount of SO_2 to counteract a doubling in SO_2 have been simulated, ranging between 2 Mt of SO_2 to 4 Mt of SO_2 per year with dependency on particle size (Rasch et al., 2008), whilst up to 10 Mt of SO_2 per year has been estimated (Wigley, 2006). Heckendorn et al. (2009) simulated a range of emissions rates, from 1-10 Mt per year, in a 3D chemistry climate model and found higher rates of injection lead to larger aerosol formation, mostly due to coagulation, and as a result a nonlinearity between stratospheric aerosol burden and injection rate due to more rapid sedimentation of larger aerosols. Sunshade reductions and fixed optical depths miss these important and uncertain processes.

As that there is no current well observed geoengineering effort, all current studies and conclusions about geoengineering are reliant on the models themselves, which have been seen to give differing response and large uncertainty ranges. If the models respond in unphysical ways or have any major systematic flaws (e.g. Driscoll and Lucarini, *in preparation for submission*) then the simulated impacts of geoengineering will be substantially different from the true climate response.

Robock et al. (2013) point to volcanic eruptions as being of integral importance in being the natural and well observed analogue to inform and constrain the climatic response to geoengineering. Other observations may also be useful. For example, Mitchell et al. (2014) note some similarities in the atmospheric circulation between the Earth and Mars. An observed Martian dust storm is seen to influence the Martian polar vortex and such studies could serve as a useful complement in aiding understanding of the Earth's polar vortex. Volcanoes are nonetheless the most relevant natural analogue and provide useful constraints and information for understanding the climatic response to sulphate aerosol geoengineering. Two of the papers that helped push sulphate aerosol geoengineering into wider attention were Wigley (2006) and Crutzen (2006) both of which make reference to volcanic eruptions. Wigley (2006) also states the opinion that the Mount Pinatubo eruption of 1991 did not seriously

disrupt the climate system, so geoengineering with sulphate aerosols should therefore "present minimal climate risks". As shall be seen later, the belief by Wigley (2006) is not entirely true, but it is true that volcanic eruptions are highly important and fundamental analogues for sulphate aerosol geoengineering. Indeed, it can be seen in e.g. Shepherd et al. (2009) that part of the attraction of sulphate aerosol geoengineering is because volcanoes have already injected sulphates into the atmosphere from an eruption, yielding better assessments of the effects than many other methods without having to speculate or rely solely on climate models. This is especially useful when appreciating the sheer magnitude of uncertainty in all of the areas discussed above.

Therefore, this thesis focuses on the interface of the observed climatic impact of volcanic eruptions, and the simulated response to both volcanic eruptions and geoengineering in an attempt to provide the most rigorous and constrained information as may be possible, and also thus serve as a platform to interpret other simulations that have and will be performed in this area. This thesis draws together the important observed and robust climatic responses to volcanic eruptions, and performs analysis of volcanic eruptions' simulated radiative and dynamical response in many of the most state of the art climate models (many of which are being used in GeoMIP). Simulations of volcanic eruptions are performed, whilst the mechanisms in the dynamical response following volcanic eruption are elucidated. Finally a set of geoengineering simulations is analysed, the thesis conclusions are presented and the further work that results from the investigations in this thesis is discussed.

Chapter 2

Volcanic Eruptions and Their Effect on Climate As Model Verification

2.1 Literature Review

Volcanoes occur on many planets and their moons, and can profoundly affect the climate system of those in a variety of ways and on a number of timescales (e.g. Fiedler and Wilson, 1975, Carr, 1976, Crumpler et al., 1997). On Earth, a long term and well known impact is the emission of CO_2 into the atmosphere, contributing in part to the greenhouse effect (e.g. Leavitt, 1982, Williams et al., 1992). However, volcanoes are also responsible for the drawdown of CO_2: enhanced weathering that arises from rare massive volcanic events produces large amounts of weatherable rock that drawdown greenhouse gases. This large drawdown of CO_2 following such eruptions is one possible cause (or contributor) of the neoproterozoic "snowball Earth" events that occured approximately 600-700 million years ago (Pierrehumbert, 2010), where the Earth underwent a fundamental change of state and the surface of the Earth became entirely or nearly frozen over for what is estimated to be many millions of years.

Some volcanoes, such as shield volcanoes are typically non-explosive, frequently releasing fast flowing lava. Other volcanoes, such as composite volcanoes, tend to be less frequent but much more explosive in their eruptions, and it is these volcanoes which have a shorter term climatic impact. One of the main ways explosive volcanic eruptions have climatic impact is through emission of sulphur dioxide (SO_2) which

converts to sulphate aerosol (H_2SO_4) once in the atmosphere. Typically, unless the sulphur dioxide reaches the stratosphere, the sulphate aerosols are rained out within a matter of days to weeks, and so often for such a climatic impact, the SO_2 must usually reach the stratosphere by direct injection - where it can then remain for months to years (Cole-Dai, 2010). However, an increased stratospheric aerosol burden has also been witnessed to occur by other mechanisms. The Nabro volcanic eruption of 2011 injected sulphur dioxide into the upper troposphere which, due to deep convection and circulation associated with the Asian summer monsoon, got lofted into the stratosphere. Large stratospheric optical depth enhancement was first observed on 1 July, 18 days after the eruption (Bourassa et al., 2012). However, these indirect stratospheric aerosol enhancing events are rare in comparison to direct injection of sulphur dioxide into the stratosphere.

Once the sulphur dioxide (SO_2) enters the stratosphere it activates a series of chemical reactions. The rate limiting step is the first reaction, where SO_2 is converted with OH to HSO_3:

$$SO_2 + OH + M \longrightarrow HSO_3 + M \tag{2.1}$$

where M is a stabilising molecule (Bork et al., 2012). Upon the creation of HSO_3, further oxidation occurs:

$$HSO_3 + O_2 \longrightarrow HO_2 + SO_3 \tag{2.2}$$

The final reaction is hydration of SO_3 to H_2SO_4, as follows:

$$SO_3 + H_2O \longrightarrow H_2SO_4 \tag{2.3}$$

This final reaction represents the main sink of atmospheric SO_3 (Morokuma and Mugurama, 1994). High rates of conversion of sulphur dioxide to aerosol can persist throughout the volcanic cloud's evolution provided that sufficient recycling of HO_2 to OH occurs (NASA, 1992). Observed and simulated e-folding times of SO_2 gas, such

as that from the Total Ozone Mapping Spectrometer (TOMS), yield values around 30-40 days (e.g. Bluth et al., 1992, Pitari and Mancini, 2002, Forster et al. 2007).

Sulphate aerosol scatters incoming shortwave radiation (SW) back to space and also absorbs solar near infrared (NIR) radiation and upwelling long wave (LW) radiation from the surface and atmosphere below (Stenchikov et al. 1998, Ramachandran et al. 2000, Andronova et al. 1999). This decrease in incoming shortwave radiation then causes a cooling of Earth's surface (Robock and Mao, 1995). For a given mass load, the scattering of SW radiation is modulated by the particle size distribution, and as the aerosol particle size increases scattering of incoming SW radiation decreases (Timmreck et al. 2009, Rasch et al. 2008), whilst the larger the aerosol particle size the greater the absorption of LW radiation.

Using the Stratospheric Aerosol and Gas Experiment measurements, Weisenstein et al. (1997) estimated that the e-folding time for sulphate aerosol decay in the stratosphere to be about 11.4 months. The typical e-folding lifetime for tropically injected volcanic aerosols in the stratosphere is estimated to be around 12-14 months from other observational studies (Lambert et al., 1993, Baran and Foot, 1994, Barnes and Hofmann, 1997), and larger particles fall out of the stratosphere faster than smaller particles. Other analysis, by Grant et al. (1996) using the Advanced Very High Resolution Radiometer, gave an estimate of 8.8 months for the e-folding time for the 20° S to 30° N region. Gravitational settling is a major factor in this sulphate aerosol stratospheric lifetime (Benduhn and Lawrence, 2013). Benduhn and Lawrence (2013) further showed in simulations that the role of sedimentation in determining the stratospheric lifetime is a complex function of all the properties, such as shape and density, but with a strong relation to the particle size. An additional factor contributing to decrease in surface temperatures is where this sedimentation of stratospheric aerosols increases the number of cloud condensation nuclei, hence cloud lifetime and planetary albedo. Sulphate aerosols can also have a longer residence time in the stratosphere if they are injected into the tropics because of uplifting due to the Brewer-Dobson circulation (Kravitz and Robock (2011), Budyko (1977), Stenchikov et al. (1998)).

Moreover, Kuebbeler et al. (2012) performed simulations that suggested increased sulphate aerosol loadings would likely cause an additional net negative forcing in the long-wave due to optically thinner cirrus clouds coming as a result in a reduction in the ice crystal nucleation rate. Increased sulphate aerosol via either volcanoes or geoengineering has also been suggested (Rasch et al., 2008, Robock, 2008) and simulated (Kravitz et al., 2009) to increase acid rain due to the aerosol sedimentation. Whilst the simulations of Kravitz et al. (2009) reveal that an injection of 5 Tg of SO_2 is not enough to impact upon most ecosystems, most aerosol deposition occurs in midlatitudes due to a strong cross-tropopause flux in the regions of the Earth's jet streams. It is possible, therefore, that this uneven distribution of the aerosol sedimentation may cause some important negative impacts upon some regions of the biosphere. Ash and other aerosols injected by the volcanic eruption into the troposphere can cause short term regional warming, and both the sulphate aerosol and ash emissions from volcanic eruptions can also have negative impacts on human health and air quality (Hansell and Oppenheimer, 2002, Hansell, 2003, Hansell and Oppenheimer, 2004, Horwell and Baxter, 2006, Hansell et al., 2006, Longo et al., 2008). Indeed, such is the potential damage from volcanic ash there is a great need for it to be sufficiently monitored, with new techniques being recently proposed (e.g. Mackie and Watson, 2014). Figure 2.1 shows some of the basic radiative and chemical effects following a volcano eruption.

When volcanoes erupt, they can emit large amounts of water vapour. Pinto et al. (1989) suggested that water vapour emissions from volcanic eruptions are thought to have negligible direct climate and chemical effects. They note that even for eruptions as large as the Mount Pinatubo eruption of 1991, the amount of emitted water vapour would increase the water vapour burden in the stratosphere by no greater than approximately 10% due to condensation in the rising volcanic plumes. Despite this, Joshi and Shine (2003) simulate with a GCM of intermediate complexity the increases in stratospheric water vapor following the Pinatubo eruption and find a global-mean radiative forcing of $+0.1$ W m^{-2}, which counteracts a small, but not negligible, portion of the radiative effects of the stratospheric sulphate aerosol.

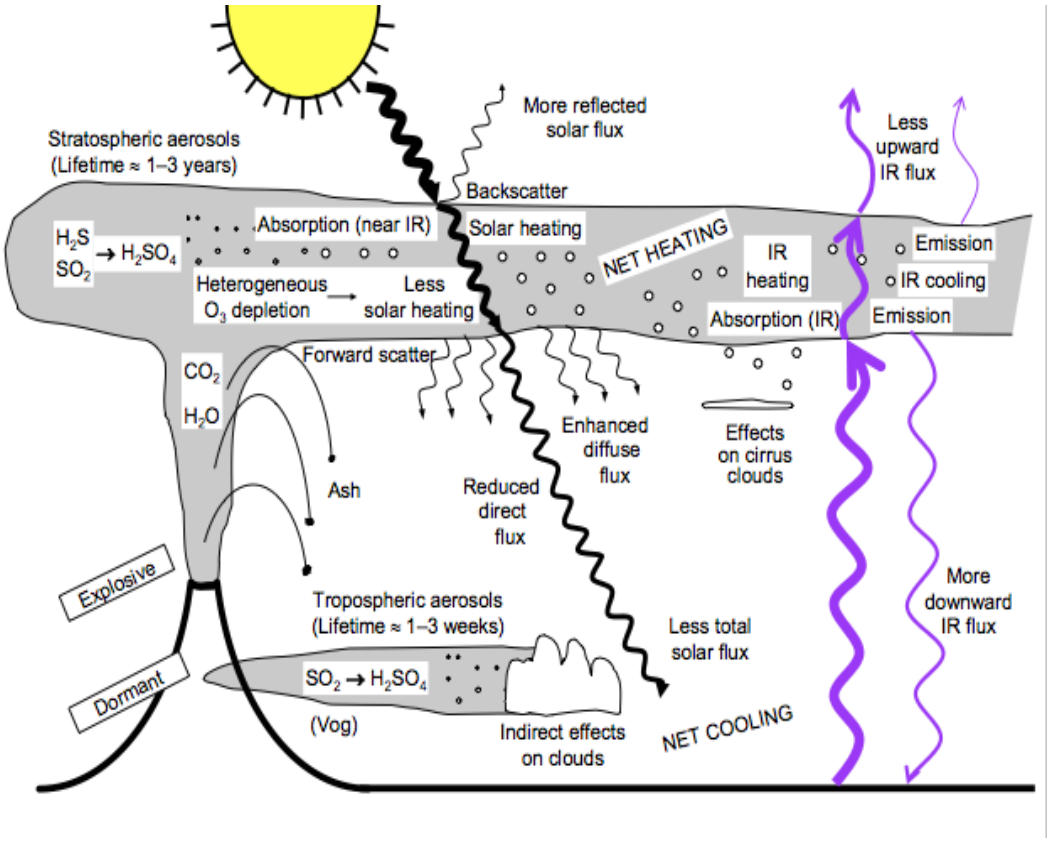

Figure 2.1: Basic radiative and chemical impact of a volcanic eruption on the Atmosphere, from Robock (2000)

The existence of an effect of volcanic eruptions upon the stratospheric ozone level has been suggested for at least a few decades (e.g. Elanskii et al., 1987). Studies have both simulated and observed stratospheric ozone reductions following volcanic eruptions (e.g. Kerr, 1993, Steil et al., 2004, Telford et al., 2009). Moreover, observations following the eruptions of St. Augustine (1976), Mt. Etna (2004, 2009) and Eyjafjallajökull (2010) have showed a strong local decrease in tropospheric ozone in the volcanic plumes (Vance et al., 2010). Whilst volcanic eruptions mainly destroy ozone as a result of the creation of stratospheric sulphate aerosols, which provide a catalytic surface for reactions to take place, they can also contribute to ozone destruction in other ways.

Volcanic eruptions can emit large amounts of hydrogen chloride (HCl), which can substantiially exceed the amount of chlorine released into the *troposphere* from anthro-

pogenic chlorine emissions. However, emissions into the stratosphere from volcanoes are low as HCl removal in the volcanic plume can reduce the HCl concentrations greatly, meaning substantially less enters the stratosphere (Tabazadeh and Turco, 1993). Despite this, the HCl that enters the stratosphere can, along with the sulphate aerosols, play a role in stratospheric ozone depletion. In the future, ozone depletion from volcanic eruptions has been proposed to be much less than today due to substantially decreased anthropogenic chlorine and bromine emissions, with resulting negligible effects of volcanic eruptions upon ozone after 2100, if future projections of anthropogenic bromine and chlorine emissions are correct (Halmer, 2005).

Banda et al. (2013) simulated changes in tropospheric methane levels following the Mount Pinatubo eruption of 1991 in a one-dimensional chemistry model coupled to a radiative transfer model. Stratospheric ozone depletion is found to be a major source of influence upon methane lifetime as the increased incoming UV radiation due to less ozone alters the tropospheric photolysis rates of important chemical species, although other natural processes have non-negligible effects upon tropospheric methane. The major response is a decreased growth rate of about 7 ppb yr^1 during 1993 that takes a few decades to return to normal levels.

The climatic effect of a volcanic eruption, particularly its local radiative and dynamical effect, can be very much dependent on latitude (e.g. Oman et al., 2005, Fischer et al., 2007, Stenchikov et al., 2006, Kravitz and Robock, 2011) and the time of year of the eruption (Kravitz and Robock, 2011). The Kasatochi eruption of August 2008, for example, was the largest eruption since Mount Pinatubo, injecting about 1.5 Tg of SO_2 into the stratosphere. Despite this, it showed negligible climatic effects because the injection was too late in the year and too high latitude to cause any major effect shortly after the eruption, whilst also being too low in magnitude and too high in latitude to last into spring.

Miller et al. (2012) show from analysis of ice-cap growth from Arctic Canada and Iceland, that between 1275 and 1300 AD summer cold and ice growth began abruptly, coinciding with one of the two most volcanically active half centuries of the past thousand years. They also perform climate simulations which show similar results

and moreover that this perturbation can then be maintained by sea ice and ocean feedbacks, indicative that many proximate eruptions might have caused sufficiently large and longtermed anomalous loading of sulphate aerosol in the stratosphere to cause the onset of what is known as the "Little Ice Age".

Occassionally in the Earth's past, there have been 'supervolcanoes'. Supervolcanoes have been considered to be those which yield more than 450 km^3 of magma (Self, 2006). Substantial climatic effects can be expected from a supervolcanoes. The best studied supervolcano is Toba. Estimates of stratospheric sulphate aerosol loading caused by the Toba eruption vary between 100 Mt to 10 Gt (see Oppenheimer, 2002, for more details). Jones et al. (2005) performed simulations of a 'hundred times Pinatubo' volcanic eruption in the HadCM3 model by scaling the optical depths seen for Pinatubo by one hundred, which falls in the range of estimates for Toba. The simulations produced a cooling of about 10 °C for a few months after the eruption, with temperatures continuing to be affected for many years after the eruption. Robock et al. (2009) also performed simulations of the Toba eruption with sulphate aerosol injection. They perform simulations with two different models and also with and without interactive chemistry. Some simulations were forced with the SO_2 history of Pinatubo, but scaled up by a factors on the order of magnitude of 10, 100 and 1000 the SO_2 amounts of Pinatubo. Other experiments include interactive chemistry in the simulations. They conclude that the Toba eruption certainly could produce a a decade-long volcanic winter, with severe impacts upon the biosphere.

Despite these simulations, Timmreck et al. (2010) performed simulations of the Toba eruption using an interactive aerosol scheme. A larger eruption causes higher collision rates, larger particle sizes and so higher fall out, thus limiting the impact of the eruption. In their simulations, they find a temperature response that last around ten years and is about three times weaker with a maximum global temperature reduction of approximately -3.5 °C. Regional impacts show a greater maximum local cooling of approximately -12 °C suggesting that significant regional impacts are possible, although much more of the biosphere experiences milder climatic conditions compared to previous super-eruption estimates. Timmreck et al. (2009) performed

simulations of a large eruption occuring in 1258. They note again a similar simulated response such that despite a large aerosol loading, the surface temperature response of $\approx 0.4\,^{\circ}\mathrm{C}$ was not substantially larger than that of Pinatubo, which they attribute once again to increased aerosol particle sizes for larger eruptions. Consistently, Lane et al. (2013) find no major evidence of a temperature cooling in East Africa from their analysis of sediments in the region that would correspond to being able to cause extremely large impacts upon the biosphere as previously suggested. Conflicting results from simulations and observations suggest substantial uncertainty into the effects of super-eruptions and highlight the importance of accurate aerosol microphysics in climate model simulations for super-eruptions and the magnitude of surface cooling experienced post-eruption.

In contrast to this surface cooling following volcanic eruptions there is heating in the lower stratosphere due to the increase in longwave and near visible wavelength absorption in the region from the presence of aerosols. Following this surface cooling and lower stratospheric heating, an important dynamical effect occurs (see figure 2.2 for a schematic diagram), which is believed to result in Northern Hemisphere winter surface warming over Eurasia and North America, and cooling over Greenland and the Eastern Mediterrean (e.g. Robock and Mao, 1992, Robock, 2000, Shindell et al., 2004, Fischer et al., 2007). The warming of the tropical lower stratosphere creates an anomalous temperature/density gradient between the equator and poles. By thermal wind shear, this causes a strengthening of the zonal winds, which results in the stratospheric polar vortex strengthening. Moreover, reduced surface temperatures in the tropical regions reduce the meridional surface temperature gradient, which causes a reduction in the Eliassen Palm Flux - essentially, a measure of the eddy heat flux and momentum flux (Andrews et al., 1987) - into the vortex, which means that the vortex is less disturbed and thus stronger. Further, chemical reactions which result in ozone depletion (e.g. Telford et al., 2009) cool and strengthen the vortex, and the reduced temperatures cause more ozone depletion, creating a feedback loop. Model simulations have shown that an atmosphere with an intentionally cooler polar stratosphere (without the increased temperature gradient in the equatorial stratosphere),

and thus stronger zonal winds, can divert wave activity equatorward which further strengthens the vortex (Borovko and Krupchatnikov, 2009).

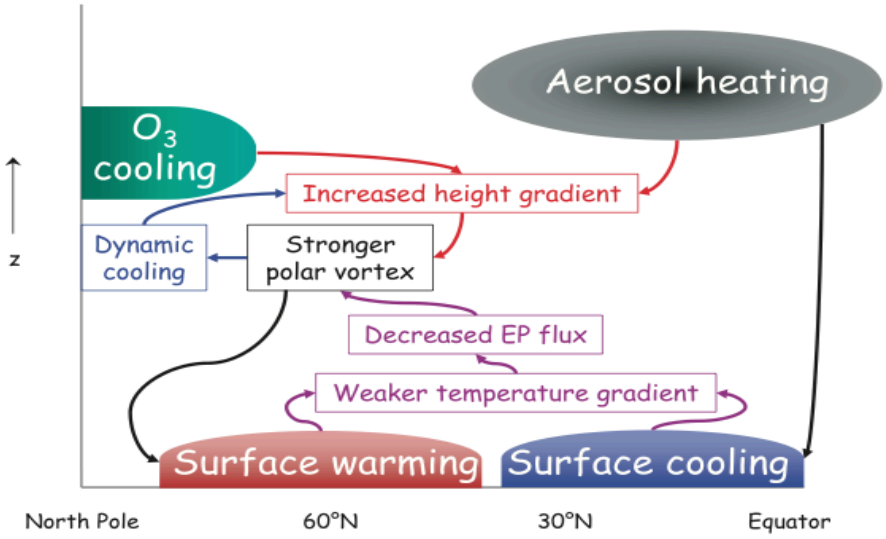

Figure 2.2: Schematic diagram illustrating the proposed volcanic mechanism from Stenchikov et al. (2002)

If the vortex is sufficiently strong, its influence can extend down to the surface, causing a positive North Atlantic Oscillation/Arctic Oscillation. The North Atlantic Oscillation (NAO) is an index corresponding to the difference in MSLP between the Azores and Iceland (Rodwell et al., 1999), and the Arctic Oscillation (AO) is defined as the first hemispheric empirical orthogonal function (EOF) of sea level pressure variability (Stenchikov et al., 2002). Essentially the NAO can be thought of as the AO over the Atlantic region, with the AO previously being termed as a global extension of the NAO (Christiansen, 2008). Positive values correspond to anomalously low pressure over the poles, and anomalously high pressure at the midlatitudes and hence a stronger East-West stormtrack (see figure 2.3 for a diagram of effects in positive and negative AO phases). After large volcanic eruptions a positive phase of the AO has been observed for the following one to two winters (Stenchikov et al., 2002), and the stronger east-west winds cause advection of energy due to anomalous strong wind blowing warm oceanic air overland, and this causes anomalously warm temperatures over major northern hemisphere landmasses. The effect of this changing circulation

can be seen in the DJF temperature anomaly following Mount Pinatubo, shown in figure 2.4. The anomalous warming over NH land is typical for the two winters following a tropical volcanic eruption that injects into the stratosphere (Stenchikov et al., 2006).

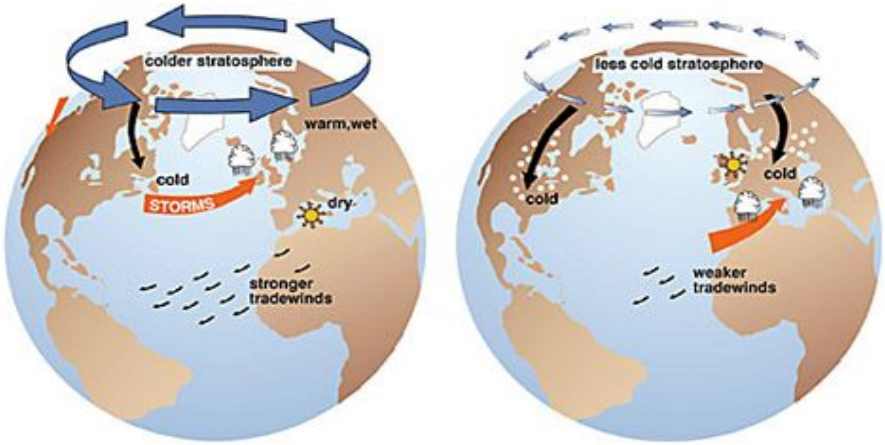

Figure 2.3: Some of the effects of a positive phase AO (left) and a negative phase (right)

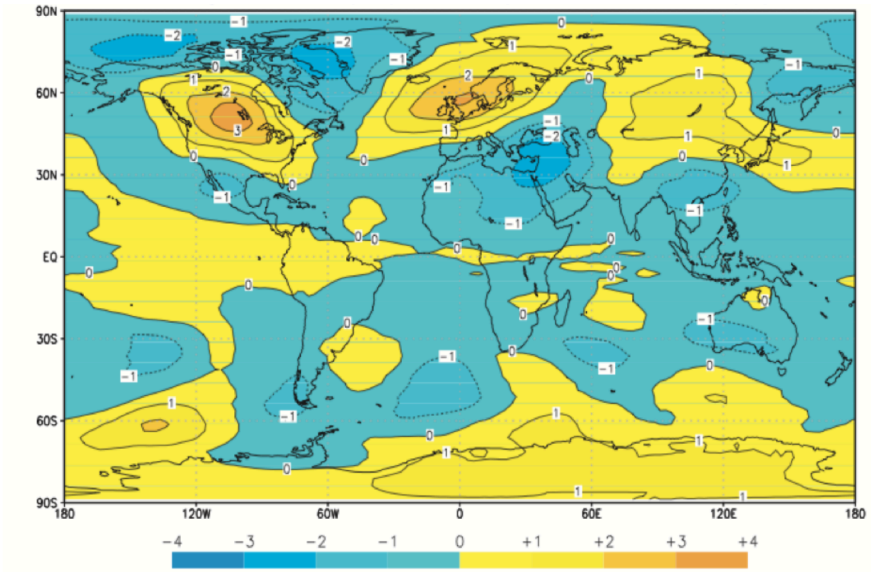

Figure 2.4: Post Pinatubo 1991-1992 DJF Lower Troposphere Temperature Anomalies from the 1984-1990 average showing anomalous surface warming over North America and Eurasia, from Robock (2003)

During a positive NAO the stormtracks also shift northwards, Northern Europe becomes anomalously warm and wet, whilst Southern Europe becomes anomalously

dry (Walter and Graf, 2005). Christiansen (2008), analysed 13 volcano eruptions over the period 1883 to 1991 and found that the AO, the NAO and the Pacific North American Oscillation (PNA) are all positive in the first winter after eruptions. This is statistically significant for the NAO in particular, with both the numbers of events and their amplitudes being statistically significant. There has been some debate about which is physically more meaningful, for example Ambaum et al. (2001) and Christiansen (2008). Christiansen (2008) concludes that from his results the NAO should be credited as the physical mode of variability, with the interpretation that the NAO is excited following an eruption is more simple and economical than the alternative explanation that the AO and PNA patterns negatively interfere in the Pacific so as to cancel each other out to give the observed MSLP fields. However, it should be recalled that nonetheless both the NAO and the AO indexes are positive following volcanic eruptions. Large magnitude values of the AO are associated with significant changes in the likelihoods of extreme weather events, such as cold air outbreaks, snow and high winds across Europe, Asia and North America, as well as modulating the position of surface cyclones over the Atlantic and Europe (Baldwin and Dunkerton, 2001).

As mentioned, the Pinatubo eruption caused serious effects on the hydrological cycle, namely a large decrease in precipitation and a period of record decrease in runoff and river discharge into the ocean (Trenberth and Dai, 2007). They note that this is of concern for sulphate aerosol geoengineering studies - in contrast with the view of Wigley (2006) who suggested that the Mount Pinatubo did not severely disrupt the climate system. Figure 2.5 shows changes to precipitation, runoff and the Palmer Drought Severity Index (PDSI) following Mount Pinatubo from Trenberth and Dai (2007). The PDSI is a diagnostic developed by Palmer (1965) as a measure of drought in the region. It incorporates not only drought in a region but other measures such as evapotranspiration into a single diagnostic, and can be seen as a more complete assessment of the effects on hydrology than precipitation and is an important diagnostic for assessing water availability in a region (see Palmer, 1965, for extensive documentation). Precipitation effects following volcanic eruptions are

not purely radiatively driven, but indeed the effects of the dynamical response to a volcanic eruption on precipitation in the Asian monsoon region can often overwhelm the radiative effects on precipitation (Anchukaitis, 2010).

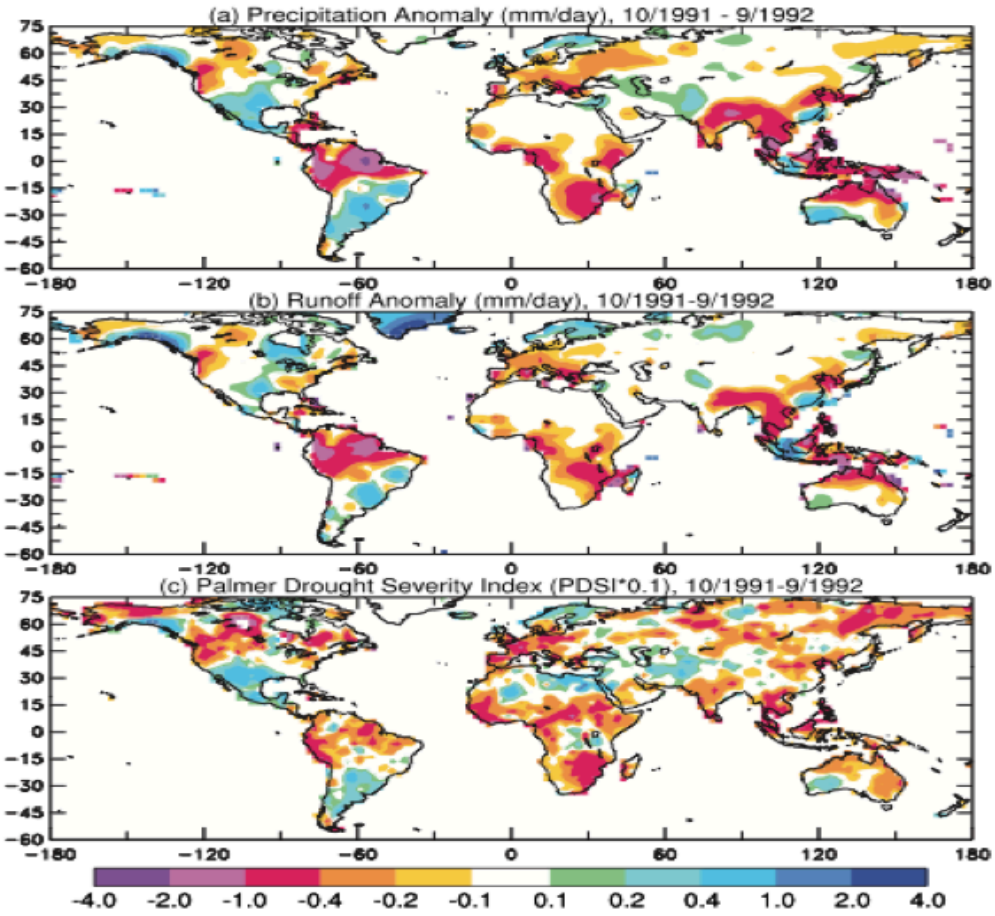

Figure 2.5: (a) Precipitation and (b) Runoff Anomalies, and (c) Palmer Drought Severity Index following Pinatubo, from Trenberth and Dai (2007)

2.2 Ocean Response

Following the reduced surface flux of radiation into the oceans caused by a volcanic eruption, ocean heat content and sea level can reduce (Gleckler et al., 2006, Stenchikov et al., 2007). The cooling of the surface causes subduction of water downwards into the ocean (Gleckler, et al., 2006) where the signal persists for decades. The relaxation timescale for the SST's to return to close their unperturbed climate state from model

simulations has been estimated at about ten years (Stenchikov et al., 2009). However the entire relaxation process for the whole ocean might take more than a century (Stenchikov et al., 2009).

Decrease in precipitation following volcanic eruptions causes increased ocean salinity whilst the reduced temperatures increase the density of the northern hemisphere high latitude upper ocean, causing vertical instability and encouraging ocean convection. Moreover, increased zonal winds in the NH following a volcanic eruption causes a strengthening of ocean stirring in high latitudes. Therefore, volcanoes, can increase the strength of the Atlantic Meridional Circulation (AMOC) (Stenchikov et al., 2009). The model simulations performed by Stenchikov et al. (2009) found a maximum increase in the AMOC of 2.7 Sverdrup (Sv, 1 Sv $= 0.001\,\mathrm{km^3 s^{-1}}$) and 1.8 Sv for the 1816 Tambora and 1991 Pinatubo eruptions respectively. The decadal time scales of this circulation mean that the maximum occurs at 5-15 years post-eruption. Their simulations also show increases in sea-ice extent and mass following a volcanic eruption - consistent with geoengineering studies demonstrating that sulphate aerosol geoengineering could reduce sea ice loss. A possible cause for concern for modelling studies and also controllability of sea ice under a sulphate geoengineering scenario, however, is that Stenchikov et al. (2009) note that the radiative forcing effects on sea ice extent are less than linear as the sea ice is also affected by ocean circulation changes that are nonlinear.

Negative surface temperature anomalies in the Middle East are a distinctive feature of the positive phase of the AO caused by a volcanic eruption (e.g. Robock, 2000, Stenchikov et al., 2006, Fischer et al., 2007). Correspondingly, the resulting dynamical changes following a volcano can be important for ocean circulation and ecosystems. Robock (2003) suggests that such a large local cooling followed the Pinatubo eruption that the Red Sea underwent a total overturning, killing coral at the seabed. This is also an important feedback to capture in a geoengineering modelling study. However, the strong sporadic forcing from a volcano intensifies vertical mixing processes, notably turbulent diffusion, seasonal convection and overturning, whilst a constant

forcing of the same average intensity, such as that in a geoengineered world, may produce a different vertical ocean thermal structure (Stenchikov et al., 2009).

2.3 Interactions with ENSO and the QBO

Of the past four major eruptions - Agung (1963), Fuego (1974), El Chichón (1982) and Pinatubo (1991) - two of them (El Chichón and Pinatubo) have erupted during the El Nino phase of the El Nino Southern Oscillation (ENSO, Robock (2000)). ENSO is a major mode of atmospheric variability, characterised by sea surface temperature changes off the west of coast of South America in the tropics. It is often hard to separate the signals between volcanoes and ENSO particularly due to low numbers of well observed volcanic eruptions, and the contribution to the resultant effects on climate and the NAO phase is not completely clear (Graf et al., 2007). The polar vortex has been suspected to be influenced by ENSO (e.g. Thomas et al., 2009), by an increased flux of planetary waves propagating up through the troposphere and into the stratosphere during El Nino, which then propagate towards the vortex and weaken it (Graf et al., 2011). Graf and Zanchettin (2012) also identify a tropopsheric pathway, in identifying a "subtropical bridge" where planetary wave activity can propagate through the troposphere and affect the NAO pattern. Therefore, it is possible that ENSO can obscure the true volcanic signal not only in the tropics but also over the Northern Hemispheric continents. Christiansen (2008) analysed 13 volcanic eruptions since 1883 to present day, and assessed the role that ENSO plays in the NAO signal in observations and concludes that the NAO and AO signals are both positive and statistically significant for the first winter after an eruption. Christiansen (2008) finds no evidence that the ENSO phase influences the NAO following a volcanic eruption - although adds that due the low numbers of ensembles, this result should be treated with caution.

The Quasi-Biennial Oscillation (QBO), has also been suggested to have an influence on the effect of volcanic eruptions on climate (e.g. Stenchikov et al., 2004, Thomas et al., 2009). The QBO is the major mode of tropical stratospheric variability. It is a

cycle of the equatorial zonal wind in the tropical latitudes in the stratosphere, where the winds switch from easterlies to westerlies and back to easterlies, and so on, in a quasi-periodic fashion on average every 28 to 29 months. The easterly, or westerly, winds develop in the upper stratosphere, around 3 hPa, and then propagate downwards (Baldwin et al., 2001). Evidence that westerly QBO winds cause a stronger polar vortex stem from research originally conducted by Holton and Tan (1980, 1982) and McIntyre (1982). The hypothesis states that westerly winds in the equatorial regions allow the propagation of planetary waves from the midlatitude and polar regions, through the lower equatorial stratosphere, whilst easterly equatorial waves block the propagation of these planetary waves and guide them polewards so that when they eventually break they are more likely to disturb the vortex (a schematic diagram is given in figure 2.6). Therefore it is believed the vortex, and hence the NAO, can be strengthened or weakened, depending on the QBO state.

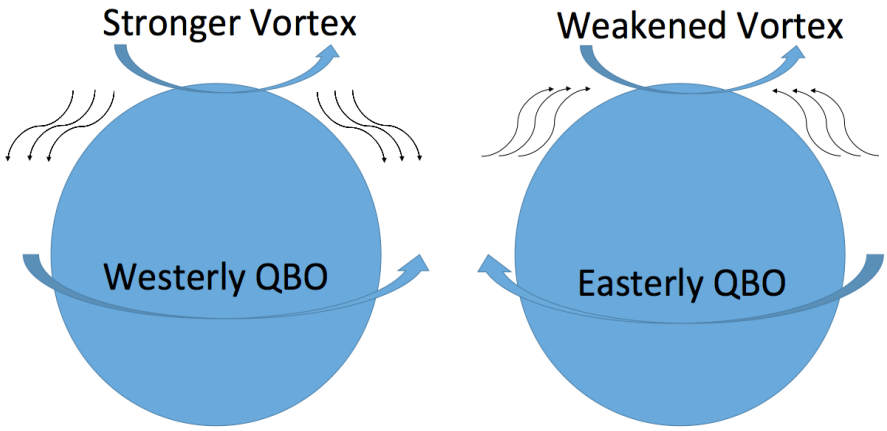

Figure 2.6: A schematic diagram representing the ability of waves to propagate into the tropical regions during a westerly QBO (left) and an inability to propagate into these regions, and thus disturb the vortex, during an easterly QBO

Stenchikov et al. (2004) detail that, following the Mount Pinatubo eruption, the vortex in both winters was strengthened relative to climatology. Despite a significant decline in the radiative aerosol forcing in the second winter, the vortex was observed to be stronger in the second winter than in the first winter. They therefore proposed that the QBO played a role in the vortex being stronger in the second winter than

in the first - noting that the QBO was in an easterly phase in the first winter and westerly phase in the second winter. They perform model simulations of the Mount Pinatubo nudging the simulated equatorial winds to the observed winds, and note that this achieves a more strengthened vortex in the second winter. They conclude that modelling the correct phase of the QBO is crucial for simulating the temperature change in the lower stratosphere. Moreover, they note that the volcanic aerosol and QBO effects are unlikely to be a simple linear superposition of the two effects, due to a threshold depedence of the refraction of planetary waves on the strength of the polar night jet. Other studies have also suggested that the QBO could have a significant modulation on the volcanic effect on climate (e.g. Thomas et al., 2009). However, whilst in their study Thomas et al. (2009) investigate the effect of the phases of the QBO on the stratosphere in model simulations and find, similarly, that an easterly QBO phase leads to a weaker vortex during volcanic winters.

An additional source of complexity in identifying the volcanic signal on climate is the changes in the solar cycle that have been seen to cause changes in stratospheric temperatures and winds and there is a complex interaction between the 11-year solar cycle and the QBO which is not fully understood and has yet to be successfully simulated by climate models (Gray et al., 2010). There are only four well observed large eruptions (Agung, 1963, Fuego, 1974, El Chichón, 1982, and Pinatubo, 1991) and solar maxima have occured close to the times of Fuego, El Chichón and Pinatubo (Solomon et al. 1996). Indeed, it has been noted that more work remains to assess the dynamical interactions between all these modes of variability and the atmosphere following a volcano eruption (e.g. Graf et al., 2007).

2.4 Simulations of Climate following Volcanic Eruptions

Climate models have traditionally not simulated the observed response to stratospheric aerosol loading caused by volcanic eruptions sufficiently. Stenchikov et al.

(2006) analysed seven models used for the fourth assessment report that were uploaded to the Coupled Model Intercomparison Project 3 (CMIP3). These were all the models that specifically included representation of volcanic eruptions by including a layer of aerosol, instead of either not representing them, or representing them simply by a reduction in the solar constant. They found that the lower equatorial stratospheric temperature increase, caused by radiative heating from the aerosol, is represented in all the models sampled. However, the models showed less of an agreement with the observed post eruption northern hemisphere winter northern lower polar stratospheric cooling. Further, the 50 hPa geopotential height anomalies in the models generally show almost no anomaly relative to climatology whereas the observations show a very large negative anomaly of about 200m, indicative of an anomalously strong stratospheric polar vortex. Furthermore, the climate model simulated responses of the AO are singificantly weaker than in observations. Correspondingly the surface temperature anomalies related to observed dynamical changes are not sufficient in strength and spatial pattern in the CMIP3 models. Other simulations and assessments of why models fail to get the response have been done, such as those of Stenchikov et al. (2002), Stenchikov et al. (2004) that also show too weak a response when compared with observations.

Many proposals have been made as to why the vortex, AO, and surface response has not been captured in models, however it is presently not clear why dynamical effects are not captured (Marshall et al., 2009). Stenchikov et al. (2004) suggested the lack of a QBO could have an important effect on atmospheric processes following a volcanic eruption. Marshall et al. (2009) proposed that the climatology of the models may be inaccurate. Notably they suggest propagation of planetary waves from the troposphere into the stratosphere may be too large, such that it breaks and destabilises the vortex. Stenchikov et al. (2006) suggested that all but one of the models they analysed had winds that were too strong at 50 hPa averaged over $55 - 65^{\circ}$ N, when compared to observations. Therefore, they state that perhaps the winds in the models are too strong climatologically, which means there is a bias towards a positive AO, so therefore when a volcanic eruptions occurs, there is little anomalous effect

on the AO. Ottera (2008) suggested that models may simply fail to get a sufficiently strong positive AO to external forcings in general (also Graf *personal communication*), noting that many models have failed to reproduce the observed trend in the AO during the latter part of the twentieth century (see Shindell et al., 2001, for more details). However, this fails to explain why the models do not achieve a sufficiently strengthened polar vortex, and it is not clear whether the observed AO trend is real (e.g. Fyfe et al., 2013). Stenchikov et al. (2006), Ottera (2008) and Marshall et al. (2009) suggested stratospheric resolution may be important for capturing the relevant processes following a volcanic eruption. Dall'Amico et al. (2010) note that stratospheric processes in model simulations as recent as those used by the Intergovernmental Panel on Climate Change Fourth Assessment Report have been poorly represented. Whilst the stratopause height is typically around 1 hPa (Andrews et al. 1987) around half the Atmosphere and Ocean General Circulation Models (AOGCMs) used for the AR4 have a model top level beneath 2 hPa, and furthermore show significant cold bias around their 10 hPa levels suggesting compromised simulations in these regions due either to a low model top or insufficient stratospheric levels (Cordero and Forster, 2006). Specifically with regards to models used in previous volcanic investigations, of the seven models tested by Stenchikov et al. (2006) two of the models (GISS-EH, GISS-ER) have lid heights above the 1Pa level (at both 0.1 hPa, or roughly 70 km, each), whilst all the other models have model lid heights below the stratopause level - GFDL CM 2.0 (3 hPa), GFDL CM2.1 (3 hPa), NCAR CCSM3 (2.2 hPa), NCAR PCM1 (2.9 hPa), MIROC-medres (10 hPa). Furthermore, although the top lid of these latter models may appear to include most of the stratosphere, the vertical resolution of the model is usually severely degraded at these upper levels and there is strong damping applied to any wave disturbances.

Other suggestions as to why models have traditionally failed to simulate the observed response following volcanic eruptions include realistic changes in ozone which cause additional cooling of the stratospheric polar vortex (e.g. Ottera, 2008), however, as noted by Marshall et al. (2009) the response to the past major eruptions (before major ozone loss and larger amounts of ozone destroying chlorine in the atmosphere)

is similar to that of El Chichón and Pinatubo combined. Thus it is less likely for ozone inclusion to be a major factor in the simulation of a volcanic eruption. Finally, another proposal has been that of the realism of the aerosol implemented in the models is not sufficient (Ottera, 2008, Marshall et al., 2009). Marshall et al. (2009) also assessed the possibility that the strengthened vortex and positive NAO following volcanic eruptions was due to internal variability, but they conclude it is 'extremely unlikely' to be an artifact of internal variability, and so it is extremely likely that models are failing to capture a robust high-latitude climate response to volcanically injected sulphate aerosol. It is clear, therefore, that not only are models are failing to reproduce the observed response to stratospheric sulphate aerosol injected by volcanic eruptions - of concern for the accuracy of sulphate aerosol geoengineering modelling studies - and there is no single clear reason as to why this is the case, but also the precise response of the atmosphere to sulphate aerosol loading is unclear.

Chapter 3

Coupled Model Intercomparison Project 5 (CMIP5) Simulations of Climate following Volcanic Eruptions

3.1 Introduction

Climate model simulations of the historical period have, so far, been able to produce only a slightly strengthened stratospheric vortex that is very much weaker than the observations, and have failed to reproduce a positive AO and warming/cooling patterns over Eurasia and the Middle East, respectively, for the two NH winters following volcanic eruptions Stenchikov et al. (2006, S06 hereafter). S06 analysed seven models used for the Fourth Assessment Report of the Intergovernmental Panel on Climate Change (Intergovernmental Panel on Climate Change, 2007). They included all the models that specifically represented volcanic eruptions by including a layer of aerosol, and excluded those that either did not represent them, or represented them simply by a reduction in the solar constant. They found that the temperature increase in the lower equatorial stratosphere, caused by radiative heating from the aerosol, was reproduced by all the models. However, the models showed less agreement with the observed post-eruption NH winter polar lower stratospheric cooling. Further, the 50 hPa polar geopotential height (indicative of the strength of the stratospheric polar vortex) in the models generally showed almost no change, whereas the observations

show a large negative anomaly of about 200 m, revealing a statistically significant stronger than average polar vortex at the 90% level. Furthermore, the AO responses in the model simulations were significantly weaker than in observations; indeed, Otterå (2008) notes that some model simulations show no AO response. Correspondingly, the strength and spatial pattern of the surface temperature anomalies were not well reproduced.

Since the previous analysis of S06, which used simulations from the the World Climate Research Programme's (WCRP's) Coupled Model Intercomparison Project phase 3 (CMIP3) multi-model dataset (Meehl et al., 2007), climate models have undergone changes and improvements, and spatial and vertical resolutions have been increased. In this study, model simulations from the Coupled Model Intercomparison Project phase 5, (CMIP5, Taylor et al., 2011) are analysed with a particular focus on the impact of the largest volcanic eruptions on the NH winter circulation.

3.2 Models and Experiments

The model runs analysed in this study come from the historic simulations of the climate of the 20th century as standardised for the CMIP5. Models were forced with natural and anthropogenic forcings from the late 19th century to the early 2000s. Although the major external forcings (such as solar, greenhouse gases, land use) are standardised based on the most recent observational databases, no specific recommendations were issued for other forcings such as the stratospheric injection of sulphate aerosols from explosive volcanic eruptions. As for the CMIP3, most modelling groups imposed the stratospheric emissions for volcanic eruptions either from the reconstructions of Ammann et al. (2003, AM hereafter), its update Ammann et al. (2007, AM07 hereafter), or from the updated version of Sato et al. (1993, ST hereafter, updates available at data.giss.nasa.gov/modelforce/strataer). The AM dataset provides monthly latitudinal distributions of stratospheric optical depth for each volcanic event in 64 latitude bands, computed with an explicit representation of the spread of the aerosol cloud, taking into account the seasonal variations in

stratospheric transport. A fixed particle size distribution is assumed for all eruptions, with spherical droplets of sulphuric acid of effective radius of 0.42 μm. AM, however, only extends back to 1890. An updated dataset AM07 provides data well before the start of the historical simulations (1850) and many modelling groups use either AM07 or combine AM with ST to overcome this problem, as is detailed for individual models in Table 3.1.

The ST dataset provides monthly latitudinal zonal mean stratospheric optical depths for 24 layers between 15 km and 35 km together with variations of the particle's effective radius based on the observations of the 1991 Mount Pinatubo and 1982 El Chichón eruptions. In the GFDL-CM3 model the optical characteristics were calculated following Stenchikov et al. (1998) using the optical depths from the ST dataset and its updates.

Unlike the other models, MRI-CGCM3 interactively computes the conversion from SO_2 amount to stratospheric aerosol. It includes the aerosol model MASINGAR mk-2 (Tanaka et al., 2003), which calculates five species (sulphate, black carbon, organic carbon, mineral dust, and sea-salt) of aerosols from emissions and other processes, including sulphate aerosol of volcanic origin. The aerosol model is interactively coupled with the atmospheric component that calculates radiation and cloud microphysics and utilises the inventory of volcanic SO_2 emissions provided by Stothers (1996), Bluth et al. (1997), Andres and Kasgnoc (1998), Stothers (2001) and the optical properties of spherical sulfate aerosol droplets provided by OPAC (Optical Properties of Aerosol and Clouds) as in Hess et al. (1998).

Model analysis was restricted to those models that were forced with volcanic aerosol in the stratosphere which yielded a total of 13 different climate models at the date of commencing the analysis. Gillett et al. (2013) analyse a larger set of CMIP5 models' response to many forcings including volcanic eruptions. Whilst their analysis is not as detailed on volcanic eruptions, they perform a multi-model analysis of the NAO index following volcanic eruptions and this is very consistent with the results presented here. The models, with a brief description of the basic characteristics, are

listed in Table 3.1. Three models, GISS-E2-R, CCSM4 and GFDL-CM3, in their updated version, are common to both our analysis and that of S06.

Table 3.2 lists the nine major volcanic eruptions between 40° S and 40° N for 1883-present day as well as the anomaly period, the latitudes of eruption and the SO_2 injected in the lower stratosphere as reconstructed by Stothers (1996), Bluth et al. (1997), Andres and Kasgnoc (1998), and Stothers (2001). Following S06 the eruptions listed in Table 3.2 are a subset of the volcanic events analysed by Robock and Mao (1992). In the same approach as S06, high-latitude eruptions from those studied by Robock and Mao (1992) are not included because they appear to produce a qualitatively different effect on circulation than lower-latitude eruptions (Robock and Mao, 1995, Oman et al., 2005, Kravitz and Robock, 2011). The volcanoes listed in Table 3.2 also correspond to the volcanoes south of 40° N in Christiansen (2008) with the caveat that different dates are used for the first winter after the eruptions of Santa María and Fuego, shifting them forward one year with respect to the convention in Christiansen (2008). The implication of this choice is explored in section 3.4.

For comparison with observations the reanalysis of the 20th century version 2 (20CRv2) is employed (for more details on the dataset, see Compo et al., 2011). From this dataset only near-surface temperature and Mean Sea-Level Pressure (MSLP) fields for the period of 1871 to 2008 are used. The results compare similarly across a number of observational reconstructions such as HadCRUT2v and HadSLP1 (used in S06), and so the choice of product does not alter our conclusions. More information about the database is provided at http://www.esrl.noaa.gov/psd/. The ERA40 (Uppala et al., 2005) and NCEP/NCAR (Kistler et al., 2001) reanalysis fields are also used to compare with middle atmosphere circulation changes during the winter season for the largest eruptions after 1950.

To isolate the anomalies of the post-volcanic seasons and generate the average volcanic composite, the same averaging procedure employed by S06 is adopted, choosing a different reference time for each eruption and averaging two winter seasons after each eruption. The statistical significance of anomalies from the mean climatology is evaluated with a local two-tailed t-test. Also computed are the multi-model mean of

the post-volcanic anomalies averaging with equal weight the ensemble mean of each model. All models have been interpolated to a common 2.5° latitude x 3.75° longitude grid.

Using a large number of eruptions (lending an equal weight to each ensemble member in the computation) should help to average out spurious effects, for example due to incorrect sampling of the El Niño Southern Oscillation (ENSO) cycles, which cannot be controlled in these coupled ocean atmosphere simulations.

However, the 3.4 ENSO index is *also* calculated for each model (Table 3.3) using SST data by computing the area averaged total SST from the Niño 3.4 region, computing the monthly climatology (1950-1979) for area averaged total SST from the Niño 3.4 region, and subtracting the climatology from the area averaged total SST time series to obtain anomalies. These anomalies are then smoothed with a five-month running mean, and then normalised by the standard deviation over the climatological period (1950-1979).

Christiansen (2008) showed through analysis of observations that the largest volcanic eruptions of the 20th Century tend to be followed by a positive index of the North Atlantic Oscillation (NAO). He noted that the NAO signal is strongest and significant in the first year after the eruption and does not appear to be influenced by ENSO events or by the specific volcanic eruption chosen for the composite.

We computed the NAO index for each model and each ensemble member to test whether the simulated dynamical response to volcanic forcing projects onto the NAO index as noted by Christiansen (2008) from the observations. The NAO index is computed for each ensemble member of each model, as in Christiansen (2008). We first compute the Empirical Orthogonal Functions (EOFs) of the monthly winter (DJF) MSLP anomalies north of 20° N and between 110°W and 70°E for the period 1948-2000. Each pressure data point is weighted by the square root of the grid area it represents, consistent with Christiansen (2008). The seasonal winter (DJF) NAO index is computed from the monthly indices, defined as the principal component of the monthly anomalies of the MSLP projected onto the first EOF for the total period

1860-2000 and normalised to unit variance. The same index is computed for the 20CRv2 MSLP data. The EOF pattern for each model is shown in Fig. 3.1

Models and reanalysis are compared using a superposed epoch analysis of the winter NAO (DJF) for the nine volcanic eruptions listed in Table 3.2. Winters in the neighboring ten years close to the first winter after each eruption (five years before and five years after) are taken, as defined in Table 3.2, and generate an "eruption matrix" whose rows represent each eruption event. The eruptions in each ensemble member are considered to be independent events, hence the number of rows in the "eruption matrix" is different for each model because it depends on the number of ensemble members. The rows are then averaged to obtain the epoch composite of 11 years, from winter in year -5 to winter in year +5 with year 0 the first winter after an eruption.

The statistical significance of the epoch analysis is estimated using the bootstrap method (Efron and Tibshirani, 1986). This is reshuffled with replacement of the elements of each row to generate a new "random eruption matrix" and average the rows into a new epoch composite. The procedure is repeated 5,000 times obtaining a distribution of NAO values for each lag of the epoch composite. The random composites are drawn from the original epoch matrix to preserve the structure of the sample. The normalization procedure described in Adams et al. (2003) is also adopted to avoid possible biases due to single outliers in each volcanic window, but the main conclusions are not affected by the normalization. Furthermore, the level of the NAO index is compared for each year of the composite with the 5 %-95 % and 1 %-99 % percentile levels of the bootstrap distribution.

We explore the value of the NAO in both the first and second post-volcanic winters and assess the significance of these using a bi-nomial distribution with the probability of the single event (σ) estimated from the full timeseries. As noted in Christiansen (2008), σ is in general different from 0.5 which is due to the probability distribution of the NAO index not being normal. σ for each model is reported in Fig. 3.10 and 3.11.

The main conclusions are robust with respect to the definition of the winter season (DJF or DJFM) and presented here are the results for the NAO index computed for the DJF composite to allow comparison with previous results in the literature.

Table 3.1: Models used in the study and their basic characteristics (horizontal resolution, vertical levels and model top), imposed aerosol forcing and number of ensemble members available. In the last column are listed the variables analysed for each model (T ≡ 1.5 m temperature, P ≡ mean sea level pressure, Z ≡ geopotential height).

Model Name	Modeling Group	Atmospheric Resolution	Model Top	Volcanic Forcing	N. of ens. members	Variables
bcc-csm1.1[a]	Beijing Climate Center, China Meteorological Group	T42L26	2.9hPa	Ammann et al. (2003)*	3	T,Z,P
HadGEM2-ES[b]	Met Office Hadley Centre	1.25° x 1.875° L38	3hPa	Sato et al. (1993)	4	T,Z,P
HadCM3[c]	Met Office Hadley Centre	2.5° x 3.75° L19	5hPa	Sato et al. (1993)	10	T,Z,P
CanESM2[d]	Canadian Centre for Climate Modelling and Analysis	T63L35	1hPa	Sato et al. (1993)	5	T,Z,P
CNRM-CM5[e]	Centre National de Recherches Meteorologiques / Centre Europeen de Recherche et Formation Avancees en Calcul Scientifique	T127L31	10hPa	Ammann et al. (2007)	10	T,Z,P
GISS-E2-H[f]	NASA Goddard Institute for Space Studies	2° x 2.5° L40	0.1hPa	Sato et al. (1993)	5	T,Z,P
GISS-E2-R[f]	NASA Goddard Institute for Space Studies	2° x 2.5° L40	0.1hPa	Sato et al. (1993)	5	T,Z,P
NorESM1-M[g]	Norwegian Climate Centre	0.9° x 1.25° L26	2.9hPa	Ammann et al. (2007)	3	T,Z,P
CCSM4[h]	National Center for Atmospheric Research	0.9° x 1.25° L26	2.9hPa	Ammann et al. (2007)	6	T,Z,P
CSIRO-Mk3-6-0[i]	Commonwealth Scientific et Industrial Research Organization with Queensland Climate Change Centre of Excellence	T63L18	10hPa	Sato et al. (1993)	10	T,Z,P
MRI-CGCM3[l]	Meteorological Research Institute	T159L48	0.01hPa	interactive**	3	T,Z,P
MPI-ESM-LR[m]	Max Planck Institute for Meteorology	T63L47	10hPa	Sato et al. (1993)	3	T,Z,P
GFDL-CM3[n]	NOAA Geophysical Fluid Dynamics Laboratory	C48L48	0.01hPa	Sato et al. (1993) and Stenchikov et al. (1998)	5	T,Z,P

The references for each model are: a) Wu et al. (2008), b) Collins et al. (2011), c) Collins et al. (2001), d) Chylek et al. (2011), e) Voldoire et al. (2011), f) Schmidt et al. (2006), g) Kirkevag et al. (2012) and Kirkevag et al. (2008), h) Gent et al. (2011), i) Rotstayn et al. (2010), l) Mizuta et al. (2012) and Yukimoto et al. (2011), m) Raddatz et al. (2007), Marsland et al. (2003),n) Donner et al. (2011)

*The Ammann et al. (2003) dataset spans the period 1890-1999. bcc-csm1.1 uses updates by Ammann in 2004 to cover 1870-1999 combined with Sato et al. (1993) for the period 1850-1869

**From stratospheric SO_2 injection data from Stothers (1996), Bluth et al. (1997), Andres and Kasgnoc (1998), and Stothers (2001).

Table 3.2: Major low latitude eruptions from 1883 to present day.

Volcano	Eruption Date	Latitude	Winters analysed	Reference Period	Lower Strat. SO_2 mass (Tg)*
Krakatau	Aug 27, 1883	6.10° S	1883-1884 1884-1885	1860-1882	22
Tarawera	Jun 10, 1886	38.23° S	1886-1887 1887-1888	1860-1882	4-5
Bandai	Jul 15, 1888	37.60° N	1888-1889 1889-1890	1860-1882	3-4
Santa María	Oct 24, 1902	14.76° N	1903-1904 1904-1905	1890-1901	4
Quizapu	Apr 10, 1932	35.65° S	1932-1933 1933-1934	1915-1931	3
Agung	Mar 17, 1963	8.34° S	1963-1964 1964-1965	1934-1955	17
Fuego	Oct 10, 1974	14.47° N	1975-1976 1976-1977	1965-1973	4
El Chichón	Apr 4, 1982	17.36° N	1982-1983 1983-1984	1976-1981	14
Pinatubo	Jun 15, 1991	15.13° N	1991-1992 1992-1993	1985-1990	20

*From stratospheric SO_2 injection data from Stothers (1996), Bluth et al. (1997), Andres and Kasgnoc (1998), and Stothers (2001), Gao et al. (2008)

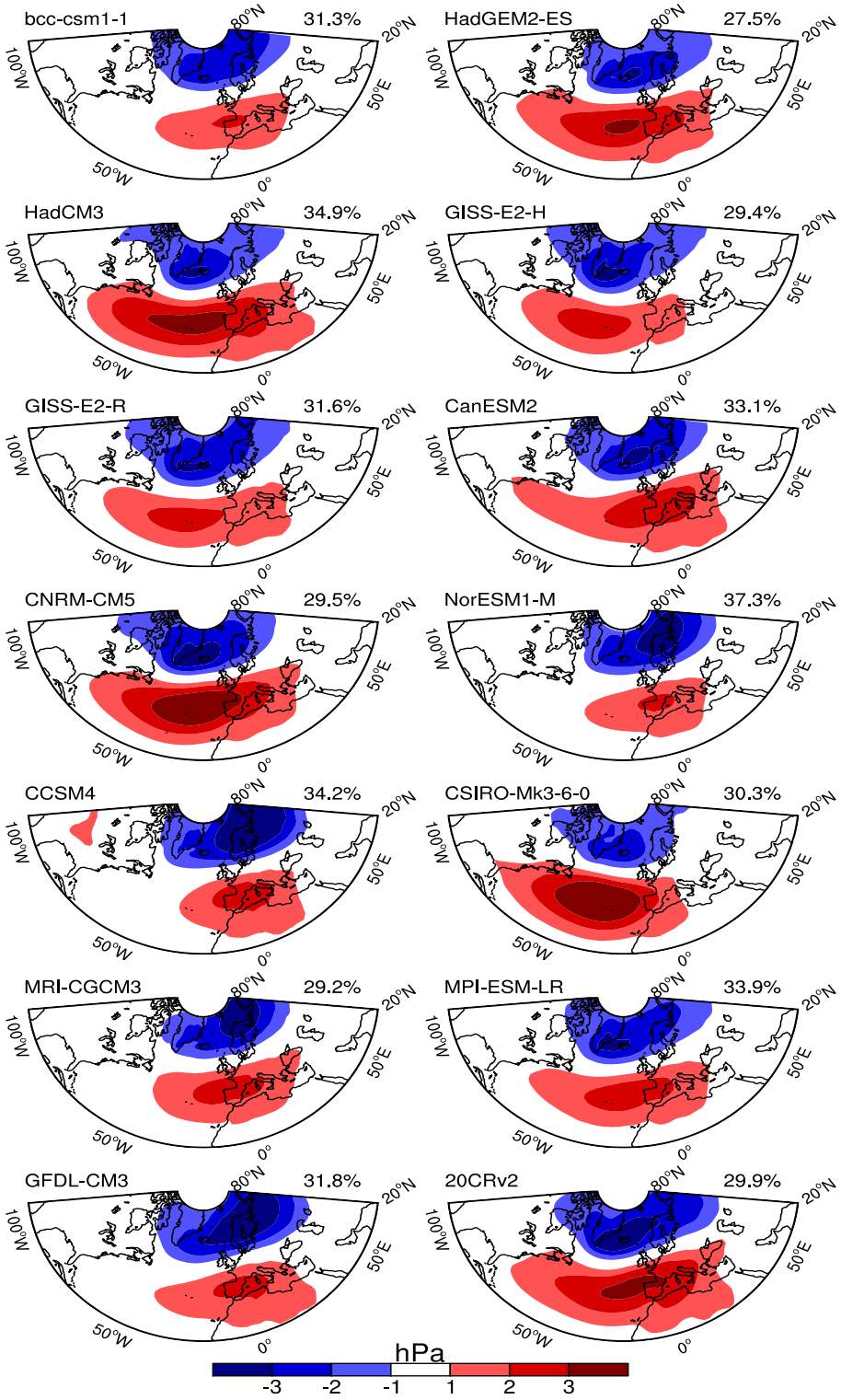

Figure 3.1: Leading EOF of the monthly winter (DJF) mean sea level pressure anomaly over the North Atlantic region (110° W-70° E) for each model ensemble mean and 20CRv2 over the period 1860-2000. EOF values are expressed as hPa. In the top right corner of each plot is indicated the percentage of variance explained by the first EOF.

3.3 Results

3.3.1 Direct Radiative Effect of Volcanic Aerosol

Due to a lack of direct information on the radiative forcing of volcanic aerosol for each model, the time series of the anomalies in the reflected short wave (SW) radiation at the top of atmosphere (TOA) (Fig. 3.2) is chosen as a rough proxy for the global radiative effect of the stratospheric aerosol, as in S06 (their Fig. 1). All the models perform consistently with each other and show the increase in the reflected SW radiation corresponding to the major explosive eruptions and do not show any appreciable differences compared with the CMIP3 models shown in S06. The largest anomaly in the reflected SW radiation is observed for the bcc-csm1-1 model whereas MRI-CGCM3 simulates the lowest signal among the models. MRI-CGCM3 computes interactively the effect of the volcanic aerosol from the stratospheric SO_2 load and shows a lower scattering efficiency of incoming SW radiation with respect to the other models, even in the satellite-constrained era. This is possibly due to the interactive chemistry conversion processes affecting the properties of the aerosol created from the SO_2 in the lower stratosphere. Large differences between this model and all other models, forced by imposed changes in lower stratospheric optical depths, raises questions about the realism of the MRI model with regards to the TOA anomalies.

As noted in S06, a larger spread among the model responses is observed for the early eruptions and less uncertainty appears for the most recent El Chichón and Pinatubo events. Notably, the largest effect on the reflected SW radiation for the eruptions pre-1900 is observed in the models that adopt the AM reconstruction.

As a measure of the anomalous heating forced by the volcanic aerosol in the lower stratosphere, the anomalies in the de-trended 30° S-30° N, 50 hPa temperature are analysed. Fig. 3.3 shows that the models simulate an increase in the lower stratospheric temperature of about 2 K, up to 4 K for the largest eruptions of Pinatubo and Krakatau. The largest temperature anomalies are simulated by the models using the AM database, with heating for the Pinatubo eruption up to 10 K for CCSM4 and 7 K for NorESM1-M. MRI-CGCM3 shows anomalies close to the multi-model mean

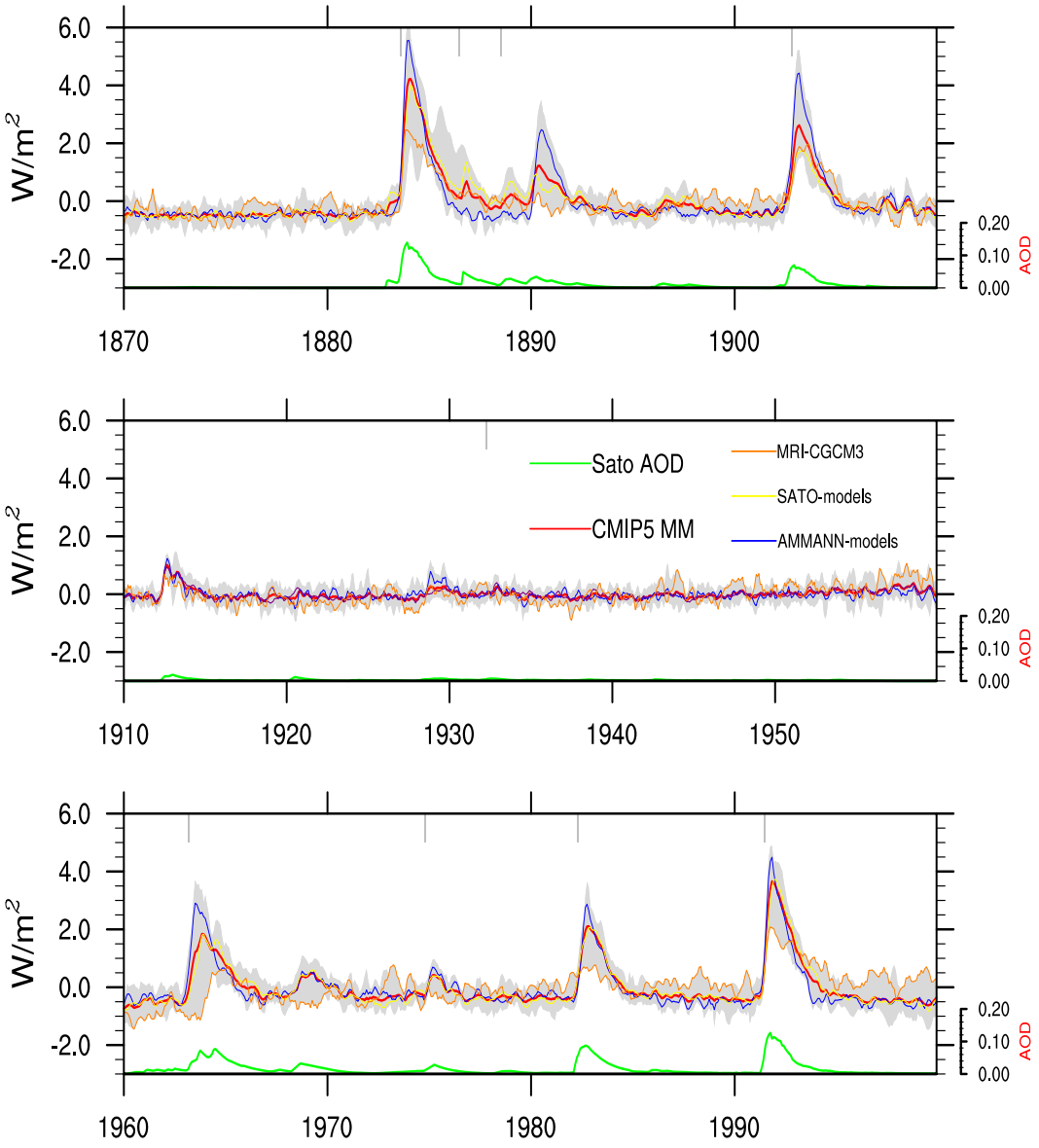

Figure 3.2: 3-months running average of global averaged de-trended and de-seasonalised TOA outgoing shortwave radiation anomalies for the 13 CMIP5 models listed in Table 3.1, over the period of 1860-2000. The gray shading shows the spread among the minimum and maximum of the means of each model ensemble. The lines show the multi-model mean (CMIP5-MM) and the multi model mean for the models using Sato et al. (1993) database and Ammann et al. (1993). The ensemble mean for MRI-CGCM3 is shown, which computes interactively the evolution of volcanic aerosol. The green line at the bottom shows the 30° S and 30° N volcanic aerosol optical depth (AOD) at 550 nm from Sato et al. (1993) and updates. The grey bars at the top of plots indicate the occurrence of the nine volcanic eruptions listed in Table 3.2.

and generally larger than observed for the models using Sato et al. (1993) database, but places the peak of the warming associated with the eruption of Agung about one year later than the other models.

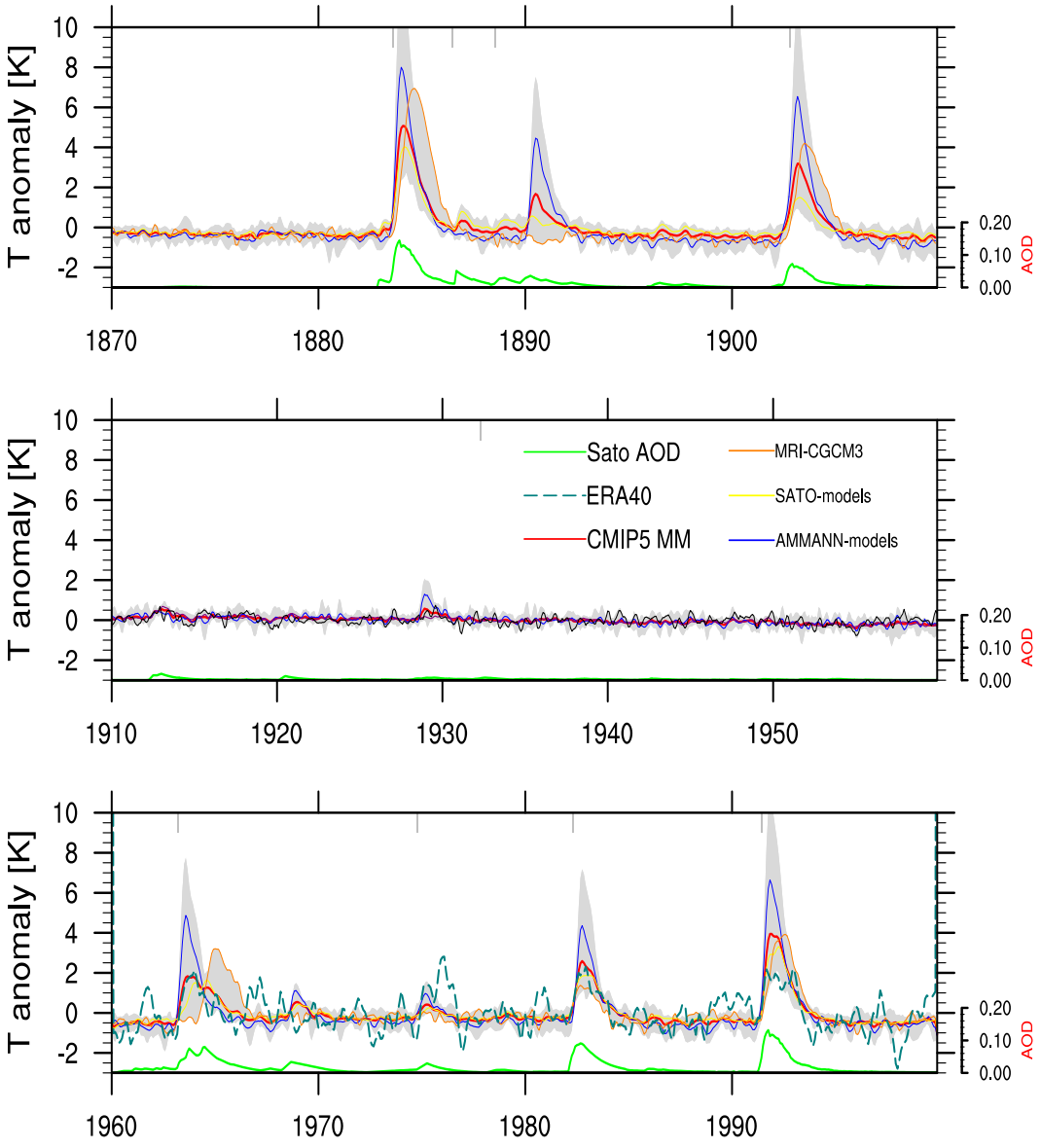

Figure 3.3: As Fig. 3.2 but for the 50 hPa temperature anomalies averaged between 30° S and 30° N. In the bottom panel the corresponding 50 hPa temperature anomalies from ERA40 are included.

The multi-model mean appears in good agreement with the temperature anomalies from the ERA40 reanalysis for the eruptions after 1960. The overestimation of the warming associated with Pinatubo is likely in part due to the cooling effect of the easterly phase of the QBO in the winter 1991-1992 (Ramachandran et al., 2000, Stenchikov et al., 2004), not accounted for in the CMIP5 models.

3.3.2 Surface Temperature and Mean Sea Level Pressure - Multi-Model Averages

Fig. 3.4 shows the NH composites of surface temperature, mean sea-level pressure (MSLP) and geopotential heights for the observations and the multi-model mean. Near-surface temperature and MSLP for the post-volcanic winter season (as given in the fourth column in Table 3.2) are first focused upon. Fig. 3.4a shows in the reanalysis the well known significant surface warming signal over northern Europe and Asia, where anomalies reach up to 2 K. Significant cooling is observed over NE America and also, though not significant, over the Middle East. As noted in S06, a warming signal also appears on the Eastern Pacific but this could be spurious due to a positive ENSO sampling bias. A general cooling is observed in the Tropical region, although weak and barely significant. The reanalysis surface temperature anomaly in the Arctic region appears unusually warm, but the reliability of the reconstructed lower tropospheric temperature at high latitudes reduces the significance of the anomaly (Compo et al., 2011).

The observed surface temperature anomalies in the NH post-volcanic winters are closely related to changes in the winter circulation as confirmed by the MSLP anomalies (Fig. 3.4c). In agreement with previous studies (e.g., S06), in the reanalysis a significant positive NAO-like pattern marks the North-Atlantic region, with negative pressure anomalies in the Arctic region and positive over the North-Atlantic. Notice that the minimum and maximum of the anomaly are both displaced northward with respect to the pattern of the leading mode of variability in the MSLP anomalies in the region as observed in Fig. 3.1 for the 20CRv2.

The multi-model aggregate of surface temperature and MSLP shows no such pattern (Fig. 3.4b,d). A general cooling is observed in the surface temperature anomaly field, however no dynamical response to a large tropical volcanic eruption can be seen in the multi-model aggregate. Fig. 3.5a,b reveals large areas of significantly different temperature and MSLP between the observations and models, especially over areas associated with the positive NAO and DJF surface warming.

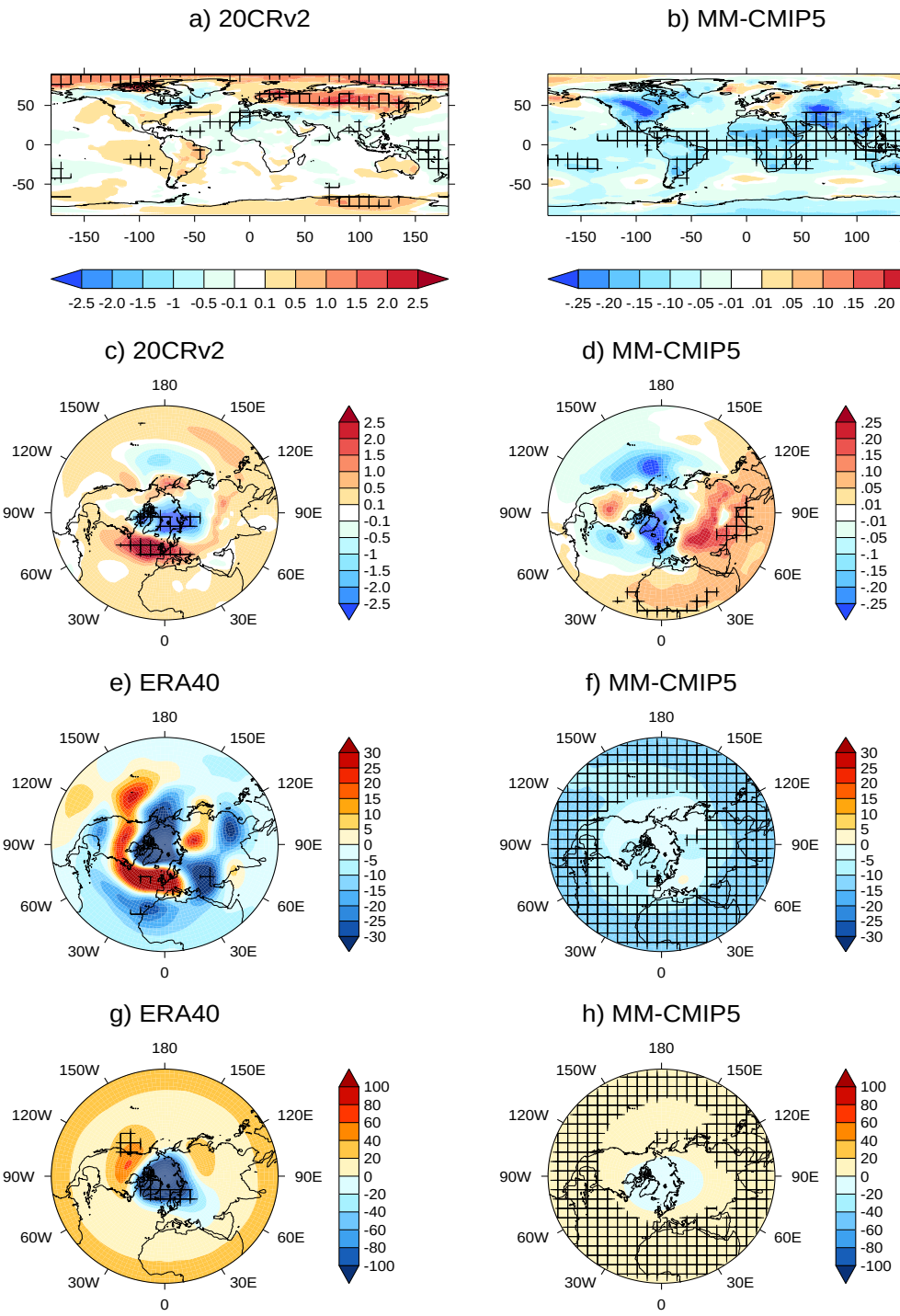

Figure 3.4: Comparison between reanalysis and multi-model mean. Composite anomaly averaged after 2 post-volcanic winters for (a,b) near-surface temperature (K), (c,d) mean sea level pressure (hPa), (e,f) and (g,h) respectively 200 and 50 hPa geopotential (m). The anomalies in (e,g) are computed for the last four volcanoes listed in Table 3.2. Hatching displays, for the left column areas at or over 95 % significance using a local two tailed t-test, for the right column where at least 90 % of models agree on the sign of the anomaly. Notice the different scale in (a,b) and (c,d)

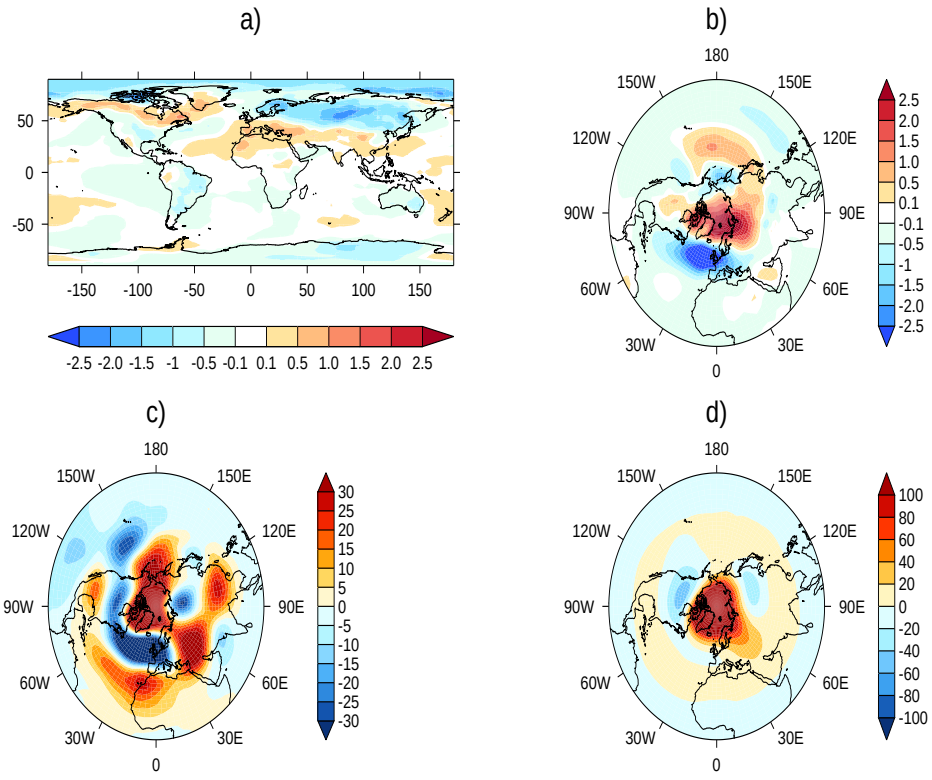

Figure 3.5: Difference in the composite anomaly averaged after two post-volcanic winters between the multi-model mean and the reanalysis. a) near-surface temperature, b) mean sea level pressure, c) 200 hPa geopotential, d) 50 hPa geopotential. a) and b) refer to the nine eruptions listed in Table 3.2 and 20CRv2 is used , c) and d) are for the most recent four eruptions and ERA40 is used. Coloured areas are significant at the 99 % level using a 2-tailed one-sample t-test

3.3.3 Surface Temperature and Mean Sea Level Pressure - Individual Models

Fig. 3.6 and 3.7 shows the NH composites of surface temperature and MSLP for the post-volcanic winter season in the individual models. Large variability is observed between the models in their NH response: the observed warming in the northern Eurasia is simulated by a few models but is much weaker than in the observations. For example, GISS-E2-H and GISS-E2-R simulate the northern European warming pattern reasonably well but the maximum amplitude is only 0.5 K. The cooling over NE Canada seems to be simulated more widely, independent of how well the northern Eurasian warming is captured. Some models (CSIRO-Mk3.6, HadGEM2-ES, NorESM1) simulate a general cooling in the Asian-European area, opposite to the observations, and the majority show a significant cooling in the tropical lower latitudes, of around 0.2 K over the oceans.

Large inter-model differences in MSLP pattern are shown in Fig. 3.7. Only CNRM-CM5 and CanESM2 reproduce a weak dipole over the North-Atlantic, whereas NorESM1 shows anomalies opposite to those observed. The other models only show weak anomalies with minimal statistical significance. The two GISS models simulate weak surface temperature anomalies but do not show any significant anomaly in the MSLP. The GISS-E2-R model differs from GISS-E2-H in that its response is weaker, and not statistically signficant. The only difference between the GISS-E2-H and GISS-E2-R models is the ocean model to which the atmosphere is coupled. GISS-E2-R uses the ModelE atmospheric code and is coupled to the Russell ocean model (1°x1.25° L32), whilst GISS-E2-H uses the same ModelE atmospheric code but is coupled to the Hycom ocean model (1°x1.25° L26) (Schmidt et al., 2006). In a modelling study on the effects of volcanic eruptions on the oceans Stenchikov et al. (2009) reported changes in sea level, temperature, ocean heat content, salinity, and also significant strengthening of the Atlantic Meridional Overturning Circulation (AMOC) $40-60°$ N in the first few years following an eruption. Whilst it is therefore possible that part of the surface response could be due to changes in NH ocean circulation, it is generally

believed for AMOC changes, in particular, to be caused by the changes in wind stress due to positive NAO (Delworth and Dixon, 2000) that is a result of a stronger vortex following volcanic eruption (Stenchikov et al., 2009), not that the ocean affects the surface to cause a positive DJF warming for up to two years following a volcanic eruption. Therefore it is unlikely that the response witnessed in GISS-E2-H which differs slightly to GISS-E2-R, particularly with no strong positive NAO, is due to an activation of the volcanic mechanism. The analysis of surface temperature and MSLP in the CMIP5 ensemble shows a poor correspondence with observations during the first two NH winters following large tropical eruptions.

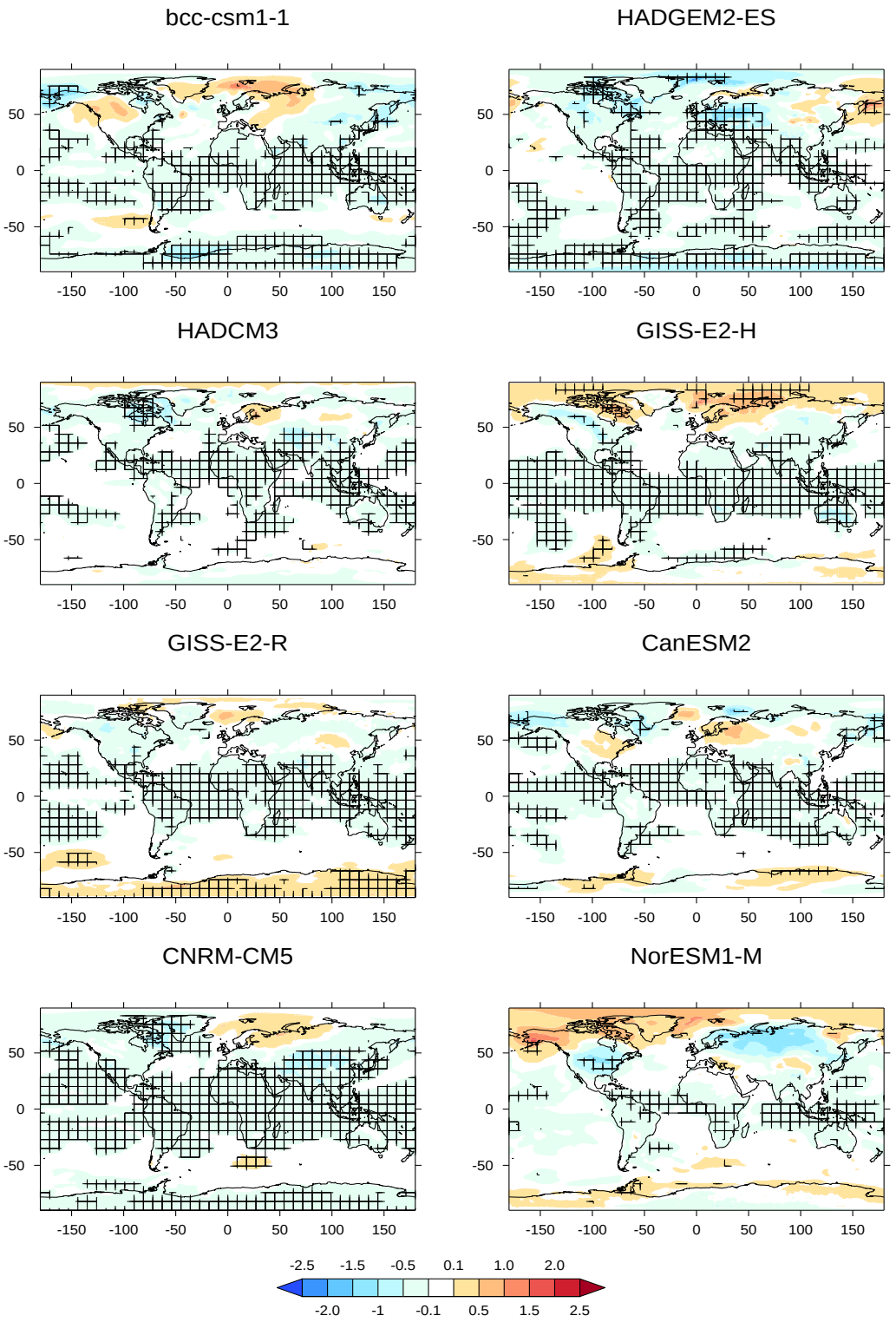

Figure 3.6: Composite near-surface temperature anomalies (K) for the two following winters of the past nine most recent large tropical volcanic eruptions (Table 3.2) in all models and the 20th century reanalysis (20CRv2). Hatching displays areas at or over 95 % significance using a two tailed t-test.

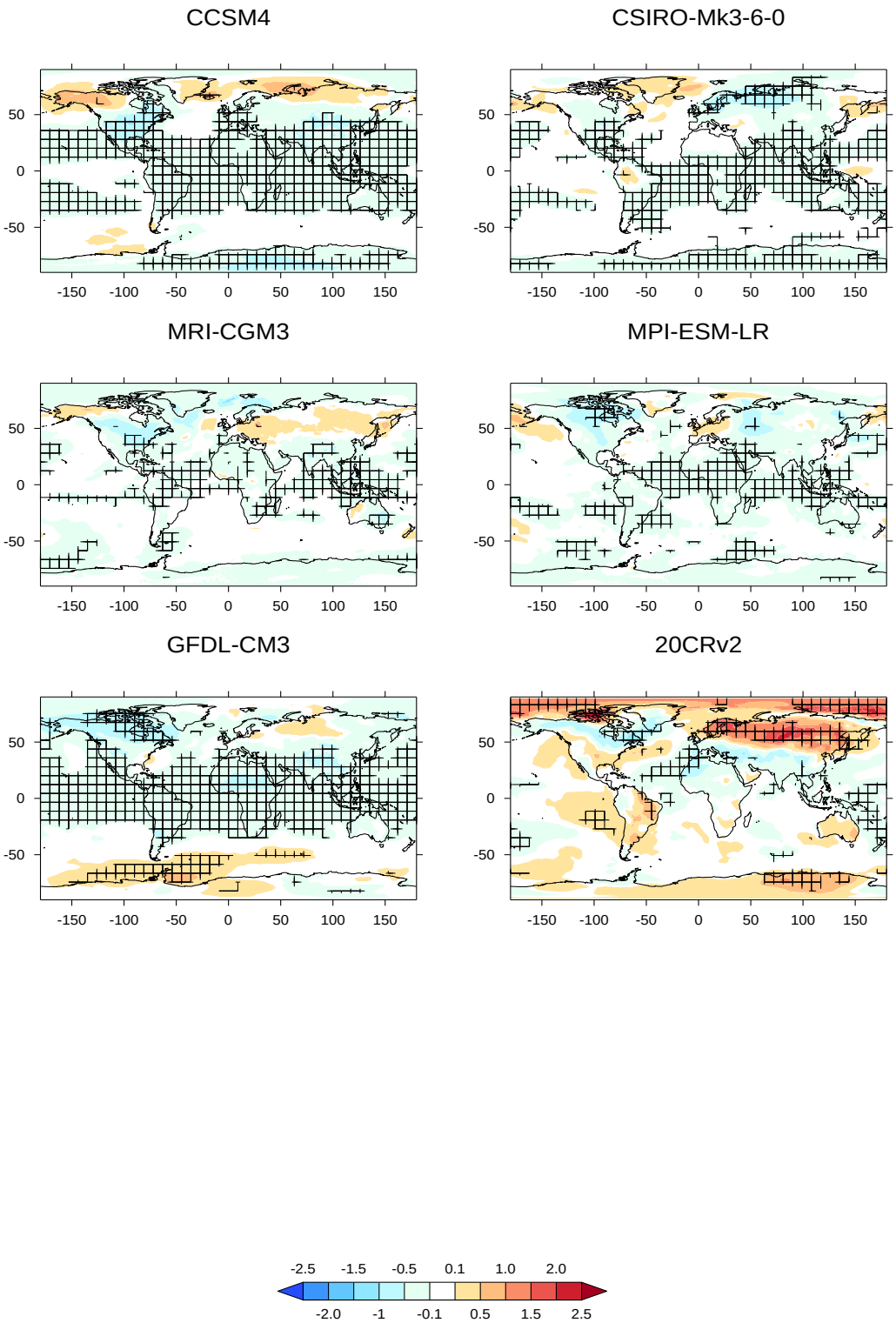

Figure 3.6: **(continued)**

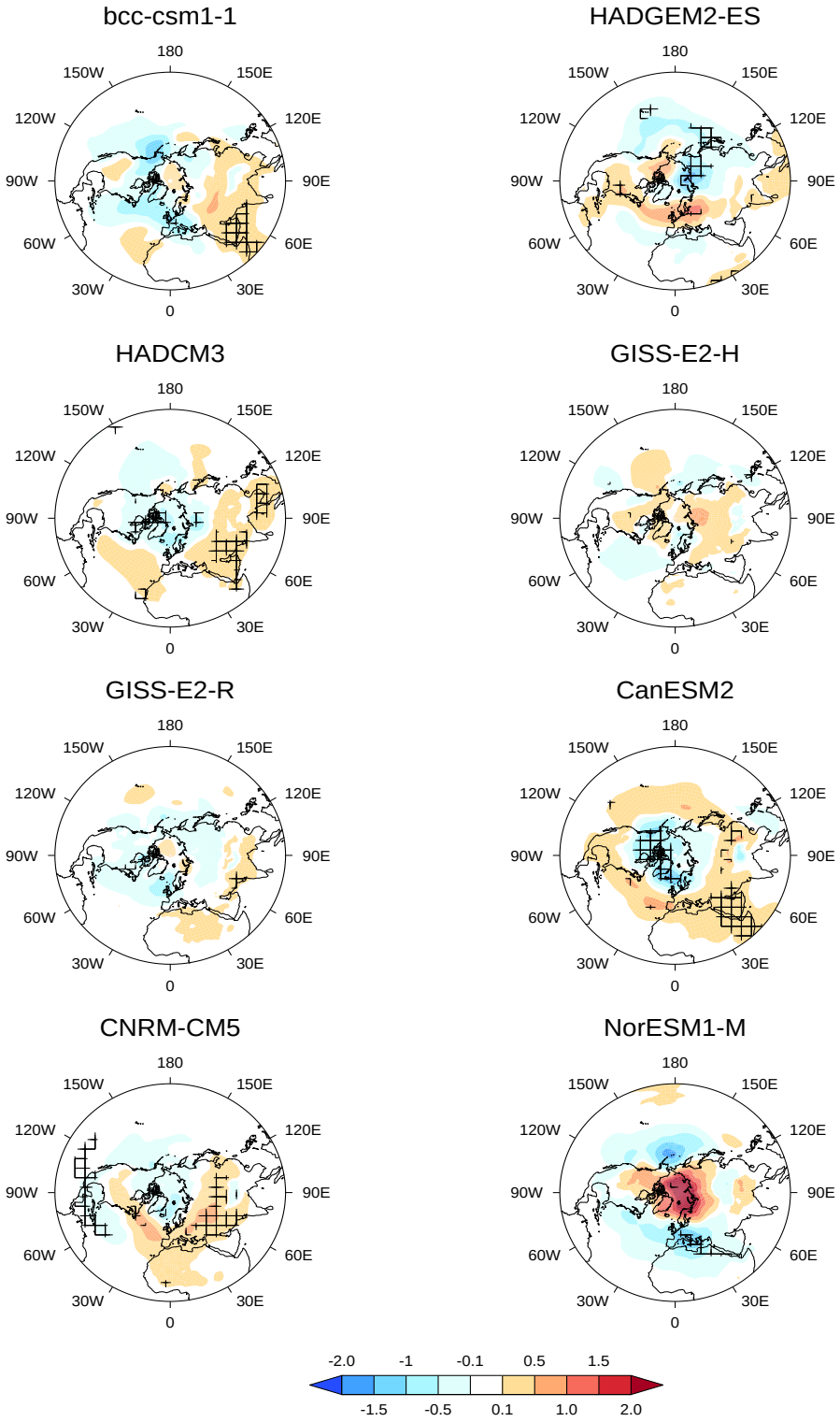

Figure 3.7: NH stereographic plot of composite MSLP anomalies (hPa) for the two following winters of the past nine most recent large tropical volcanic eruptions in all models and the 20th century reanalysis (20CRv2). Hatching displays areas at or over 95 % significance using a two tailed t-test.

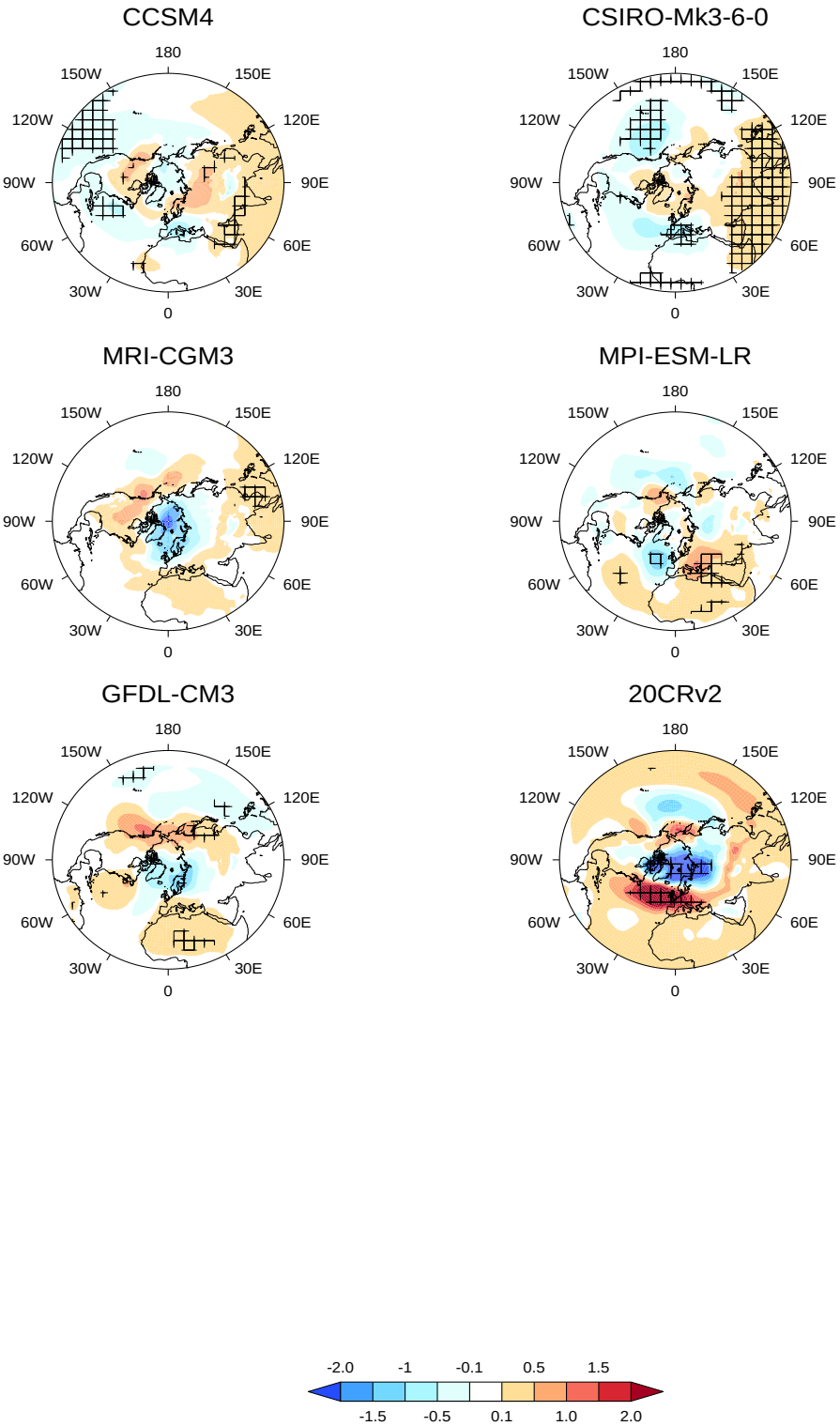

Figure 3.7: **(continued)**

3.3.4 Geopotential Height

Geopotential height anomalies in the upper troposphere and mid stratosphere help define circulation changes during winters following large volcanic eruptions. Due to the high uncertainty in the 20CRv2 reconstructions of upper air fields (Compo et al., 2011), we decide to analyse only the last four eruptions since 1950 using the ERA40 dataset. In the upper troposphere (Fig. 3.4e), the observed 200 hPa geopotential height anomalies are linked to the MSLP anomalies, with a general decrease over the North Pole surrounded by positive geopotential height in the mid latitudes and a strong dipole over the North Atlantic region. A general decrease in the observed geopotential height dominates at low latitudes, consistent with the generalised cooling tendency observed in the tropical troposphere.

In observations the anomaly pattern in the troposphere is mirrored in the stratosphere by a cold and deep polar night vortex, as observed in the 50 hPa geopotential height anomalies (Fig. 3.4g) showing a large statistically significant decrease in geopotential height over the pole of around 200 m. A weaker anomaly at 50 hPa is observed at low latitudes, with a geopotential height increase of about 25 m which has been attributed to the direct heating effect of the volcanic aerosol in the lower tropical stratosphere (Ramachandran et al., 2000; Stenchikov et al., 1998). The observed low 50 hPa geopotential height at high latitude is associated with a colder polar lower stratosphere, which suggests a stronger and persistent polar vortex. Recent studies suggest that this might be a characteristic of the early stage of the post-volcanic winter season. For example, Graf et al. (2007) saw no clear weakening of the wave activity during post-volcanic winter in observations and Mitchell et al. (2011) show that the observed polar vortex in the upper stratosphere is weaker than normal from the end of January into February after the three major volcanic eruptions since 1960.

As for the MSLP, the modeled geopotential height anomalies at 200 hPa are highly variable (Fig. 3.8). Most models simulate a significant uniform decrease in the geopotential height roughly south of 30° N, as can be seen in the multi-model composite Fig. 3.4f, stronger than in the observations. The strongest anomaly is observed for

the GFDL model. A significant uniform decrease over the Pole is observed only for MRI.

A few of the models capture the anomalies observed in the stratosphere (see Fig. 3.9) as in the reanalysis, though much weaker. HadGEM2, MPI, CNRM-CM5 and MRI simulate a decrease in the geopotential height of order of 25 m, although such a response is not a substantial change with regards to the background variability of the polar vortex. Thompson and Wallace (1998) noted that over 1958-1997, as observed in ERA40, the leading EOF of 50 hPa wintertime geopotential height anomalies, which accounts for about 50% of the variance, is around -270 m. Other models show no significant anomaly at high latitudes. As observed from the multi-model mean Fig. 3.4h, the most robust feature in the stratosphere is a statistical significant increase in the geopotential height at low latitude in agreement with the observations. This is weaker than in the ERA40 composite (see Fig. 3.5d) and is likely due to the stronger cooling simulated in the tropics (Fig. 3.4b) which tends to shrink the atmospheric column, as noted in S06.

As with temperature and MSLP, the difference in the anomalies of 50 hPa and 200 hPa geopotential height between the multi-model mean and the observations, Fig. 3.5 c,d, is highly significant and confirms the difficulty of models to simulate the observed circulation changes in the stratosphere and upper-troposphere.

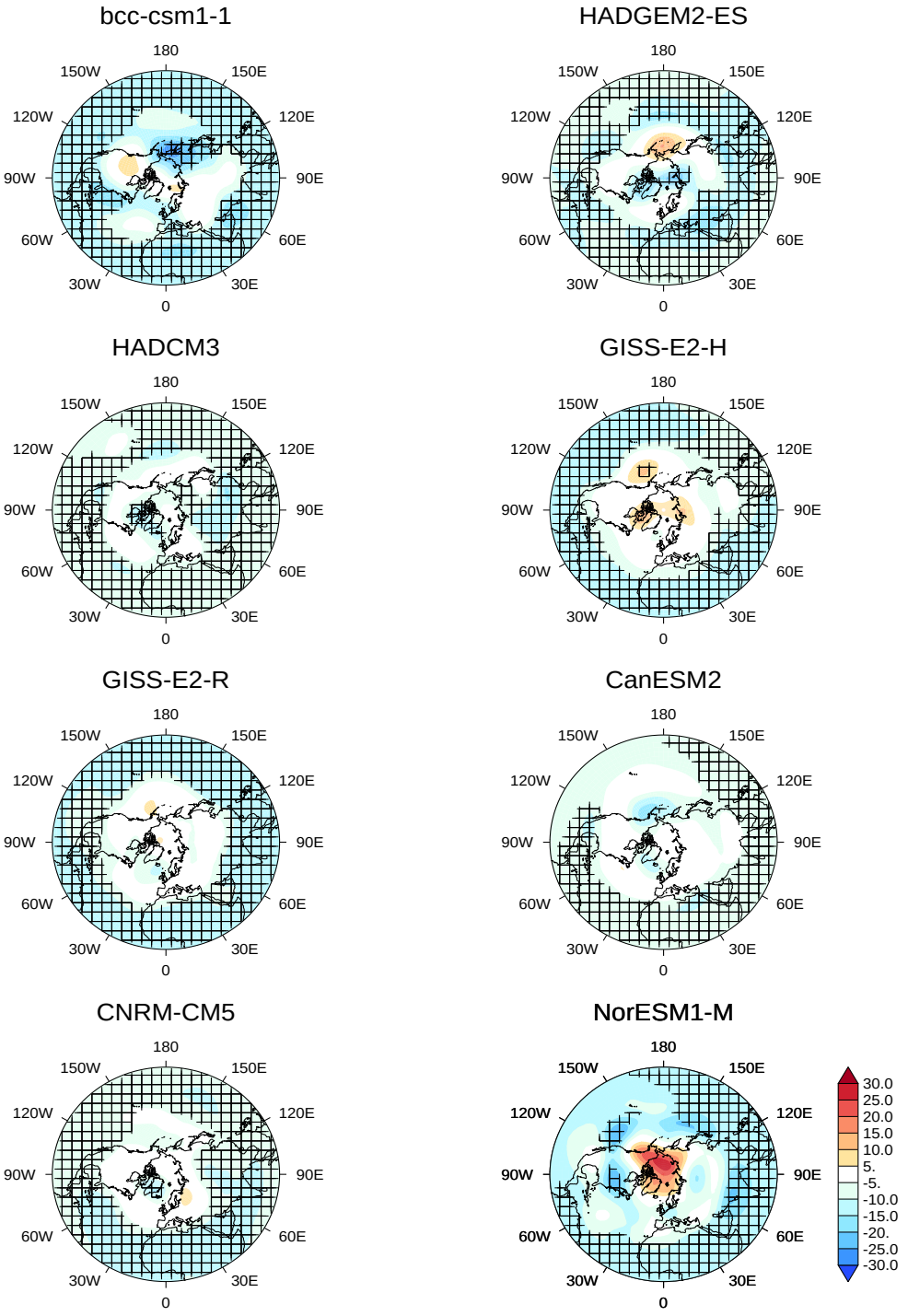

Figure 3.8: NH stereographic plot of composite 200 hPa Geopotential Height anomalies (m) for the two following winters of the past nine most recent large tropical volcanic eruptions in all models and ERA40 reanalysis. The anomalies in the reanalysis are computed for the four eruptions after 1960. Hatching displays areas at or over 95 % significance using a two tailed t-test.

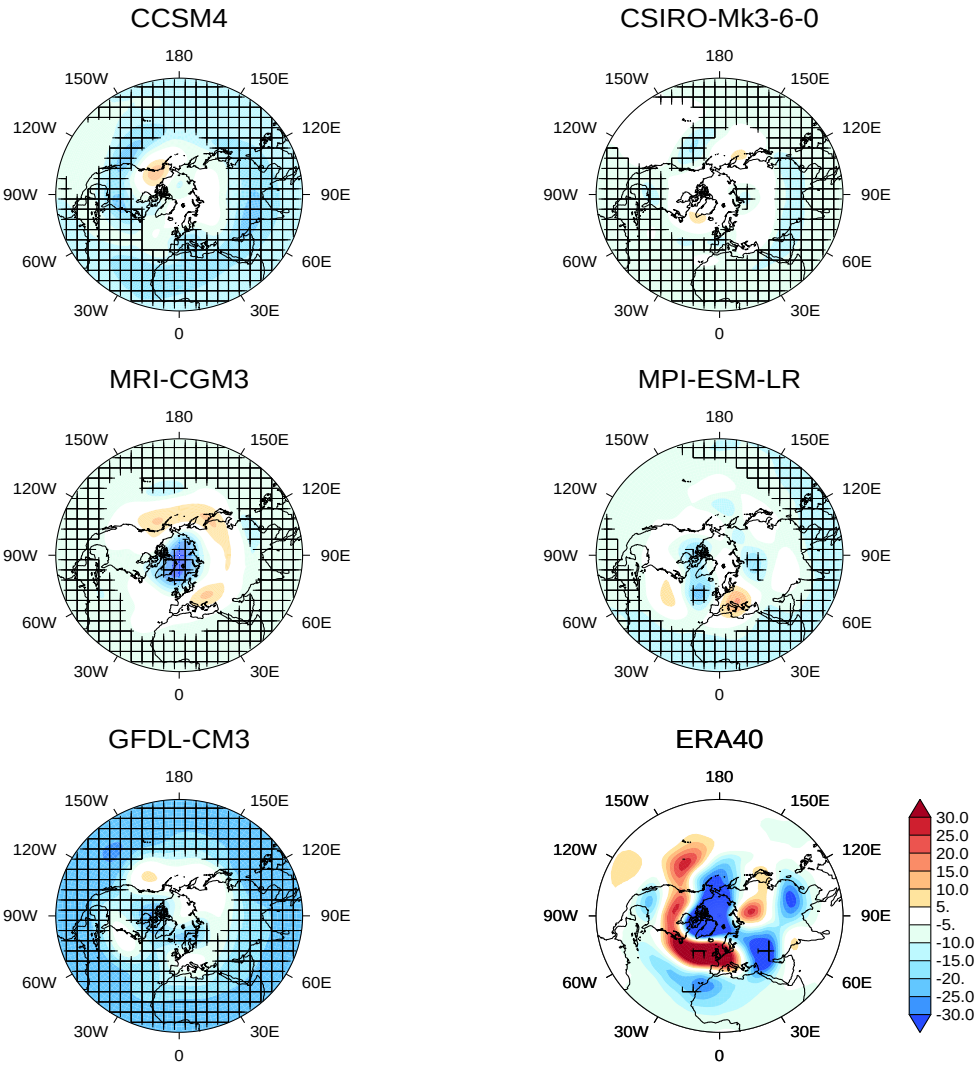

Figure 3.8: **(continued)**

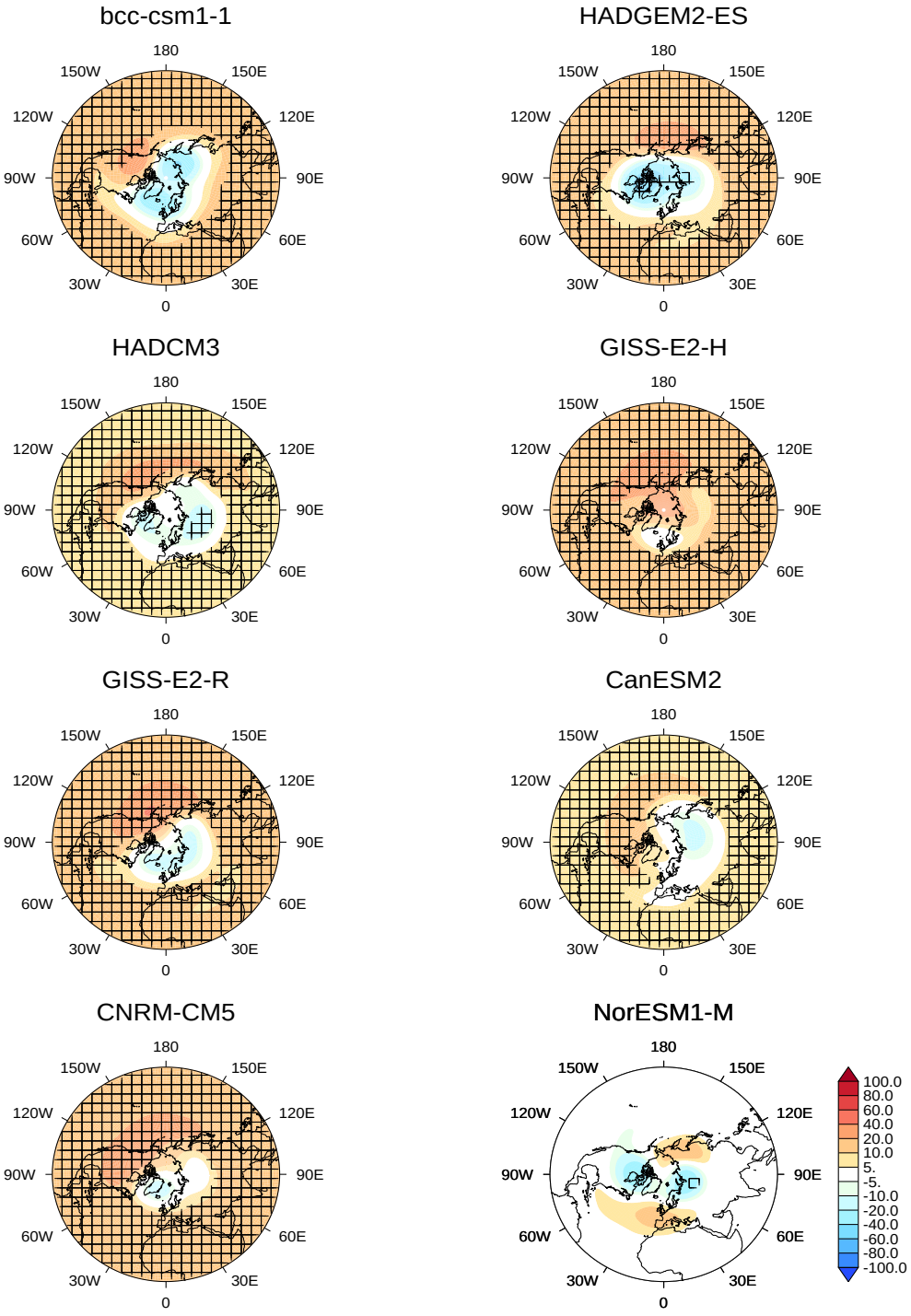

Figure 3.9: NH stereographic plot of composite 50 hPa Geopotential Height anomalies (m) for the two following winters of the past nine most recent large tropical volcanic eruptions in all models and ERA40 reanalysis. The anomalies in the reanalysis are computed for the four eruptions after 1960. Hatching displays areas at or over 95 % significance using a two tailed t-test.

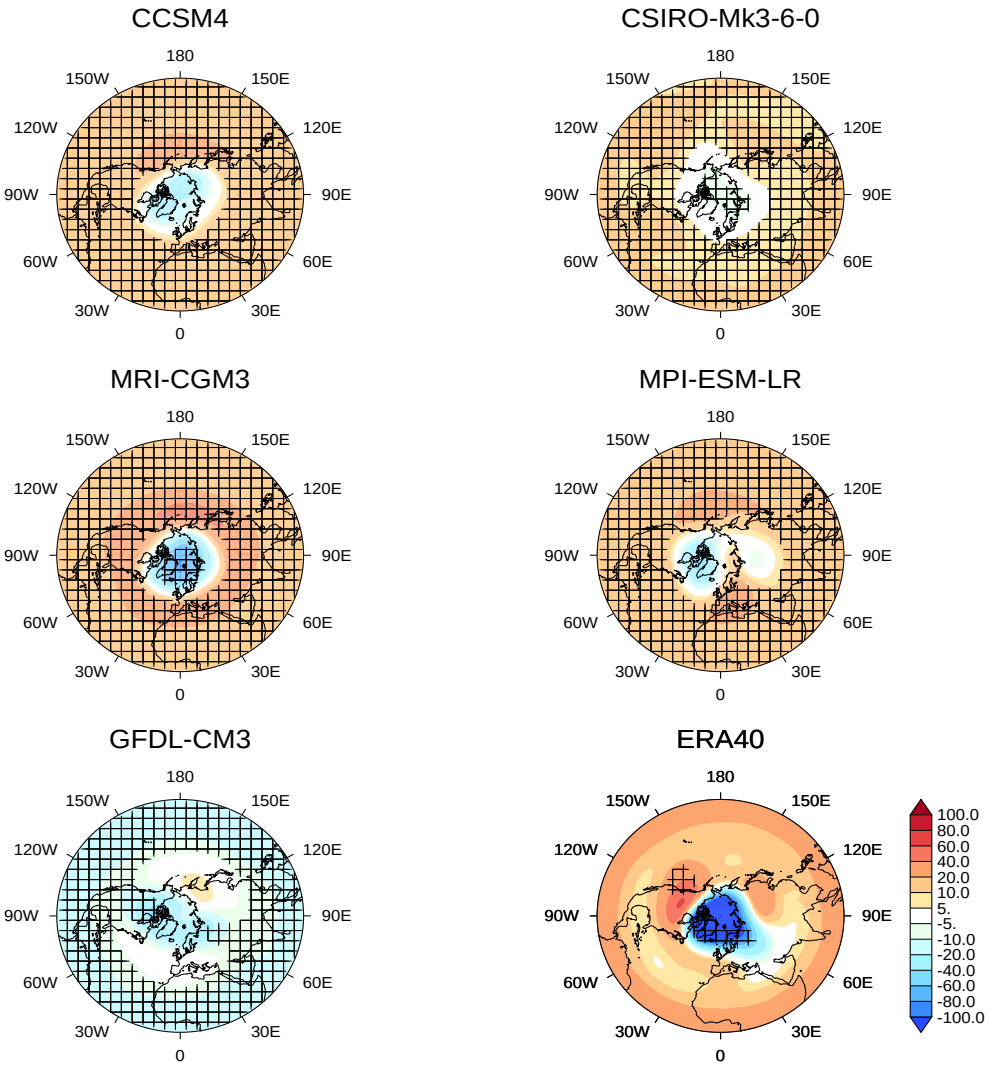

Figure 3.9: **(continued)**

3.3.5 NAO Index

As noted in section 3.2, the observed anomalies in the MSLP in the post-volcanic winters are not well reproduced by the CMIP5 models. The observed MSLP anomalies in the winters after the largest volcanic eruptions since 1880, project onto the leading variability mode of the NH circulation, especially the NAO index, with a significant prevalence of positive NAO in the first winter after the eruption (Fischer et al., 2007), both in terms of amplitude and number of positive events (Christiansen, 2008).

In this section the idea that looking at the principal modes of variability could help to better isolate the dynamic response in the model simulations is tested. As mentioned in section 2, the same time convention adopted by Fischer et al. (2007) and S06 is used to identify the 1st and 2nd winter after each eruption. The majority of the volcanoes erupted in the spring-early summer but two erupted in autumn, the minor eruption of Fuego in October 1974 and the large eruption of Santa María at the end of October 1902. It is likely that their full effect won't be present in the first winter immediately after the eruption and therefore the first winter should be considered to be a full year after the eruption time, as listed in our Table 3.2. This differs from the time convention adopted by Christiansen (2008) who considered the first winter immediately after the eruption for all the volcanoes, hence changing the years of winters considered for the two eruptions of Fuego and Santa María. In his paper he reported the robustness of his results when those two eruptions are excluded from the analysis. However, it is showed here that with the different dating convention the results are affected when these two eruptions are included.

When all nine eruptions south of 40° N as listed in Table 3.2 are included, the 20CRv2 shows a clear prevalence of positive NAO index in the first year after the eruptions (Fig. 3.10, 20CRv2, lag 0). The amplitude is significant roughly at the 4% level with seven volcanoes out of nine with positive NAO in the first winter and this occurrence is significant at the 9% level. No significant signals are observed for the second post-volcanic winter.

Only two post-volcanic winters show a negative NAO, after the eruptions of Agung and Quizapu, which both erupted in the southern hemisphere. Agung's aerosol was mostly concentrated south of the Equator (Robock, 2000) and Quizapu has the weakest effect on the stratospheric optical depth and temperature between 30° S and 30° N among all the analysed volcanoes (Figs. 3.2 and 3.3). This could affect the dynamics associated with the forcing of the NAO circulation. Our results are unchanged if the Quizapu eruption is excluded from the volcanoes used in the composite. It is also noted that, although positive, the winter 1903-04 after the Santa María eruption has a NAO signal close to zero (0.03, also consistent in the DJFM composite with -0.04 as confirmed in Christiansen (2008, his Fig. 2)), which further reduces the number of occurrences of positive NAO events in the first winter after an eruption.

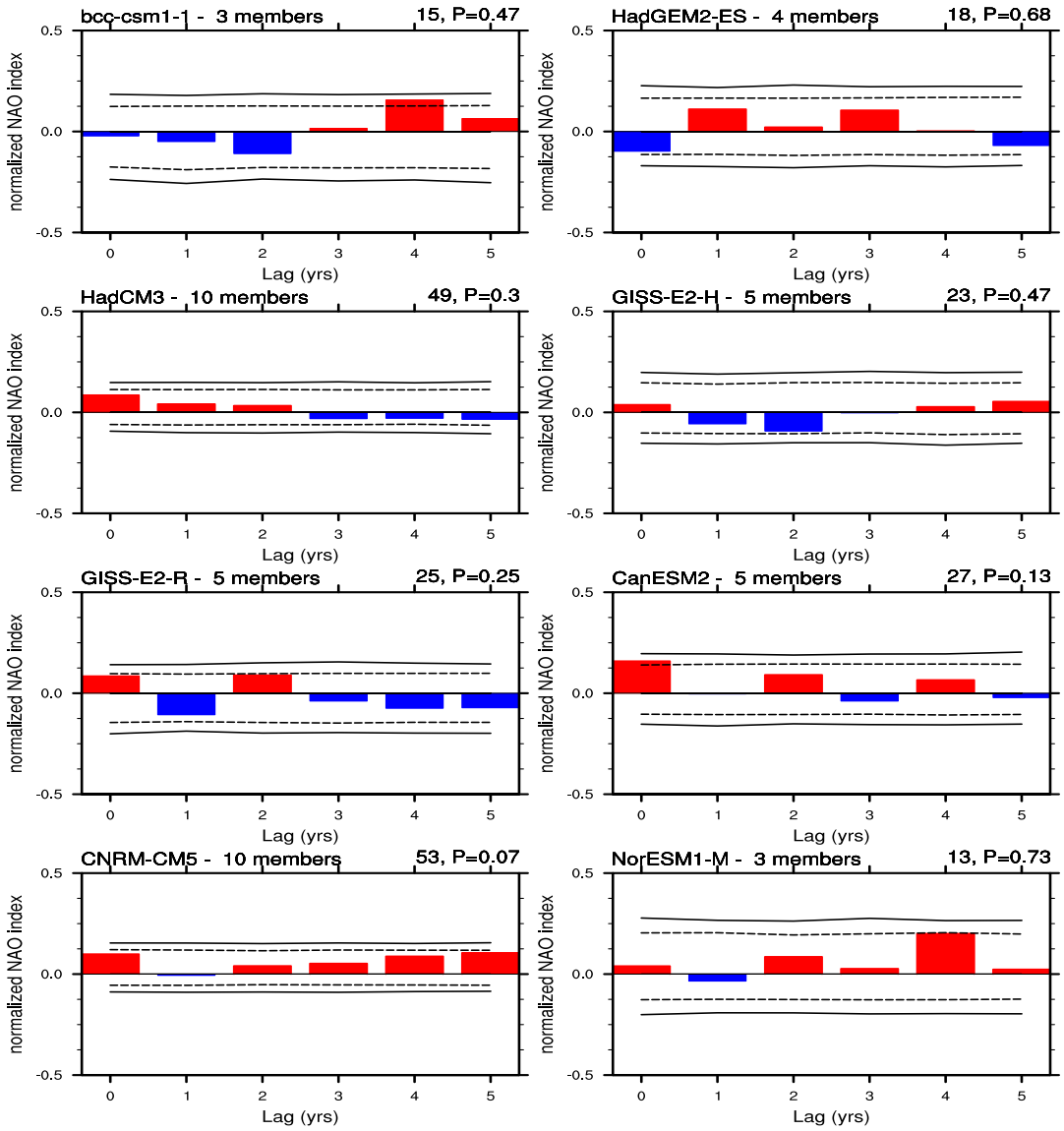

Figure 3.10: Superposed epoch analysis for the winter (DJF) NAO index for the 13 CMIP5 models and the 20th century reanalysis (20CRv2) for the nine eruptions listed in Table 3.2. The average over nine volcanic eruptions is shown at different lag time. Lag 0 indicates the first winter after a volcanic eruption. The horizontal lines show, from bottom to top, the 1st, 5th, 95th and 99th percentiles of the bootstrap distribution. For each plot is indicated the number of ensemble members (r), the ratio of total number of winters with positive NAO with respect to the total number of winters in each ensemble (σ) and the number of winters at lag 0 with positive NAO (N_0) with the relative p-value.

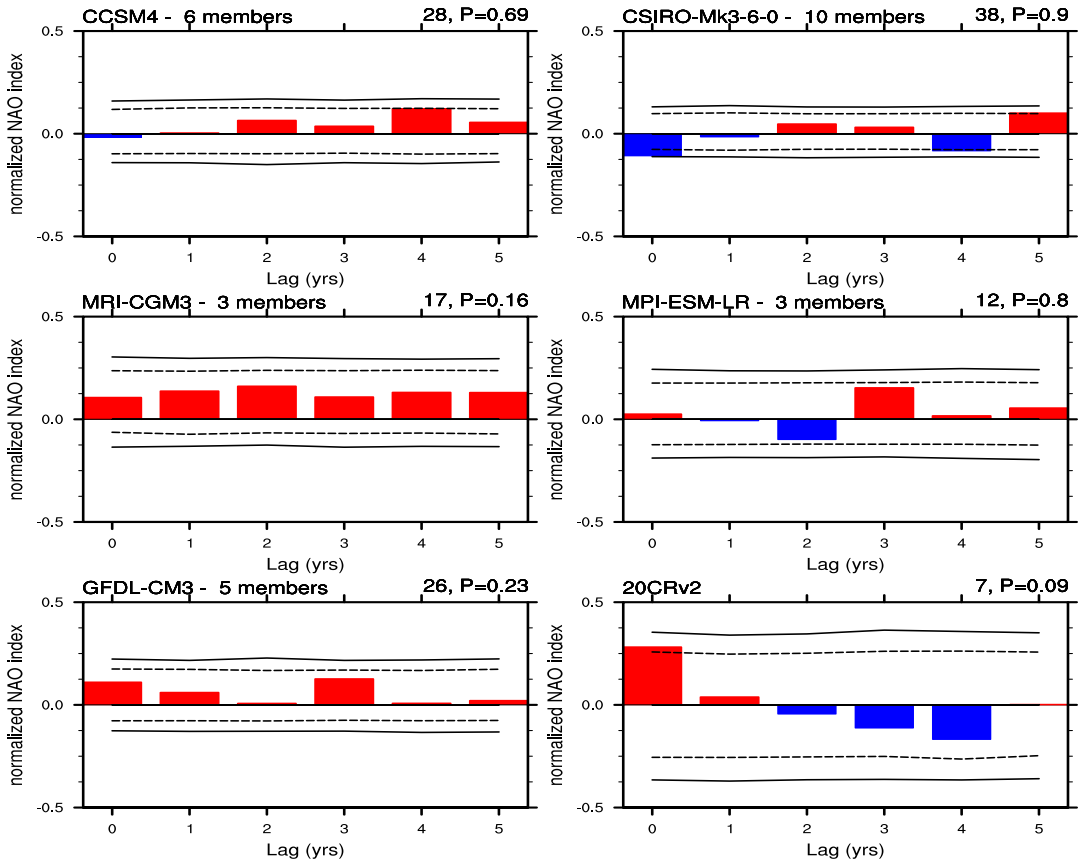

Figure 3.10: **(continued)**

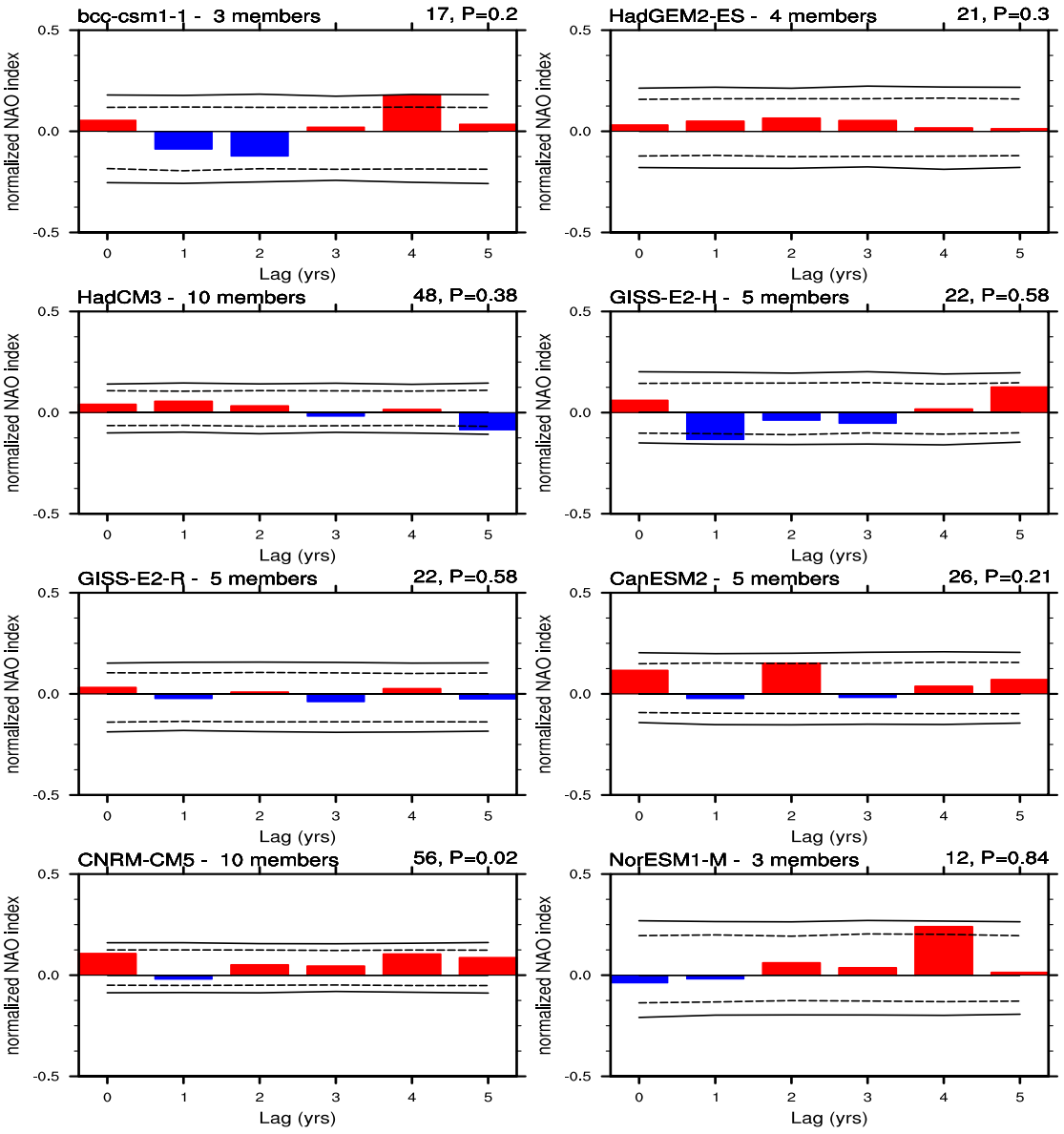

Figure 3.11: As Fig 3.10 but using the convention adopted in Christiansen (2008) for the first winter after the eruptions of Santa María (1902-1903) and Fuego (1974-1975).

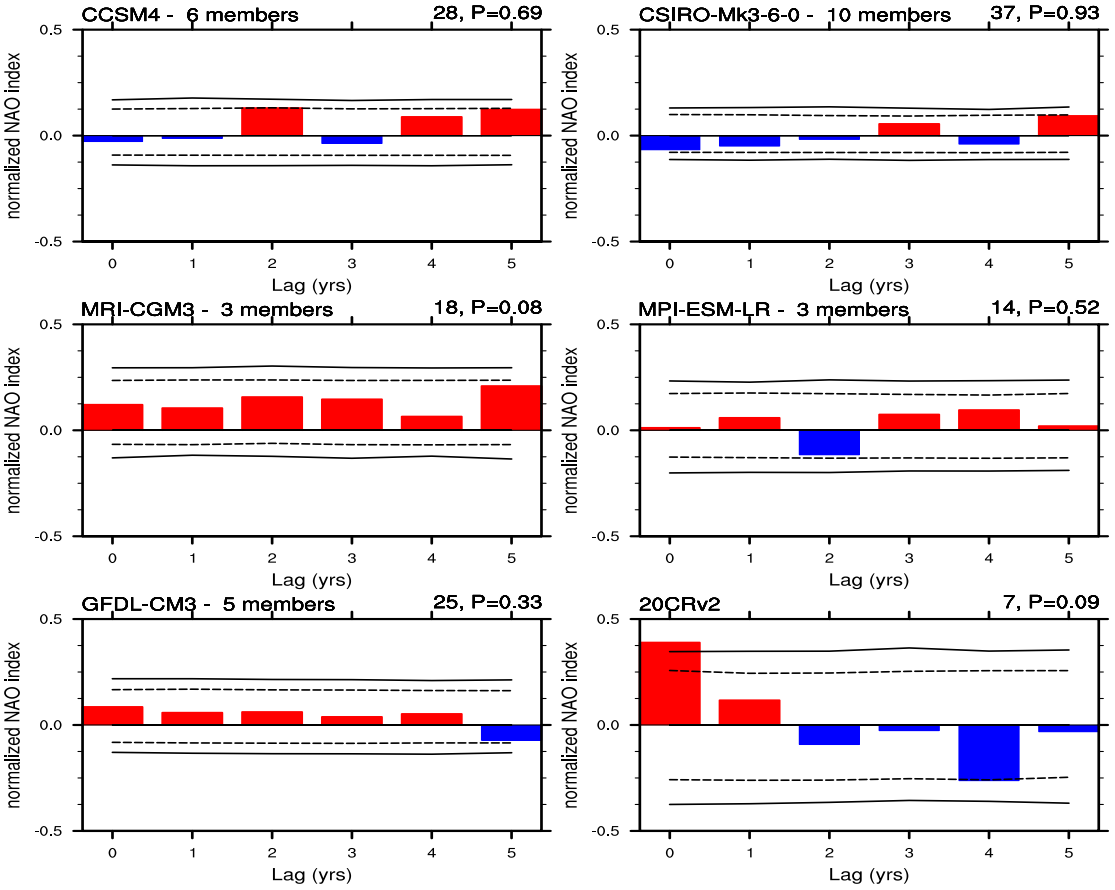

Figure 3.11: **(continued)**

Among the 13 models analysed in this study, positive NAO signal at lag 0 is observed only for GISS-E2-R (at the 7% significance level) and CanESM2 at the 3% significance level. Only CNRM-CM5 shows a significant number of positive NAO events at lag 0 (52/90, p=0.07) but the composite amplitude reaches only 11 % of significance level. The analysis is confirmed by the MSLP gridded anomalies shown in Fig 3.7 where CanESM2 also shows a weak NAO-like dipole when averaged across two winter seasons. The MRI-CGM3 is the only model that shows a significant number of positive NAO sevents in the second winter after the eruptions (p=0.08) but the model appears to have a positive NAO at all lag times, so it is not clear whether this response is necessarily associated with the volcanic eruption. The other models show no significant positive anomaly at lag 0.

As mentioned above, when a different convention is used to identify the closest winters affected by the eruption of Santa María and Fuego, changes are observed in the superposed epoch analysis. Figure 3.11 examines the robustness of the analysis with respect to the choice of the winters after Santa María and Fuego, using the convention adopted in Christiansen (2008). Since the reanalysis based on a limited sample, they prove to be highly sensitive to changes in the epoch key date. The signal at lag 0 becomes now highly significant (1 % level) with an occurrence of seven positive NAO out of nine events (p=0.09). Most of the change in the signal comes from the Santa María event, which shows a strong positive NAO in the winter 1902-1903, immediately after the eruption and positively contributes to enhance the epoch composite at lag 0.

The largest effect of the change of the year of the first winter after the eruptions of Santa María and Fuego is observed for HadGEM2, which does not detect any significant signal at any lag. With 10 ensemble members, CNRM-CM5 is the only one that still detects a positive NAO at lag 0. The amplitude is small but slightly more significant than in the previous composite (it reaches now the 10% level of significance) and the number of events is significant (56/90, p=0.02). Among the other models, only MRI-CGM3 detects a significant number of positive events at lag 0 (18/27, p=0.08) but, as noted before, the models tends to show positive NAO almost at all

lags. Although this model shows the strongest decrease of the geopotential height at high latitudes both at 50 hPa and 200 hPa, this seems not enough to reproduce a significant NAO signal or surface temperature anomaly.

The main conclusions of this section are 1) the superposed epoch analysis of the 20CRv2 NAO index confirms previous findings of a positive NAO in the first winter following the major tropical eruptions in the 19th and 20th century, but the strength of the signal is sensitive to the choice of the key dates for each eruption, which points to the sparseness of observations hampering our understanding of processes. 2) as observed in the previous sections, the models struggle to reproduce a detectable positive NAO signal in the first post-eruption winter. With 10 ensemble members, the CNRM-CM5 model results are the most robust to changes in the definition of the post-volcanic key dates. With less ensemble members, the other models show sensitivity to the definition of the key dates. It is finally noted that, since in this work only the ensemble of CMIP5 historical runs is analysed, the bootstrap distribution might give a conservative estimate of the significance associated with the signal. Clearer signal detection could be achieved by drawing the random matrix from the CMIP5 control simulations, therefore relying only on natural variability not influenced by volcanoes or other forcings.

3.4 Discussion and Conclusions

All available models submitted to the CMIP5 archive as of April 2012 that had a reasonably realistic representation of volcanic eruptions have been analysed for their ability to simulate post-volcanic radiative and dynamic responses. With substantially different dynamics between the models it was hoped to find at least one model simulation that was dynamically consistent with observations, showing improvement since S06's analysis. Disappointingly, it is found that again, as with S06, despite relatively consistent post volcanic radiative changes, none of the models manage to simulate a sufficiently strong dynamical response. Although all the models reproduce reasonably well the increase in geopotential height in the lower stratosphere at low latitudes, none of the models simulate a sufficiently strong reduction in the geopotential height at high latitudes and correspondingly the MSLP pressure fields and temperature fields show major differences with respect to the observed anomalies. This is despite some models having 10 ensemble members, giving a potentially strong signal to noise ratio.

From the analysis conducted in the thesis so far, it is unclear why models fail to simulate the dynamics following volcanic eruptions. The dynamical mechanism proposed by Stenchikov et al. (2002, their Fig. 13) involves lower stratosphere tropical heating caused by the presence of volcanic aerosols, which gives rise to a stronger polar vortex due to the thermal wind relationship. A stronger vortex also could be due to a decrease in planetary wave forcing from the troposphere, although the evidence for this is unclear. The modelling results of Stenchikov et al. (2004) showed a decreased EP flux into the stratosphere following the Pinatubo eruption but observations suggest an increase in the EP flux following the Agung, Fuego, El Chichón and Pinatubo eruptions Graf et al. (2007). S06 suggested that models might be biased towards an unrealistically strong polar vortex which results in a weak wave feedback between stratosphere and troposphere. From column three of Table 3.3 a large variability among the 13 models in their climatological 50 hPa zonal wind at high latitudes is observed. Some models have stronger zonal winds compared to ERA40 but their response to volcanic forcing does not differ from what is observed

for the models characterised by a lower climatological wind. Although this does not confirm the findings of S06, based on a limited number of models, it is also noticed that all models show considerably less variability in high-latitude stratospheric winds than observed, suggesting a stable polar vortex and more resistance to changes from external forcings, as found by S06.

Table 3.3: Climatological indices

Model Name	U50hPa 30° S-30° N m/s	U50hPa 55° N-65° N m/s	ENSO 3.4 Index
bcc-csm1.1	-5.9(0.5)	27.4(2.5)	-0.06
HadGEM2-ES	-5.7(0.5)	24.1(2.2)	-0.12
HadCM3	-3.1(0.3)	14.7(1.0)	-0.11
CNRM-CM5	-5.0(0.2)	17.6(1.0)	-0.22
GISS-E2-H	-3.1(0.5)	13.0(1.3)	-0.67
GISS-E2-R	-2.7(0.6)	13.8(2.0)	-0.33
NorESM1-M	-7.9(0.8)	20.2(2.1)	-0.06
CCSM4	-8.2(0.7)	25.1(2.4)	-0.12*
CSIRO-Mk3-6-0	-0.7(0.3)	8.7(0.3)	-0.11**
MRI-CGCM3	-3.3(0.4)	25.2(2.9)	-0.10
MPI-ESM-LR	-8.4(0.5)	17.9(2.5)	-0.15
GFDL-CM3	-9.0(0.6)	24.2(1.8)	-0.33
Reanalysis	-3.7(5.0)	19.4(5.4)	0.07

U50hPa is the winter (DJF) seasonal climatological zonal wind computed for two regions, 30° S-30° N and 55° N-65° N. In bracket is the standard deviation. The last column shows the ENSO 3.4 index (see text). In the last row the climatological wind from ERA40 and the ENSO 3.4 index from 20CRv2 based on HadISST. *with five ensembles **with eight ensembles

There are therefore still uncertainties in the dynamical mechanisms following volcanic eruptions particularly regarding the wave propagation through the polar stratosphere as seen in EP flux diagnostics (Graf et al., 2007).

In addition, the degree of El Niño influence and interaction following volcanic eruptions is unknown. Based on the superposed epoch analysis of post-volcanic winters stratified according to the ENSO phase, Christiansen (2008) concluded that the ENSO does not change the impact of volcanic eruptions on the Northern Hemisphere winter circulation, although the low number of cases imposes caveats on the conclusions. A recent work (Graf and Zanchettin, 2012) argues that ENSO has a different effect on the Northern Hemispheric winter circulation when the differences between Central-Pacific (CP) and East-Pacific (EP) El Niño events are taken into account. In particular, CP El Niño events appear to have a significant effect on winter NH circulation, with a tendency towards a negative NAO index. According to their definition, CP El Niño occurred in 1963-1964 and 1991-1992 but not in 1982-1983, which could explain the strong Eurasian warming signal observed after El Chichón, even though a strong El Niño event was taking place, and the relatively disturbed vortex in January 1992 (Graf et al. 2007). Moreover, biases in model representations of ENSO variability (Guilyardi, 2006) could in the same way affect their response to volcanic forcing. The issue is also complicated by the intrinsic problems in defining the modes of ENSO variability (Takahashi et al., 2011). In our analysis the large number of ensemble members should help to smooth out possible contaminations induced by the Pacific SST variability. Despite this, the models have a tendency to be in a weak La Niña phase. However, this should not lead to a weakening of the volcanic response in the models. Whilst Manzini et al. (2006) saw in model simulations that during the El Niño phase there was an increase in the vertical propagation of quasi-stationary planetary waves into the stratosphere from the troposphere, which caused a weaker, more disturbed vortex, during the La Niña phase they noticed no influence distinguishable from variability. Further studies using observations and model data have concluded similar results (Garcia-Herrera et al., 2006, Calvo et al., 2009). Despite the model performance, the 20CRv2 reanalysis dataset, which uses HadISST sea surface

temperatures, yields an averaged ENSO 3.4 index of 0.07 during the volcanic eruptions analysed here. It has also been suggested that large volcanic eruptions could actually trigger a positive phase of ENSO. Tung and Zhou (2010) performed linear regressions on the HadISST and the Extended Reconstructed SST (ERSST) dataset. Whilst finding a weakly negative temperature volcanic response from linear regressions of the HadISST and the ERSST datasets using the ST dataset as the volcanic signal, if the cold tongue index is assumed not independent of volcanoes in their linear regression, they find a large positive ENSO like pattern. Their findings, independent of the choice of volcano index, suggests a statistically significant El Niño response to a volcanic eruption in observations.

Whilst uncertainty still remains on the interactions between volcanoes and ENSO, the DJF warming signal can be seen independent of the choice of volcanoes. The choice of the last four major eruptions, the last nine as used here, or longer term reconstructions of temperature from 1600 (Shindell et al., 2004) and the past half millenium (Fischer et al., 2007) all reveal a statistically significant DJF warming following major volcanic eruptions. Hence, as noted by Marshall et al. (2009), the DJF warming signal is extremely unlikely to be an artifact of internal variability. Despite this, calculations of the DJF temperature anomaly for also the five biggest volcanoes (Krakatau, Santa María, Agung, El Chichón and Pinatubo) are performed and also for the four best observed volcanoes that erupted in the satellite era (Agung, Fuego, El Chichón and Pinatubo) for all the models and the observations. Despite the observations showing, independent of these choices, a strong statistically significant warming, none of the models successfully simulate the observed response. GISS-E2-H shows a slightly increased DJF warming pattern, yet further investigation of MSLP anomalies reveal neither a large nor anywhere statistically significant positive NAO. bcc-csm1.1 also shows a small increase in surface temperature over the Eurasian region, yet the spatial response is not correct. Moreover, there is almost no statistical significance in the bcc-csm1.1 temperature fields over the Eurasian region and further investigation in this model reveals neither a positive or significant NAO signal.

Finally, Stenchikov et al. (2004) found that including the Quasi-Biennial Oscillation (QBO) in the model made a substantial difference to the volcanic impact on the vortex. They found in observations following the Pinatubo eruption that the vortex was strengthened more in the second winter than the first, despite more aerosol being present in the stratosphere in the first winter. They proposed that this could be explained by the QBO being in the East phase in the first winter, which tends to weaken the vortex, and was in the West phase in the second winter, which tends to strengthen it. They concluded that a model with a QBO in the correct phase could better represent the dynamical simulation of the Pinatubo eruption. It is noted here that none of the models tested have a QBO in them, as can be observed from Table 3.3 by the low standard deviation in the climatological winter 50 hPa zonal wind over the equator, which could affect the performance of the dynamical simulation.

Another factor which could account for the poor simulation of the dynamical response following a volcanic eruption is related to how the aerosol is imposed in the model. It is noted that it is typical for a model to employ a very crude representation of aerosol in four latitude bands (Marshall et al., 2009), and the question of the suitability of this aerosol representation has been raised before (Otterå, 2008, Marshall et al., 2009). Another reason for the "common failure" of models to simulate the dynamics following volcanic eruptions may be their representation of the AO. Otterå (2008) notes that it may be that models have a general inadequacy that does not allow a sufficiently strong AO response to large-scale forcing. Others have pointed to ozone as being an important factor (Stenchikov, 2002, Otterå, 2008), however, as noted by Marshall et al. (2009) the response to the past major eruptions (before major ozone loss and larger amounts of ozone destroying chlorine in the atmosphere) is similar to that of El Chichón and Pinatubo combined, which suggests that inclusion of ozone chemistry is unlikely to be a major factor in the simulation of a volcanic eruption.

The impact of volcanic eruptions on surface climate is the closest natural analogue to sulphate aerosol geoengineering, despite the differences in injection method and duration of the perturbation. Unlike sulphate aerosol geoengineering, the ability of models to accurately reproduce the response to volcanic eruptions can be tested

against observations. Despite it being likely that a more uniform profile of aerosol in the stratosphere would occur from geoengineering than following volcanic eruptions, the results of GCM simulations of stratospheric geoengineering need to be considered in the light of their limitations when it comes to certain aspects of their responses to volcanic eruptions. This is of concern not only for the temperature response, but also for the precipitation response, as the dynamical effects following an eruption can often overwhelm the radiative response (Anchukaitis et al., 2010). Accordingly, research into the climate response to volcanic eruptions and their simulations is an area of major importance, not only in its own right, but for stratospheric aerosol geoengineering.

Chapter 4

Simulations of NAO Changes following the 1991 Mount Pinatubo Eruption Using High-Top and Low-Top Configurations of HadGEM2

4.1 Pinatubo as a Case Study

In this section simulations of volcanic eruptions are performed in order to test the influence of both stratospheric resolution and changes to the volcanic aerosol profile on the post-volcanic Northern Hemisphere winter dynamical response. The Pinatubo eruption is focused on for these simulations. Not only is this the most comprehensively observed large eruption (Robock, 2000), but performing many short simulations of Pinatubo greatly reduces computational expense as opposed to doing entire historical simulations.

Between June 12th and 16th in 1991 Mount Pinatubo, one of a chain of volcanoes constituting the Luzon volcanic arc (Wolfe and Hoblitt, 1996), erupted in what was the second most explosive volcanic eruption of the 20th Century (following Katmai, 1912) and what is believed to be the largest volcanic eruption of the 20th Century in terms of stratospheric sulphate gas injection (Self et al. 1996). It erupted after months of volcanic unrest involving tremors and earthquakes and phreatic explosions,

increasing ash emissions (Wolfe and Hoblitt, 1996) and the COSPEC IV spectrometer showing increased sulphur dioxide emissions (Daag et al. 1996).

Between June 14th-15th there were thirteen short surge-producing eruptions, and on June 15th, a nine hour climactic eruption which emitted 80% of the total ejecta (for extensive details, see Holasek et al. 1996). The eruption emitted an estimated 5 cubic km of vapour-saturated dacite (Gerlach et al. 1996), as well as injecting large amounts of ash and gas columns to great altitudes that is typical of Plinian eruptions (Scott et al. 1996).

Holasek et al. (1996) analysed the eruption plumes following Pinatubo using satellite observations. Using a combination of the Geostationary Meteorological Satellite Himawari 4 (GMS 4) and the National Oceanic and Atmospheric Administration (NOAA) Advanced Very High Resolution Radiometer (AVHRR) they analysed 31 visible and 55 thermal IR GMS 4 images during the eruption and 17 scenes from the NOAA 10 and 11 satellites taken during the eruption and for several months thereafter. During the climactic phase of the eruption, the plumes reached 40 km in altitude, undergoing a 55 K cooling of the plume top, and producing a >1,000,000 km^2 umbrella plume. The plume, which released 15-20 Mt SO_2, 42 Mt CO_2, 3 Mt Cl and 491 Mt H_2O (Gerlach et al. 1996, Andres and Kasgnoc, 1998), had the greatest values for altitude, undercooling and volume of deposits from a volcanic eruption in modern times (Holasek et al. 1996).

Whilst the eruption itself had immediate tropospheric effects and damage on agriculture, aircraft, buildings and the surrounding environment of the order of US$ 500 million (Casadevall et al. 1996, Bautista 1996, Mercado et al. 1996), it continued to affect the climate system and caused many longer living impacts through injecting sulphate gas into the stratosphere. Approximately half of the sulphur dioxide released had converted to sulphate aerosols within 21 to 28 days (Winker and Osborn, 1992), whilst minor amounts of unoxidised SO_2 were observed up to 170 days following Pinatubo by the Microwave Limb Sounder (MLS) on the Upper Atmosphere Research Satellite (UARS) (see Barath et al. 1993 for extensive details). Observations indicated very small particles created by gas to particle conversion, which increased in

size due to condensation of sulphuric acid and water vapour and coagulation, giving rise to optical depth spectra peaking at mid-visible or longer wavelength beginning about two months after Pinatubo (Grant et al., 1992, Valero and Pilewskie, 1992, Thomason, 1992, Russell et al. 1993, Dutton et al. 1994, Self et al. 1996).

Within two weeks, the majority of the aerosol cloud had circled the Earth, bound in latitude between 20° S and 30° N (McCormick and Veiga, 1992). This is suggested to be due in part to stratospheric aerosol transport regimes that Trepte et al. (1993) term a 'lower transport regime' where rapid poleward and downward movement is observed for aerosol deposited in the lower stratosphere (similarly noted by Fujiwara et al. 1982, Kent and McCormick 1984, and McCormick et al. 1984), and an 'upper transport regime' for material injected to higher altitudes - as is the case for the Pinatubo eruption. Trepte et al. (1993) note that in the upper transport regime, rapid detrainment of the volcanic aerosol is dependent on the planetary wave activity and the QBO phase. Poleward eddy transport from the tropical regions occurs largely within the winter stratospheric surf zone. During an easterly QBO phase planetary waves are shielded from the equator, so the surf zone is unable to penetrate as deeply into the tropics as during a westerly QBO phase where eddy mixing can occur in the tropical aerosol reservoir. Consequently, in an easterly QBO phase, which Pinatubo erupted into, only aerosol in the subtropics experiences poleward mixing, which amounted to a comparatively small amount of the aerosol, whilst the rest remained in the tropics (Trepte and Hitchman, 1992, Trepte et al. 1993). Very similar aerosol pathways have been seen in more recent chemistry-climate modelling studies (e.g. Aquila et al. 2012).

In all the eruption created around 15-20 Mt of stratospheric sulphate aerosol (Stothers, 1996, Bluth et al., 1997, Andres and Kasgnoc, 1998, and Stothers, 2001), which produced a persistent cooling for one to two years after the eruption of around 0.5 K (Robock, 2003). Clear impacts on the climate and upon stratospheric ozone were observed - with ozone depletion rates being the fastest ever recorded to date, midlatitude ozone concentrations reaching the lowest recorded levels during 1992-93 and increases in the Southern Hemisphere ozone hole being so large that it reached

an unprecedented size shortly after the eruption (Hofman et al. 1991, Dutton and Christy, 1992, Prather, 1992, Gleason et al. 1993, Solomon et al., 1993, McCormick et al., 1995).

Simulations using the Geophysical Fluid Dynamics Laboratory Coupled Model version 2.1 (GFDL CM2.1) have shown reductions in ocean thermosteric height by 10 mm and ocean heat content by around 5 x 10^{22} J due to the radiative cooling from the eruption (Stenchikov et al., 2007), neither of which recover to their normal values within the twenty year simulated time period. Stenchikov et al. (2007) also saw substantial simulated strengthening of the Atlantic Meridional Overturning Circulation (AMOC), with anomalies peaking around 1.5 Sverdrups (1 Sv = $10^6\,\mathrm{m^3 s^{-1}}$) in the period of around half a decade to a decade following the Pinatubo eruption.

Mount Pinatubo erupted into an easterly QBO phase (Seol and Yamazaki, 1998), and a positive NAO can be seen in the following two winters with the corresponding spatial pattern of surface warming in Eurasia and North America and cooling in Eastern Canada, the Arctic and the Eastern Mediterranean regions (Kirchner et al. 1999, Stenchikov et al. 2002), which is typical for a tropical volcanic eruption - as described earlier in the thesis. The first post-Pinatubo winter being in an easterly QBO phase and the second post-Pinatubo winter being in a westerly QBO phase has been shown in simulations to substantially and nonlinearly decrease, and increase, respectively, the positive NAO in the first and second winters (Stenchikov et al. 2004). The results of Stenchikov et al. (2004) showed geopotential height anomalies in the second winter from volcanic forcing and a westerly QBO being three times as large as the anomalies from volcanic forcing alone. From longer composites analysing the NAO index, it has been seen that only the first winter gives a statistically significant positive NAO (Driscoll et al. 2012, Christiansen 2008). Similarly, Fischer et al. (2004) analyse near-surface temperature in winters following volcanic eruptions in proxy records dating back to 1600. They produce composites where radiative forcing from aerosol loading was expected to be greater than 1 $\mathrm{Wm^{-2}}$ and 3 $\mathrm{Wm^{-2}}$, and see a larger Eurasian warming in the composites of winters that had a radiative forcing of at least 3 $\mathrm{Wm^{-2}}$ than those with a radiative forcing of at least 1 $\mathrm{Wm^{-2}}$.

One of the most profound responses to Pinatubo, and yet one poorly simulated in GCMs, was the strengthened stratospheric polar vortex response and corresponding NAO and Eurasian surface warming. The positive NAO following Pinatubo caused such a large cooling in the Eastern Mediterranean (likely in combination with the radiative cooling) that Jerusalem experienced rare snowfall whilst coral at the bottom of the Red Sea died due to cooling of surface waters that caused convective mixing of the entire depth of water (Genin et al. 1995, Robock et al. 2003). Polar bears benefited substantially from the cooler conditions in the Hudson Bay area (in North East Canada), producing heavier and healthier cubs now known as "Pinatubo Bears" (Stirling, 1997).

Many people have proposed that increased stratospheric resolution is necessary to obtain the post-volcanic NH wintertime response (e.g. Stenchikov et al. 2006, Graf et al. 2007, Ottera 2008). In particular Graf et al. (2007) proposed from analysis of the NCEP reanalysis dataset that it was possible that wave reflection at the stratopause region was the dominating dynamical process, and therefore any models that do not sufficiently represent this region will not be able to capture the dynamics they suggest to be important. The stratopause is at heights of 50-55 km in the atmosphere (Andrews et al., 1987) meaning it is well above the lid heights of many models. Moreover, many models' upper layers do not represent dynamics sufficiently well, meaning the lid height of the model would have to be well above this region. Therefore, a model with enhanced vertical resolution in the stratosphere that also goes beyond the stratopause must be used if either Graf et al. (2007)'s diagnosis, and implication of a necessarily well resolved stratosphere, is believed to be correct or other stratospheric dynamical processes requiring of high stratospheric resolution are important.

4.2 Experimental Set-Up and Purpose

Here simulations of the Mount Pinatubo eruption of 1991 are performed using both the high-top and low-top versions of HadGEM2-CC, 'L38' and 'L60', to assess the influence that increased resolution in the stratosphere may have on the post-volcanic wintertime dynamical response. The L38 and L60 model versions both have a horizontal resolution of 1.25° latitude × 1.875° longitude, whilst L38 has 38 vertical levels extending into the mid-stratosphere around 40 km and L60 has 60 vertical levels that extend to the mesopause around 85 km (Hardiman et al., 2010, Osprey et al., 2010). L38 has no QBO, whilst the vertically-extended model L60 represents wave breaking of the non-orographic gravity wave scheme to internally generate a QBO (Scaife et al., 2000). The L38 and L60 versions also have fully coupled identical ocean models with 40 levels and horizontal resolution of 1.0° latitude × 1.0° longitude (Martin et al., 2011). For a detailed description of L38 and L60, including an assessment of their stratospheric variability, see Osprey et al. (2010) and Hardiman et al. (2010).

These simulations are performed on the High End Computing Terascale Resources (HECToR) supercomputer platform. HECToR is a British academic national supercomputer based in the University of Edinburgh, which runs on the Cray XE6 platorm with 90,112 cores. To create the simulations, control simulations available on the Met Office and NERC Supercomputing Node (MONSooN) supercomputer were taken through the PUMA interface, and transferred to be operable on the HECToR supercomputer where they were performed and also modified to include the effects of volcanic eruptions.

Identical simulations using both the high-top and low-top models are performed, consisting of separate 20 year control simulations and 10 separate Pinatubo eruptions. The models incorporate the Sato et al. (1993) optical depth dataset to implement realistic spatial and temporal Pinatubo simulations. Figure 4.1 is a schematic diagram which represents the implementation of the simulations. Each year a new run with a volcanic eruption branches off from the main control run in order to sample the

different QBO and ENSO phases, minimising their influence on the results of the simulations.

For comparison with observations, the data used are taken from the European Reanalyses (ERA40), which come from the European Centre for Medium Range Weather Forecasting (ECMWF). The data are provided on a regular 2.5° × 2.5° horizontal grid on 23 vertical pressure levels from 1000 mb to 1 mb. The data span the period January 1958 to December 2001.

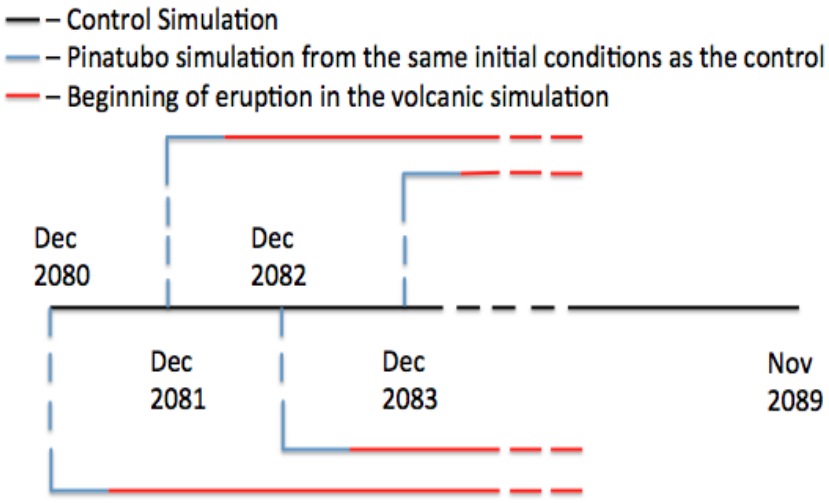

Figure 4.1: Simple schematic diagram representing experimental set-up.

In addition to stratospheric resolution, another possible source of error in the dynamical ability of models simulating volcanic eruptions is the implementation of the forcing. In the L38 and L60 the models' volcanic forcings are applied by specifying variations in optical depth of stratospheric sulphate aerosol at 0.55 micrometre in wavelength, the data for which is provided by Sato et al. (1993) - a very common dataset employed in many major climate models for representation of volcanic forcing (chapter three of this thesis). From this aerosol optical depth values are calculated and prescribed for four latitudinal bands with equal area (90° N - 30° N, 30° N - 0°, 0°-30° S, 30° S - 90° S - see figure 4.2) for every month of the model run. Importantly,

this is distributed in the vertical in proportion to the mass of air in each stratospheric level above the tropopause to a lid at 30hPa.

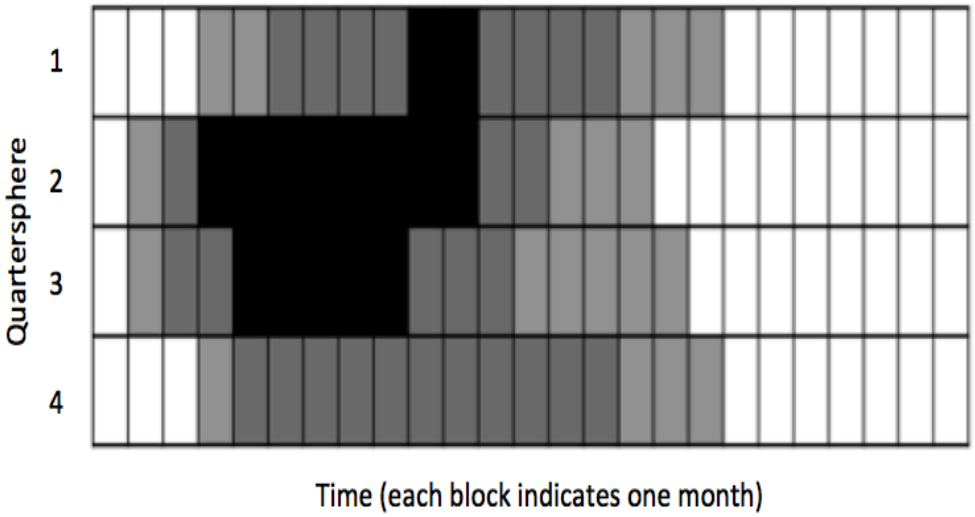

Figure 4.2: A diagram to represent the time evolution of volcanic stratospheric aerosol in HadGEM2. The aerosol is applied in four quarterspheres of approximately equal area: 90° N to 30° N, 30° N to 0°, 0° to 30° S, 30° S to 90° S. Shading corresponds to aerosol optical depth values at 0.55 μ m of 0-0.05 (white), 0.05-0.10 (light gray), 0.10-0.15 (dark gray) and 0.15-0.20 (dark black) and demonstrates how a volcano would be represented.

It is postulated that the important influence of the aerosols on the stratosphere that is responsible for the observed surface Eurasian warming is the lower stratospheric temperature gradient. Another notable property of the Pinatubo eruption is that observations show that the sulphate aerosol does not directly follow the 30 hPa pressure level, but slopes away from the tropics, Trepte et al. (1993). It may also be possible, therefore, that the *gradient* of the aerosols in the stratosphere is an important contributing factor and this influence is tested in this chapter too.

In the HadGEM2 model, the 30 hPa aerosol lid is implemented by a constant set at 30. As this is a constant, information on the position of the latitude in the model is therefore not required in the subroutine that distributes the aerosol between the tropopause and 30 hPa, only time. Therefore, a third set of simulations is performed where the subroutines in the L60 model have been modified such that the model passes

down latitudinal information to allow the maximum height of the volcanic aerosol to be set according to the following formula, where θ is the latitude ranging from $-90°$ to $90°$ - in better accordance with the observations of Trepte et al. (1993). Whilst the predominant focus of the chapter is the Northern Hemispheric dynamical response, other notable features are briefly mentioned, including the radiative response and Southern Hemispheric dynamics.

$$\mathrm{V}(\theta) = 0.650\,((1 - w(\theta))(a(\theta)) + w(\theta)b(\theta)) \tag{4.1}$$

where

$$a(\theta) = (12 - 10e^{-(\theta/65.0)^{4.0}})/2.0 \tag{4.2}$$

$$b(\theta) = -0.0461\theta^2 + 15.0000 \tag{4.3}$$

The quadratic weighting function, $w(\theta)$, is

$$w(\theta) = (1.0/(90.0^2))(\theta + 90)^2 \;\forall\; \theta \in \text{[-90,0]} \tag{4.4}$$

$$w(\theta) = (1.0/(90.0^2))(\theta - 90)^2 \;\forall\; \theta \in (0, 90] \tag{4.5}$$

The new V is therefore:

$$\begin{aligned} V(\theta) = 0.65 \left(\left[1 - \frac{(\theta + 90)^2}{90.0^2} \right] (12 - 10e^{-(\theta/65.0)^{4.0}})/2.0 \right) + \\ 0.65 \left(\left[\frac{(\theta + 90)^2}{90.0^2} \right] (-0.046\theta^2 + 15) \right) \forall\; \theta \in \text{[-90,0]} \end{aligned} \tag{4.6}$$

$$\begin{aligned} V(\theta) = 0.65 \left(\left[1 - \frac{(\theta - 90)^2}{90.0^2} \right] (12 - 10e^{-(\theta/65.0)^{4.0}})/2.0 \right) + \\ 0.65 \left(\left[\frac{(\theta - 90)^2}{90.0^2} \right] (-0.046\theta^2 + 15) \right) \forall\; \theta \in \text{(0,90]} \end{aligned} \tag{4.7}$$

Two different aerosol lids are used in simulations of the L60 model. These are shown in figure 4.3.

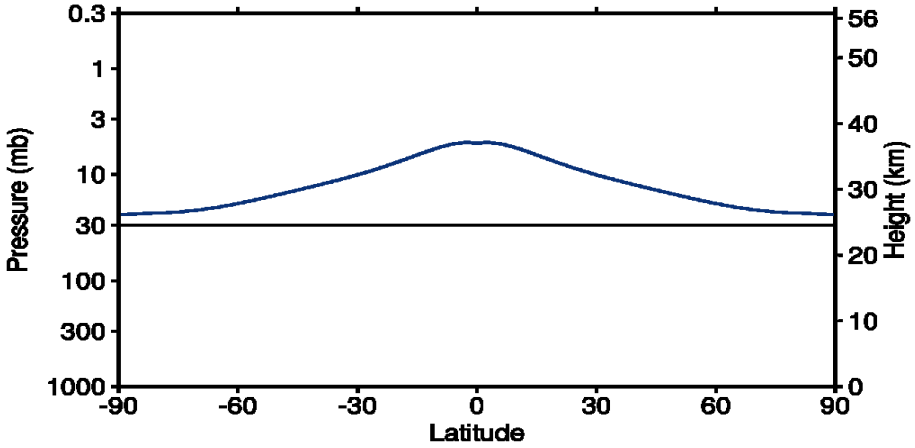

Figure 4.3: The aerosol lid of HadGEM2 when set to 30hPa (black line), which is currently implemented in all HadGEM2 simulations, and the modified lid as given in equations 4.1-4.7 (navy blue line).

4.3 Results

4.3.1 ERA40 Dataset

Whilst the post volcanic near-surface temperature anomaly composite was presented for the nine largest eruptions over the recent historical record earlier in the thesis, the near-surface temperature anomalies for the ERA40 dataset in the first and second winter periods (DJF) following the Pinatubo eruption are shown in figure 4.4. In the winter of 1991/92 Eurasian warming, eastern Mediterranean cooling, North American warming and cooling in the Canadian/polar regions is evident. Statistical significance is not very geographically extensive, but high variability in the Northern Hemisphere wintertime, reduces the significance of the anomalies. The winter Eurasian warming, Greenland cooling, North American warming and Eastern Mediterannean cooling seen in both winters here is nearly identical to plots of post-Pinatubo near-surface temperature anomalies computed using numerous datasets (e.g. Kirchner et al., 1999, Stenchikov et al., 2002, Stenchikov et al., 2004, and Ottera, 2008). As with these studies, statistical significance is set at the 90% confidence level due to the large

variability in the Northern Hemisphere and lower sample size - the hatched areas are near identical for the other datasets in these papers.

A positive ENSO phase (El Niño) can be seen, which helped to offset some of the radiative cooling following the eruption (Robock, 2000). ENSO has been suspected to influence the NAO through both enhanced planetary wave activity into the stratosphere which reduces the strength of the stratospheric polar vortex and so affects the NAO at the surface (e.g. Huang et al. 1998, Seager et al. 2010, Li and Lau 2012) and also through a "tropospheric bridge" mechanism (Graf and Zanchettin, 2012) involving propagation of a wave number five disturbance around the subtropical Northern Hemisphere which would directly weaken the NAO. Despite this, there is no current evidence of an ENSO influence on the NAO following volcanic eruptions from assessing observational data of the most recent 15 large volcanic eruptions in the historical record (Christiansen, 2008). It is nonetheless possible that a lack of sample size may have hindered the analysis of Christiansen (2008), and that the El Niño phase following Pinatubo may have reduced the size of the positive NAO and the corresponding near-surface temperature anomaly in the first winter.

4.3.2 Results from the L38 Pinatubo Simulations

Figure 4.5 presents the composite anomaly of the two following DJF periods over all simulated Pinatubo eruptions from the control simulation for zonally averaged temperature, zonally averaged zonal wind, MSLP and near-surface temperature. These plots are plotted on the same axes as the high-top model plots (shown later) for clarity and ease of comparison.

In these simulations L38 demonstrates the capability of achieving a lower stratospheric warming response to the Pinatubo eruption. Positive temperature anomalies due to the volcanic aerosol in the stratosphere are strongly evident and statistically significant, reaching around 3.5 K in the lower stratosphere. Tropical tropospheric temperature anomalies reveal statistically significant cooling throughout the entire region. At the Southern Hemisphere polar regions in the troposphere, a cooling is

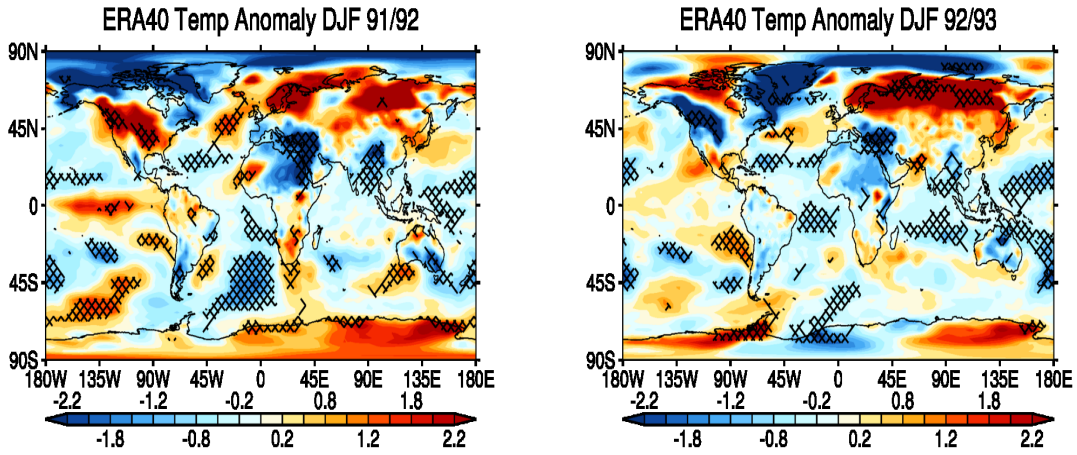

Figure 4.4: Seasonally averaged anomalies of near-surface air temperature (K) from the ERA40 analysis for the winters (DJF) 1991/92 and 1992/93. Anomalies are calculated with respect to the mean for the years 1985-1990. As with Stenchikov et al. (2002) the hatching corresponds to the 90% confidence level using a two tailed t-test. A t-test compares the difference in the mean of two groups of normally distributed data. When one value is to be compared against another group of data, that single value is compared against the mean of the other group of data. Therefore, here the hatched areas areas represent differences significant at the 90% level according to the t-test between their 1991/92 and 1992/93 values and the mean of the pdf from the 1985-1990 climatology.

observed whilst in the Northern Hemisphere tropospheric polar regions there is zonally averaged warming. One possible reason is that this is due to the decreasing of incoming solar radiation in the Southern Hemisphere during its summertime, whilst the winter hemisphere receives substantially reduced incoming solar radiation and the aerosol may act as a blanket that predominantly scatters radiation back to the surface. The stratospheric polar vortex region shows no sign of cooling, and in fact shows a warming of around 1 K, although these anomalies are not statistically significant.

Zonally averaged zonal wind anomalies in figure 4.5 demonstrate a few features. Large positive anomalies can be seen in the Southern Hemisphere. This is consistent with simulations analysed by Karpechko et al. (2010). In their paper, they analysed the OND anomalies in CMIP3 models for the El Chichón and Pinatubo eruptions. They discovered that the models simulated a strengthening of the winds in this time

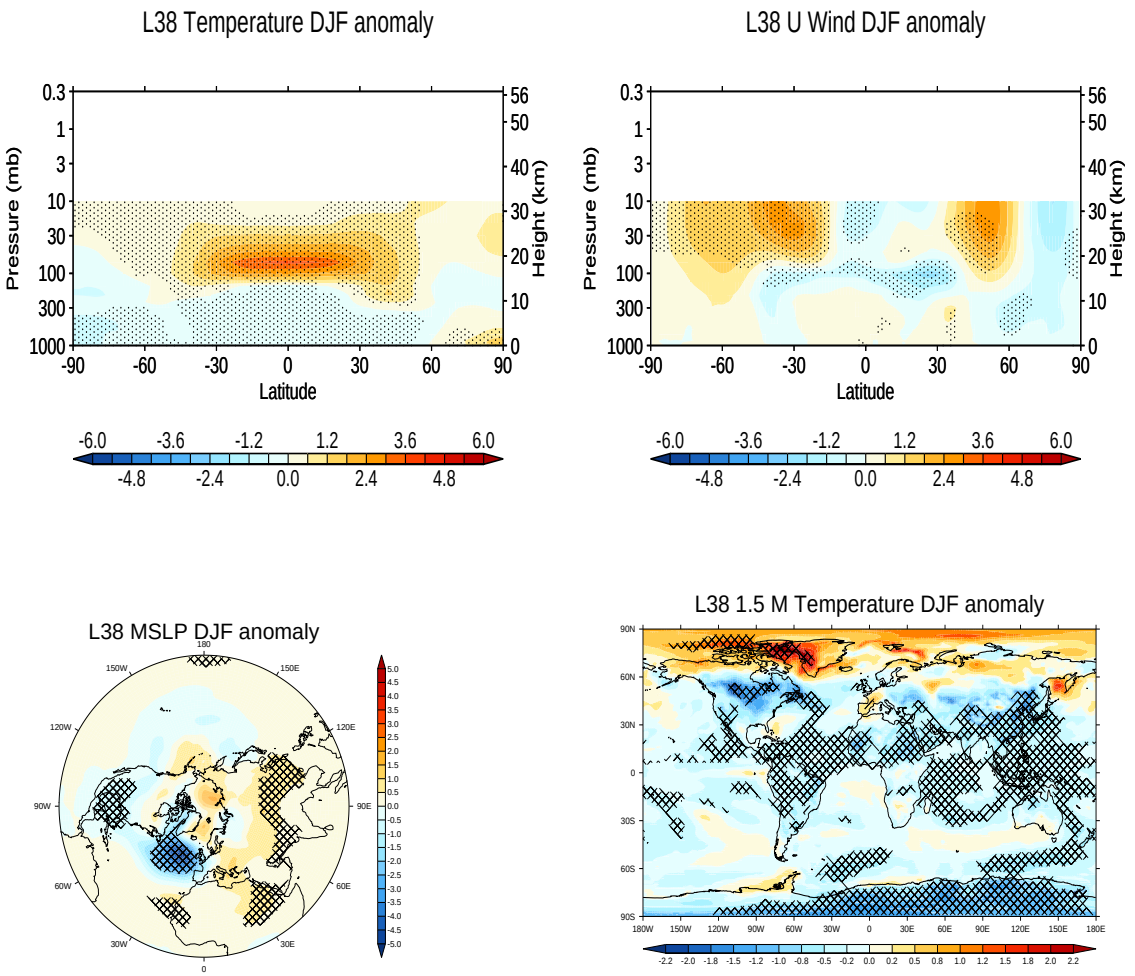

Figure 4.5: L38 anomalies of DJF temperature (K), wind (ms^{-1}), MSLP (hPa) and near surface temperature (K) for the two winters. Stippling corresponds to the 90% confidence level using a two tailed t-test. Unlike observations, for all model simulations hatching represents significant differences between the volcanically perturbed simulations and the control simulations with no volcanic perturbation (otherwise exactly alike).

period and region. However, they note that the anomalies in ERA40 reanalysis for El Chichón and Pinatubo show no such strengthening of Southern Hemisphere winds. They conclude that this lack of Southern Hemisphere strengthening cannot easily be explained by variability such as ENSO phase or other factors weakening a strong zonal wind response in the observations - contrasting that of the Northern Hemisphere case. Extending this study for the CMIP5 models and the simulations of both the L38 and L60 during the OND period to understand the response here is possible, but outside

the scope of the current chapter.

Small decreases and increases in the tropospheric wind around 60° N and 35° N, respectively, appear to represent a small but significant shift in the wintertime tropospheric jet towards the equator. Importantly, anomalies of wind in the Northern Hemisphere stratosphere associated with the temperature gradient due to aerosols can be seen. A statistically significant increase of around 3 ms^{-1} can be seen between approximately 30° N to 60° N which corresponds to the region of maximum anomalous temperature gradient, as one would expect from thermal wind shear. Despite this there is no increase in the polar stratospheric winds. In fact a decrease can be seen, although these anomalies are not statistically significant except for a small region between 85° N and 90° N in the lower stratosphere. This change in winds directly over the region of the largest temperature gradient without any propagation of the winds to the polar stratosphere appears to represent a more 'static' response of the model to volcanic aerosol heating, indicative that improved dynamics may be important in obtaining a strengthened polar vortex response and consequent positive NAO.

MSLP anomalies reveal, contrary to the positive NAO observed following volcanic eruptions in observations, a statistically significant *negative* NAO pattern in wintertime. Decreases in MSLP of around 5 hPa over the Northern Hemisphere Atlantic and increases of up to 2 hPa over the polar regions are seen, although the increases are not statistically significant. This is similar to Gillett et al. (2013) who studied CMIP5 models' response to many forcings in a much more general detail than Driscoll et al. 2012, but their analysis which also included volcanoes. Contrary to observations the multi-model average of those analysed in Gillett et al. (2013) simulated a negative NAO response to volcanic eruptions.

As is therefore expected from the fields explored so far, the near-surface temperature field shows that there is no response similar to observations for the L38 model. In fact there is a warming over Greenland, as opposed to a cooling as seen in observations, and a cooling over North America, as opposed to a warming as seen in observations. There is a hint of Eurasian warming, however it has little cohesive structure and parts of Northern Europe even cool. However, none of these positive

anomalies in Eurasia are statistically significant. The Antarctic Peninsula can also be seen to warm in these simulations, although anomalies are not significant.

Temperature anomalies do, however, reveal a clear tropical and statistically significant radiative cooling, with anomalies reaching up to approximately -2 K. Anomalies are extensive and evident over the Asian monsoon region, which indicate there may be a substantial subsequent disruption of the Asian Monsoon. Cooling over the African continent may also imply disruption to its monsoonal circulation, although detailed investigations of the circulation patterns and precipitation anomalies over these regions are oustide the scope of the current study.

Similar to the CMIP5 models studied in Driscoll et al. (2012), the correct dynamical changes are absent and radiatively induced tropical cooling appears to be more evident than in observations. This topic is returned to and discussed in the conclusions section.

The L38 model therefore does not reproduce the observed post-volcanic dynamical response at high latitudes. The model achieves a negative NAO, *opposite* to that observed, despite achieving a strengthening of winds around the direct location of the maximum temperature gradient. It is possible, therefore, that the L60 model, with an internally generated QBO, better representation of variability and much more realistic representation of sudden stratospheric warmings of the polar vortex (Martin et al., 2011) may have a substantially better representation of the stratospheric dynamical response to a volcanic eruption than the L38 model, and thus is a good candidate for exploration.

4.3.3 Results from the L60 Pinatubo Simulations

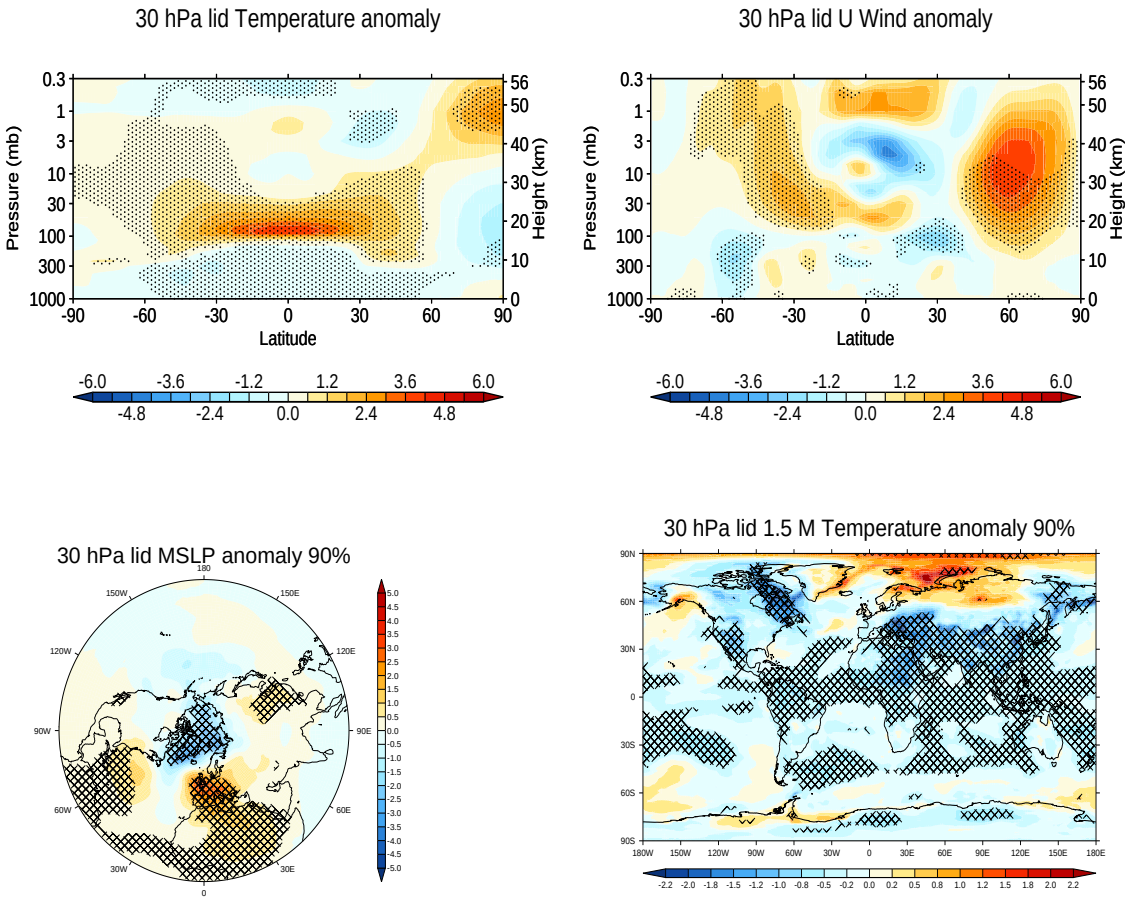

Figure 4.6: L60 anomalies of DJF temperature (K), wind (ms^{-1}), MSLP (hPa) and near surface temperature (K) for the two winters. Stippling corresponds to the 90% confidence level using a two tailed t-test.

Figure 4.6 presents the composite anomaly from the control simulation of the two following DJF periods over all simulated Pinatubo eruptions for zonally averaged temperature, zonally averaged zonal wind, MSLP and near-surface temperature for the L60 model. As with the L38 model, statistically significant anomalous lower stratospheric heating is present due to the volcanic sulphate aerosols. Very similar to the L38 model, tropical tropospheric cooling is evident due to the scattering of incoming solar radiation. The most marked difference between the two set of simulations is that instead of warming of the polar stratosphere here a cooling can be seen. Far above the extent of the L38 model a statistically significant warming is part of an

anomalous 'quadrupole' pattern of cooling and warming between 30° N and 90° N in stratosphere in the L60 model, as is seen in observations.

The anomaly of zonally averaged zonal wind shows a statistically significant increase in the Southern Hemisphere winds around 30° S - 50° S due to the aerosols heating in the tropical lower stratosphere. Anomalies in the Southern Hemisphere troposphere can be seen, with a significant decrease in wind of around 1 ms^{-1} throughout the entire height of the troposphere between 45° S and 60° S. Increases in wind closer to the equator may suggest a shift in the jet, but these anomalies are not very significant.

A substantial difference to the L38 model anomalies is a statistically significant increase in the wind between 50° N - 90° N and throughout the entire stratosphere that exceeds 6 ms^{-1}. Not only are these wind anomalies twice as large as compared to the L38 model, but they also represent a major strengthening of the stratospheric polar vortex following volcanic eruptions.

MSLP fields reveal, consistent with a strengthened stratospheric polar vortex, a statistically significant anomalous positive Arctic Oscillation pattern, with decreases in pressure directly over the polar regions peaking at -4 hPa, and increases across the Atlantic, European and Asian regions of up to 3.5 hPa.

Near-surface temperature anomalies reveal widespread tropical tropopsheric cooling consistent with the zonal averaged temperature plot. Some warming, as with the L38 model, can be seen over the Antarctic Peninsula. Unlike the L38 there is some statistical significance over this region, although the anomaly is not very large or extensive.

There is a zonally asymmetric cooling and warming pattern in the Northern Hemisphere between North East Canada and the Arctic and Eurasia, with an extensive and statistically significant cooling over North East Canada and polar regions peaking at 2.2 K and large areas of corresponding warming that exceed 2.2 K. There is some significance associated with this warming, but not much. A substantial cooling in the Eastern Mediterranean region, part of this cooling/warming pattern, peaking at over -2.2 K is seen.

These results show a marked and substantial improvement in the simulation of stratospheric dynamics and the resulting surface anomalies in comparison to the L38 simulations - with additional stratospheric resolution not only 'neutralising' an incorrect surface response, but also achieving the correct sign of response. Despite this, the magnitude of these anomalies are nonetheless less than observed over both winters following Pinatubo. Recalling uncertainty due to variability following Pinatubo and the possibility that the first winter following volcanic eruptions may be the one most substantially affected - consistent with observational record when extended over the historical period of 1883 to present day (Driscoll et al. 2012) - the first and second winters are investigated separately.

4.3.4 L60 - First and Second Winter Responses

Anomalies of MSLP and near-surface temperature for early winter, December-January (DJ), and late winter, February-March (FM), are shown in figure 4.7 - second winter responses are shown later in the chapter. These anomalies reveal an extremely large first winter response to a volcanic eruption that is very similar to the observed response following volcanic eruptions. MSLP anomalies for DJ reveal very large and extensive statistically significant increases in MSLP around the polar regions coupled with large and significant decreases in MSLP in the polar regions that corresponds to a positive Arctic Oscillation. The substantial positive Arctic Oscillation represents the change in atmospheric circulation that forces the near-temperature anomalies during this period.

DJ near-surface temperature anomalies in the tropics (due to radiative cooling) are larger than over both winters, and much more significant and widespread as expected as a consequence of a larger sulphate aerosol burden than in the second winter period. Fairly widespread statistically significant warming can be seen over the Antarctic Peninsula - suggesting that this may indeed be a real response in the L60 model, perhaps leading to a possibly important increase in melting of the West Antarctic Ice Sheet, which has suggested to be unstable although it is not currently clear (Oppenheimer et al. 2008).

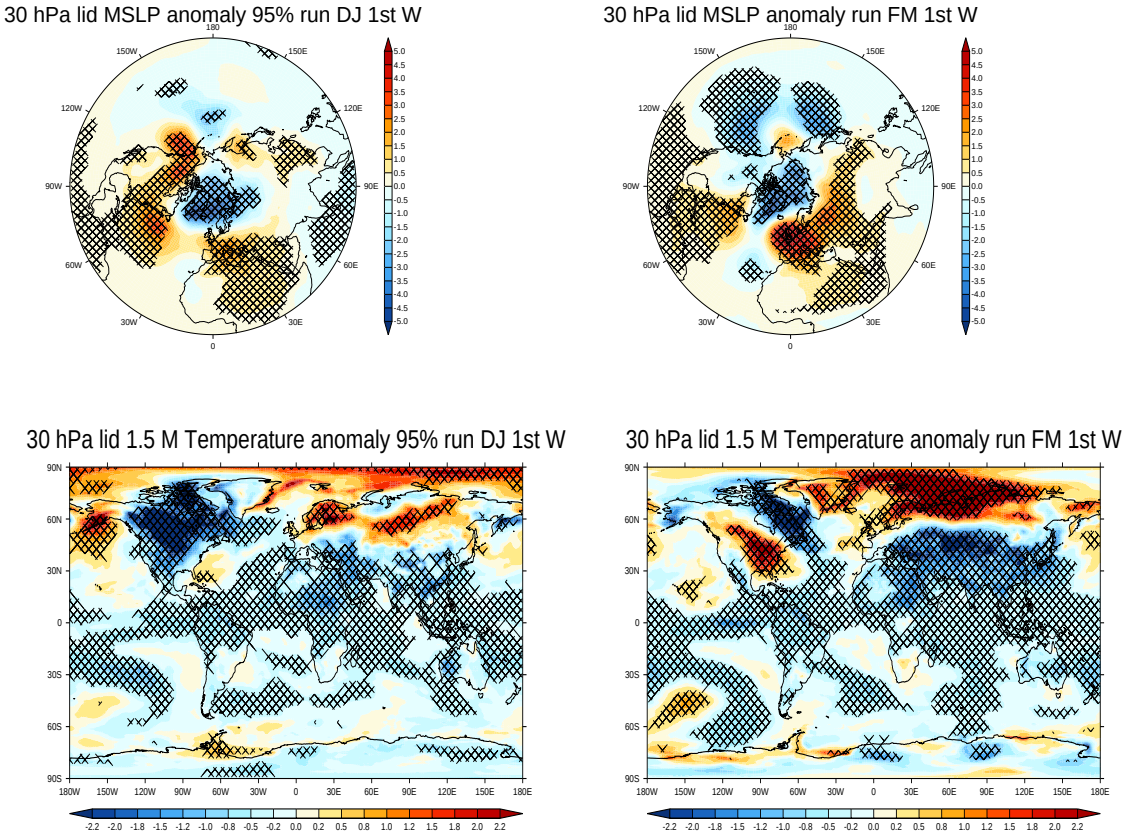

Figure 4.7: L60 anomalies of temperature (K), and MSLP (hPa) for DJ (left) and FM (right) for all the first post-Pinatubo winters. Hatching corresponds to the 95% confidence level using a t-test.

In the DJ period extremely large negative temperature anomalies that exceed -5 K are evident over North America and parts of the Altantic. Dynamical changes as a result of the eruptions are almost everywhere significant. Already in early winter there is a large and statistically significant warming over Northern Europe and Asia reaching over 2.2 K which is partnered with a corresponding cooling in the Eastern Mediterannean and the Red Sea. It is recalled that the Red Sea experienced extremely large convective mixing due to the cooling of surface waters following Pinatubo, and so a possibly interesting investigation would be to explore the oceanic changes in the model to help understand if this is a robust response to Pinatubo.

In the FM period, MSLP fields again show a strong sign of a positive and statistically significant Arctic Oscillation, with negative anomalies at the pole peaking at -

4.5 hPa and positive anomalies in the mid latitudes peaking well over 5 hPa. During late winter, circulation changes induce substantial warming over Eurasia, reaching temperature anomalies of 4.5 K. Substantial cooling over the Eastern Mediterannean can be seen, along with a cooling over North Eastern Canada and the polar regions and warming over the North American continent. Almost all anomalies associated with the change in circulation are statistically significant, and in the first winter the response of the L60 model replicates very strongly that of the observed response.

Second winter anomalies are presented in figure 4.8. In early winter (DJ) anomalies of MSLP show almost no sign of a positive Arctic Oscillation. Correspondingly, the anomalies of near-surface temperature reveal no evidence of a strong second winter dynamical response to a volcanic eruption. Cooling anomalies over the polar regions and Canada can be seen, and there is some evidence of a warming peaking at the North American continent, however this anomaly is not significant. In late winter, a weak reduction in MSLP over the Arctic Ocean can be seen. Also the positive anomaly associated with the NAO is centered much more over Western Europe (simlar spatially to that which can be seen following Pinatubo). However, the anomalies are much weaker than the first winter response and a clear positive Arctic Oscillation response is not evident. Near-surface temperature reveal some much weaker warming over Eurasia, whilst Western Europe in fact experiences cooling. North Eastern Canada and the Eastern Mediterannean show some cooling whilst there is some North American anomalous warming, but this is not very similar to the observed response.

Figure 4.9 presents anomalies of the simulations of the L60 model *from* the L38 model, instead of its own climatology, for the first DJ and FM periods. Here only the associated dynamical anomalies are present without the radiative anomalies, as the tropical tropospheric cooling occurs in both sets of simulations.

The MSLP anomaly fields reveal a large and significant positive Arctic Oscillation, indicative that not only does the L60 model attain a very large response to the Pinatubo eruption in its own right, but that stratospheric resolution makes a large difference in the simulated response. Temperature anomalies in DJ reveal large cooling over Greenland and the North American regions. During late winter large

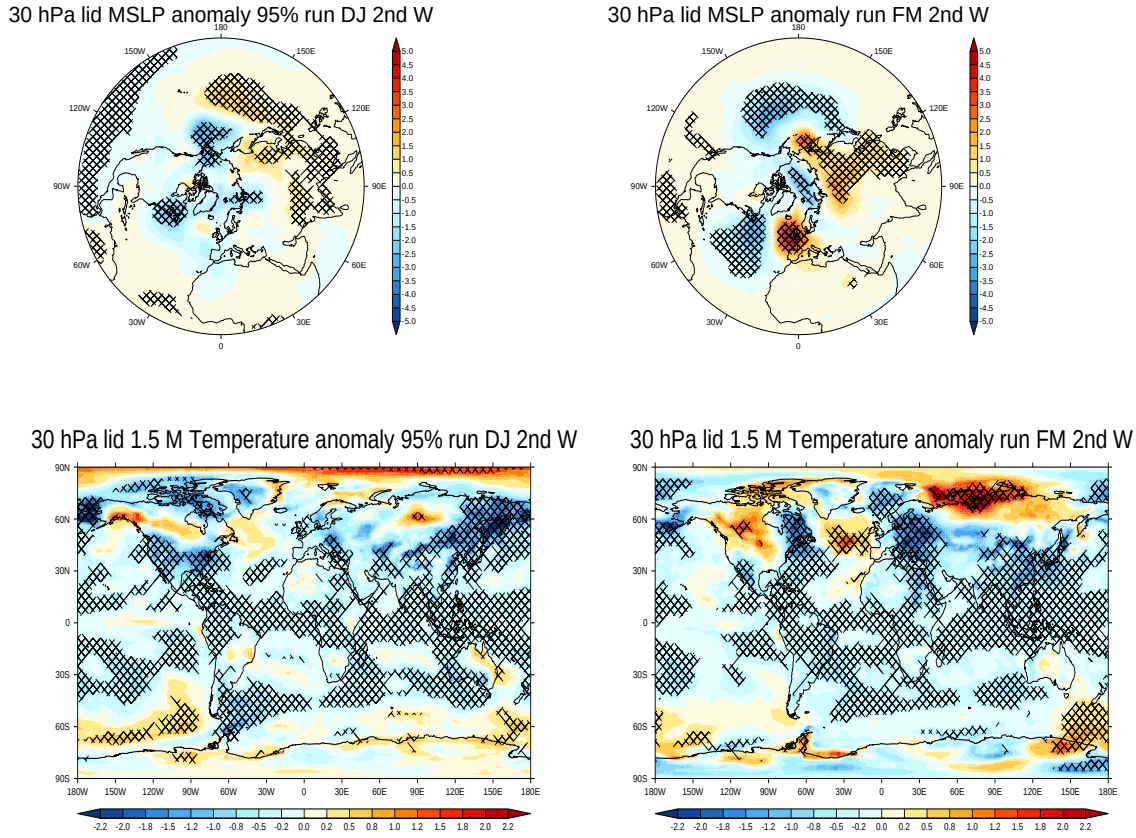

Figure 4.8: As figure 4.6 but for the second simulated winter. Hatching corresponds to the 95% confidence level using a t-test.

and extensive anomalies of Eurasian warming of again up to an extremely large 4.5 K are evident, with the associated Eastern Mediterannean showing a prominent and statistically significant cooling. Whilst very similar to the anomalies from control, anomalies of temperature over Eurasia aren't quite as extensive due the L38 anomalies possessing some random noisy warming (and cooling) - that is neither coherent nor significant.

Overall, the magnitude of the L60 model's response is at the upper end of the magnitude observed following large volcanic eruptions and these sets of simulations demonstrate a very substantial improvement of a model with enhanced stratospheric resolution (L60) over its counterpart (L38) model.

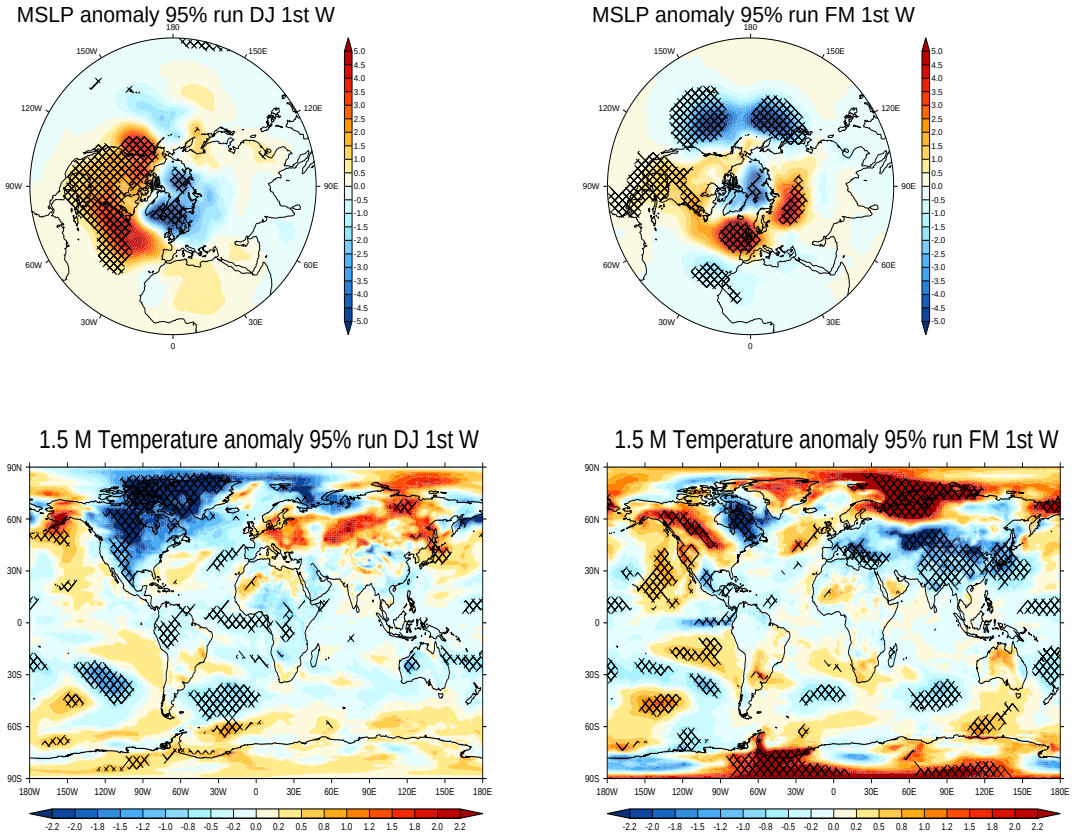

Figure 4.9: As figure 4.8, but here anomalies are the L60 from the L38 model instead of climatology. Hatching corresponds to the 95% confidence level using a t-test.

4.3.5 Stratospheric Evolution

In order to explore why this response occurs, it is useful to assess the evolution of important dynamical fields in the stratosphere. Figure 4.10 shows the month-by-month evolution of the first winter zonally averaged temperature anomalies in the stratosphere. They show lower tropical stratospheric warming during all months, and importantly, during wintertime a significantly cooler polar stratospheric polar vortex which reaches anomalies of -6 K, creating a substantial temperature gradient in the polar stratosphere. This anomaly propagates polewards and downwards throughout winter and towards the end of the winter period a systematic and statistically significant stratospheric warming can be seen.

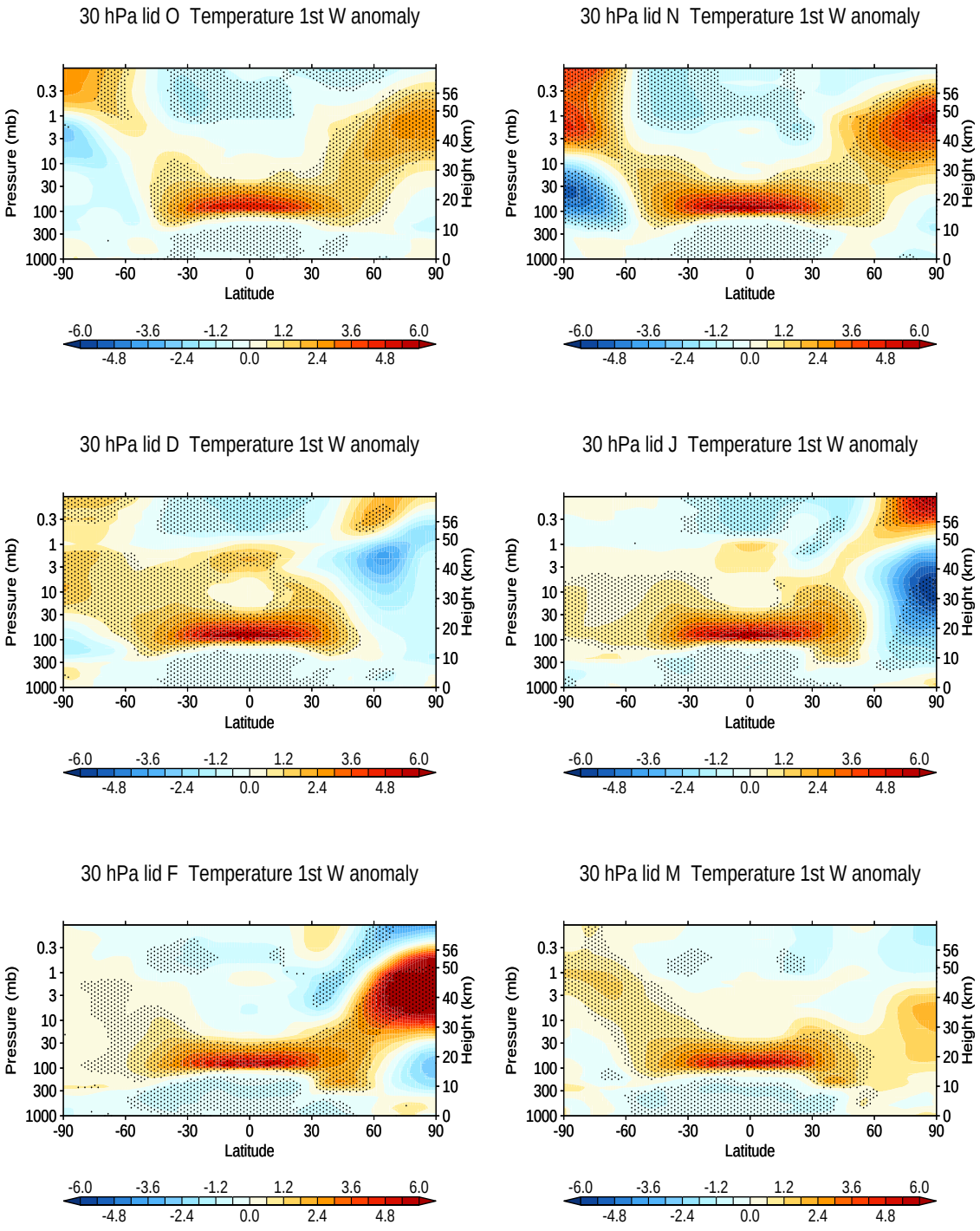

Figure 4.10: Monthly first winter temperature anomalies (K) for L60. Stippling corresponds to the 95% confidence level using a t-test.

Intriguingly, before winter, a warming of the upper polar stratosphere can be seen. These anomalies are explained later by showing changes in the Brewer-Dobson circulation due to the aerosol heating, which is dynamically counteracted in the wintertime by alterations to the planetary wave propagation.

Figure 4.11 is as Figure 4.10, but for the zonally averaged zonal wind. The wind anomalies are extremely similar, both spatially and temporally, to the anomalies shown by Ineson et al. (2011). In their paper, they analysed solar forcing of winter climate variability using the ERA40 reanalysis and a version of the Met Office Hadley Centre general circulation model, similar to HadGEM3 revision 1.1, which is similar but not identical to this model. There they demonstrate changes in the circulation of the atmosphere due to changes in solar forcing. Incorporating the Solar Irradiance Comparson Experiment and Spectral Irradiance Monitor (SIM), they estimate and implement changes in the ultraviolet radiation between solar minimum and solar maximum of the 11-year solar cycle. In doing so, the changes in incoming UV radiation alters the temperature gradients in the tropical stratosphere due to increased or decreased amounts in the absorption by ozone. This temperature gradient alters the propagation of planetary waves in the polar stratosphere, causing a more strengthened stratospheric polar vortex in the solar maximum compared to solar minimum. This signal then propagates polewards and downwards as winter progresses, in their model peaking around 5 ms^{-1} (a third of the size of the volcanic anomalies seen here).

Such a response has been seen in similar investigations from observations of not only solar cycle changes (e.g. Kodera and Kuroda, 2002), but also to volcanic forcing (Kodera, 1995). Ineson et al. (2011) demonstrate how changes in the temperature gradient alter the propagation of planetary waves and they show changes in the EP flux divergence (EP fluxes are introduced in greater detail later) during mid-winter which correspond to alteration of the path of planetary waves, reducing the disturbance of the flow and allowing an anomalously strong wind over the polar stratosphere.

Such a wind pattern is seen here following the heating induced by the sulphate aerosol. During October, statistically significant wind anomalies can be seen around

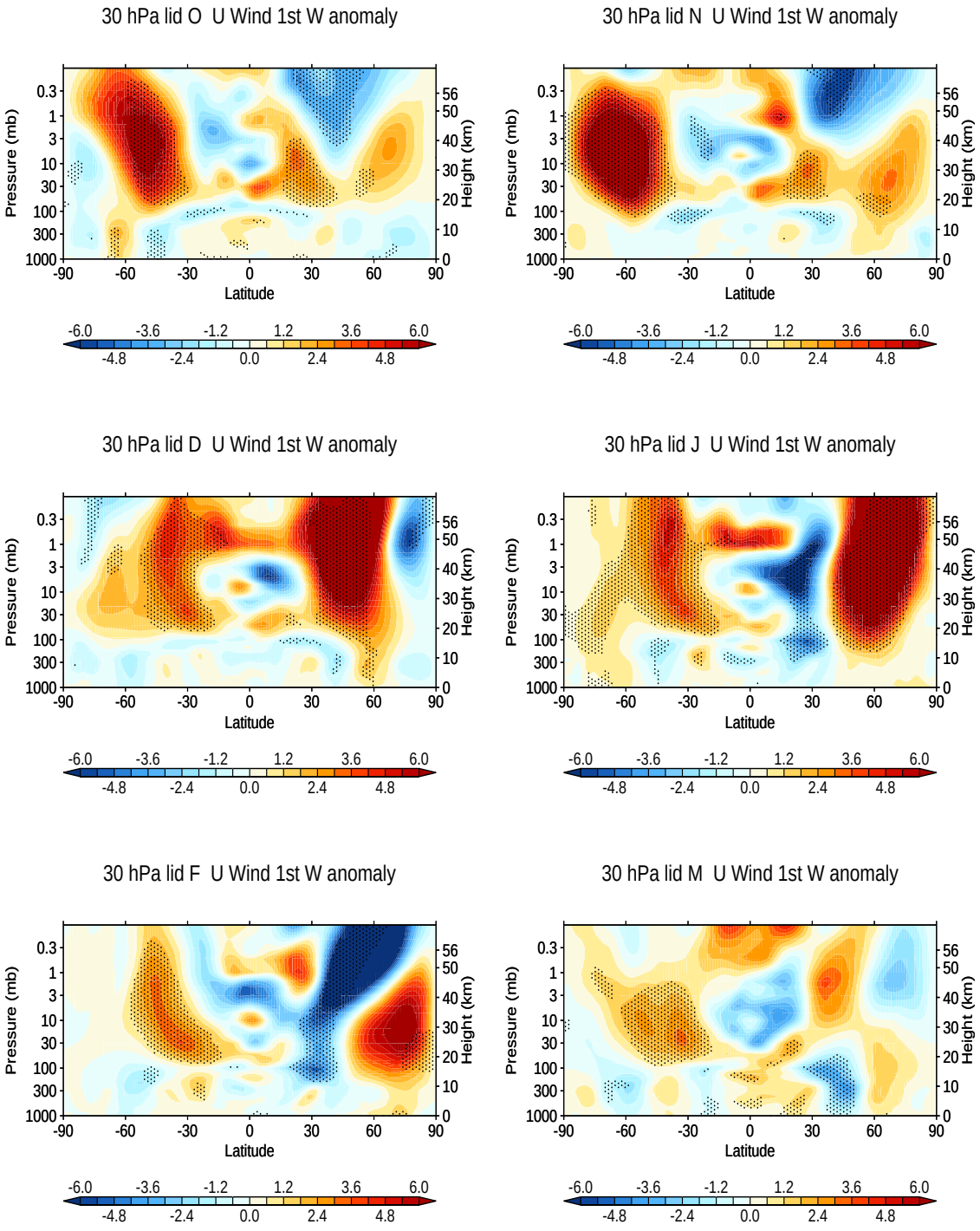

Figure 4.11: Monthly first winter u wind anomalies (ms^{-1}) for L60. Stippling corresponds to the 95% confidence level using a t-test.

30° N in the middle and upper stratosphere due to the changes in temperature gradient from the sulphate aerosol. During December, the wind anomalies grow to be extremely large, with the anomalies reaching around 15 ms^{-1} and extending from the upper stratosphere to the surface between 30° N - 60° N, with anomalies almost everywhere significant. This signal propagates polewards and downwards during the winter with anomalies reaching a maximum in January corresponding to a substantially strengthened stratsospheric polar vortex. This is then coincident with a decrease in the stratospheric winds between about 20° N - 35° N and towards the end of winter this signal decreases in strength as negative anomalies propagate from above as seen in observations (Kodera, 1995). Although the anomalies are a little weaker and less significant, the monthly response in the winds, temperature, MSLP and near-surface temperature can be seen to hold across both winters in the month-by-month analyis. It is noted that there are substantial and statistically significant changes in the Southern Hemisphere wind in the first winter, and especially during the period of major stratosphere-troposphere coupling in the Southern Hemisphere (OND).

Given such similarity in response to simulations of solar activity and observations of both solar and volcanic eruptions, it could be expected that the temperature gradients here also alter the planetary wave propagation which then leads to the strengthened vortex and positive NAO in these simulations. Whilst diagnostics such as temperature, wind and MSLP can give a strong assessment of the dynamics and are sufficient to show that the L60 model does a substantially better job at reproducing the observed response, they do not conclusively demonstrate the mechanism involved. In order to assess the mechanism in this response, the transformed Eulerian-mean equations are introduced from the well known primitive equations and then the dynamics in these simulations is revealed greater detail, and the mechanism isolated.

4.4 Mechanisms - The Transformed Eulerian-Mean Framework

The atmosphere is a thermo-hydrodynamical system which can be characterised by its composition, thermodynamical state, and mechanical state (Peixoto and Oort, 1992). The equations of motion that describe the motion for the atmosphere are:

$$\frac{d\mathbf{u}}{dt} = -2\Omega\mathbf{u} - \frac{(\nabla p)}{\rho} + \mathbf{g} + \mathbf{F} \tag{4.8}$$

where $\mathbf{u}$ is the three dimensional wind vector, Ω is the rotation rate of the Earth (7.292 x 10^{-5} s^{-1}), $\mathbf{u}$ is the apparent gravity vector $\mathbf{g} = -\nabla\phi$ (where the centripetal force is absorbed in the geopotential).

Continuity of mass is simply

$$\frac{dm}{dt} = 0 \tag{4.9}$$

which, because $\delta m = \rho\delta V$,

$$-\frac{1}{\rho}\frac{d\rho}{dt} = \frac{1}{\delta V}\frac{d}{dt}\delta V \tag{4.10}$$

which implies

$$-\frac{1}{\rho}\frac{d\rho}{dt} = \operatorname{div}\mathbf{u} \tag{4.11}$$

The first equation of conservation of energy can be expressed by the first law of thermodynamics. With the assumption that air behaves as an ideal gas:

$$P\alpha = R_d T \tag{4.12}$$

(where '$\alpha = \rho^{-1}$ is the specific volume and R_d is the gas constant for dry air - later the subscript is dropped for simplicity) then the first law is

$$c_p\frac{dT}{dt} = Q + \alpha\frac{dp}{dt} \tag{4.13}$$

where c_p is the specific heat of air at constant pressure, assumed to be constant, independent of the temperature and Q is the net heating rate per unit mass which represents various diabatic effects (radiative, latent heating, frictional heating, turbulent and conductive heating near the Earth's surface) (Peixoto and Oort, 1992). Peixoto and Oort (1992) show how this can be arranged to produce the first law of thermodyanmics in terms of potential temperature:

$$c_p \frac{T}{\theta} \frac{d\theta}{dt} = Q \tag{4.14}$$

where the potential temperature, defined as

$$\theta = T \left(\frac{P_0}{P} \right)^k \tag{4.15}$$

is the temperature that a dry air parcel would have if it were expanded or compressed adiabatically to a reference pressure $P_0 = 1000$hPa, where $k = R/c_p \approx 2/7$ is the specific heat at constant pressure, and R is the gas consant of air.

4.4.1 Decompositions of Atmospheric Circulation

Whilst the climate system is highly variable, the system is to a large exent defined by its average conditions (Peixoto and Oort, 1992), and understanding of the general circulation requires assessment of statistics of its various orders.

We define the time average of a quantity A as

$$\overline{A} \equiv \frac{1}{\tau} \int_0^\tau A(t) dt \tag{4.16}$$

and denote the deviation from the time average $\overline{A}$(t) as $A^{'}(t)$ so that

$$A^{'}(t) = A(t) - \overline{A} \tag{4.17}$$

Despite dynamical fields, such as temperature and velocity, also not being uniform in space, climatic conditions are often much more uniform along a line of constant latitude than longitude. Assessing dynamical interactions from their zonal averaged quantitues and their departures has shown to be of strong success and insight (e.g. Andrews et al., 1987). We define the zonal average of a quantity as follows:

$$[A] \equiv \frac{1}{2\pi} \int_0^{2\pi} A d\lambda \tag{4.18}$$

and the departure from the zonal average [A] as A^*, so that:

$$A^* = A - [A] \tag{4.19}$$

4.4.2 The Primitive Equations and Transformed Eulerian Means

The equations of motion are well known, but in general form they are often more complicated than is necessary or desirable to elucidate on the role and nature atmospheric forcings, responses and phenomena that occur. If we change to a rotating co-ordinate frame (using (λ,ϕ,z) instead of the cartesian co-ordinate system (x,y,z*)), where λ and ϕ are longitude and latitude, respectively and z here is now the log-pressure height coordinate:

$$z \equiv -H \ln(p(z^*)/p_s(z^*)) \tag{4.20}$$

which allows for a simpler expression of the equations compared to using z^*, the geometrical height coordinate, Andrews et al. (1987) show that the primitive equations, i.e. those that describe to good approximation the flow in the atmosphere, are as follows:

$$\frac{Du}{Dt} - \left(f + \frac{u \tan\phi}{a} \right) v + \frac{\Phi_\lambda}{a \cos\phi} = X \tag{4.21}$$

$$\frac{Dv}{Dt} + \left(f + \frac{u \tan\phi}{a} \right) u + \frac{\Phi_\phi}{a} = Y \tag{4.22}$$

$$\Phi_z = H^{-1} R\theta e^{-kz/H} \tag{4.23}$$

$$\frac{1}{a\cos\phi}\left(u_\lambda + (v\cos\phi)_\phi\right) + \frac{(\rho_0 w)_z}{\rho_0} = 0 \tag{4.24}$$

$$\frac{D\theta}{Dt} = Q \tag{4.25}$$

They describe momentum balance in zonal (1), meridional (2), hydrostatic balance in the vertical (3), shown by scale analysis to be an appropriate approximation to momentum balance in the vertical), continuity of mass, and the thermodynamic relation between diabatic heating and the material rate of change of potential temperature (θ).

Geopotential height is defined by Φ, whilst λ and ϕ express latitude and longitude, respectively, and

$$(u, v, w) = \left((a\cos\phi)\frac{D\lambda}{Dt}, a\frac{D\phi}{Dt}, \frac{Dz}{Dt}\right) \tag{4.26}$$

The material derivative, D/Dt, is defined as:

$$\frac{D}{Dt} \equiv \frac{\partial}{\partial t} + \frac{u}{a\cos\phi}\frac{\partial}{\partial\lambda} + \frac{v}{a}\frac{\partial}{\partial\phi} + w\frac{\partial}{\partial z} \tag{4.27}$$

The Coriolis parameter is defined as $f \equiv 2\Omega\sin\phi$, and X and Y are unspecified components of friction, or other nonconservative mechanical forcing: (X, Y).

If we separate these equations into their zonal mean and disturbance part, it can be shown we obtain the following set of primitive equations for the zonal mean flow:

$$\begin{aligned}[u_t] + [v]((a\cos\phi)^{-1}(([u]\cos\phi)_\phi - f) + [w][u_z] - [X] = \\ -(a\cos^2\phi)^{-1}([v^*u^*]cos^2\phi)_\phi - \rho_0^{-1}(\rho_0[w^*u^*])_z\end{aligned} \tag{4.28}$$

$$\begin{aligned}[v_t] + a^{-1}[v][v_\phi] + [w][v_z] + [u](f + [u]a^{-1}tan\phi) + a^{-1}\Phi_\phi - [Y] = \\ -(a\cos\phi)^{-1}([v^{*2}]cos\phi)_\phi - \rho_0^{-1}(\rho_0[w^*v^*])_z - [u^{*2}]a^{-1}tan\phi\end{aligned} \tag{4.29}$$

$$\Phi_z - H^{-1}R[\theta]e^{-kz/H} = 0 \tag{4.30}$$

$$(a\cos\phi)^{-1}([v]\cos\phi)_\phi + \rho_0^{-1}(\rho_0[w])_z = 0 \tag{4.31}$$

$$[\theta_t] + a^{-1}[v][\theta_\phi] + [w][\theta_z] - [Q] = -(a\cos\phi)^{-1}([v^*\theta^*]cos\phi)_\phi - \rho_0^{-1}(\rho_0[w^*\theta^*])_z \tag{4.32}$$

With appropriate boundary and initial conditions and suitable expressions for [X], [Y], and [Q] these equations are a closed set of equations for predicting the time development of the flow. The primitive equations are well known and are often presented and used when discussing dynamics. Whilst these equations are substantially more useful in elucidating the types of forcing and responses of the flow to a forcing than the most general representation of the equations of motion, a yet more desirable albeit less well known set of equations can be found by performing a set of simple mathematical manipulations to these equations. Defining a "residual mean circulation", $[v^+]$ and $[w^+]$ as:

$$[v^+] \equiv [v] - \rho^{-1}(\rho[v^*\theta^*]/[\theta_z])_z \tag{4.33}$$

$$[w^+] \equiv [w] + (a\cos\phi)^{-1}(cos\phi[v^*\theta^*]/[\theta_z])_\phi \tag{4.34}$$

and substituting these into the Eulerian mean equations, and performing rearrangement the *transformed Eulerian-mean equations* are obtained:

$$[u_t] + [v^+]((a\cos\phi)^{-1}(([u]\cos\phi)_\phi - f) + [w^+][u_z] - [X] = (\rho a\cos\phi)^{-1}\nabla\cdot F \tag{4.35}$$

$$[u](f + [u]a^{-1}tan\phi) + a^{-1}\Phi_\phi = G \tag{4.36}$$

$$\Phi_z - H^{-1}R[\theta]e^{-kz/H} = 0 \tag{4.37}$$

$$(a\cos\phi)^{-1}([v^+]\cos\phi)_\phi + \rho_0^{-1}(\rho_0[w^+])_z = 0 \tag{4.38}$$

$$[\theta_t] + a^{-1}[v^+][\theta_\phi] + [w^+][\theta_z] - [Q] = -\rho_0^{-1}(\rho_0([v^*\theta^*][\theta]_\phi/a[\theta]_z + [w^*\theta^*]))_z \tag{4.39}$$

All the terms which lead to departure from gradient-wind balance between [u] and Φ are defined as G, and usually it is small and of secondary importance. Here, the Eliassen Palm (EP) Flux, F, is introduced. Its components are given as:

$$F^{(\phi)} \equiv \rho_0 a\cos\phi([u_z][v^*\theta^*]/[\theta_z] - [v^*u^*]) \tag{4.40}$$

$$F^{(z)} \equiv \rho_0 a\cos\phi((f - (a\cos\phi)^{-1}([u]\cos\phi)_\phi)[v^*\theta^*]/[\theta_z] - [w^*u^*]) \tag{4.41}$$

where:

$$\nabla\cdot F \equiv (a\cos\phi)^{-1}\frac{\partial}{\partial\phi}(F^{(\phi)}\cos\phi) + \frac{\partial F^{(z)}}{\partial z} \tag{4.42}$$

This formulation of the primitive equations allows a substantially improved framework to understand middle atmospheric responses, and unlike the primitive equations they show the rectified eddy-forcing terms depend on simple physical characteristics of eddy or wave disturbances (Andrews et al., 1987).

Thus, these equations allow an easier understanding of the mechanism behind the post-volcanic winter response, and the roles of adiabatic heating and wave-forced interactions in the flow. The residual mean terms, $[v^+]$ and $[w^+]$, represent the zonal mean motion of material fluid elements (see, for example, Vallis, 2006, for further details). $[v^+]$ is the part of zonal mean meridional velocity required by mass conservation, whilst, $[w^+]$, linked with temporal variations of zonal mean temperature,

is the remaining part of vertical motion caused by diabatic heating. Of particular interest to us is the changes in the EP flux, which have been known to be altered due to changes in the temperature gradients, and mechanisms and modelling results are now discussed.

4.5 Analysis of Stratospheric Dynamical Changes

The transformed Eulerian-mean equations permit us to understand the forcing and response of the stratosphere to radiative and dynamical perturbations. In particular, changes to the flow and the strengthened stratospheric polar vortex could be due to aerosol heating impacting directly upon on the residual mean circulation, or temperature gradients could alter the propagation of planetary waves, or a combination of these factors.

Haigh (2010) briefly documents the history of understanding that temperature gradients induced by solar heating would influence the dynamics of the middle atmosphere. It is noted from as early as Hines (1974) that it has been suggested that alterations in the meridional temperature gradients would alter the wind structure, and resultingly the planetary wave propagation (i.e. the EP fluxes). This idea has been further developed and explored and it has resultingly been suggested to be an influence in the atmospheric dynamics related to both solar activity and volcanic eruptions, as noted before.

Of particular note here, it was explored by Kodera and Kuroda (2002) who investigated the impact of differences between solar minimum and solar maximum in NCEP reanalysis data upon the strength of the stratospheric polar vortex. Before detailing their discovery and conclusions, it is necessary that the Brewer-Dobson circulation is introduced.

4.5.1 The Brewer-Dobson Circulation

The Brewer-Dobson circulation is a stratospheric circulation pattern. It was proposed to reconcile the observation that the tropics are the region of ozone production but that there is high springtime ozone concentration over the Arctic and low ozone concentration in the tropics (Dobson et al. 1929, Brewer 1949). The circulation entails upwelling motion in the tropics and sinking motion at the poles - which explained that the ozone is therefore being *transported* from the area of production to the polar regions.

Figure 4.12 shows two simple schematics of the Brewer-Dobson circulation - figure 4.12 a) showing the circulation as proposed in the original paper to discover the circulation, and importantly for this study, figure 4.12 b) showing the region of EP flux convergence that forces the tropical rising and polar descent in the stratosphere.

The Brewer-Dobson circulation is a *dynamically* powered circulation, from tropospheric planetary waves that propagate into the stratosphere, as the stratosphere is stably *stratified* which prevents uprising of colder air from below (e.g. Mohanakumar 2008, Li et al. 2008). Andrews et al. (1987) point out the Brewer-Dobson circulation is strongly related to the Lagrangian mean flow - because the meridional circulation of the Brewer-Dobson model originates from tracer transport, it must be considered a mass circulation. Eulerian mean analysis shows a two cell structure, with rising in the tropics and poles and sinking in midlatitudes. Dunkerton (1978) demonstrated the Brewer-Dobson circulation should be understood as a Lagrangian mean circulation not Eulerian, but that it could be approximated by the residual circulation of the transformed Eulerian-mean equations.

Relatively little work has been done on assessing the Brewer-Dobson circulation's response to volcanic eruptions, although the localised tropical heating in the stratosphere following volcanic eruptions has been seen to increase the tropical upwelling in observations and modelling studies (Naujokat 1986, Seol and Yamazaki, 1998, Roscoe, 2004, Aquila et al. 2013).

Figure 4.13 shows two schematic diagrams by Kodera and Kuroda (2002) on how stratospheric heating due to solar cycles affects the planetary wave convergence, causing a region of positive EP flux in the mid and upper stratosphere and a positive wind anomaly (left image) and then show this positive EP flux divergence leads to an anomalous decrease in the Brewer-Dobson circulation which cools the polar stratosphere and warms the tropics.

With the Brewer-Dobson circulation and EP fluxes introduced both aspects are explored, but before this is done a quick but necessary note about the scaling of EP flux vectors in the plots is made.

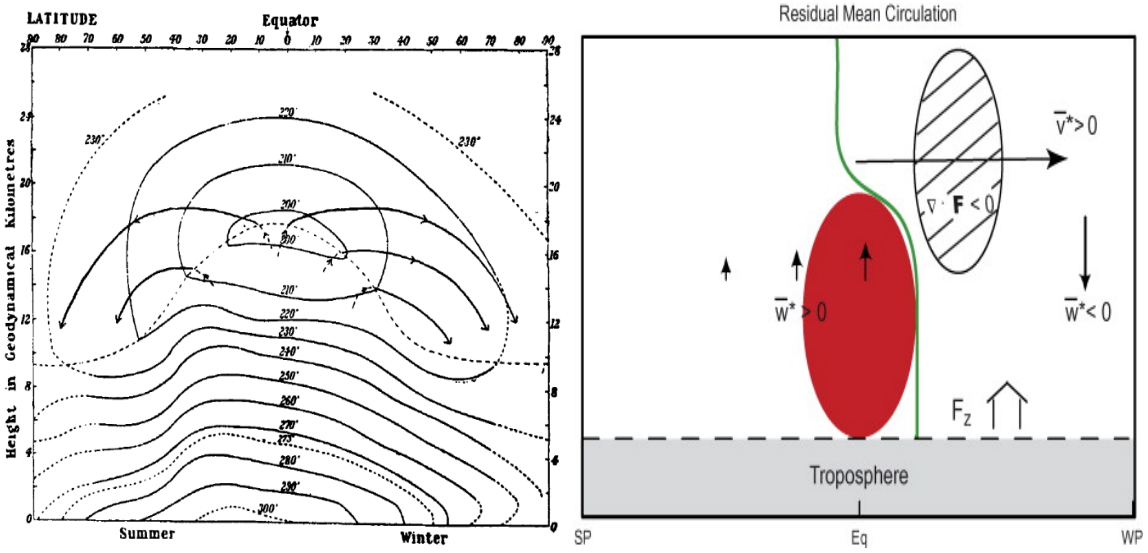

Figure 4.12: Left: A simplified diagram of the Brewer-Dobson circulation, showing rising at the tropics and descent at the poles, from Brewer (1949). Right: A schematic representation of the residual mean circulation showing the influence planetary waves and EP flux convergence in the tropics and subtropical stratosphere on driving the tropical rising and polar descent, from Salby (2008).

4.5.2 On EP Fluxes and Scaling

Although it is not obvious from the definitions alone, when creating plots the vertical and meridional components of EP fluxes need to be *scaled* (Dunkerton et al., 1981). Garfinkel and Hartman (2008) detail the scaling necessary for EP fluxes. In their study, Garfinkel and Hartman (2008) investigate the influence of ENSO and

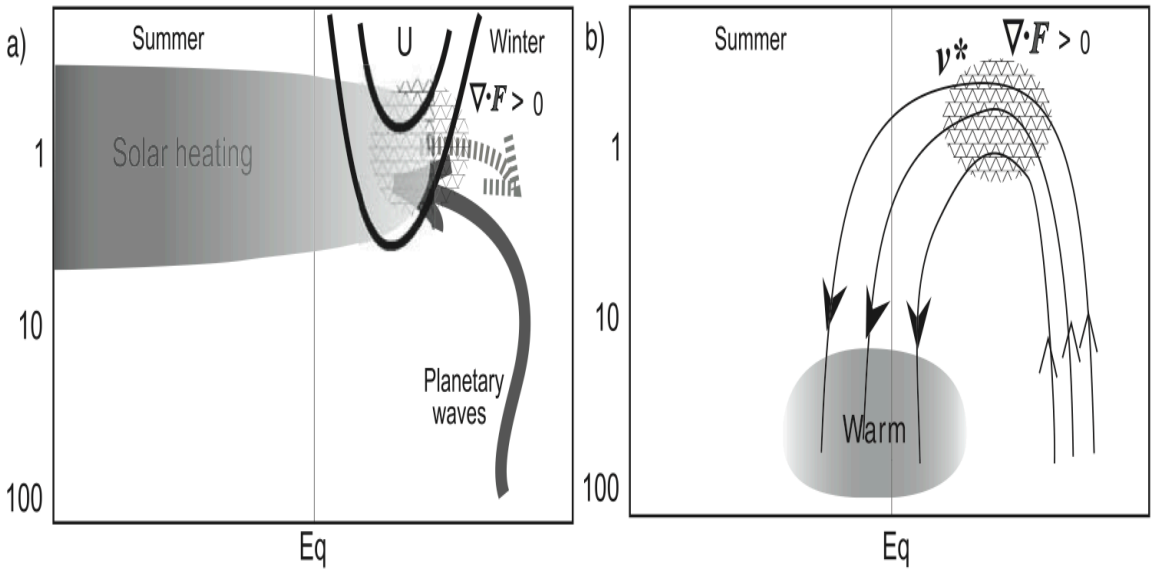

Figure 4.13: Schematic illustrations from Kodera and Kuroda (2002), showing a) a stronger jet due to the warming effect and temperature gradient of solar maximum compared to minimum deflecting planetary waves from the subtropical regions, which is represented by a large positive area of increased EP flux, and b) the change in wave forcing in this period implies an anomalous decrease in the Brewer-Dobson circulation. Both effects are seen in the L60 model simulations for a very similar situation where volcanic aerosol plays the role of the forcing that creates the stratospheric heating and temperature gradient. This is accompanied with an increase in the Brewer-Dobson circulation directly as a result of the tropical heating, also seen in other studies on volcanic eruptions and climate.

teleconnections and their effects on the stratospheric polar vortex in the ERA40 reanalysis dataset. In order to do this, they need in particular to assess wave forcing and therefore investigate EP fluxes and discuss its scaling. They note that scaling of EP flux components is necessary so that one can visually predict where convergence and divergence occur, and is given by the the ratio, R, which is:

$$R = \left(\frac{1}{r_0 \cos\phi} \frac{\partial}{\partial \phi} \right) / (\frac{\partial}{\partial z}) \tag{4.43}$$

i.e. the ratio of F^{ϕ} to F^{z} is given by the average distance between adjacent vertical levels between 500 hPa and 5 hPa divided by the radius of the Earth mutiplied by the average angular displacement between adjacent latitudes. Garfinkel and Hartman (2008) thus get a value of 0.0087 for the ERA40 dataset. This is consistent with the details in Dunkerton et al. (1981) which approaches the scaling via a completely

different physical argument, yet leads to almost exactly the same value of 0.00899, both of which confirm the scaling approach used here. The average value of the separation between height levels in L60 1.586 km and the average angular distance $\frac{1}{r_0 \cos\phi}\frac{\partial}{\partial\phi} = 277.9$ km. This renders a ratio of 0.0057 for the high-top model (whilst a value of 0.082 is obtained in the plots for the L38 model - not shown - which has a similar resolution to the ERA40 dataset). The L60 has a smaller ratio than L38 and Dunkerton et al. (1981) and Garfinkel and Hartman (2008) - which both analyse datasets with very similar ratios in grid spacing - due to an increased vertical resolution and so decreased average distance between vertical layers and thus a lower ratio.

Whilst the results from Kodera and Kuroda (2002) in their analysis of the difference between solar maximum and minimum are not precisely comparable to volcanic eruptions, the results here (figure 4.14) display remarkable similarities between the heating of the tropical stratosphere from solar activity and heating of the tropical stratosphere from volcanic eruptions. During December, the temperature gradient induces, in the volcanic simulations, very large anomalies of the EP flux divergence with planetary waves being diverted between $40^\circ - 60^\circ$ N. Recall, as aforementioned, from Kodera and Kuroda (2002) that this will alter the meridional circulation, induce a cooling at the poles during this period and subsequently create a thermal wind gradient that activates a stronger stratospheric polar vortex.

Figures 4.15 and 4.16 (displaying monthly v^+ and w^+ anomalies, respectively) agree with expectations very well. Before winter, the influence of the volcanic aerosol heating shows increases in the poleward residual mean circulation. During December, however, the effect of the EP flux divergence overwhelms the motion in the same way as seen by Kodera and Kuroda (2002), reversing the effect of the aerosol heating and causing large and statistically significant anomalies representing pole-to-equator circulation throughout the Northern Hemisphere stratosphere. The vertical meridional circulation anomaly shows large and significant upwelling in the stratosphere and a downwelling in the upper stratosphere to compensate for the reversal in the direction of the meridional circulation. Consistent with planetary waves being guided away

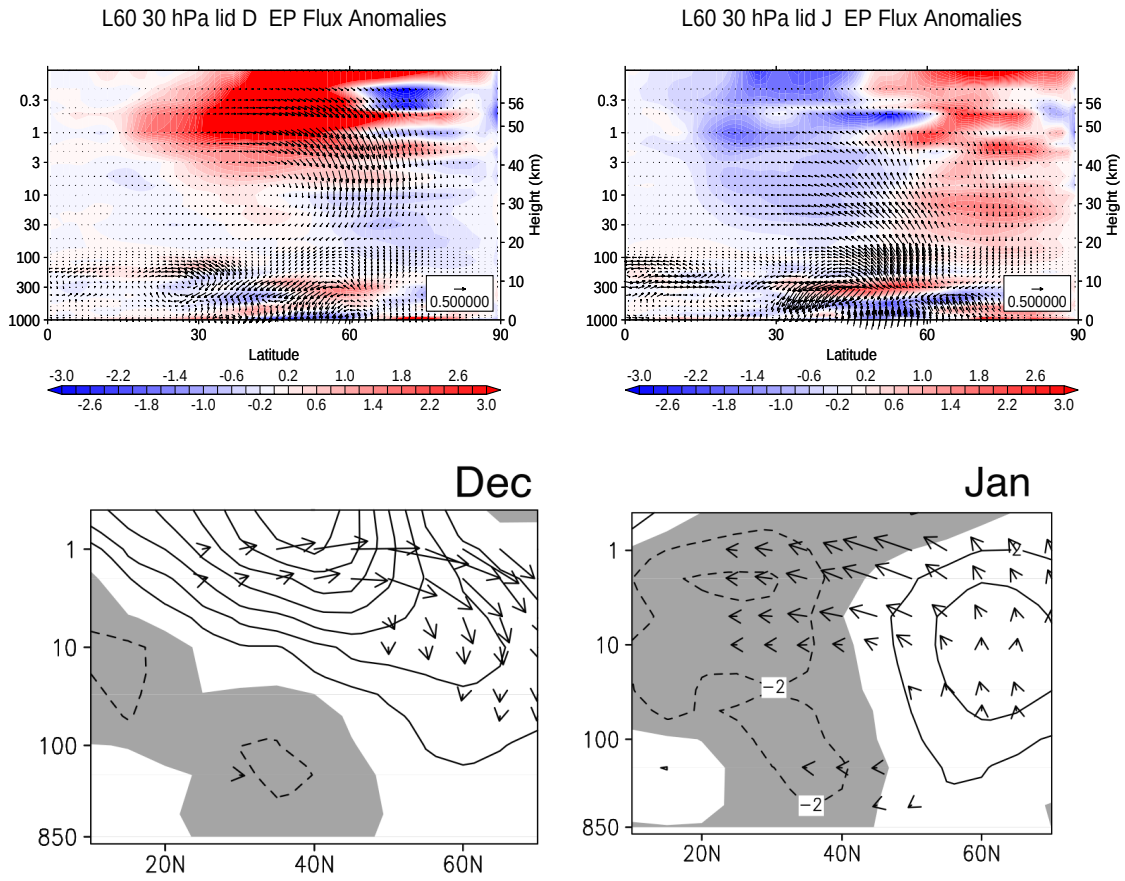

Figure 4.14: Top: December (left) and January (right) vertical and meridional EP flux anomalies and divergence ($\mathrm{ms}^{-1}\,\mathrm{day}^{-1}$) for L60. Below, images from Kodera and Kuroda (2002), the contours show composite differences of zonal mean zonal wind (with interval is $2\mathrm{ms}^{-1}$) and the arrows show composite differences of EP flux vectors, both for the solar maximum minus solar minimum for December (left) and January (right) using the NCEP Reanalysis dataset over the period of 1979-1998. They do not show the anomalies for February. Note the differences in the latitude and height range presented between the images computed here and those used in Kodera and Kuroda (2002).

from the polar stratosphere and a reversal of the Brewer-Dobson circulation, figure 4.17 reveals a large decrease in the meridional heat flux ($[v^*\theta^*]$ - this is somewhat absorbed in the definition of EP flux and has important implications on u and the residual circulation) into the polar stratosphere in December and January with large, but smaller, increases in the heat flux outside of the polar regions.

For both the L60 simulations presented here and the Kodera and Kuroda (2002) study, the substantial cooling of the stratospheric polar vortex (here up to 6 K)

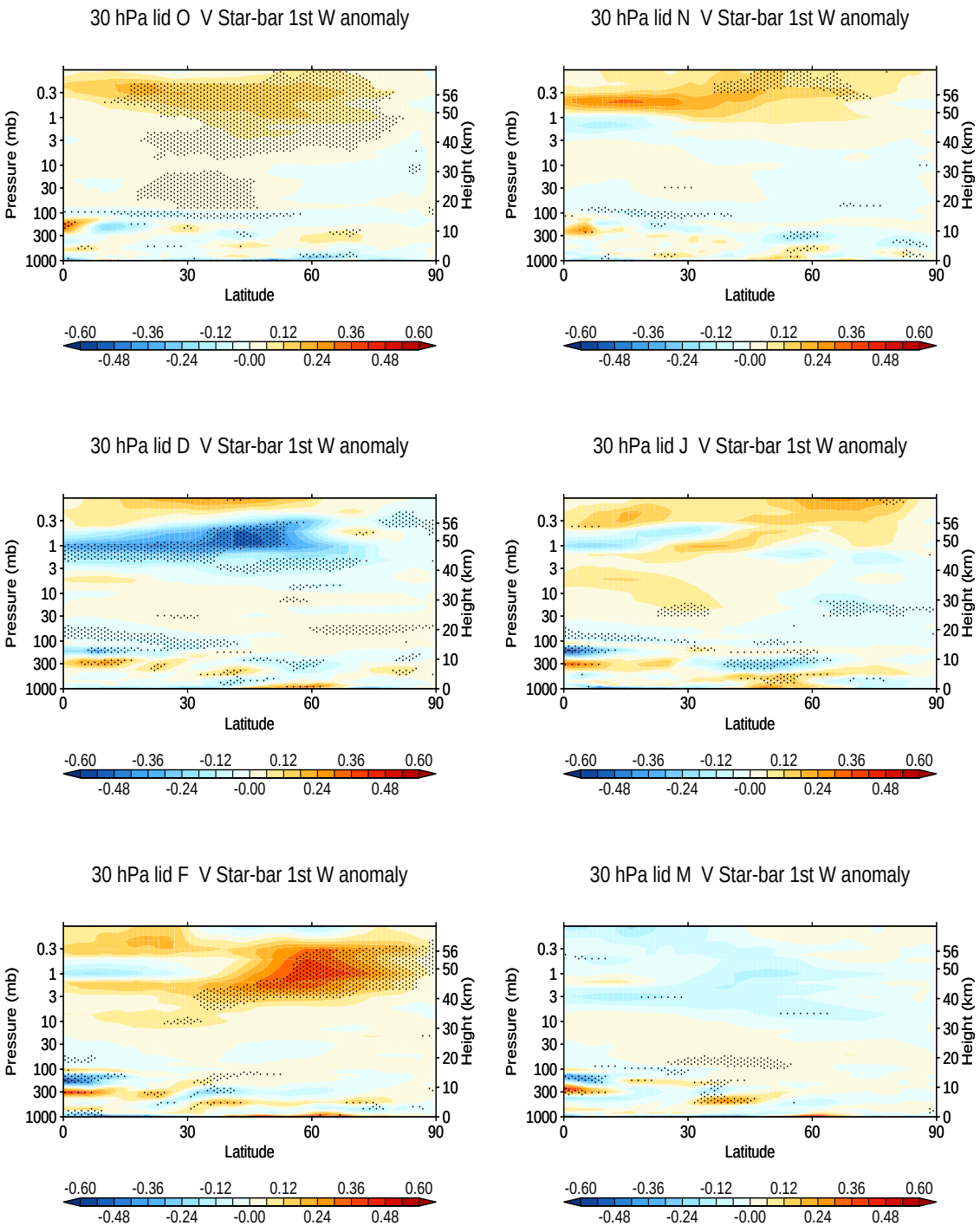

Figure 4.15: Monthly v^+ anomalies (ms^{-1}) for L60. Stippling corresponds to the 95% confidence level using a t-test.

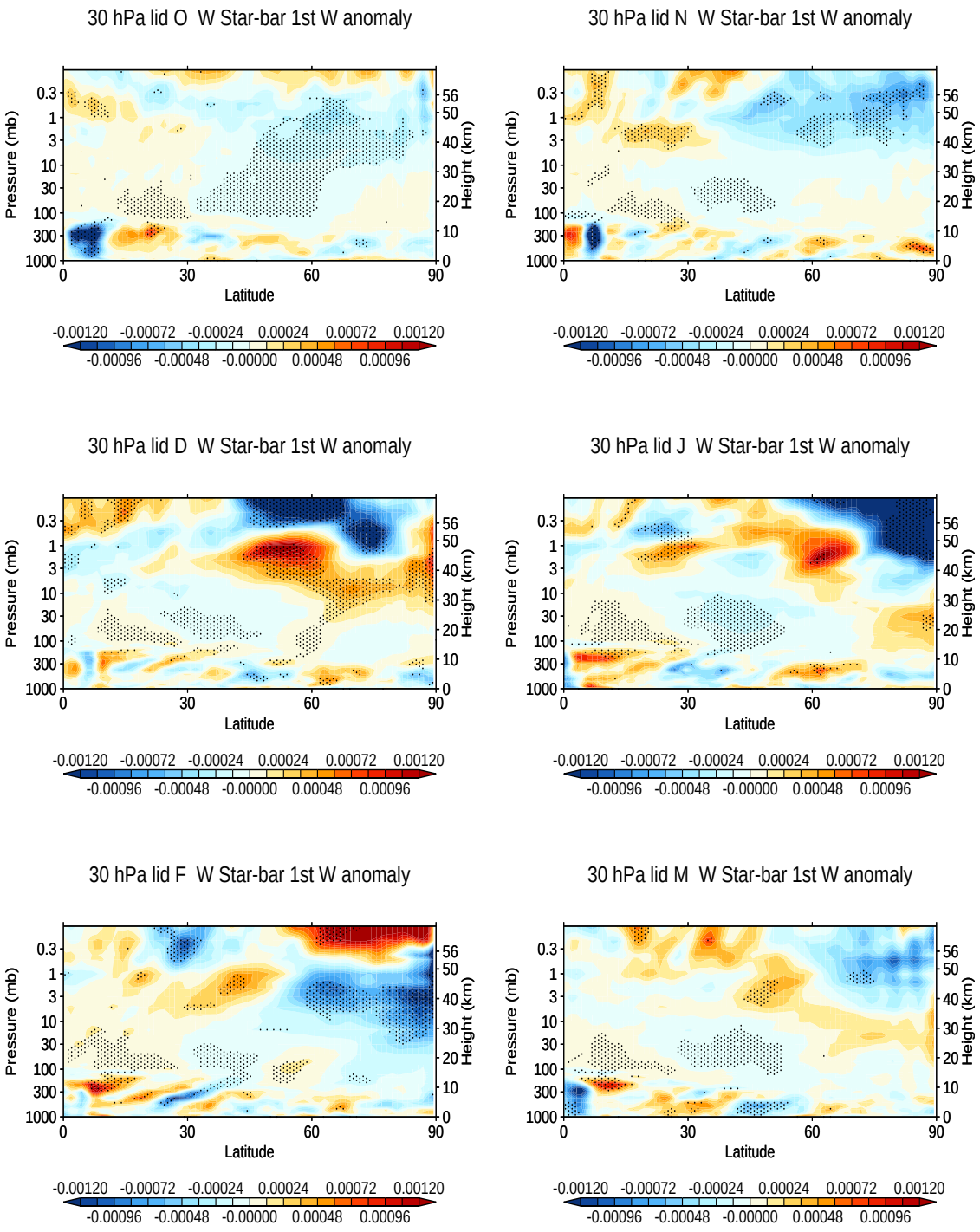

Figure 4.16: Monthly w^+ anomalies (ms^{-1}) for L60. Stippling corresponds to the 95% confidence level using a t-test.

throughout the polar stratosphere, leads to a substantially altered temperature gradient, diverting planetary wave activity away from the polar stratosphere and towards the midlatitudes where it causes large and statistically significant negative anomalies in the zonal average zonal wind in January (figure 4.11). This mechanism allows the substantially strengthened stratospheric polar vortex of 15 ms^{-1} seen in figure 4.11, which is linked with in the pattern of Eurasian warming, Eastern mediterannean cooling, Arctic cooling and North American warming during the wintertime.

Figure 4.18 presents the EP flux divergence anomalies without the EP flux vectors to show that the large divergence in December and divergence of planetary waves from the lower polar stratosphere to the lower midlatitude stratosphere are indeed statistically significant at the 95% level.

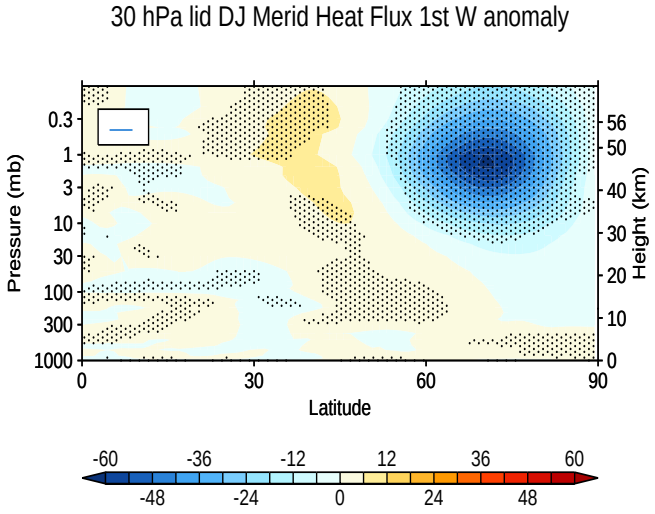

Figure 4.17: Anomalies of heat flux, $[v^*\theta^*]$ ($K\,m\,s^{-1}$), for L60 for December and January. Stippling corresponds to the 95% confidence level using a t-test.

Finally, the convergence of the planetary waves at the midlatitudes which slows down the flow in the midlatitudes can be seen to propagate polewards, and in February EP flux convergence is visible in the polar stratosphere, which leads to an enhanced Brewer-Dobson circulation in February (February anomalies in figures 4.15 and 4.16

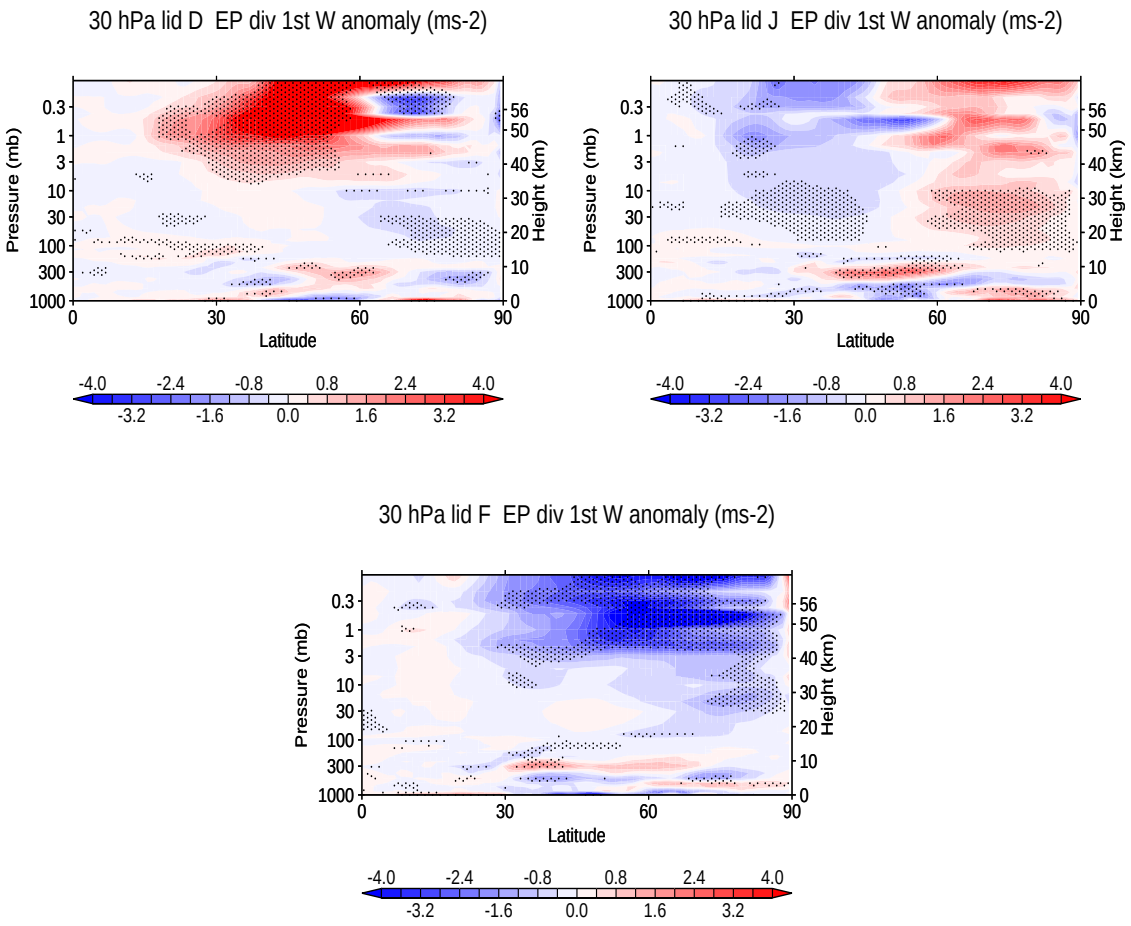

Figure 4.18: December (left) and January (right) $(\rho a \cos\phi)^{-1}\nabla \cdot F$ anomalies ($\mathrm{ms}^{-1}\,\mathrm{day}^{-1}$) for L60. Stippling corresponds to the 95% confidence level using a t-test.

show an increased poleward movement and resulting downwelling between approximately between 20-50 km and upwelling above this due to conservation of mass), and induces a warming of the polar stratosphere at the end of the winter season, as seen following volcanic eruptions.

4.5.3 Frequency of Negative Refractive Index Squared

The conditions for propagation of Rossby waves in the stratosphere are defined by the atmospheric index of refraction n^2 (Matsuno, 1970), controlled by the zonal mean wind and temperature. In its spherical quasi-geostrophic form, n^2 for quasi stationary

planetary waves, is defined as:

$$n^2 = aq_\phi/[u] - (k/(cos\phi))^2 - (af/2NH)^2 \tag{4.44}$$

with N being the buoyancy frequency, H the density scale height, k zonal wave number, a the Earths radius, f the Coriolis parameter and q_ϕ is the quasi geostrophic potential vorticity gradient. The first term dominates over the others (Hu and Tung, 2002), and in pressure coordinate is given by (Edmon et al., 1980):

$$q_\phi = 2\Omega cos\phi + f(\theta_\phi/\theta_p)_p - ((acos\phi)^{-1}(ucos\phi)_\phi)_\phi \tag{4.45}$$

where the first term on the right hand side is the planetary vorticity gradient, the second term in the vortex stretching related to the variation of isentropic slopes with height and the last is the relative vorticity gradient. a is the Earths radius, θ the potential temperature and p pressure. Subscripts indicate derivatives. Wave activity by planetary Rossby waves tends to propagate somewhat like light rays and there are a few mechanisms that affect Rossby waves and their propagation. One mechanism is the refraction of the wave by spatial variations of the basic state. Karoly and Hoskins (1982) showed that the group velocity of Rossby waves refracts up the gradient of the index of refraction. Moreover, it is expected that waves propagate in regions where $n^2>0$ and avoid regions where $n^2<0$. In regions with negative n^2 the waves amplitude decays rapidly whilst at the zero u line n^2 tends to infinity, denoting non-linear wave breaking.

One may, therefore, use refractive indices to understand propagation of Rossby waves following a volcanic eruption. The only known study assessing changes in refractive index following volcanic eruptions is that of Graf et al. (2007). In their study they compare the frequency of negative squared refractive index, which they note provides a much smoother and easier to interpret pattern. This is discussed in detail in other articles - see, for example, Li et al. (2006) who perform analysis of the refractive index in understanding the propagation of Rossby waves during Northern Hemisphere winter from NCEP/NCAR reanalysis data.

The frequency of negative refractive index, $f_{n^2<0}(\phi, p)$, unlike other fields shown in the chapter, is generated from daily data by counting the number of days with negative n^2 in the whole dataset at all latitudes and heights. Then, dividing the total number of days, a 2D probability distribution of refraction of planetary waves is obtained. Areas with large probabilty indicate low ability for Rossby wave propagation, whilst lower probabilities indicate good chance of Rossby waves to propagate. As is noted in Li et al. (2006), information regarding total energy flux, for example, is not provided. However, the diagnostic clearly represents a picture of probable wave propagation by "channels" of low probability of negative n^2. Moreover, use of the frequency of negative refractive index provides the ability for some comparison with previous work where frequency of negative squared refractive index was assessed for post volcanic winters.

Anomalies of frequency of refractive index squared for the December, January and February months are plotted in figure 4.19. Given areas of higher frequency of refractive index squared represent areas of lower ability for Rossby wave propagation, positive anomalies reflect areas where the ability for propagation of Rossby waves is lower following volcanic eruptions than climatology.

Figure 4.19 shows in the simulations, during the winter months (when propagation of the zonal mean zonal wind occurs resulting in a strengthened polar vortex), the frequency of negative refractive index squared is positive in the stratosphere over the polar regions, whilst being negative in the midlatitudes. For both December and January, the strong anomalous zonal mean zonal wind coincides with Rossby waves being less likely to propagate into the polar latitudes (and thus disturb the vortex) and more able to propagate in the midlatitudes. During February, when the anomalously positive zonal mean zonal wind weakens substantially, consistently, the opposite pattern is seen. The pattern is qualitatively similar to that of Graf et al. (2007), although due to larger signal to noise ratio (from a larger volcanic eruption simulated and more ensembles than their observational study) the pattern of reduced ability for Rossby wave propagation is stronger here. The frequency of negative refractive index squared therefore represents a result consistent with the

other diagnostics shown in the chapter, and shows the reduced likelihood for Rossby waves to propagate into the polar regions and disturb the vortex.

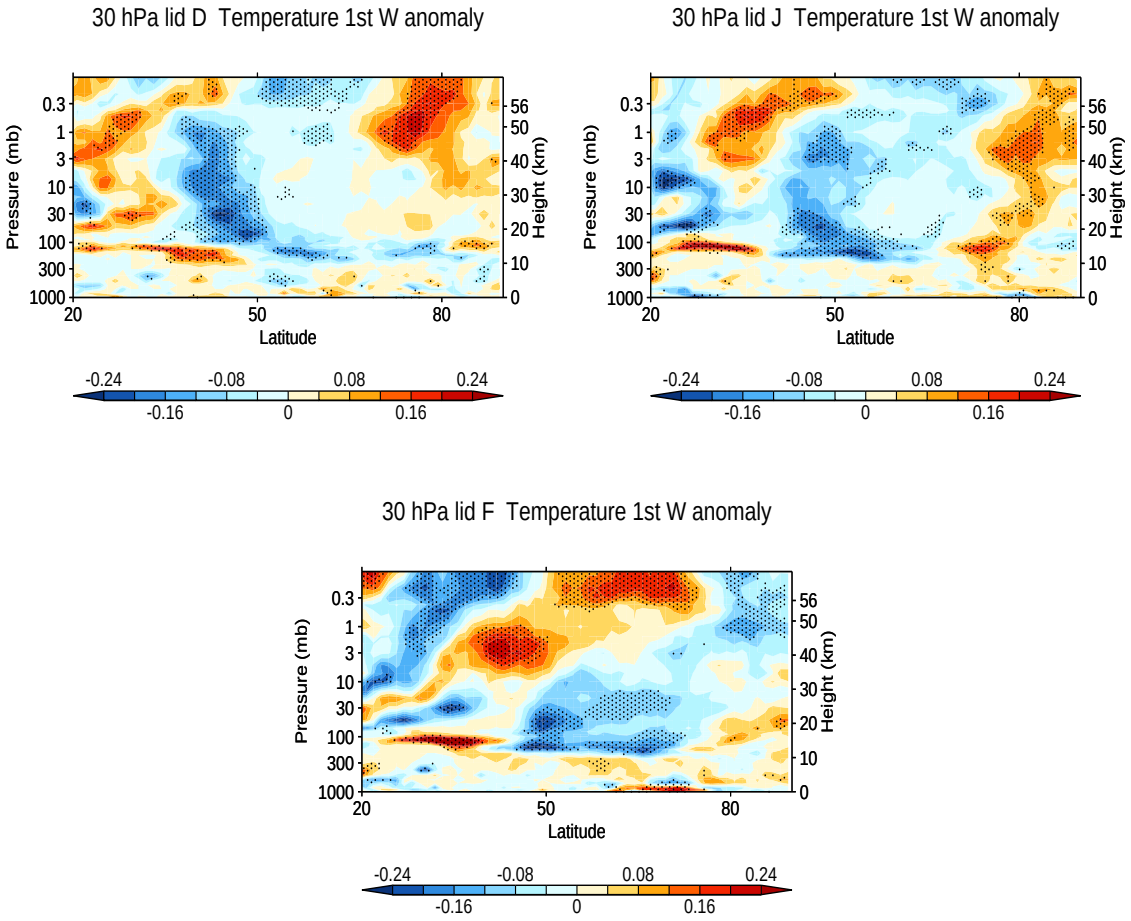

Figure 4.19: December (top left), January (top right) and February anomalies of frequency of negative refractive index squared, n^2. Stippling corresponds to the 95% confidence level using a t-test.

This study, therefore, represents the first comprehensive successful simulation of explanation of volcanic eruptions and explanation of the dynamics in terms of the transformed Eulerian-mean equations, and a summary of findings to date is presented.

4.5.4 Summary of L60 and L38 Comparison

Simulations were performed with both the L60 and L38 versions of the HadGEM2 model, of the Pinatubo eruption and the simulations were assessed for their ability

to reproduce the observed post-volcanic climate. The L38 model simulated basic features, such as a tropical tropospheric cooling as expected from decreased incoming surface shortwave radiation and a change in the winds around the region of maximum temperature gradient created by the volcanic aerosols in the lower stratosphere, but failed to show the dynamical changes that have been observed. This is consistent with the low-top model being unable to simulate other important features and processes representing variability and dynamics of the stratosphere, and polar vortex in particular such as a poor representation of sudden stratospheric warmings.

The L60 model also simulated a tropical tropospheric cooling, but also, demonstrated changes in the zonal mean zonal wind corresponding to a strengthened stratospheric polar vortex during the Northern Hemisphere wintertime. Previous studies show how alterations in the heating of the tropical stratosphere can alter the propagation of planetary waves, and that this leads to a cooling of the polar regions allowing for an altered residual mean circulation - often well above the L38 model lid. Here exactly the same response of the stratosphere is shown but via volcanic forcing, with the L60 model demonstrating changes in the planetary wave propagation - notably the divergence of EP flux was often above the lid of the L38 model - with associated changes in the residual mean circulation and a cooling of the polar stratosphere.

During mid winter, extremely large wind anomalies were situated over the polar regions and propagated downwards as seen in many other studies and simulations (e.g. Kodera, 1995, Kodera and Kuroda, 2002, Ineson et al. 2011) which forced the positive NAO pattern at the surface. This change in the circulation near the surface in the model resulted in the changes in near-surface temperature, yielding extensive and very large temperature anomalies of up to 4.5 K over Eurasia, coupled with cooling over the Eastern Mediterranean, the polar regions and warming over North America.

The first winter achieves a very large response whilst the second winter displays almost no dynamical response. It is noted that this coincides with what has been seen in observations - this is seen over records dating over long periods of time (Christiansen, 2008) - whilst Stenchikov et al. (2004) noted a substantially stronger vortex

more positive NAO in the second year following Pinatubo due to the westerly phase QBO.

One experimental caveat was that these simulations do not represent any ozone loss following the Pinatubo eruption. However, it is noted that the response in the model would likely be even more pronounced, as there would be enhanced cooling in the polar vortex region, amplifying these feedbacks (Stenchikov et al., 2002).

Whilst these results show a marked and substantial improvement in the simulation of stratospheric dynamics and its resulting surface anomalies and whilst there remains uncertainty over the true magnitude of the influence of Pinatubo due to QBO phase and other variability, these anomalies over two winters are nonetheless smaller in magnitude than observed following Pinatubo. It could be that the signal is larger than the 'true' volcanic signal for Pinatubo in the observations due to low numbers for sampling, or it could be that the L60 model underestimates the response. Therefore, an investigation into a possible further improvement to the simulation of volcanic dynamics is conducted to see if the model can simulate a very large response over both winters. This involves changing the gradient of the aerosol lid in the model.

4.5.5 Changed Aerosol Profile in the L60

Figure 4.19 presents anomalies of zonally averaged temperature, zonally averaged zonal wind, MSLP and near-surface temperature for the slightly raised lid of aerosol in HadGEM2 - according to the set of equations 4.1-4.7. The model reads in aerosol optical depth and it distributes it between the lower stratosphere and the lid, weighted according to pressure, meaning that the bulk of the aerosol will still be in the lower stratosphere, although it will be weaker and thus less significant compared to the more concentrated simulations previously, and that aerosol amounts at higher levels will become increasingly negligible.

The effects of volcanic aerosol can be clearly seen, although the anomalies are slightly lesser in the lower stratosphere than in the original model setup. Again, tropical tropospheric cooling can be seen, showing the radiative impact of volcanic eruptions on the troposphere. Intriguingly, however (something addressed and explained

in more detail later) there is little evidence over the two winters of a stratospheric cooling. This is due to extra stratospheric warmings in the second winter following the eruptions in these simulations compared to the original simulation when the aerosol amounts are lower and the meridional temperature gradients weaker. Whilst the model simulates again a successful simulation in the first winter, in the second winter the vortex is more disturbed leading to a composite over both where first winter vortex cooling is less evident. Recalling the competing effects of the tropical heating which increases the warming of the polar stratosphere, and the direct temperature gradient of the aerosols which alters the path of propagation of planetary waves, these results are explained in this context later emphasising the importance of the anomalous temperature gradient in the lower tropical stratosphere. Similarly the wind patterns show a slight increase in winds, but over both winters there is not an indication of a large vortex strengthening.

The surface fields, however, do show indications of the volcanic signal from a strong first winter response, and a second winter response that does not substantially activate a positive or negative NAO at the surface in the simulations. MSLP fields reveal increases over the Altantic and decreases over the polar regions, showing a positive NAO pattern. Near-surface temperature fields also demonstrate the effect of the radiative impact of a volcanic eruption on the tropical troposphere, and there is evidence of a statistically signifcant dynamical post-volcano cooling and warming pattern.

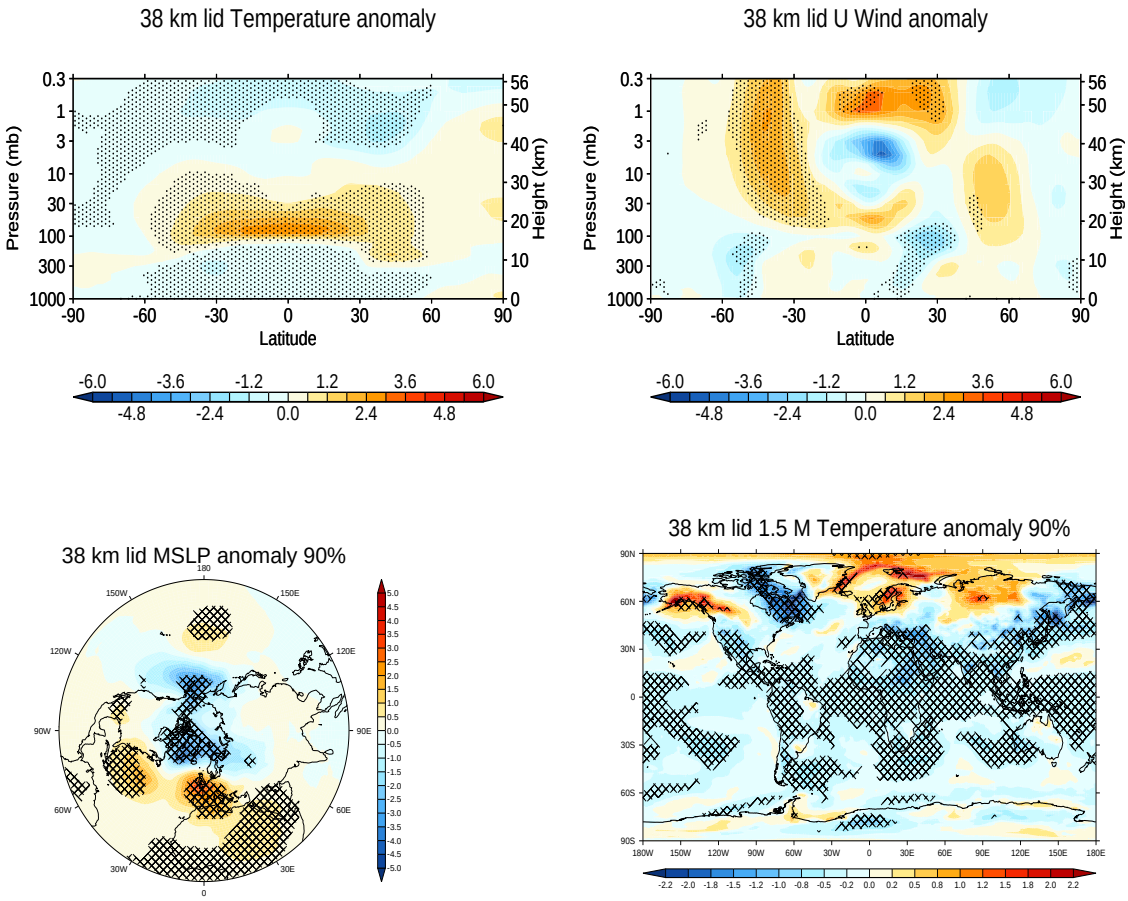

Figure 4.20: L60 anomalies of DJF temperature (K), wind (ms^{-1}), MSLP (hPa) and near surface temperature (K) for the two winters. Stippling corresponds to the 90% confidence level using a two tailed t-test.

4.5.6 Results from the L60 - First Winter Response

Figure 4.20 again shows a clear volcanic signal can be observed in the first winter. In the early winter, MSLP fields show a clear and statistically significant positive NAO with anomalies over the Atlantic around 5 hPa and negative anomalies over the poles of -5 hPa. Near-surface temperature anomalies reveal, as expected and observed, extremely large negative anomalies over the Canadian and Arctic regions of around -4 K with a corresponding warming pattern over Northern Europe. Statistically significant increases just off the Eastern coast of America show a warming pattern.

In late winter, the positive NAO anomaly has decreased (due to a reduced temperature gradient not causing as much cooling of the polar stratosphere as previously),

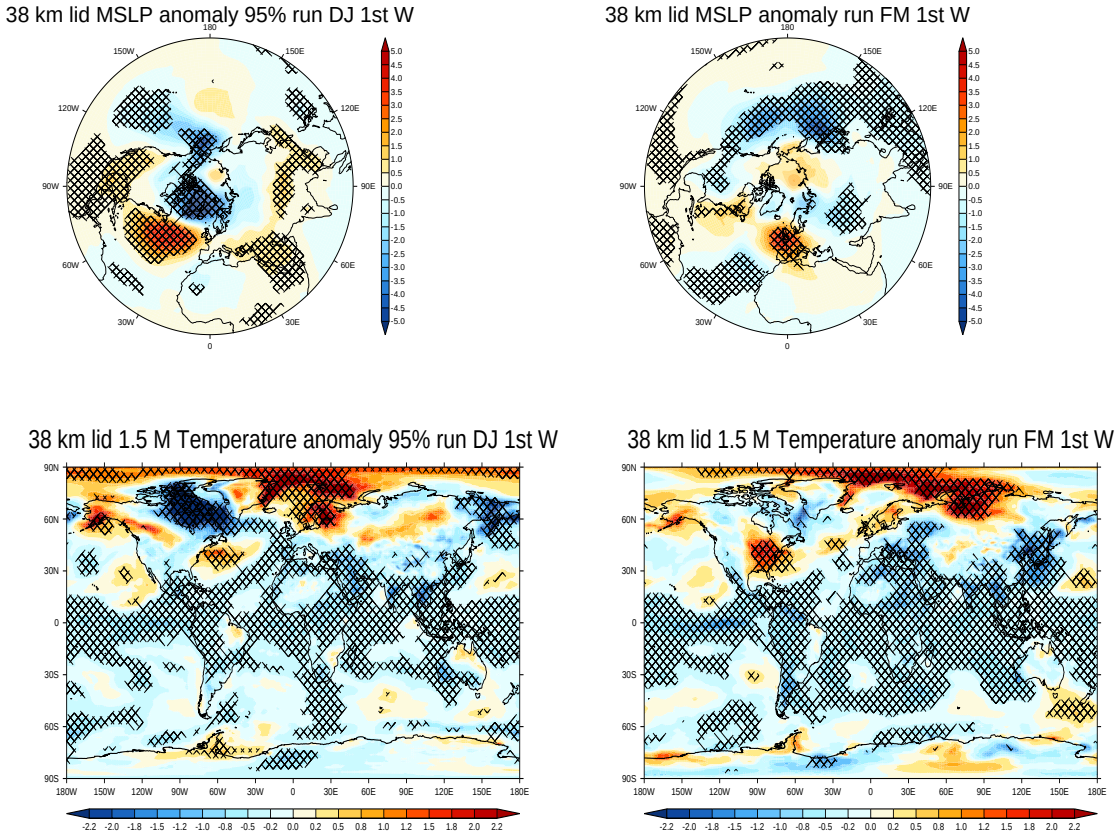

Figure 4.21: L60 anomalies of temperature (K), and MSLP (hPa) for DJ (left) and FM (right) for all the first post-Pinatubo winters. Hatching corresponds to the 95% confidence level using a two tailed t-test.

with a nonetheless large positive anomaly being focused over Western Europe. Accordingly, a similar but weaker pattern of Eurasian warming (reaching around 4 K) with Eastern Mediterannean cooling can be seen, with the warming pattern over North America being statistically significant, but the Canadian/Arctic cooling barely significant. These anomalies alone would demonstrate the use of the L60 model compared with the L38 in achieving a volcanic response, but compared to the previous simulations they are weaker.

Second winter anomalies are presented in figure 4.21. DJ MSLP pressure fields still show a robust positive AO response, yet it is of little surprise that the anomalies in all fields are again similar but weaker than previously simulated. Small anomalies of warming over Northern Europe and cooling over Canada and the Arctic can be

seen, but these anomalies are neither as large nor as extensively significant - whilst in late winter there is substantial cooling over the European region which masks a first winter response over two winters.

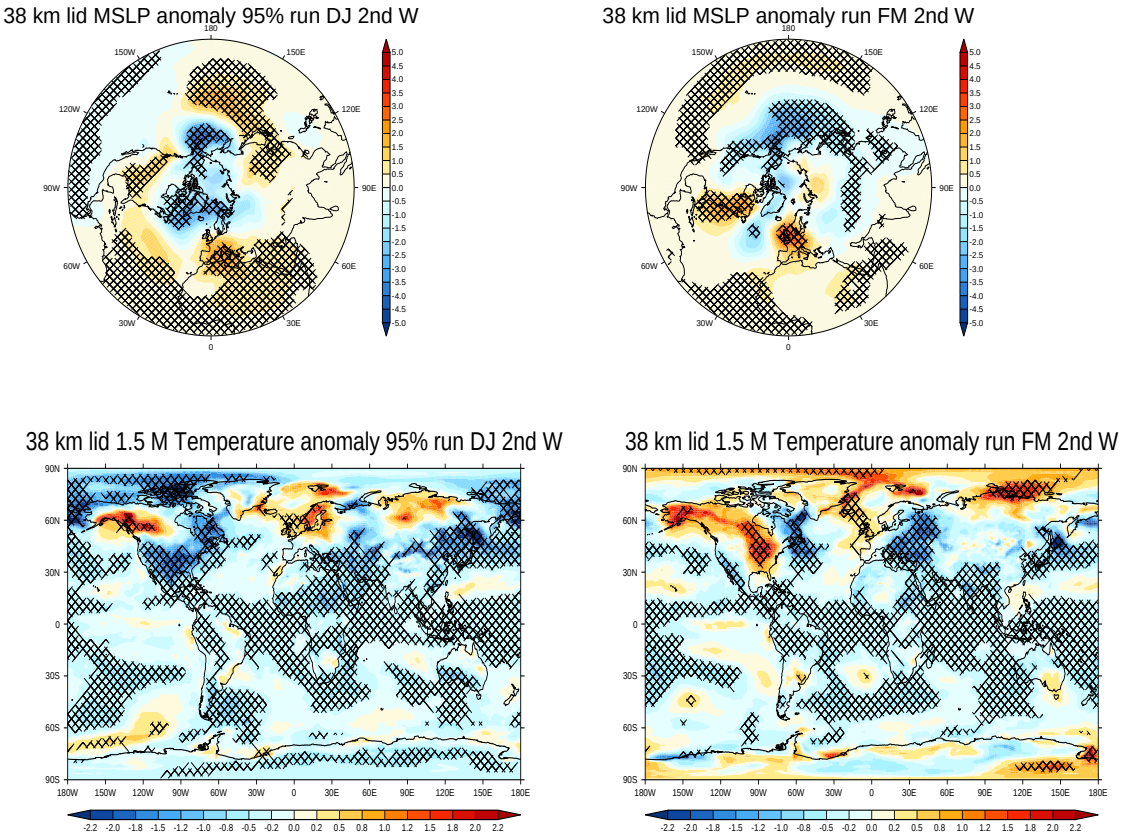

Figure 4.22: As figure 4.6 but for the second model winter. Hatching corresponds to the 95% confidence level using a t-test.

Figure 4.22 and 4.23 show anomalies of zonal average temperature and zonal wind. Radiatively induced tropical stratospheric warming, and tropical troposphere and upper stratospheric cooling are seen as previously (figures 4.10 and 4.11), whilst the temperature anomalies in the lower stratosphere are not as intense and the polar stratospheric cooling in January is not significant as it is in the previous simulations. The pre-winter months show warming in the polar stratosphere due to an increased residual mean meridional circulation.

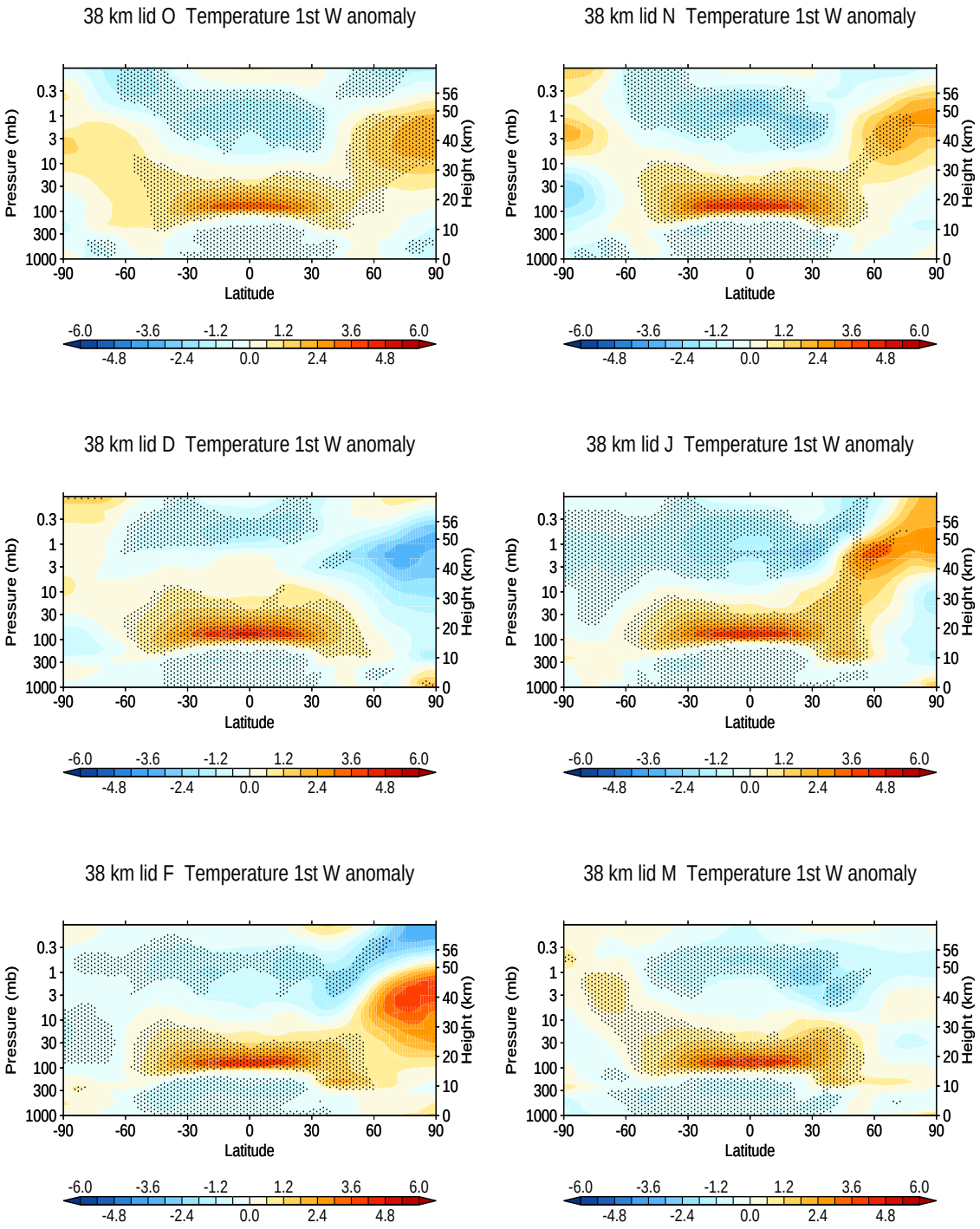

Figure 4.23: Monthly first winter temperature anomalies (K) for L60. Stippling corresponds to the 95% confidence level using a t-test.

Wind fields show in December substantial stratospheric wind anomalies reaching around 10 ms^{-1} and a similar pattern of poleward and downward propagation in January. One noticeable difference between these simulations and the previous simulations with the L60 model is that the anomalies here in January are about half the size and consequently display much less statistical significance. Negative wind anomalies just south of these are large and significant and represent EP flux convergence slowing down the flow with EP flux divergence at the pole.

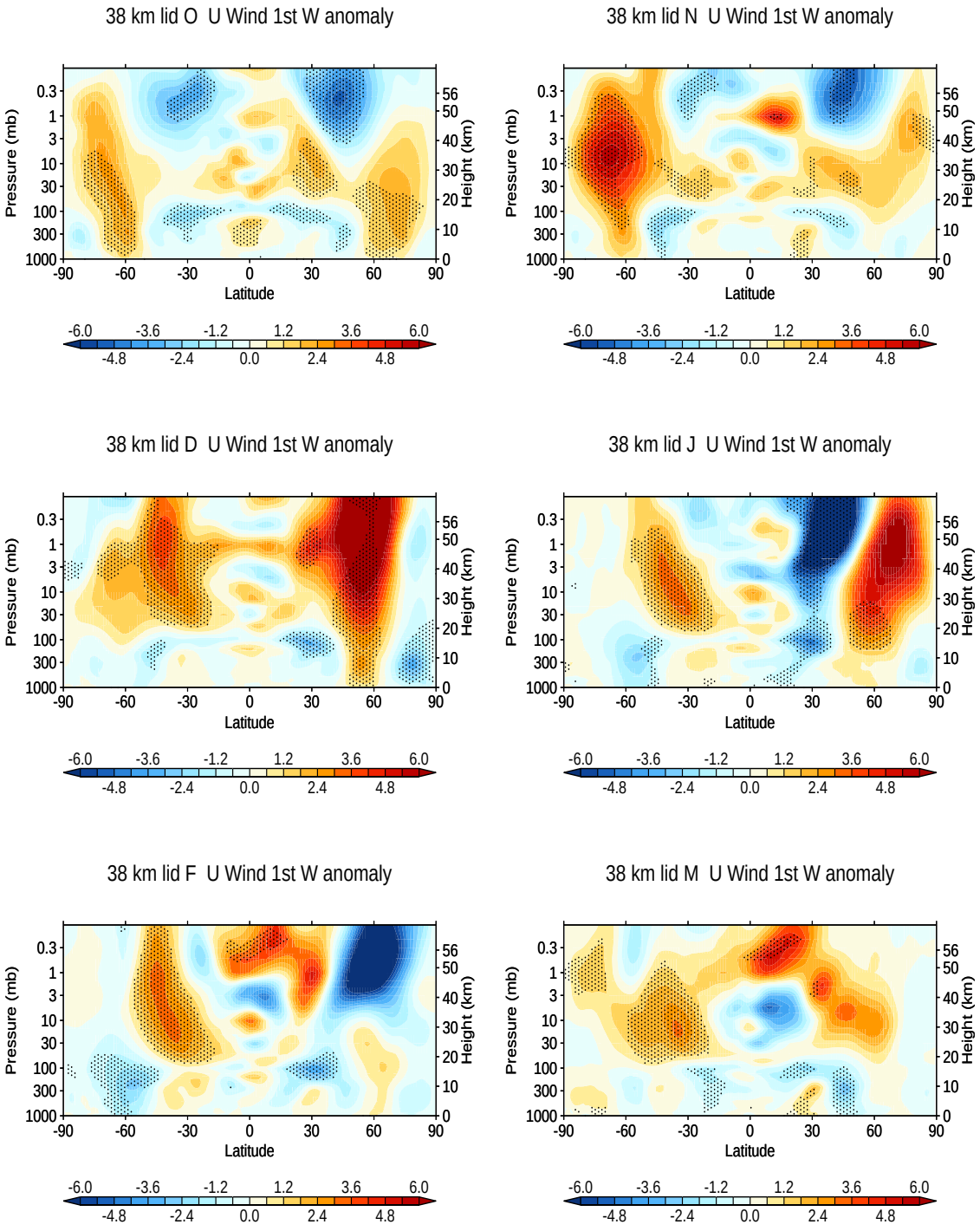

Figure 4.24: Monthly first winter u wind anomalies (ms^{-1}) for L60. Stippling corresponds to the 95% confidence level using a t-test.

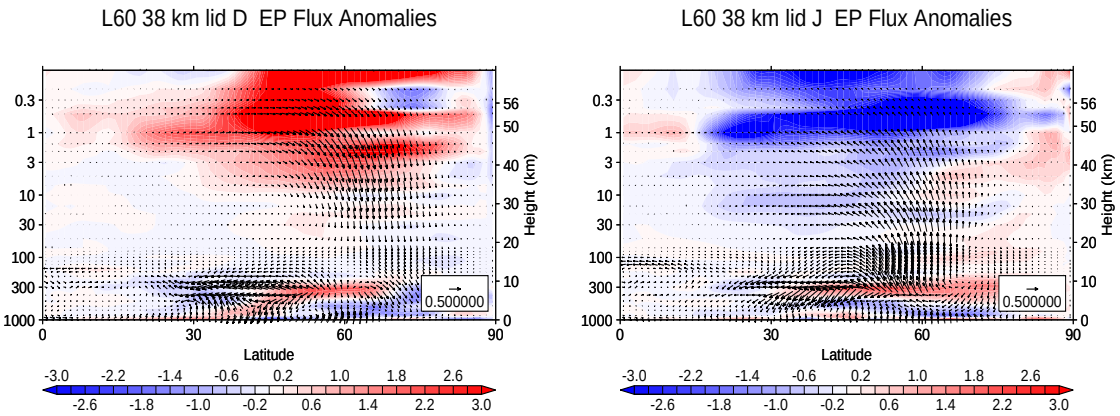

Figure 4.25: Monthly vertical and meridional EP flux anomalies and divergence ($\mathrm{ms}^{-1}\,\mathrm{day}^{-1}$) for L60.

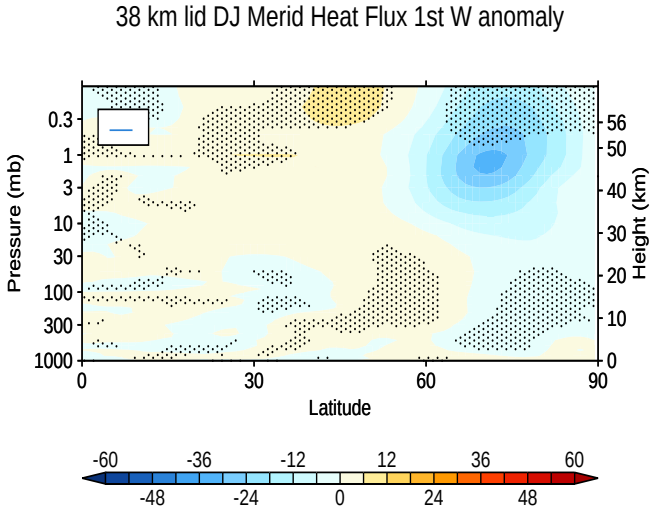

Figure 4.26: Anomalies of heat flux, $[v^*\theta^*]$ ($\mathrm{K\,m\,s}^{-1}$), for L60 for December and January. Stippling corresponds to the 95% confidence level using a t-test.

Figure 4.24 shows the EP flux anomalies and divergence in December and January. Again, a similar response is seen here of the model to solar activity, observations and the previous simulations. The temperature gradients in the first winter alter the propagation of planetary waves in the model during December, showing the ability of the model to achieve a volcanic response. However, the anomalies are not as large as those for the previous L60 simulations. Figure 4.25 shows that there is accordingly

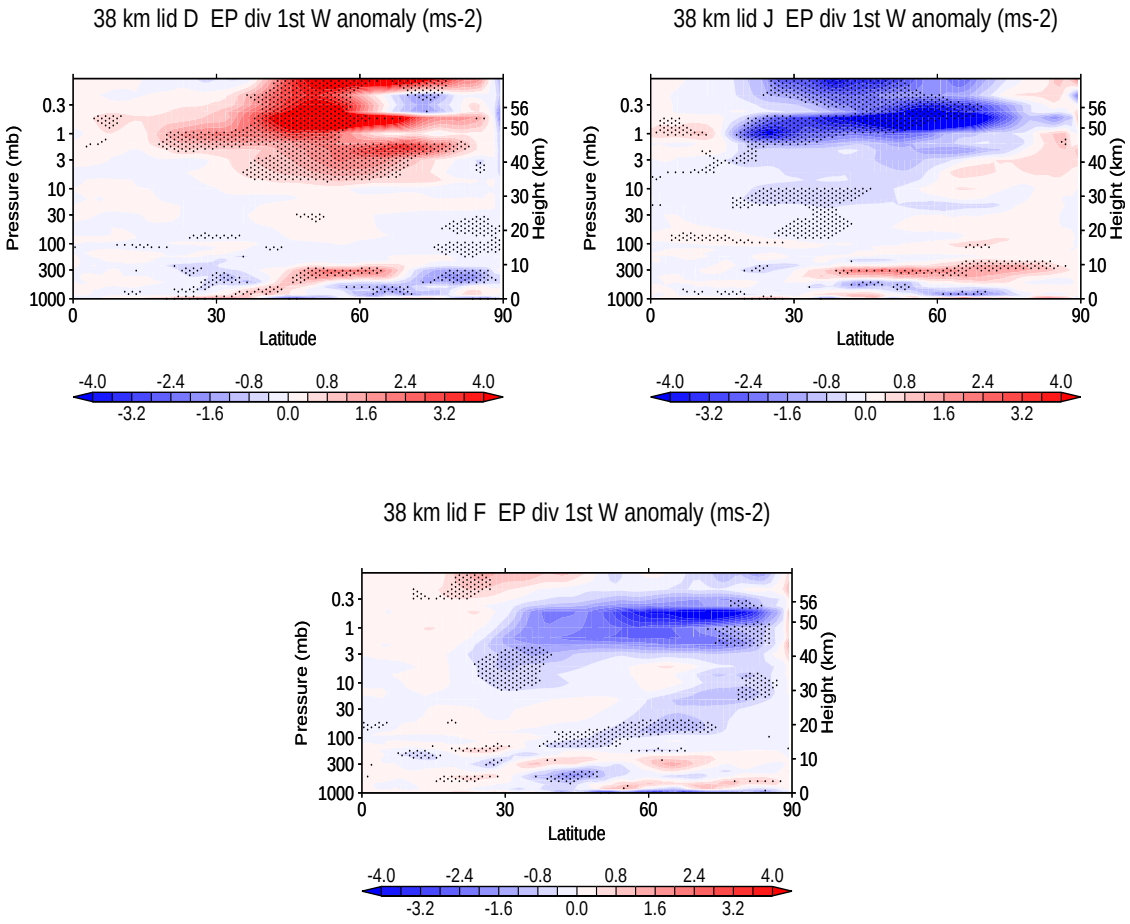

Figure 4.27: Monthly $(\rho a \cos\phi)^{-1}\nabla \cdot F$ anomalies ($\mathrm{ms}^{-1}\,\mathrm{day}^{-1}$) for L60. Stippling corresponds to the 95% confidence level using a t-test.

a substantially reduced negative anomaly of heat flux into the polar stratosphere - with much less statistical significance. Consistently, the polar stratosphere does not cool as much as in the previous L60 simulations.

The reduced anomaly of cooling in the polar stratosphere in these experiments will, therefore, imply that the temperature gradients in the polar stratosphere, and thus the change in planetary wave propagation is reduced. Figure 4.26, which displays the anomalies of EP flux divergence alone, demonstrates this. There is some convergence in the lower midlatitude stratosphere during January, but there is no statistically significant region of EP flux divergence over the polar stratosphere.

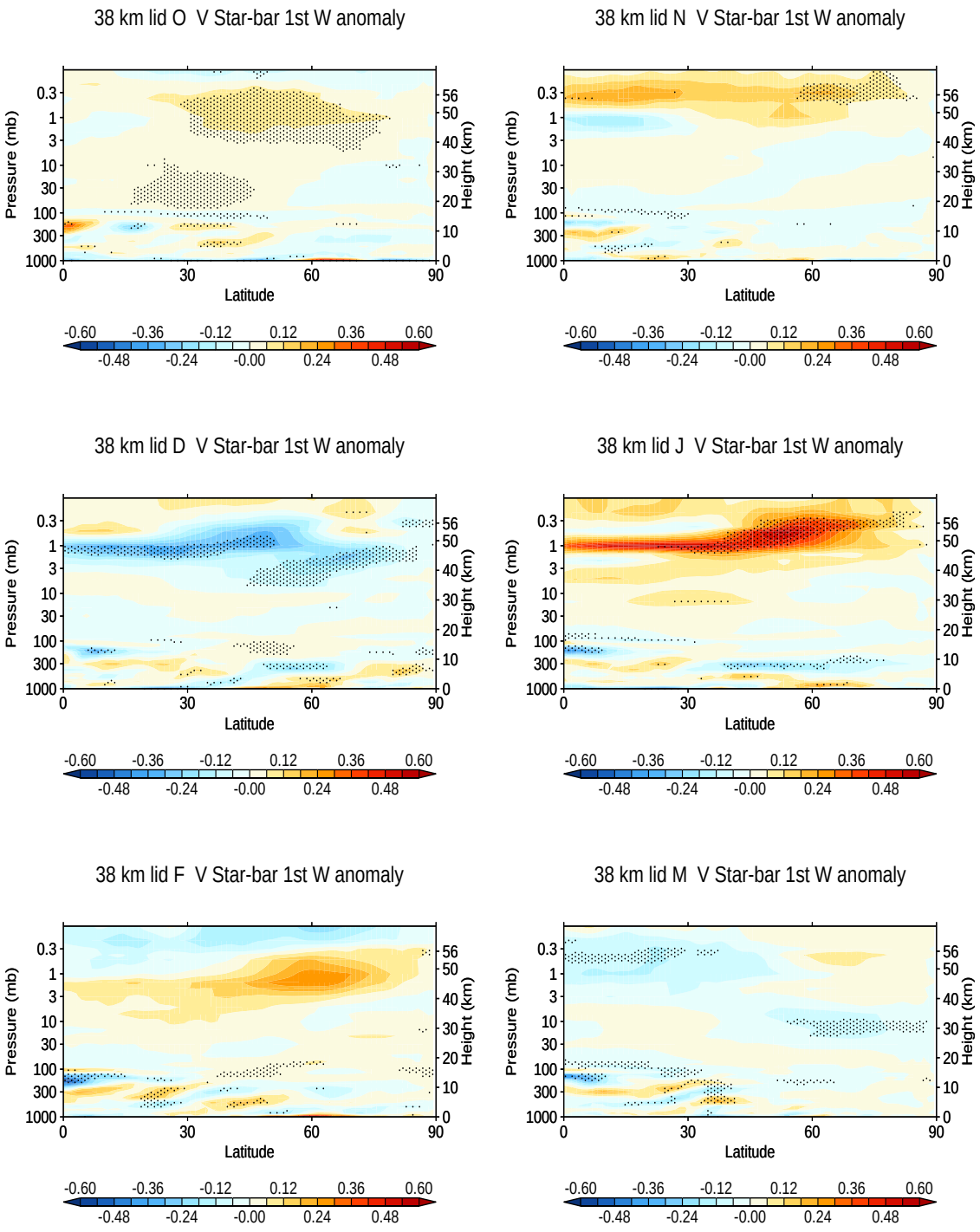

Figure 4.28: Monthly v^+ anomalies (ms^{-1}) for L60. Stippling corresponds to the 95% confidence level using a t-test.

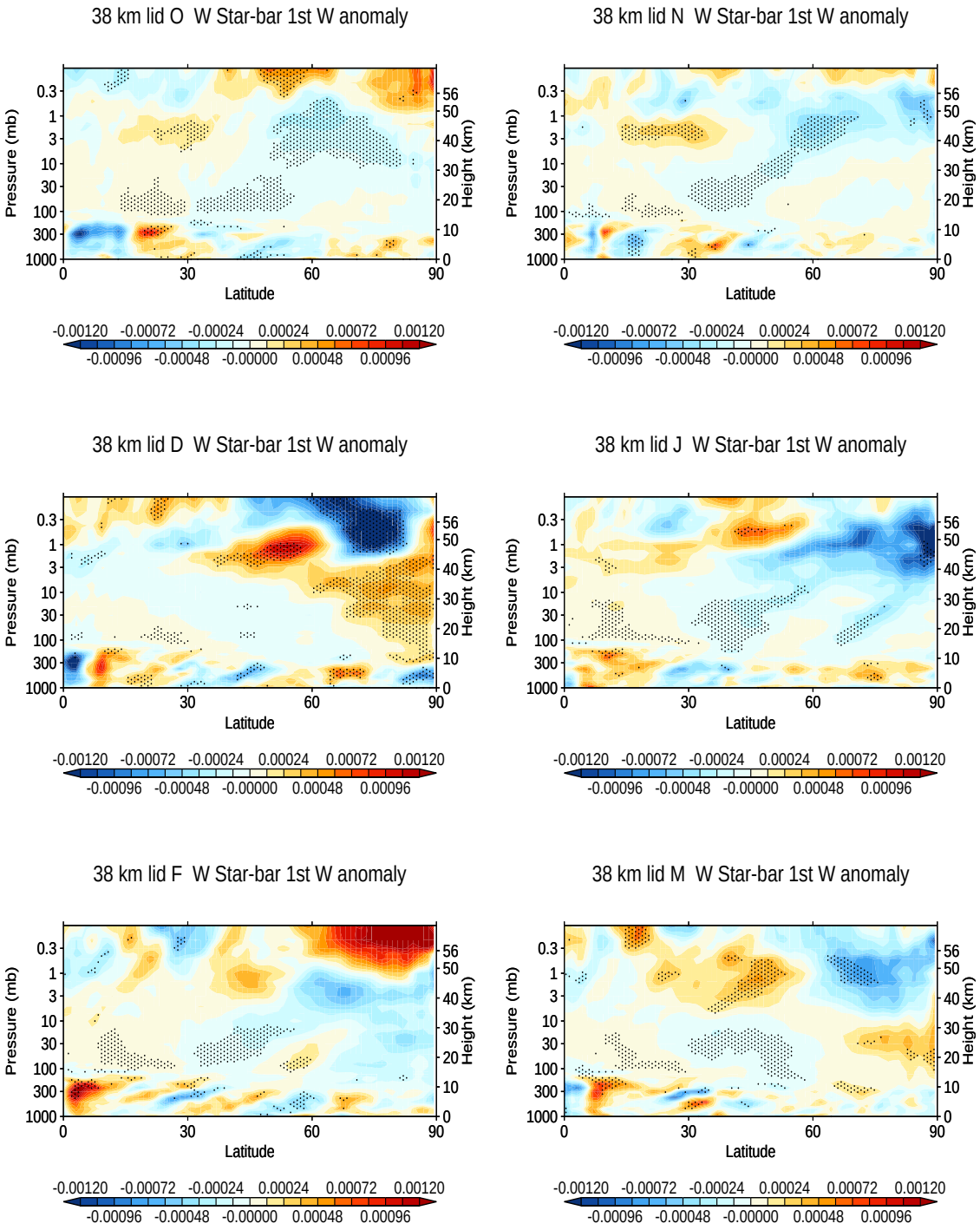

Figure 4.29: Monthly w^+ anomalies (ms^{-1}) for L60. Stippling corresponds to the 95% confidence level using a t-test.

As expected from this, the anomalies in the mean meridional circulation (figures 4.27 and 4.28) during reversal of the circulation are reduced. They are still significant, and show the influence of the aerosol heating on reducing the Brewer-Dobson circulation during the early winter, but they are smaller, as is the temperature gradient in the lower stratosphere. Following this, large and statistically significant poleward transport of the residual mean circulation resumes in late winter, causing the polar stratosphere to warm.

Whilst the processes involved are still similar, statistically significant and demonstrate a response of the L60 model to volcanic eruptions, the response overall in the wind fields, temperatures and MSLP are smaller. The results suggest that the magnitude of temperature gradient in the stratosphere is important in causing a reversal of the mean meridional circulation - that otherwise causes anomalous heating of the polar stratosphere - to lead to cooling the polar stratosphere and that this then creates a temperature gradient over the polar regions which alters the propagation of the planetary waves to allow for such large and statistically significant responses in the polar winds, NAO and consequently near-surface temperature response that is seen in the simulations. This is highly consistent with the simulated response in the second winter in the model, where the temperature gradients are subtantially reduced 18 months after the eruption, and the effect on the residual mean circulation is not as large.

This is not to suggest that the altered aerosol simulations are not responding to produce the NAO that can be seen, but that the temperature gradient is integral in stimulating the chain of mechanisms in altering planetary wave propagation and the Brewer-Dobson circulation - seen here and nearly identical to that of Kodera and Kuroda (2002) in their analysis of the solar cycle from observations which reproduces the well known poleward and downward propagation of winds seen in both volcanic and solar observational studies and recent simulations of solar influence on Northern Hemisphere winter climate using a very similar high-top model as the L60 here (Kodera 1995, Ineson et al. 2011).

4.6 Chapter Summary and Discussion

In this chapter, the response of two versions of HadGEM2 with 'standard' and increased vertical resolution and vertical extent - that were otherwise identical - and simulations with a changed aerosol profile in the increased vertical resolution version were set-up, performed and investigated for the changes on the atmospheric circulation following the Mount Pinatubo eruption of 1991. This represents the first study to show the importance of stratospheric resolution and explore the mechanisms involved using the transformed Eulerian-mean framework in a successful simulation of volcanic eruptions that reproduced all of the major observed features of volcanic eruptions - and sometimes exceeded them in magnitude. Improved representation of stratospheric dynamics appears core to simulating the observed changes following volcanic eruptions, and this study opens up the possibility of many other possible pieces of research.

The volcanic aerosol causes reductions in tropical tropospheric temperature as expected. Before wintertime, the presence of volcanic aerosol enhances residual mean meridional in the tropical stratosphere. During wintertime, the period of major stratosphere-troposphere coupling, temperature gradients due to the volcanic aerosol alter the propagation of planetary waves emanating from the troposphere in nearly identical ways to that observed to solar cycles which reverse the effect on the residual mean meridional circulation. This causes substantial stratospheric polar cooling and a strengthened vortex. This signal propagates to the surface, which alters the circulation and results in the Eurasian warming following volcanic eruptions. Importantly, the L38 simulations were useful in demonstrating that the response is not *purely* a temperature gradient and thermal wind shear response as has been quoted in the literature before (e.g. Robock 2000) because the area of the largest anomalous temperature gradient in these simulations, and in observations, is in the tropics and subtropics.

Whilst the magitude of the Pinatubo eruption was reproduced in the first winter, the results over the second winter were not as large - consistent with the mechanism

seen. This disparity may be due to enhancing of the observed signal due to variability (Stenchikov et al. 2002) and the 'true' signal of Pinatubo may be more similar with anomalies seen over a longer time period (e.g. Shindell et al., 2004) or it could be that the model's internal dynamics (planetary wave propagation, residual mean meridional circulation, and so on) may not still respond strongly enough to a stratospheric temperature perturbation. Nevertheless, these simulations represent the first marked and clear response to volcanic eruptions and demonstrate the importance of stratospheric dynamics in achieving this response. In the following chapter the same model as used here (L60) is used to simulate and understand the response of the NAO to sulphate aerosol geoengineering, after understanding and successfully simulating volcanic eruptions. This then closes the thesis, returning to geoengineering after investigating, simulating and understanding the effects of its natural analogue in order to better interpret current and future simulated responses of the NAO to geoengineering, and thereby contribute more solid foundations towards creating an informed literature on the response of the NAO to stratospheric sulphate aerosol geoengineering.

Chapter 5

Asymmetries Between the Onset and Termination of Geoengineering in the UM-CLASSIC Configuration of HadGEM2

5.1 Introduction

Assuming that a sulphate aerosol programme would not continue indefinitely, any sulphate aerosol geoengineering programme would need to be discontinued. Ideally, the end of a sulphate aerosol geoengineering programme would be a slow and steady ramp down, rendering the impacts upon the climate to be relatively small. However, if the discontinuation of sulphate aerosol geoengineering were to be rapid (what is know as a 'termination' of geoengineering), due to any problematic political or social factors for example, then there would be a much larger disturbance to the climate system. Baum et al. (2012) studied the viability of termination occuring within a social context. Whilst their results are not of direct interest from a physical sciences perspective, it is worthy to note they conclude that termination is a non-negligible possibility, thus making it an important topic of study to understand its physical implications.

The 'termination effect' has been addressed in previous studies. Brovkin et al. (2009) used a coupled climate-carbon model to investigate the climatic effect of a variety of aerosol loadings to offset a CO_2 induced warming. Brovkin et al. (2009)

simulate a stabilisation of the global average temperature under an idealised emissions scenario, involving a substantial overall emission of 5,000 GtC, with 90% emitted over the period 2000-2300. The non-geoengineered simulations result in a temperature increase of almost 7 K relative to present day. The geoengineered scenarios they perform using this CO_2 emissions scenario are designed to keep global average temperature increase relative to pre-industrial at 2 K, and in a subset of these simulations a termination of aerosol geonengineering was also simulated. The termination effect yields a rapid modelled increase of temperature of up to 5 K in a few decades, i.e. back to the temperature increase that would otherwise have occured were it not for the sulphate aerosol geoengineering. The warming that is experienced following termination is also globally non-uniform, with mid and high latitude areas experiencing more warming than low latitude areas, although the model used in their study is of intermediate complexity (with a spatial resolution of 10° in latitude and 5° in longitude), meaning regional dynamical changes would not likely be sufficiently represented.

Another study of the termination effect is that of McCusker et al. (2013) who simulated the termination effect in Community Climate System Model, version 4, CCSM4. The simulations also result in a rapid warming following termination of geoengineering that is well outside of the simulated variability. The simulations showed precipitation increases following termination, but as with Brovkin et al. (2009), they also showed substantial differences in regional effects with many land areas experiencing a reduction in precipitation.

The most comprehensive study of the termination effect to date is that of Jones et al. (2013) who analysed the termination effect in eleven different climate models that simulated an experiment of the Geoengineering Model Intercomparison Project (GeoMIP, see Kravitz et al., 2011, for extensive details on the project). The simulations of Jones et al. (2013) include a termination after 50 years of offsetting a 1% yearly increase in CO_2. Simulations show a rapid increase in temperature and precipitation and rapid losses in sea ice following termination. Similarly to Brovkin et al. (2009) they find that rates of warming are greatest at high latitudes and over land. They find less agreement in the regional patterns of precipitation than temperature, and

no agreement between models on the rate of change in the global averaged plant net primary productivity (NPP).

Given the substantial changes in temperature and other variables (e.g. as noted from Brovkin et al., 2009) the termination effect has proposed to alter the climate system so rapidly so as to be catastrophic (Baum et al., 2012). Volcanic eruptions also represent a large and rapid instant radiative forcing that can have substantial, but in general not catastrophic, effects. The climate often does not have time to equilibrate to transient volcanic forcing as it would due to a continuous injection due to effects such as aerosol sedimentation and lack of replenishment of sulphate aerosol from volcanic eruptions, hence they generally do not lower global average temperature by as much as 5 K (as has been simulated for geoengineering). Nonetheless, the fact volcanic eruptions have occured and that the effects have not been catastrophic may suggest that a termination effect of *similar* temperature increase may not be catastrophic if the climatic response were "equal, yet opposite". If the climatic response between the two were to be substantially different in global average rates of change or substantial regional differences, it could be possible that termination remains a substantial concern for geoengineering.

Despite the general mirrored similarities between the climate response of volcanic eruptions and geoengineering termination, such as temperature increases (decreases) and precipitation increases (decreases) that have been both simulated and observed following termination (volcanic eruptions), it is not inherently obvious that the climatic response to an equal but opposite radiative forcing are necessarily the same. Moreover, analysis of paleoclimate records have suggested that the climate response to an increase and decrease of solar constant is not regionally symmetric (Chiang and Friedman, 2012), suggesting differences in the dynamical response of the climate to decreasing and increasing solar constant.

The simulations performed in the termination study of Jones et al. (2013) follow one of the four GeoMIP scenarios (Kravitz et al., 2011). GeoMIP was established in order to lend greater confidence and ability to interpret geoengineering simulations. Often not only scenarios, but also models, were different leading to difficulties in

interpretation of results (e.g. Bala et al., 2008, Caldeira and Wood, 2008, Jones et al., 2010). The GeoMIP project aimed to establish a set of experiments for all modelling groups to perform so as to give greater confidence in predictions of stratospheric aerosol geoengineering. There are four experiments in GeoMIP (named "G1-G4" - schematic diagrams of the experiments are shown in figure 5.1):

- G1: models simulate the climate response to an abrupt quadrupling of CO_2 from preindustrial concentrations brought into radiative balance via uniform insolation reduction.

- G2: a solar constant decrease balances a 1% per year increase in CO_2 concentration for fifty years, at which point the solar constant reduction is switched off and the simulation run for twenty years.

- G3: an approximate balance is maintained over the 2020 to 2070 period from the positive radiative forcing due to CO_2 in the RCP4.5 scenario with SO_2 or sulphate aerosol injection into the lower tropical stratosphere.

- G4: at year 2020, a 5 Tg per year injection of SO_2 is implemented into the RCP4.5 emissions scenario.

These scenarios offer increasing complexity - the effects of the G1 scenarios have been described in the introductory chapter of this thesis. As can be seen in figure 5.1, the simulations analysed by Jones et al. (2013), in the G2 scenario, can only therefore analyse termination without offering information on the effect of a rapid onset. Other GeoMIP simulations are being performed which do offer this - such as the G4 scenario, although little output is available for GeoMIP's G4 scenario at the time of writing. Some studies have already been conducted on the G1 and G2 experiments (e.g. Kravitz et al., 2013), not only as they are computationally easier to implement but also as they are seen as the predecessors to the more complicated experiments. In comparison, the G4 scenario offers a relatively largely unanalysed set of simulations to date.

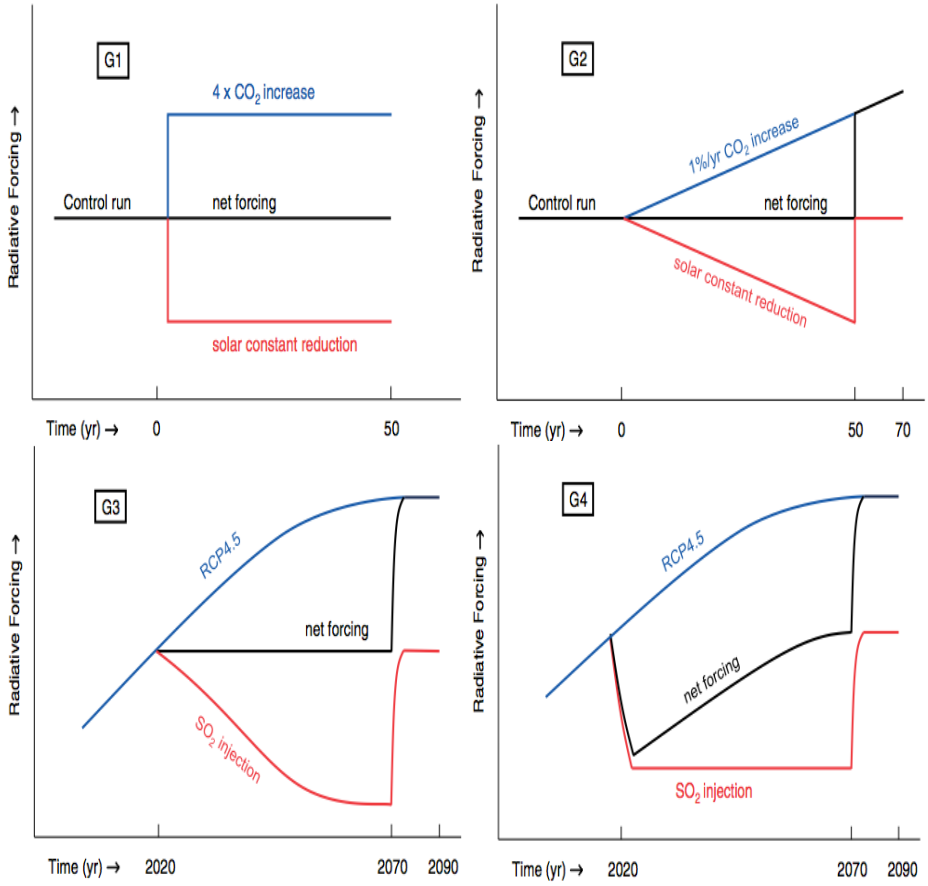

Figure 5.1: Schematic diagrams illustrating the four GeoMIP experiments, G1 (top left), G2 (top right), G3 (bottom left), G4 (bottom right), from Kravitz et al. (2011)

Despite the availability of a small number of models to analyse the G4 scenario, Driscoll et al. (2012) showed the inability of many state-of-the-art models to simulate important dynamical effects to sulphate aerosol loading from volcanic eruptions, whilst chapter 4 demonstrated the importance of enhanced stratospheric resolution in simulating the dynamical effects of sulphate aerosol loading - and particularly the increased success in the L60 version of the HadGEM2 model in comparison to the L38 version. Therefore, we anticipate more confident simulations of the G4 scenario performed with the L60 version of the HadGEM2 model.

5.2 Experimental Set-Up

Here, simulations of a modified version of the G4 experiment are performed (referred to in the rest of the chapter as G4mod) where twice the amount of aerosol is injected (10 Tg a year) instead of the 5 Tg a year prescribed by the standard G4 scenario, in order to increase the signal to noise ratio for the set of simulations. The scenario simulated is otherwise identical to GeoMIP's G4 scenario. Here the HadGEM2-L60 model (with a horizontal resolution of 1.875° x 1.25°, 60 vertical levels, coupled to an ocean model that has 40 vertical levels as in the previous chapter) uses the UM Coupled Large-scale Aerosol Simulator for Studies In Climate (CLASSIC) aerosol scheme.

The simulations directly inject sulphur dioxide (SO_2) into the tropical lower stratosphere, at a single source located at the equator, which converts into sulphate aerosol (H_2SO_4). Unlike many other GeoMIP simulations, the G4 scenario in HadGEM2 L60 involves the direct injection of SO_2 to convert into aerosol and sediment out of the stratosphere via gravitational settling and model dynamics (such as tropopause folding). The injection rate is constant from the start of the experiment - i.e. no 'ramp-up' of geoengineering exists in the experiments. Whilst imposing an observed aerosol profile (such as that of the Pinatubo eruption as simulated in the previous chapter) helps isolate the model's comparative performance to observations of the dynamics alone, a prescribed aerosol profile here is less suitable given uncertainty around the precise aerosol profile that would arise due to there being no observations of a directly injected aerosol geoengineering programme.

The three simulations which run from December 2019 to December 2090 are initialised by taking the atmospheric and oceanic state at December 2019 from three RCP4.5 simulations as initial conditions. In order to create anomalies, the same three RCP4.5 simulations are used, representing two sets of simulations that are otherwise identical but for sulphate aerosol geoengineering.

As mentioned, Jones et al. (2013) analysed the impacts of termination upon precipitation, near-surface temperature, sea ice and NPP for the ten years following

termination. Here the impacts upon precipitation, near-surface temperature and sea ice are explored. In particular, temperature and precipitation are often the two sole variables included in damage function estimates (e.g. Ricke et al., 2013, Kravitz et al., 2014), playing an integral role in the assessment of climate impacts. Moreover, not only is climate change likely to result in larger warming at the high latitudes (polar amplification), but (as has been noted elsewhere in this thesis) the potential of geoengineering for sea ice preservation has been particularly focused upon. However, NPP is not studied. Not only is NPP much less associated with physics of climate, but also the near total lack of agreement between models on NPP, as seen from Jones et al. (2013), suggests that results on this under termination are highly unreliable.

5.3 Results

5.3.1 RCP4.5 Scenarios

RCP4.5. scenarios are briefly assessed for their physical realism as they form a control set of simulations. Figure 5.2 shows the global mean annual mean near-surface temperature, precipitation and sea ice fraction for the three member RCP4.5 ensemble. Global mean near-surface temperature values for the ensemble are approximately 287.5 K at the beginning of the simulation - 'year 0', corresponding to 2020. Near-surface temperature across the ensembles increases almost linearly to approximately 289 K, corresponding to approximately 1.5 K warming over the 2020-2090 period. This is close to the average estimate of warming over the period as given by all IPCC models in the Fifth IPCC assessment report (Stocker et al., 2013).

Figure 5.2 b) shows the globally averaged yearly averaged precipitation over the 2020-2090 period. Global average precipitation is much noisier than the temperature signal, however, precipitation increases are seen over the 2020-2090 period. Two major effects are thought to go into the changes in precipitation under climate change. The first is a strengthening of the precipitation due to increase of surface temperatures which result in an intensification of the hydrological cycle. The second is a reduction in the ability of the precipitation to form as a result of increased carbon dioxide

trapping of radiation locally upon condensation (Allen and Ingram, 2002). Despite the second effect, precipitation is universally expected to increase in the global average (Stocker et al., 2013) due to the substantially greater intensification of the first effect.

Climate feedbacks have been postulated to play substantial roles in sea ice levels. For example, observed increases in Antarctic sea ice since 1970 have been suggested to be the result of changes in the circumpolar westerly flow, which extends from the surface up to the stratosphere, due to ozone loss (Gillett and Thompson, 2003). Other explanations have been offered, such as that by Zhang (2007), who notes that the ocean around the Antarctic is reducing in salinity from increased precipitation and snowfall as well as increases in meltwater from Antarctic *land* ice. The altering of composition causes decreased mixing between cold and warm ocean layers, and a reduction in melting of Antartic sea ice. However, Turner et al. (2009) note from model simulations that the observed increases in Antarctic sea ice may still be within the range of natural variability. Therefore, despite, feedbacks possibly playing substantial roles in sea ice levels, global average values have been observed to decrease as a result of increasing temperatures (Stocker et al., 2013). Figure 5.3 c) shows a decline of sea ice as expected, with a decrease in total surface area of the Earth covered in sea ice to approximately 2%.

To explore regional changes under the RCP4.5, figure 5.3 a) shows latitude longitude plots of average decadal rate of change for the same three variables. Near-surface temperature decadal rates of change can be seen in figure 5.3 a). All areas show warming, with exceptions of those around the edge of the Antarctic continent which show minor cooling, possibly due to similar complex and nonlinear sea ice interactions that have lead to the observed increase in sea ice. As expected from many previous studies (such as the analysis of CMIP5 models as conducted by Collins et al., 2013), the Northern Hemisphere regions show the greatest increase in warming, with values peaking at around 0.15 K per decade in the Arctic region.

Whilst increases in precipitation can be seen over most of the globe, substantial increases in precipitation can be seen in the Northern Hemisphere tropics, paired with decreases in the Southern Hemisphere tropics. This can likely be explained by, and

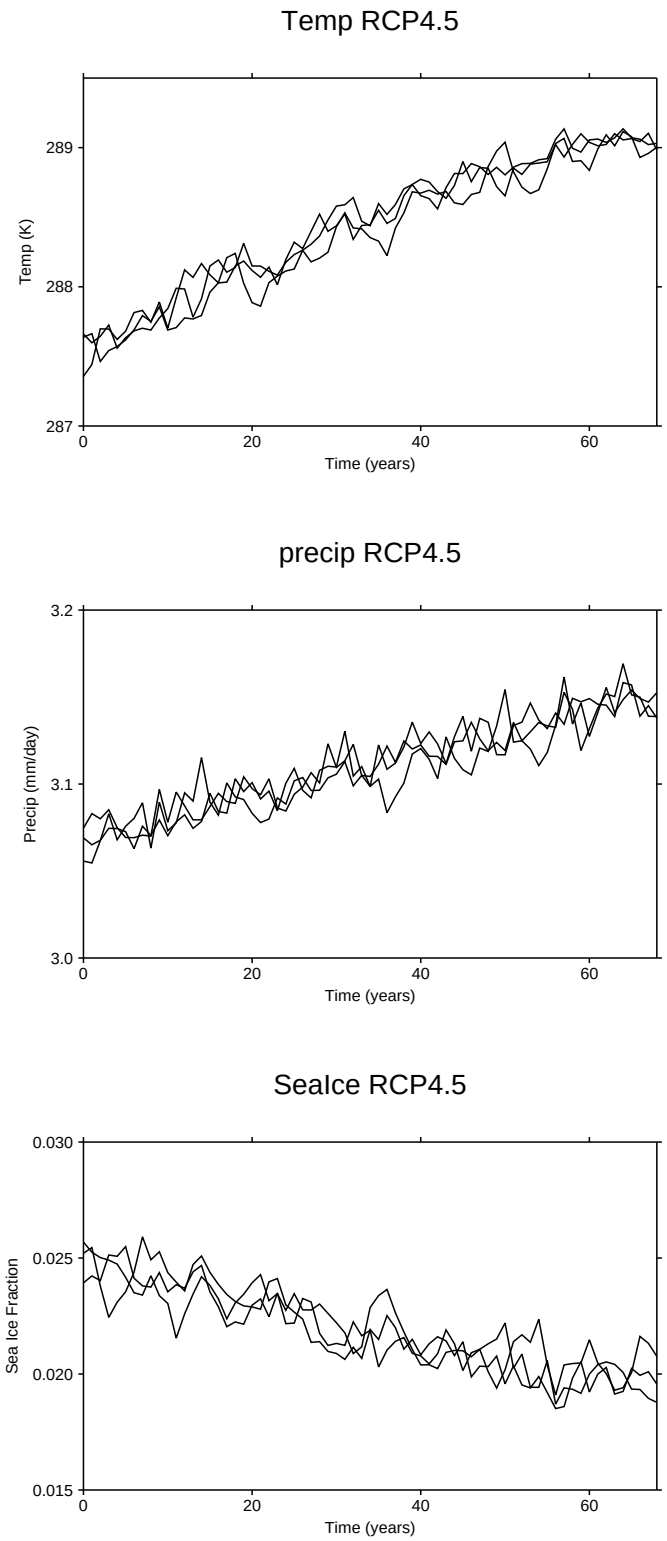

Figure 5.2: Global mean annual mean values of near-surface temperature, precipitation and fraction of global surface area covered in sea ice for the three RCP4.5 simulations.

is consistent with, previous research that demonstrates that with climate change or radiative perturbations (such as that induced by stratospheric sulphate aerosols) the Intertropical Convergence Zone moves away from the cooler hemisphere and towards the warmer hemisphere, and results in shifting monsoon circulation (e.g. Held et al., 2005, Haywood et al., 2013).

Sea ice anomalies show substantial decreases everywhere in the Northern Hemisphere, indicative that temperature is the leading order factor in sea ice levels for the Arctic. Decreases in sea ice are also visible in the Southern Hemisphere, however, there are also increases in sea ice. This is consistent with dynamical influences suspected to play substantial and complex roles in determining the level of Antarctic sea ice - such as possible influences from circulation change due to ozone recovery. Nonetheless, on the global average sea ice levels decrease - consistent with expections. Thus the RCP4.5 simulations here represent a set of simulations consistent with previous research studies across all major models, such as those used in the IPCC report (e.g. Stocker et al., 2013, Collins et al. 2013).

5.3.2 G4mod: Onset and Termination

Figure 5.4 shows global mean anomalies of temperature, precipitation and sea ice from the RCP4.5 scenarios. With the onset of geoengineering, temperature anomalies can be seen to decrease fairly linearly, with the climate stabilising to a globally averaged near-surface temperature anomaly of just larger in magnitude than 1K. Berdahl et al. (2014) analysed the G4 scenario in 5 participating climate models for the Arctic cryosphere response. Whilst the focus is upon the Arctic cryosphere, their figure 1 shows decreases in G4 of slightly less than 1 K. Therefore, one may anticipate a slightly larger magnitude of anomaly for these simulations. However, for the L60 simulations of G4, the global mean near-surface temperature anomalies obtained are smaller than those with the low-top (L38) version, likely due to increases in resolution yielding a more accurate aerosol distribution, improved representation of important processes for stratosphere aerosol lifetimes, such as the Brewer Dobson circulation and tropopuase folding as well as differences in injection location: namely the simulations

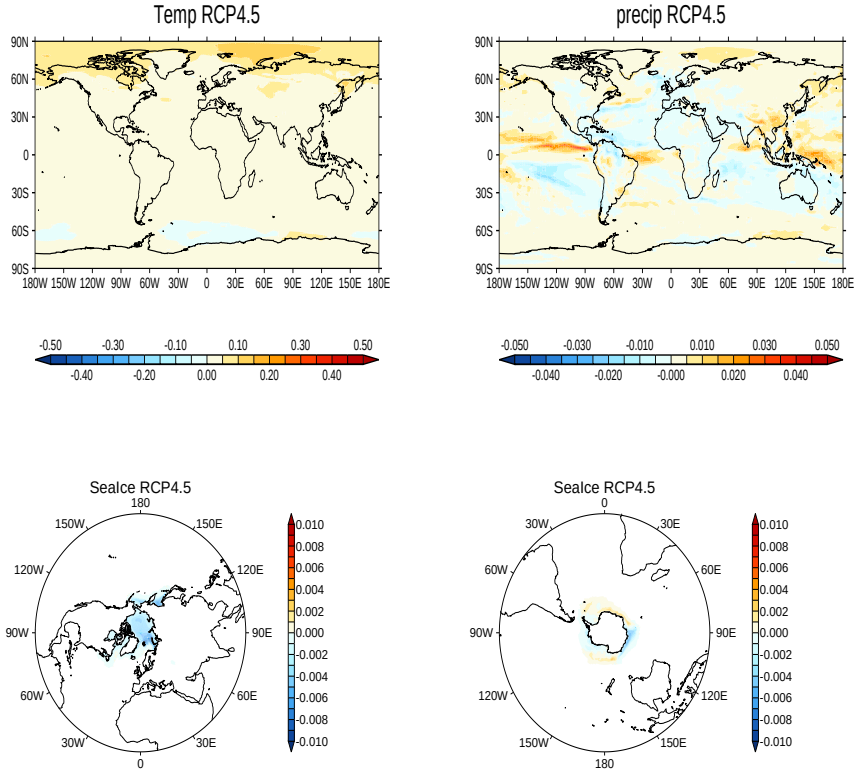

Figure 5.3: Linearly fitted rate of change in temperature (top left), precipitation (top right), and per cent of area covered in sea ice for the Northern Hemisphere Sea Ice (bottom left) and the Southern Hemisphere (bottom right) over the RCP4.5 scenario.

for L38 injected aerosol at all latitudes, whilst this experiment injects aerosol at the equator only.

As expected, precipitation decreases can be seen over the same time period in figure 5.4 b), resulting in approximately 0.1 mm/day less precipitation in the geoengineered scenario as compared to the RCP4.5 scenario. As mentioned, there are thought to be two major competing effects following increased carbon dioxide on the hydrological cycle. Under geoengineering, the decrease in global mean temperature means that the first effect is decreased or nullified (or reversed), whilst the second effect remains, hence overall, a decrease in precipitation would be expected for a net radiative forcing balance.

Ferraro et al. (2014) note a further mechanism of how geoengineering can reduce precipitation. Their simulations show that substantial amounts of sulphate aerosol geoengineering could alter the lapse rate of the atmosphere, which reduces the amount of convection, and hence result in reduced precipitation. The simulated stratospheric aerosol amounts here are substantially lower than their study, meaning that this feedback is likely to play only a minor to negligible role in the simulated climate response.

Figure 5.4 c) shows the global averaged anomalies of sea ice of the geoengineered scenario relative to the RCP4.5. As expected from reduced incoming solar radiation caused by increased shortwave scattering due to increased stratospheric aerosols and reductions in temperature relative to the RCP4.5 scenario, the geoengineering simulations reveal considerable reductions in globally averaged sea ice anomalies. Sea ice increases relative to RCP4.5 show between approximately 0.002 and 0.004 extra fraction of total Earth surface covered in sea ice. A very large peak is observed after ten years of geoengineering in one ensemble, although this is likely to be natural variability, given the quick return to more normal values of sea ice.

Previous work has discussed the efficacy of geoengineering to offset sea ice loss from global warming showing geoengineering to be successful in reducing sea ice loss. Moore et al. (2014) analysed the Arctic cryosphere response of 8 GeoMIP models in the G1 scenario, as well as a 4 x CO_2 increase. Under the 4 x CO_2 scenario, models

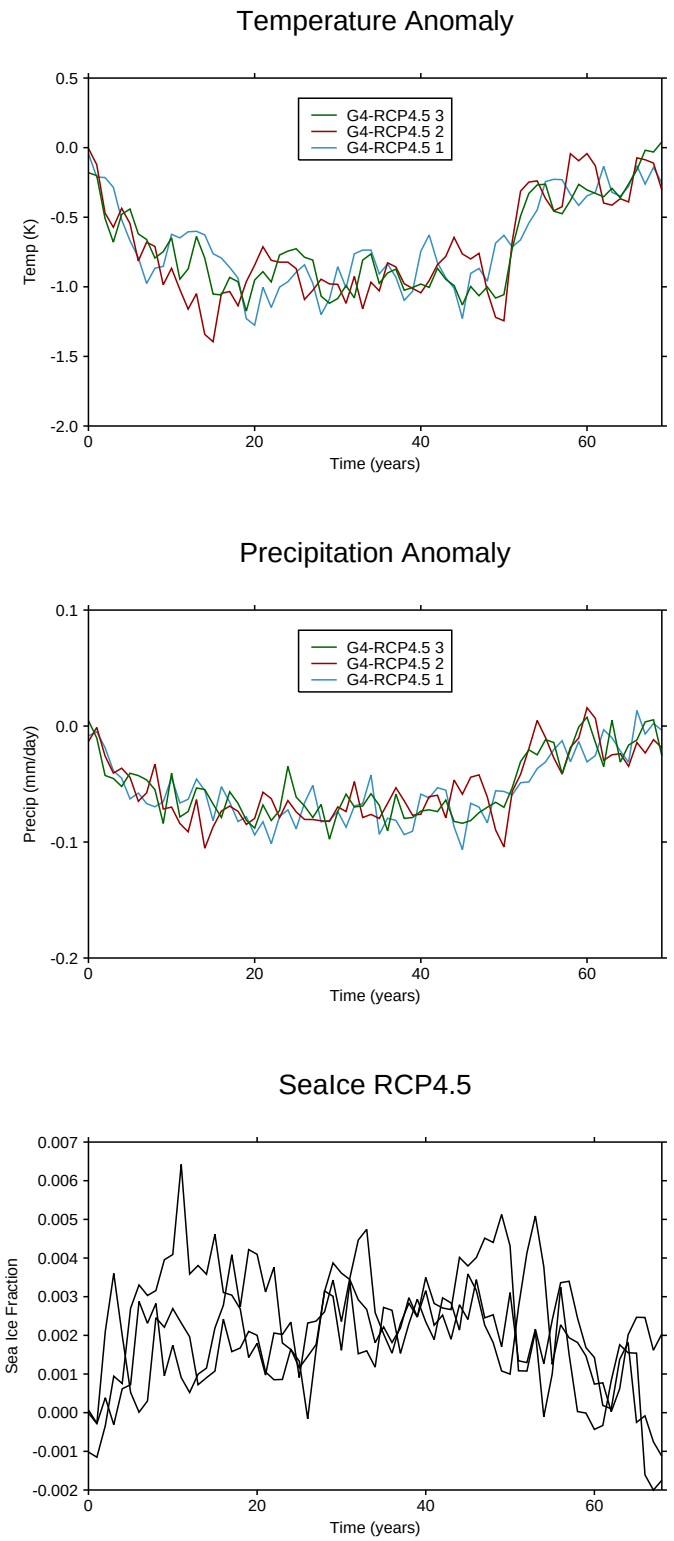

Figure 5.4: Global averaged, yearly averaged anomalies of near-surface temperature, precipitation and fraction of global surface area covered in sea ice of G4mod from each respective RCP4.5 simulation.

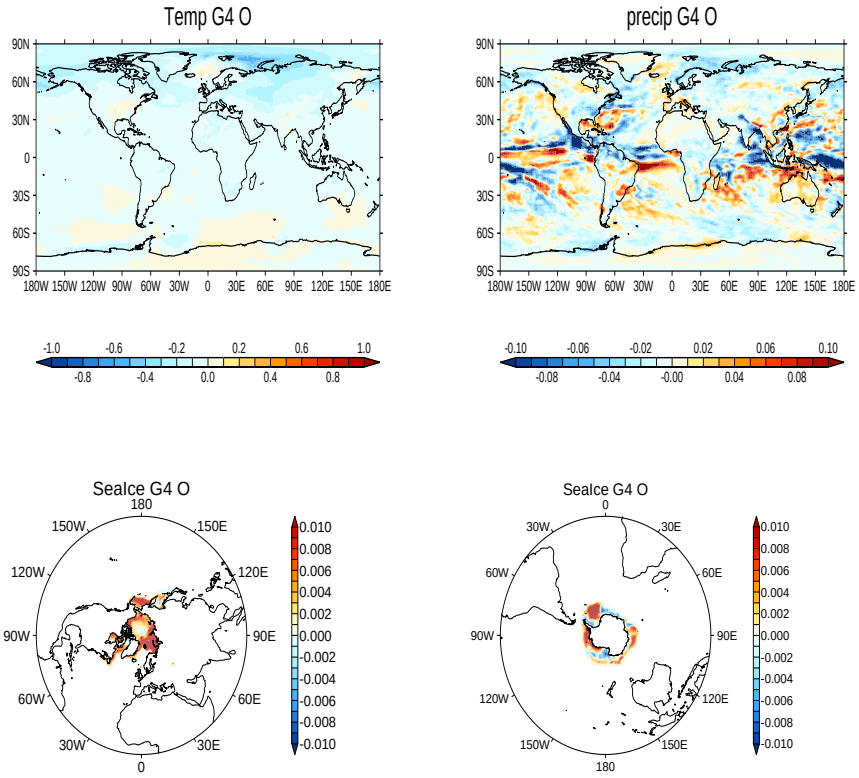

Figure 5.5: Linearly fitted changes in temperature (top left), precipitation (top right), and per cent of area covered in sea ice for the Northern Hemisphere Sea Ice (bottom left) and the Southern Hemisphere (bottom right) over the ten years following the onset of geoengineering.

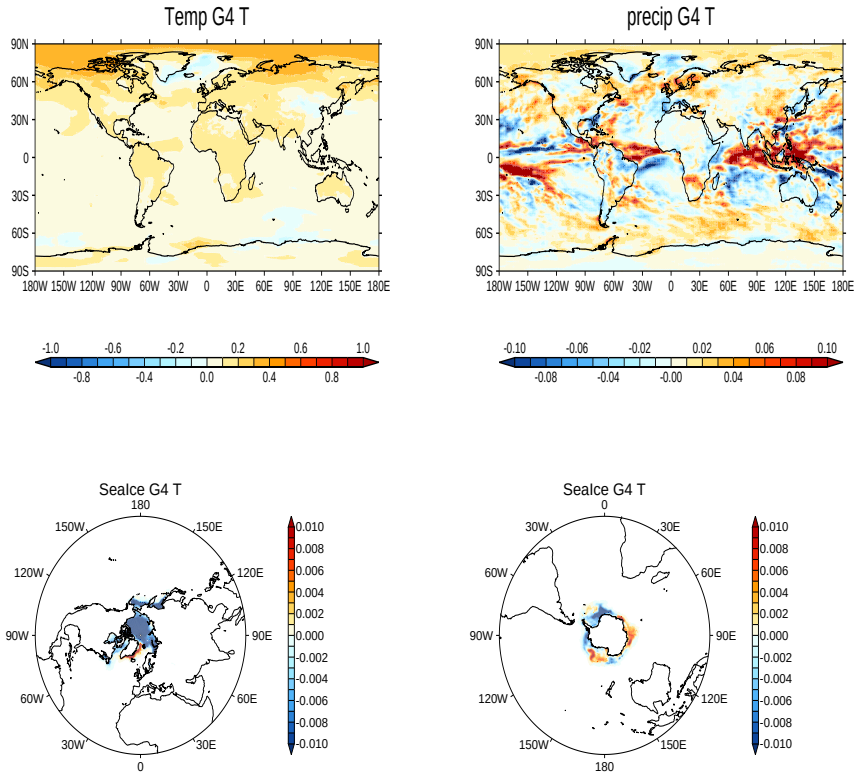

Figure 5.6: Linearly fitted rate of change in temperature (top left), precipitation (top right), and per cent of area covered in sea ice for the Northern Hemisphere Sea Ice (bottom left) and the Southern Hemisphere (bottom right) over the ten years following the termination of geoengineering.

showed an annual total surface area change in sea ice ranging between -29% and -82% over the whole simulated period. Under the G1 scenario, whose reductions in the solar constant achieve a net zero radiative forcing to the 4 x CO_2 increases, annual total surface area change in sea ice ranges between 1% and -8% over the whole simulated period. Robock et al. (2008) simulated the effects of geoengineering via tropical and Arctic sulphate aerosol injection. Arctic geoengineering was found to be more effective at reducing sea ice loss . Effects from Arctic aerosol injection were not just confined to the Arctic, however, with disruptions to both the Asian and African monsoons simulated in both tropical as well as Arctic injection scenarios. Similar studies have simulated the efficacy of geoengineering to reduce sea ice loss (e.g. Rasch et al., 2008, Berdahl et al., 2014, Moore et al., 2014).

5.3.3 Onset and Termination

Figure 5.5 shows the decadal rates of change for the same three variables. During the onset of geoengineering, negative rates of change of temperature are seen globally, with notable exceptions in areas of the Southern Ocean and Antartica. Values reach their minimum in the Arctic on the order of -0.5 K/decade. This is likely in part to be due to the substantial increase in Northern Hemisphere sea ice increasing albedo, and reducing the amount of absorption by the oceans. Sea ice increases may also be seen in the Southern Hemisphere, although there are areas of decreasing sea ice too. Precipitation values decrease on the global average (figure 5.4), whilst the plot of the rate of change of precipitation over the surface reveal substantial noise. As expected, there are signs of increases in precipitation in the Southern Hemisphere tropics, with decreases in precipitation in the Northern Hemisphere tropics, suggesting some movement of the ITCZ opposite to that seen in the RCP4.5.

Figure 5.6 shows the same plots as figure 5.5, but for the termination period. Rates of temperature increase are almost everywhere positive with a few exceptions - notably along the East coast of Greenland where Arctic Sea Ice can be seen to increase. Southern Hemisphere sea ice shows less uniformity with approximately half of the Southern Hemisphere sea ice increases and decreasing. Rates of increase during

the termination phase can be seen to reach approximately 0.4 K per decade over large parts of the Earth northwards of 60 °N. Tropical land regions can be seen to have higher rates of change, as expected given the slower response time of the ocean. Rates of change of precipitation are again noisy, however, there is a general band of increasing rate of precipitation at the equator with decreases often immediately South of this band, indicative again of shifting circulation associated with the ITCZ. It can be seen from the figure 5.6) a) most notably, that the rates of change following termination of geoengineering are more severe than the rates of change experienced following an onset of geoengineering.

5.3.4 Onset and Termination Acceleration Factors

Jones et al. (2013) calculate for the termination a nondimensional termination acceleration factor α, defined as the average rate of increase in the ten years immediately following termination obtained by a linear regression, so as to rule out noise induced by sampling only the endpoints, normalised by the rate of change over the carbon dioxide without geoengineering scenario. Here the same nondimensional termination acceleration factor is used, but is also applied to the first ten years of onset also, thus yielding α (Onset) and α (Termination) for all of the variables explored. An α_{Ratio} is also defined as the ratio of the rate of change in the termination divided by the rate of change during onset. Specifically:

$$\alpha(\theta,\lambda)_{Onset} = \beta_{Onset}(\theta,\lambda)/\beta_{RCP4.5}(\theta,\lambda) \tag{5.1}$$

$$\alpha(\theta,\lambda)_{Termination} = \beta_{Termination}(\theta,\lambda)/\beta_{RCP4.5}(\theta,\lambda) \tag{5.2}$$

$$\alpha(\theta,\lambda)_{Ratio} = \beta_{Termination}(\theta,\lambda)/\beta_{Onset}(\theta,\lambda) \tag{5.3}$$

where the β's are the linear fits for the ten year rate of change (those values presented in figures 5.4, 5.5 and 5.6, respectively) and θ and λ represent latitude and longitude, respectively. These are computed for each RCP4.5 and G4mod pairing,

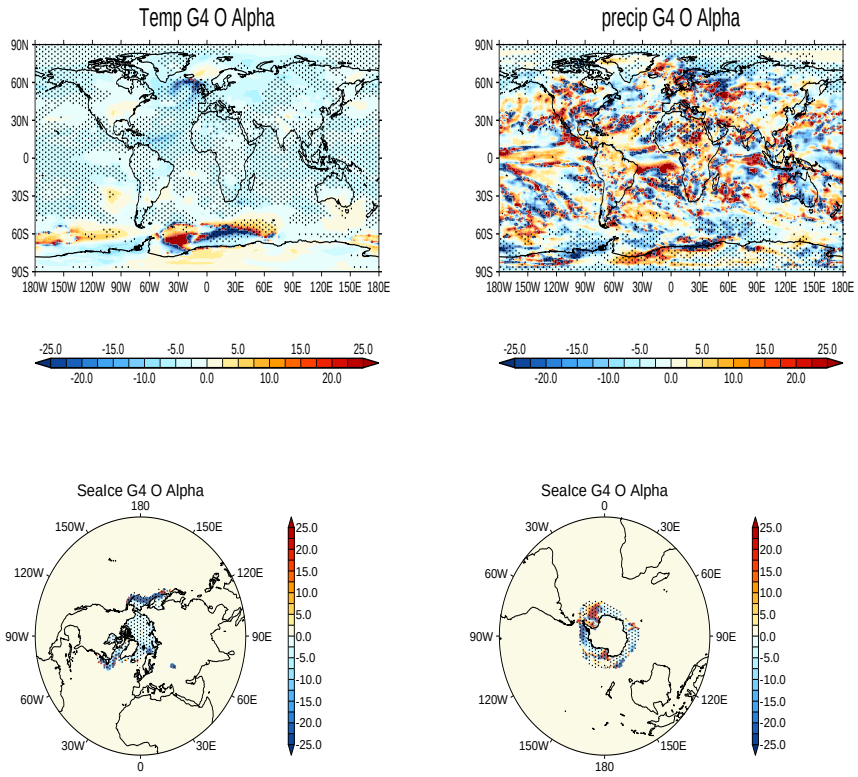

Figure 5.7: RCP4.5 scenario at the 95% level. for temperature (top left), precipitation (top right) and and per cent of area covered in sea ice for the Northern Hemisphere (bottom left) and Southern Hemisphere (bottom right). Statistical significance represents where the onset period are statistically significantly different to the α_{Onset}

and then averaged. The onset, and termination, acceleration factor plots are shown in figures 5.7, 5.8 and 5.9, respectively, whilst the global average values are presented in table 1.

In figure 5.7 α_{0nset} for temperature can be to be negative and statistically significant almost everywhere, with some exceptions in the high latitudes. Steep gradients can be seen, which may appear almost unphysical, around the Antarctic. However, they are simply caused by regions where the climate is changing substantially greater during onset whilst the RCP4.5 scenario rate of change changes sign in a smooth fashion, so extremely steep gradients in some regions are to be expected not only for the α values here, but for all variables and especially noisy variables. Substantial differences in the rates of change are seen over the north of the Atlantic, suggesting

changes in the Atlantic Meridional Overturning Circulation (AMOC) - which has been simulated to change in response to volcanic eruptions (Stenchikov et al., 2009).

As expected, values for precipitation show many steep gradients, highlighting the uneven nature of impacts between sulphate aerosol geoengineering and carbon dioxide forcing upon the climate system. Northern hemisphere sea ice values show substantially greater rates of change for the G4mod onset as opposed to the RCP4.5 scenarios, whilst differing rates of change for sea ice in the Southern Hemisphere are reflective of dynamical changes influencing sea ice levels. Similar patterns can be seen for the termination α values: temperature shows almost everywhere statistically significant differences with substantially larger rates than the RCP4.5 simulations, noisy values for precipitation, greater and almost everywhere positive increases in Northern Hemisphere sea ice, and less uniform changes in Southern Hemisphere sea ice.

Plots of $\alpha_{\text{Termination}}$ (figure 5.8) reveal that the termination effect is more intense than the RCP4.5 scenario almost everywhere. As with onset, precipitation reveals substantial noise whilst changes in Northern Hemisphere sea ice are more uniform than changes in Southern Hemisphere sea ice that shows negative $\alpha_{\text{Termination}}$ over approximately half of the area covered in sea ice, with the other half showing increases. α_{Ratio} plots are shown in figure 5.9 reflecting what has been noticed from these previous two figures.

Table 1 shows the values of the globally averaged α_{Onset}, $\alpha_{\text{Termination}}$ and the absolute values of the globally averaged α_{Ratio}. From the table it can be seen that the rate of termination is approximately 1.6 times that of onset. Whilst being approximately 1.3 times more for rate of change of precipitation. The rate of change for sea ice, however, is slightly less during termination than onset. In all individual ensembles for every variable except for one, termination is more severe than onset. One ensemble demonstrates substantial increases following onset precisely ten years following onset, as can be seen in figure 5.4. Given the ensemble member's sea ice drops to almost half its value the following year, the α_{Ratio} for sea ice appears to be skewed by random variability precisely at the ten year point. Nonetheless, it remains that

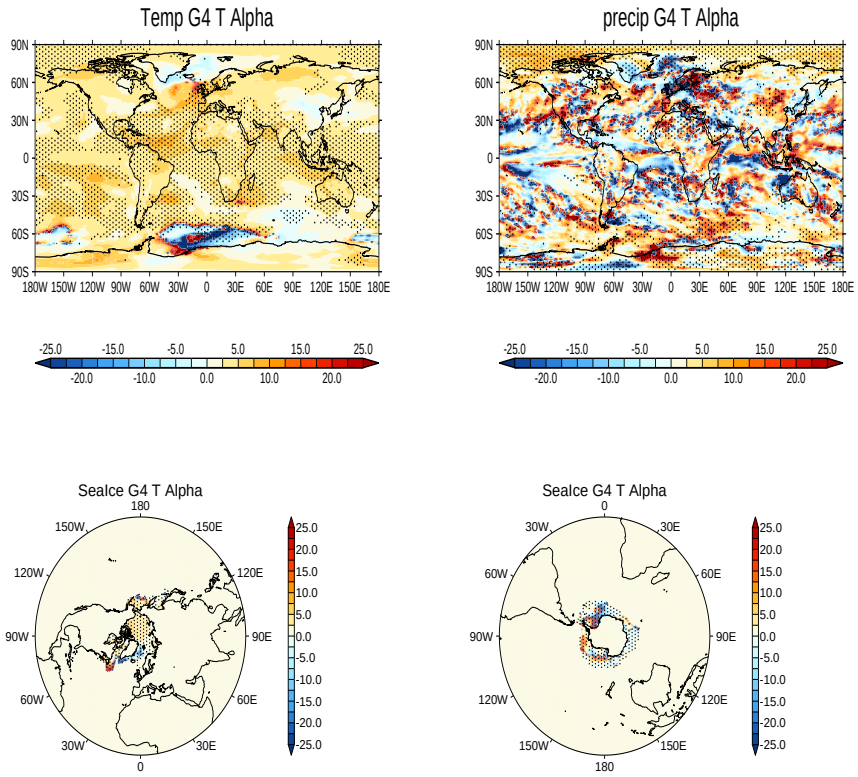

Figure 5.8: RCP4.5 scenario at the 95% level. for temperature (top left), precipiation (top right) and and per cent of area covered in sea ice for the Northern Hemisphere (bottom left) and Southern Hemisphere (bottom right). Statistical significance represents where the termination period are statistically significantly different to the $\alpha_{\text{Termination}}$

for one of the most fundamental variables for climate impacts (temperature), changes over a termination period are substantially more intense than over the onset period.

5.3.5 Exploring Imbalances Between Sulphate Aerosol Amounts between Onset and Termination

Whilst it may indeed be that the climate response is asymmetric to an onset and termination due to dynamical factors, at least one simpler explanation may be possible. If, during an onset, the globally averaged sulphate aerosol has a substantially different temporal profile to termination then effects could perhaps be explained in terms of different aerosol amounts implying substantially different amounts of total incoming

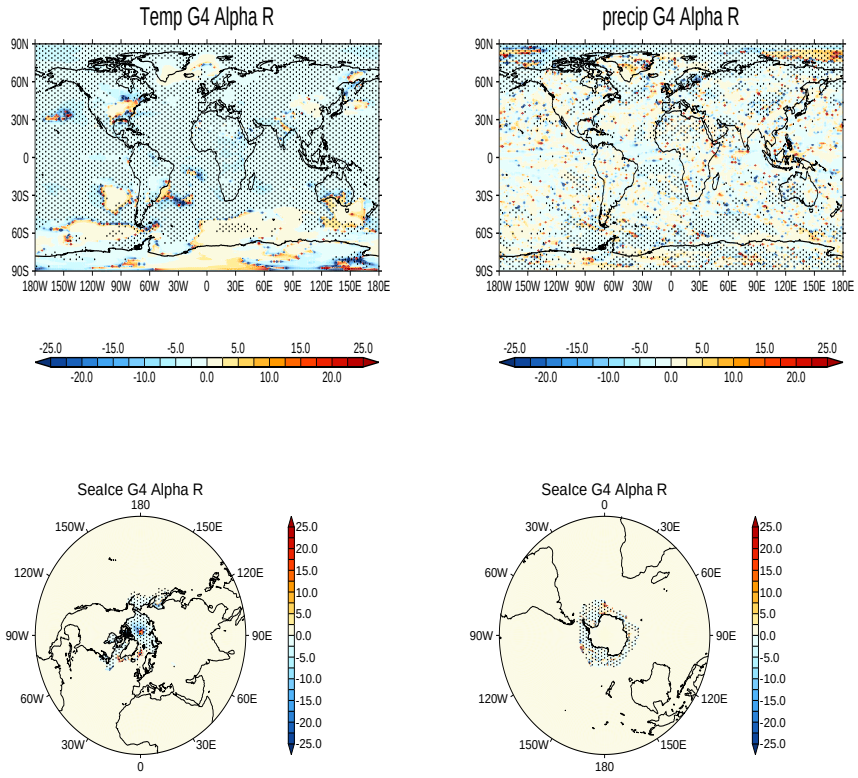

Figure 5.9: α_{Ratio} for temperature (top left), precipiation (top right) and and per cent of area covered in sea ice for the Northern Hemisphere (bottom left) and Southern Hemisphere (bottom right). Statistical significance represents where the onset period are statistically significantly different to termination at the 95% level.

	Termperature	Precipitation	Sea Ice
α(Onset)	-2.36	-4.61	-3.51
α(Termination)	3.74	5.94	3.00
$\mid \alpha$(Ratio) $\mid$	1.59	1.29	0.86

Table 5.1: α values

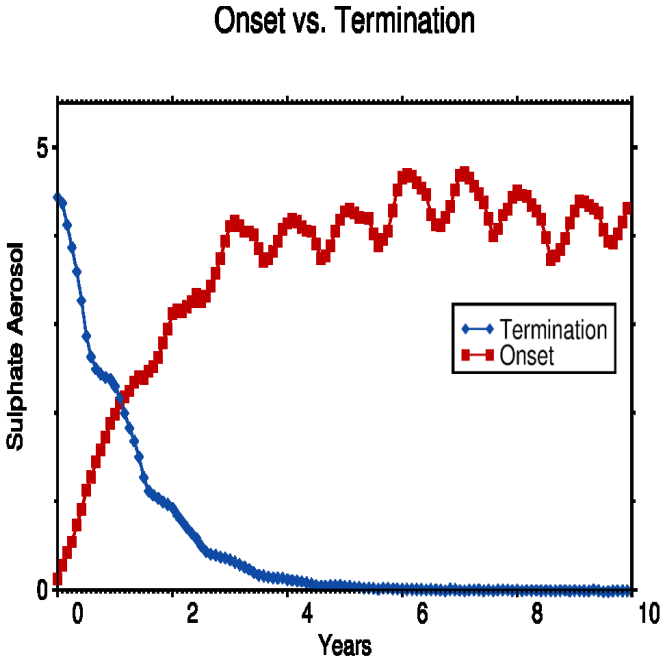

Figure 5.10: Globally averaged sulphate aerosol throughout the entire atmosphere during the onset and termination periods.

solar radiation over the two periods - thus affecting temperature. If the values are approximately equal but opposite and the effect on the incoming solar radiation and energy budget, therefore, are approximately equal it would suggest that the changes seen are more dynamically influenced.

Figure 5.10 shows the globally averaged aerosol for the whole atmosphere for the onset and termination periods. For the onset a rapid increase in the aerosol amounts are seen increasing in an exponential manner, until the loading generally stabilises around the fourth year of continuous injection. An annual oscillation, corresponding to differing amounts of sedimentation due to changes in stratospheric circulation, is seen.

Following termination of aerosol geoengineering, there is a rapid decline in stratospheric aerosol loading which also has an exponential form. Aerosol amounts decrease until around approximately 4 years when no aerosol from sulphate aerosol geoengineering remains. One may fit exponential functions to these points. For termination, we assume the following form:

$$\frac{dy}{dt} = -by, \tag{5.4}$$

where -b (b>0) represents the rate of decrease of aerosol. This has the solution:

$$y = \Lambda_1 e^{\Lambda_2 t} \tag{5.5}$$

The function coefficients that fit the data points have a solution given by a least squares approach, where:

$$\ln(\Lambda_1) = \frac{\sum_{i=1}^{N}(t_i^2 y_i)\sum_{i=1}^{N}(y_i \ln_i) - \sum_{i=1}^{N}(t_i y_i)\sum_{i=1}^{N}(t_i y_i \ln y_i)}{\sum_{i=1}^{N} y_i \sum_{i=1}^{N}(t_i^2 y_i) - (\sum_{i=1}^{N} t_i y_i)^2} \tag{5.6}$$

$$\Lambda_2 = \frac{\sum_{i=1}^{N} y_i \sum_{i=1}^{N}(t_i y_i \ln_i) - \sum_{i=1}^{N}(t_i y_i)\sum_{i=1}^{N}(y_i \ln y_i)}{\sum_{i=1}^{N} y_i \sum_{i=1}^{N}(t_i^2 y_i) - (\sum_{i=1}^{N} t_i y_i)^2} \tag{5.7}$$

yielding values of $\Lambda_1 = 4.94$ and $\Lambda_2 = -0.076$.

Onset of geoengineering has a slightly different form, of

$$\frac{dy}{dt} = a - by \tag{5.8}$$

where -b (b>0) is as above, and a corresponds to the injection rate (independent of any previous level of stratospheric sulphate aerosol). The has the solution:

$$y = \Lambda_0 + \Lambda_1 e^{-\Lambda_2 t} \tag{5.9}$$

Notably for the onset form, one requires an initial guess based on initial guess parameters input into numerical techniques, such as the Levenberg-Marquardt algorithm. However, an analytical solution can be given. Defining:

$$f(t_j) = y(t_0 + jh) - y(t_0 + jh - h) \tag{5.10}$$

then it can be seen that

$$f(t_j) = ke^{\Lambda_2(t_j)} \tag{5.11}$$

where

$$k = \Lambda_1 e^{\Lambda_2 t_0}(1 - e^{-\Lambda_2 h}). \tag{5.12}$$

And definining $g = f^2$

$$g(t) = me^{nt} \tag{5.13}$$

Therefore, one may perform least squares on the function g, to obtain m and n, and then one may obtain Λ_1 and Λ_2 as:

$$\Lambda_1 = \frac{(n)^{1/2}}{e^{\Lambda_2 t_0}(1e^{\Lambda_2 h})} \tag{5.14}$$

$$\Lambda_2 = n \tag{5.15}$$

and using $\Lambda_0 = -\Lambda_1$, $\Lambda_0 = 4.4$, $\Lambda_1 = -4.4$, $\Lambda_2 = -0.051$ are obtained. The least square estimates along with the outputted values are shown in figure 5.11. The difference in rates ($0.076/0.051 \approx 1.5$) is consistent with the difference in the α values, indicating a strong dependence of these variables on the stratospheric aerosol loading.

It is likely that other possible factors also influence the climate response, such as sea ice decline and dynamics. Over time, whilst the G4 scenario stabilises *relative* to the RCP4.5 scenario, overall temperatures are still increasing. Thus when a termination occurs, the climate will be in a slightly warmer state, with slightly less sea ice.

Sea ice plays an important role in heat transfer between the atmosphere and ocean, acting to a certain extent as a blanket prohibiting transfer between the atmosphere and ocean, as well as possessing substantially higher albedo than the ocean surface itself. It is possible that lower sea ice amounts in the termination phase permit greater absorption of incoming solar energy into the climate system, and also greater release of energy into the atmosphere.

Another possible cause is change to the ocean, and in particular ocean dynamics. Changes in the Atlantic Meridional Overturning Circulation (AMOC) have followed increased stratospheric sulphate aerosol loadings. As noted in chapter 2, Stenchikov et al. (2009) analysed the ocean response to simulations of the Pinatubo and Tambora eruptions in the GFDL-CM2.1 atmosphere-ocean model, and found increases of around 1 and 2 Sverdrups following Pinatubo and Tambora, respectively. Differences in changes to the AMOC from onset and termination are therefore possible.

Localised warming south of Greenland has been associated with strengthening of the AMOC (Schaller et al., 2014), whilst increased sea ice has been posited to prevent convection in the North Atlantic and therefore reduce the strength of the AMOC (Li et al., 2005). Therefore reductions in the sea ice during the termination period compared to the onset would suggest that this contributes to a generally warmer climate, although it is still unclear how this would influence substantially the much larger *rate* of temperature change that is experienced in the termination scenario, although the precise mechanisms contributing to the response are considered beyond the scope of this chapter. Nonetheless, these results suggest that a future terminated geoengineering programme is likely to be more severe in magnitude to similar aerosol injections such as from volcanic eruptions in the present climate.

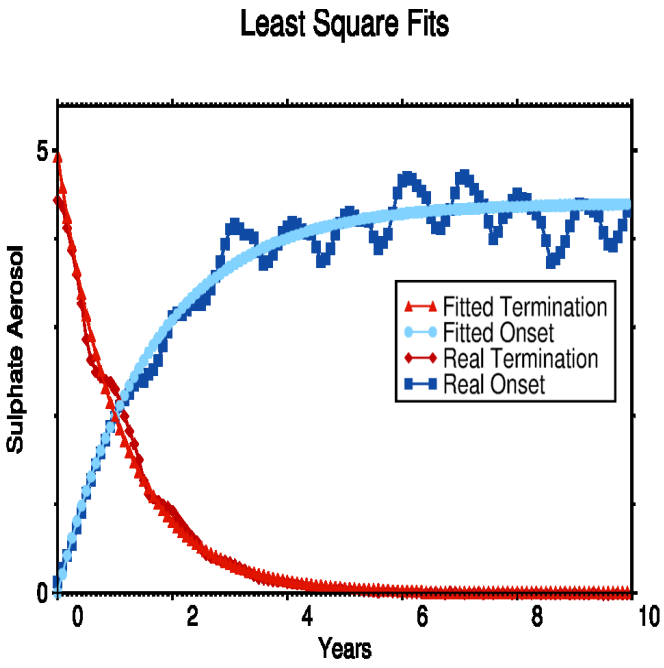

Figure 5.11: Globally averaged sulphate aerosol in the entire atmosphere during the onset and termination periods.

5.4 Discussion and Conclusions

Simulations of stratospheric aerosol geoengineering were performed, using the UM-CLASSIC configuration of HadGEM2 in the high top model. Three simulations of a 'modified G4' experiment, G4mod, were performed using the RCP4.5 scenario for taking anomalies. RCP4.5 scenarios simulated values for the diagnostics explored well within the expected range from other previous modelling studies. The three geoengineering simulations showed rapid reductions in global average temperature following the onset of geoengineering, keeping temperatures anomalously lower than their RCP4.5. counterparts, until a termination of geoengineering was simulated in which global average temperatures rapidly returned to their RCP4.5 counterparts within approximately a decade.

Analysis focused on temperature, precipitation and sea ice. These diagnostics were focused on to complement the study of Jones et al. (2013), whilst NPP was ignored due to the lack of reliability found in that study. Bulk features were shown to be largely radiative driven . Global averaged precipitation decreased during the

onset of sulphate aerosol geoengineering, whilst decreased in termination as a direct result of the changes in temperature. All variables in all simulations show more intense responses to the termination effect with the exception of one sea ice in one simulation.

One would expect that, all else equal, temperature is negatively correlated with stratospheric sulphate aerosol loading. Therefore, one could expect differences in climate response to be differences in amount and rates of change of stratospheric sulphate aerosol. Global average plots were given, and exponential functions were fitted using least squares to the data points. The values of the rates were shown to be consistent with differences in in the α values, ahd hence, the climatic response was consistent with the differing aerosol (and hence incoming shortwave radiation) amounts.

The simulations suggest one may expect termination to be more severe than an onset and perhaps more severe than the large and rapid drop in temperatures due to volcanic eruptions. However, another factor in these simulations is likely to be the background increase due to carbon dioxide. Whilst Jones et al. (2013) define their nondimensionless termination factor as being simply the temperature increase over the ten year period following termination of sulphate aerosol geoengineering and compare this rate with the RCP4.5 rate, there is still *increase* over this period.

This increase in carbon dioxide also increases during the onset, acting as a break or 'damper' on the rates of change of temperature experience during onset. One may consider the need to define a modified α therefore. Whilst nonlinearities in internal dynamics may mean anomalies in the rate of change are not additive such that the rate of change in geoengineered climate with increasing carbon dioxide is not the same as the rate of change in a geoengineered climate added to the rate of change with increasing carbon dioxide, analysing these are still likely to be informative from a physical perspective.

There are numerous caveats and extensions to the work therefore. Ideally, the experiment would be conducted from a control scenario, and an instant lowering of the simulated solar constant with a corresponding instant increase in the solar constant

at a later date. However, these simulations take advantage of the GeoMIP scenarios, and future work involves exploring whether the response seen here is consistent across all models simulating the GeoMIP G4 scenario. Whilst many models contributing to GeoMIP were shown in chapter three, to be insufficient in reproducing the Northern Hemisphere winter dynamical response to volcanic eruptions, and whilst the signal to noise is lower in the standard G4 experiment, one might suspect there is still substantial useful information from performing an extended analysis of all models contributing simulations to G4.

Chapter 6

Conclusions and Further Work

6.1 Summary

This thesis has focused upon the impact of stratospheric aerosols on the climate system. Initially focusing on sulphate aerosol geoengineering, the first chapter brought to light the suggestion of stratospheric aerosol geoengineering as a way to ameliorate some of the effects of climate change. The current state of knowledge of the effects of stratospheric aerosol geoengineering as discerned from modelling studies were discussed, as well as their caveats and uncertainties. The chapter noted that many modelling studies have lacked realistic representation of aerosols as well as discussing the difficulties of verifying such studies - such as verification through observations such as that done to improve weather forecasting models or climate model simulations occuring over the historical period.

Palmer et al. (2008) noted that many models have common deficiencies, as well as offering the idea that understanding how the models perform on weather prediction where observations exist can offer constraints upon model predictions out into the future where no observations exist. Similar thinking of seeking observational constraints guided this thesis after an initial survey of geoengineering studies. Volcanic eruptions represent the closest natural analogue to stratospheric sulphate aerosol geoengineering. Accordingly, the next chapter sought to understand the effects of volcanic eruptions and how well models simulate their effects on the climate system.

In chapter three all available and suitable models on the CMIP5 archive (which represent the most state-of-the-art models used for many predictions in the latest IPCC report), at the time of April 2013, were analysed for their radiative and dynamical responses with a particular focus on their ability to reproduce a major observed response to volcanic eruptions: namely an increase in the NAO. Models were shown to have differences in incoming solar radiation based on the choice of optical depth dataset they employed and also if they injected aerosol, although agreement improved for the later eruptions where improved observations of volcanic eruptions provided better constraints on the inputs to the datasets being used. Stratospheric temperature anomalies were often large when compared to the ERA40 dataset.

Despite substantial increases in equatorial stratospheric temperatures, models failed to achieve the observed increase in the NAO following volcanic eruptions. One possible explanation offered as to why models did not reproduce the observed response was tested; namely, that of sufficient representation of the NAO itself independent of volcanic eruptions. The leading empirical orthogonal functions were calcuated for all models and the NOAA's 20th Century reanalysis version 2 and general agreement was found, contradicting the hypothesis that poor representation of the NAO may be the cause of the disparity between observations and simulations. Other explanations, such as variability and the influence of ENSO and the QBO upon the NAO, were explored, but were found unsuitable to be explanations as to the discrepancy between observations and the models tested. Analysis of climatological stratospheric winds in models and observations indicated that all models show considerably less variability in high-latitude stratospheric winds than observed, suggesting a stable polar vortex and more resistance to changes from external forcings.

The results align with that of Fyfe et al. (2013) who performed a more bulk analysis of more CMIP5 models than were analysed in chapter 3 and their response to many external forcings. Although their paper did not go into the same level of detail for volcanic eruptions, they analyse the multimodel average NAO response to volcanic eruptions and conclude there is no simulated increase of the NAO to volcanic eruptions. The study brought into focus the reliability of models for geoengineering

studies and suggested further research on volcanic eruptions before geoengineering simulations were to be performed.

In chapter four, the response of two versions of HadGEM2 with 'standard' and increased vertical resolution - but were otherwise identical - as well as simulations with a changed aerosol profile in the increased vertical resolution version of HadGEM2 were set-up, performed and analysed for the changes on the atmospheric circulation following the Mount Pinatubo eruption of 1991. This represented the first study to show the importance of stratospheric resolution and explore the mechanisms involved using the transformed Eulerian mean framework in a successful simulation of volcanic eruptions that reproduced all of the major observed features of volcanic eruptions - and sometimes exceeded them in magnitude. Improved representation of stratospheric dynamics appears core to simulating the observed changes following volcanic eruptions, and this study opens up the possibility of many other possible pieces of research.

The volcanic aerosol causes reductions in tropical tropospheric temperature as expected. Before wintertime, the presence of volcanic aerosol enhances residual mean meridional circulation in the tropical stratosphere. During wintertime, the period of major stratosphere-troposphere coupling, temperature gradients due to the volcanic aerosol alter the propagation of planetary waves emanating from the troposphere in nearly identical ways to that observed due to solar cycles which reverse the effect on the residual mean meridional circulation. This causes substantial stratospheric polar cooling and a strengthened vortex. This signal propagates to the surface, which alters the circulation and results in the Eurasian warming following volcanic eruptions. Importantly, the L38 simulations were useful in demonstrating that the response is not *purely* a temperature gradient and thermal wind shear response as has been quoted in the literature before (e.g. Robock 2000) because the area of the largest anomalous temperature gradient in these simulations, and in observations, is in the tropics and subtropics.

Whilst the magnitude of the Pinatubo eruption was reproduced in the first winter, the results over the second winter were not as large - consistent with the mechanism

seen. This disparity may be due to enhancing of the observed signal due to variability (Stenchikov et al. 2002) and the 'true' signal of Pinatubo may be more similar to anomalies seen over a longer time period (e.g. Shindell et al., 2004) or it could be that the model's internal dynamics (planetary wave propagation, residual mean meridional circulation, and so on) may not respond strongly enough to a stratospheric temperature perturbation. Nevertheless, these simulations represented the first marked and clear response to volcanic eruptions and demonstrate the importance of stratospheric dynamics in acheiving this response.

In chapter five, simulations of the RCP4.5 emissions scenario and separately stratospheric aerosol geoengineering on this scenario were performed. The study implemented the UM-CLASSIC configuration of HadGEM2-L60 - the choice of model informed by chapter four. Analysis of changes to surface temperature, sea ice and precipitation were explored in the RCP4.5 scenarios and they demonstrated good consistency with other studies. The study then focused upon the changes during the ten years following the immediate onset and termination of geoengineering - it was shown that global average temperatures and precipitation change at a more rapid rate during termination than during onset for all ensembles, with sea ice demonstrating the same features for two of the three ensembles, and the reverse for one of the three. The results indicated that the changes experienced during volcanic eruptions from rapid lowering in temperatures may not be a useful indicator of the changes that one may experience given the different gradients between onset and termination - suggesting that termination could have potentially severe impacts upon society.

6.2 Further Work - Extension of the Thesis

There are many further studies that both remain in volcanic eruptions and goengineering in general as well as stemming from this thesis. Climate models still need assessment on their ability to capture other main features following volcanic eruptions. Whilst it is not guaranteed that the Northern Hemisphere dynamical changes observed following volcanic eruptions may arise in a geoengineering scheme (such as

if a geoengineering scheme sought only to inject in Arctic region of the stratosphere, or injection at numerous points to yield aerosol with a much more equally spread out profile over all latitudes) many other important features need to be verified.

With improved simulations of the volcanic response in HadGEM2-L60 as well as observations from ERA40 and other datasets, one may analyse changes in storm tracks, and dynamically induced changes in precipitation and soil moisture over the European region following large tropical volcanic eruptions. One would expect that the changes in the NAO would alter the path of the storm tracks, and shift precipitation over Europe northwards, causing decreases in precipitation in the Southern European regions, and increases in Northern Europe. However, this area remains unexplored to date.

One consideration regarding multi-model performance is the extension of the study of Haywood et al. (2013), who explored the impact of volcanic eruptions upon Sahelian rainfall following volcanic eruptions in observations and the HadGEM2 model, to all CMIP5 models to assess robustness of the impacts across models. Another CMIP5 comparison that would aid and underpin understanding of geoengineering's effects upon the climate is to compare the simulated changes of the models in sea ice following volcanic eruptions over the historical period with that of the observed. It is in general seen (and has been discussed in this thesis) that global average sea ice amounts are expected and simulated to decrease following sulphate aerosol geoengineering. The amounts, however, are unclear. A complementary study would be to assess the response of sea ice to volcanic eruptions in the CMIP5 archive and compare them to observations. NOAA's 20th Century Reanalysis dataset (Version 2) would provide a suitable dataset - sea ice concentrations in the dataset are direct observations and not reanalysis model simulations. Understanding whether models in general overestimate or underestimate the changes following volcanic eruptions, and whether it is due to model dynamics or more due to radiative effects, and so on, would provide information that would aid interpretation of geoengineering simulations that have at least a part focus on sea ice changes during geoengineering.

There is a substantial focus on Northern Hemispheric dynamical changes following volcanic eruptions (e.g. Stenchikov et al., 2002., Stenchikov et al., 2004, Stenchikov et al., 2006, Graf et al. 2007, Robock et al., 2008, Thomas et al., 2009a, Thomas et al., 2009b, Driscoll et al., 2012) compared to Southern Hemispheric dynamics (indeed, the author is only aware of Robock et al., 2007 and Karpechko et al., 2010), and the impacts of volcanic eruptions upon Southern Hemisphere dynamics, both simulated and observed, remain unclear from these studies. Analysis of Southern Hemispheric changes in CMIP5 models and the simulations performed in this thesis remains a study of interest likely to be conducted, and the recent release of the ERA-INTERIM dataset would likely yield increased accuracy over datasets previously used in their analysis of Southern Hemispheric changes following volcanic eruptions. This is especially important given the comparative lack of observations in the Southern Hemisphere compared to the Northern Hemisphere.

It is still not clear if the Earth is more or less sensitive, in terms of global average temperature reductions to volcanic forcing compared to simulations. Whilst it has been noted in this thesis that CMIP5 models appear to overestimate the global average temperature reduction to volcanic eruptions, Canty et al. (2013) even suggest that the attributed observed cooling due to Pinatubo, when all other influences are factored out, may be half of what is has previously been estimated. The methodology in their analysis has, however, been heavily disputed (Alan Robock, *personal communIcation*, Piers Forster, *personal communcation*). Santer et al. (2014) analysed the volcanic contribution to recent changes in the tropospheric warming rate since 1998, and suggest neither of these, and that there may actually be more reasonable agreement between modelled and observed anomalies of global average temperature.

A complementary study to aid understanding on the true difference would implement the HadGEM2-L60 model, which has shown a more realistic representation of regional temperature response to volcanic eruptions in this thesis. Quantification of the adjustments to volcanic forcing and comparison to adjustments with a 2 x CO2 forcing using fixed SSTs at climatology or an AMIP run would help isolate part of the simulated response which would then inform back to atmosphere-ocean simulations.

6.3 Further Work - Geoengineering Studies

Whilst it has been shown that geoengineering can reduce global average temperature and precipitation (although not-uniformally) back to pre-industrial levels (e.g. Robock et al., 2008, Rasch et al., 2008, Jones et al., 2010, Ammann et al., 2010, Kravitz et al., 2013), a lot less research has been done on the exit strategy following geoengineering. Moreover, not only have previous modelling studies focused more on the impacts that geoengineering may have on the climate during continuous injection, but (as with climate change scenarios in general), they have also more commonly assessed the effects of geoengineering upon monthly means, long term averages, and so on.

Despite this, it is known that damage often occurs from the extreme weather events at the tails of the distribution (e.g. Pall et al., 2011, Shepherd et al., 2013). The relative lack of extreme weather studies is likely due to most climate models not typically being able to resolve the weather systems associated with extreme weather events, as well as the lack of sufficiently long observational datasets to easily understand extremes events in the climate system. However, a recent report compiled by Risk Management Solutions, the UK Meteorological Office and the Chronic Poverty Advisory Network has underlined the importance of extreme weather events, describing extreme weather events from climate change as arguably the most important cause of impoverishment for many nations - able to cancel progress on poverty reduction. There is still uncertainty in understanding where extreme weather disaster areas are most concentrated (Shepherd et al., 2013).

To better understand the impacts of geoengineering upon extreme events in climate, thousands of ensembles of a high-resolution global atmosphere model, forced by Sea Surface Temperatures (SSTs) and Sea Ice Fractions (SIFs), would be performed. Initially, simulations would be performed of the historical period, taking in SSTs and SIFs from all models in the CMIP5 archive. Comparison against historical observations would be performed as a way of validation and discovering any necessary bias correction that would need be applied. SSTs and SIFs from the GeoMIP project would then be taken and used to power atmosphere only simulations. This would

yield sufficient resolution and ensemble size to capture extreme weather events. To compare the change in extreme weather events to the geoengineered scenario, simulations would also be performed for the GeoMIP baseline scenarios (those without geoengineering) also. This would allow a baseline with which to compare the change in extreme weather events both during geoengineering and during geoengineering termination to otherwise identical but non-geoengineered simulations during the same time period.

Such work would use the climateprediction.net and BOINC distributed computing platform to run an atmosphere only model over the whole globe, powered by the SSTs and SIFs. The current atmosphere only model that exists is HadAM3P. This model has been developed by the UK Meteorological Office and is based upon the atmospheric component of the HadCM3 mode (Pope et al., 2000; Gordon et al., 2000) with some improvements to the sulphur cycle and cloud parametrisations (Jones et al., 2004).

As an extension to the study, one could consider that geoengineering is an unacceptable risk if the damage from termination is greater than the damage reduced by geoengineering over the period of time it is implemented as opposed to assessing damage reduced only during the geoengineered time period without termination as is done in Kravitz et al. (2014). They assess the damage that occurs from simulations of four times current carbon dioxide levels as well as the damage in a four times carbon dioxide world with geoengineering at a level to offset the radiative forcing by the increased carbon dioxide levels. Their damage function is a function of temperature and precipitation, copying that used in previous studies.

An identical damage function could be implemented to assess damage offsetted during geoengineering with the damage experienced during termination of geoengineering, from thousands of simulations from climateprediction.net scenarios - ranging from large amounts of geoengineering with a large termination to no geoengineering with no termination. The acceptable level of damage from termination may then be calculated for the damage that geoengineering would offset during its continuous implementation. One may then obtain an adjusted optimal level (a termination

accounted risk level) of geoengineering that would be permissible in light of the termination threat (despite if slightly higher geoengineering levels were optimal over only the geoengineering without termination phase). It is arguable that nonlinear feedbacks are more likely to occur with an intense rate of change as opposed to a slower equivalent increase in temperature, hence performing analysis of equivalent damage ameliorated during geoengineering and occurring during termination would likely provide an strong upper limit on the maximum amount of geoengineering.

Palmer et al. (2008) explored ideas based around seamless prediction to compliment interpretation of future CMIP projections of climate impacts. Given common model deficiencies, model agreement is not necessarily a proof of greater accuracy of projections. Unlike climate projections, seasonal forecasts may be verified against observational data. Palmer et al. (2008) analysed seasonal forecasts from the IPCC class multimodel ensemble project DEMETER (see Palmer et al., 2004, for more details) for their ability to forecast weather on seasonal timescales. The DEMETER project consisted of ensembles of IPCC class coupled atmosphere-ocean climate models performing forecasts over the 1981-2000 period, initiated 4 times every year. Palmer et al. (2008) argue that future climate projections may therefore be calibrated to incorporate model deficiencies discovered from their forecasts. The study shows substantial differences between their uncalibrated and calibrated projections for a range of greenhouse gas emissions scenarios - making the case that normal uncalibrated simulations may potentially yield substantial errors. Despite this, analysis of GeoMIP models has so far focused only on the uncalibrated data - highlighting that uncertainty around the effects of geoengineering could be substantial. Given the generality of approach, the technique could be applied to geoengineering and volcanic eruptions, understanding how well models simulate weather following volcanic eruptions to calibrate future simulations of volcanic eruptions and geoengineering.

Further extensions from this work and for geoengineering in general exist. Ricke et al. (2013) incorporated game theory into their climate simulations to allow regions to 'decide' upon the preferred amount of geoengineering (that level which would minimise the damage to their region) and then enable coalition building to decide

upon the global average level of geoengineering (those regions which desired a similar level of geoengineering would unite). It was shown in this setting that whilst it would be unlikely for a single small region to unilaterally implement geoengineering, strategic incentives are created that promote coalitions to form that are as small as possible but sufficiently powerful to implement geoengineering - creating many 'actors'.

There are numerous situations where large numbers of small actors able to decide upon a certain action can lead to suboptimal outcomes. Bostrom et al. (2013) introduce the unilateralist's curse. Here, individual agents (or groups) each have a valuation of the value of an action. However, their estimate of the value is unlikely to be exactly accurate. Bostrom et al. (2013) introduce examples to demonstrate this. They consider a group of people all aware of a surprise birthday party. Each agent will have an estimate of the value of telling the agent whose birthday party it is of their surprise birthday party in advance. They may of course act unilaterally, and therefore destroy the outcome for all other agents. The larger the number of agents, the greater the chance that one will possess an estimate so inaccurate as to perceive the action as positive. For even five agents, it is shown that the probability of such actions proceeding is likely to be unacceptably high.

It is therefore possible to suspect that, given Ricke et al. (2013) simulate many independent coallitions can form, that the likelihood of one coallition (recall sufficiently powerful to act unilaterally) estimating the optimal amount of geoengineering highly incorrectly is large. Despite this, Ricke et al. (2013) only perform simulations with regions having an exactly accurate estimate of the damage and their resulting desired outcome. One may improve the realism of the study by incorporating random error drawn from a normal distribution in the estimates of the desired level of geoengineering for each region and exploring the climate impacts that arise (and indeed if termination occurs from more complex interactions between regions).

Large quantities of methane are stored in Arctic permafrost (soil at or below the freezing point of water) and clathrates (solid compounds in which large amounts of methane are trapped). Whilst methane is known to be emitted naturally into the atmosphere (e.g. Walter et al., 2006) it has been proposed that increased temperatures

due to increased carbon dioxide levels may lead to rapid release of methane as melting of permafrost occurs. From analysis of paleoclimate data Vaks et al. (2013) suggest that substantial permafrost melting may occur at a temperature approximately 1.5 K higher than pre-industrial times. Such an instant release of large quantities of methane could raise global average temperatures considerably. Here, methane itself may be considered the 'termination' risk. Methane has a much shorter residence time than carbon dioxide (Stocker et al., 2013), and temperatures would return to normal levels within a decade or two, meaning that geoengineering could be implemented on a short term basis to reduce rapid temperature rise.

Simulations could be performed with simple models that have been used in simulations for short lived climate pollutants (e.g. Bowerman et al., 2011, Bowerman et al., 2013) where methane release could be imposed based upon estimates of methane stores that would be released or with global climate models that represent permafrost melt and methane release to increases in temperature. The efficacy of geoengineering to reduce the damage experienced from a large rapid release of methane into the atmosphere could then be explored.

Still more work on volcanic eruptions and geongineering remains. Whilst all of this work remains outside of the scope of the thesis, it can be seen that many new studies on volcanoes and geoengineering remain and some have been, in part, inspired by the findings in this thesis. It is intended that some of the studies will be pursued, influenced and benefitting from work conducted in this thesis.

In the introduction, the potential for substantial uncertainty of the results of geoengineering was noted. This was due to two parts - inherent model uncertainty, and sufficient representation of model processes (such as implementation of aerosols as opposed to a reduction of the solar constant). In light of this uncertainty, as opposed to doing only geoengineering simulations, the thesis addressed these problems by focusing substantially on understanding the inherent model uncertainty. First, this was approached by constraining model simulations to observations (namely volcanic eruptions), and then by identifying a model with more suitable representation of

the dynamical response to sulphate aerosol injection via volcanic eruptions. Following substantial work on identifying a suitable model and understanding underlying mechanisms, this model was then used to inform on what has been postulated to be a major risk from sulphate aerosol geoengineering (the termination problem) and the differences between the termination and onset of sulphate aerosol geoengineering.

‘

Bibliography

Adams, B. J., M. E. Mann, and C. M. Ammann, 2003, Proxy evidence for an El Niño-like response to volcanic forcing, Nature, 426, 274–278.

Akbari, H, H Damon Matthews, D. Seto., 2012, The long-term effect of increasing the albedo of urban areas. Environmental Research Letters 7:2, 024004.

Allen, M. R., and W. J. Ingram, 2002, Constraints on future changes in the hydrological cycle. Nature, 419, 224228.

Ambaum, M. H. P., B. J. Hoskins, and D. B. Stephenson, 2001, Arctic Oscillation or North Atlantic Oscillation?, J. Climate, 14, 34953507.

Ammann, C. M., W. M. Washington, G. A. Meehl, L. Buja, and H. Teng, 2010, Climate engineering through artificial enhancement of natural forcings: Magnitudes and implied consequences, J. Geophys. Res., 115, D22109

Ammann, C. M., G. A. Meehl, W. M. Washington, and C. S. Zender, 2003, A monthly and latitudinally varying volcanic forcing dataset in simulations of 20th century climate, Geophys. Res. Lett., 30, 1657

Ammann, C. M., F. Joos, D. S. Schimel, B.L. Otto-Bliesner, and R.A. Tomas, 2007, Solar influence on climate during the past millennium - results from transient simulations with the NCAR Climate System Model, Proceedings of the National Academy of Sciences of the United States, 104, 3713-3718.

Anchukaitis, K. J., B. M. Buckley, E. R. Cook, B. I. Cook, R. D. D'Arrigo, and C. M. Ammann 2010, Influence of volcanic eruptions on the climate of the asian monsoon region, Geophys. Res. Lett., 37(22)

Anderson, K., Bows A., 2011, Beyond dangerous climate change: emission: scenarios for a new world. Phil. Trans. R. Soc. A 369, 2044

Andres, R. J., and A. D. Kasgnoc, 1998, A time-averaged inventory of subaerial volcanic sulfur emissions, J. Geophys. Res., 103 (D19), 25,25125,261

Andrews, D., J. Holton, and C. Leovy, 1987, Middle Atmosphere Dynamics, Academic Pr, Orlando, Fla.

Andronova, N. G., E. V. Rozanov, F. Yang, M. E. Schlesinger, and G. L. Stenchikov, 1999, Radiative forcing by volcanic aerosols from 1850 to 1994, J. Geophys. Res., 104, (D14), 16,807–16,826

Aquila, V., L. D. Oman, R. S. Stolarski, P. R. Colarco, and P. A. Newman, 2012, Dispersion of the volcanic sulfate cloud from a Mount Pinatubo-like eruption, J. Geophys. Res.

Aquila, V., L. D. Oman, R. Stolarski, A. R. Douglass, and P. A. Newman, 2013, The response of ozone and nitrogen dioxide to the eruption of Mt. Pinatubo at southern and northern midlatitudes, J. Atmos. Sci., 70(3), 894900

Bala G., Duffy P. B., Taylor K. E., 2008, Impact of geoengineering schemes on the global hydrological cycle, Proceedings of the National Academy of Sciences, 105(22):7664-69

Baldwin, M. P., and T. J. Dunkerton, 1999, Propagation of the Arctic Oscillation from the stratosphere to the troposphere, J. Geophys. Res., 104 (D24), 30,937–30,946

Baldwin, M. P., and T. J. Dunkerton, 2001, Stratospheric harbingers of anomalous weather regimes, Science, 294 (5542), 581–584

Baldwin, M.P., L.J. Gray, T.J. Dunkerton, K. Hamilton, P.H. Haynes, W.J. Randel, J.R. Holton, M.J. Alexander, I. Hirota, T. Horinouchi, D.B.A. Jones, J.S. Kinnersley, C. Marquardt, K. Sato, and M. Takahashi, 2001, The Quasi-Biennial Oscillation, Reviews of Geophysics, 39, 179- 229, 2001.

Banda, N., Krol, M., van Weele, M., van Noije, T., and Rockmann, T., 2013, Analysis of global methane changes after the 1991 Pinatubo volcanic eruption, Atmos. Chem. Phys., 13, 2267-2281

Ban-Weiss, G. A., K., Caldeira, 2010, Geoengineering as an optimization problem, Environmental Research Letters, 5, 034009, (9pp)

Baran, A. J., and J. S. Foot, 1994, New application of the operational sounder HIRS in determining a climatology of sulphuric acid aerosol from the pinatubo eruption, J. Geophys. Res., 99 (D12), 25,673–25,679

Barath, F. T., M. C. Chavez, R. E. Cofield, D. A. Flower, M. A. Frerking, M. B. Gram, W. M. Harris, J. R. Holden, R. F. Jarnot, W. G. Kloezeman, G. J. Klose, G. K. Lau, M. S. Loo, B. J. Maddison, R. J. Mattauch, R. P. McKinney, G. G. Peckham, H. G. Pickett, G. Siebes, F. S. Soltis, R. A. Suttie, J. A. Tarsala, J. W. Waters, W. J. Wilson, 1993, The Upper Atmosphere Research Satellite Microwave Limb Sounder instrument. J. Geophys. Res., 98, 10 75110 762.

Barnes, J. E., and D. J. Hofmann, 1997, Lidar measurements of stratospheric aerosol over Mauna Loa observatory, Geophys. Res. Lett., 24 (15), 1923–1926

Baum, S. D., T. M. Maher, Jr., J. Haqq-Misra, 2013, Double catastrophe: Intermittent stratospheric geoengineering induced by societal collapse. Environment, Systems and Decisions, vol. 33, no. 1, pg 168-180

Battisti, D. S., Naylor, R. L., 2009, Historical Warnings of Future Food Insecurity with Unprecedented Seasonal Heat. Science, 323, 240-244.

Bautista, C. B., 1996, The Mount Pinatubo disaster and the people of Central Luzon, Fire and Mud, edited by C. G. Newhall and R. S. Punongbayan. Quezon City: Philippine Institute of Volcanology and Seismology; Seattle: University of Washington Press. Edition available online, at: http://pubs.usgs.gov/pinatubo/index.html

Benduhn, F., and M. G. Lawrence, 2013, An investigation of the role of sedimentation for stratospheric solar radiation management, J. Geophys. Res. Atmos., 118, 79057921

Berdahl, M., A. Robock, D. Ji, J. C. Moore, A. Jones, B. Kravitz, and S. Watanabe, 2014, Arctic cryosphere response in the Geoengineering Model Intercomparison Project (GeoMIP) G3 and G4 scenarios. J. Geophys. Res. Atmos., 119, 1308-1321

Black, R. X., 2002, Stratospheric Forcing of Surface Climate in the Arctic Oscillation, Journal of Climate, 15 (3), 268–277

Bluth, G. J. S., Doiron, S. D., Schnetzler, C. C., Krueger, A. J., Walter, L. S., 1992, Global tracking of the SO2 clouds from the June, 1991 Mount Pinatubo eruptions, Geophysical Research Letters, Volume 19, Issue 2, pages 151154

Bluth, G. J. S., W. I. Rose, I. E. Sprod, and A. J. Krueger, 1997, Stratospheric loading of sulfur from explosive volcanic eruptions, J. of Geology, 105 (6), 671684.

Bork, N., Kurtn, T., Enghoff, M. B., Pedersen, J. O. P., Mikkelsen, K. V., and Svensmark, H., 2012, Structures and reaction rates of the gaseous oxidation of SO2 by an O3(H2O)0-5 cluster a density functional theory investigation, Atmos. Chem. Phys., 12, 3639-3652

Borovko, I. V. , V. N. Krupchatnikov., 2009, The influence of stratospheric polar vortex dynamics upon lower tropospheric circulation. Numerical Analysis and Applications, 118-130

Bostrom, N., Sandberg, A., and Douglas, T., 2013, The Unilateralist's Curse: The Case for a Principle of Conformity. Working Paper. Retrieved August 20, 2014, available at www.nickbostrom.com/papers/unilateralist.pdf

Bourassa, A. E., A. Robock, W. J. Randel, T. Deshler, L. A. Rieger, N. D. Lloyd, E. J. Llewellyn, and D. A. Degenstein, 2012: Large volcanic aerosol load in the stratosphere linked to Asian monsoon transport. Science, 337, 78-81

Bowerman, N. H. A., Frame, D. J., Huntingford, C., Lowe, J. A. and Allen, M. R., 2011, Cumulative carbon emissions, emissions floors and short-term rates of warming: Implications for policy. Phil. Trans. R. Soc. A 369, 4566

Bowerman NHA, Frame DJ, Huntingford C, Lowe JA, Smith SM, Allen MR., 2013, The role of short-lived climate pollutants in meeting temperature goals. Nat. Clim. Change 3:102124

Brewer, A. W., 1949, Evidence for a world circulation provided by the measurements of helium and water vapour distribution in the stratosphere. Quarterly Journal of the Royal Meteorology Society, 75: 351363

Brovkin, V., Petoukhov, V., Claussen, M., Bauer, E., Archer, D., Jaeger, C., 2009, Geoengineering climate by stratospheric sulfur injections: Earth system vulnerability to technological failure, Climatic Change, 92, 243-259

Budyko, M. I., 1977, Climate Changes (Engl. transl.), American Geophysical Union, Washington, DC

Caldeira, K; Wood, L, 2008, Global and Arctic climate engineering: numerical model studies, Philosophical Transactions of the Royal Society A-Mathematical Physical and Engineering Sciences 366 (1882):4039-4056

Calvo, N., M. A. Giorgetta, R. Garcia-Herrera, and E. Manzini, 2009, Nonlinearity of the combined warm ENSO and QBO effects on the Northern Hemisphere polar vortex in MAECHAM5 simulations, J. Geophys. Res., 114 (D13)

Canty, T., Mascioli, N. R., Smarte, M. D., and Salawitch, R. J., 2013, An empirical model of global climate Part 1: A critical evaluation of volcanic cooling, Atmos. Chem. Phys., 13, 3997-4031

Carr, M., 1976, Change in Height of Martian Volcanoes With Time. Geologica Romana v.15 pp.421-422.

Carr, M. H., 1976, The volcanoes of Mars, Sci. Am., 234, pp. 3234

Casadevall, T. J., P. J. Delos Reyes, and D. J. Schneider, 1996, The 1991 Pinatubo eruptions and their effects on aircraft operations, Fire and Mud, edited by C. G. Newhall and R. S. Punongbayan. Quezon City: Philippine Institute of Volcanology and Seismology; Seattle: University of Washington Press. Edition available online, at: http://pubs.usgs.gov/pinatubo/index.html

Chiang, J.C.H., and A.R. Friedman, 2012, Extratropical cooling, interhemispheric thermal gradients, and tropical climate change, Ann. Rev. Earth Planet. Sci., 40, 383412

Christiansen, B., 2008, Volcanic Eruptions, Large-Scale Modes in the Northern Hemisphere, and the El Niño - Southern Oscillation, J. Clim., 21, 910–922.

Chylek, P., J. Li, M. K. Dubey, M. Wang, and G. Lesins, 2011, Observed and model simulated 20th Century Arctic temperature variability: Canadian Earth System Model CanESM2, Atmospheric Chemistry and Physics Discussions, 11 (8), 22,893–22,907

Climate Change 2007: The Physical Science Basis. Contribution of Working Group I to the Fourth Assessment Report of the Intergovernmental Panel on Climate

Change [Solomon, S., D. Qin, M. Manning, Z. Chen, M. Marquis, K.B. Averyt, M.Tignor and H.L. Miller (eds.)]. Cambridge University Press, Cambridge, United Kingdom and New York, NY, USA.

Christensen, M. W., and G. L. Stephens, 2012, Microphysical and macrophysical responses of marine stratocumulus polluted by underlying ships: 2. Impacts of haze on precipitating clouds, J. Geophys. Res., 117, D11203

Chen, Y. C., Christensen, M. W., Xue, L., Sorooshian, A., Stephens, G. L., Rasmussen, R. M., and Seinfeld, J. H.: Occurrence of lower cloud albedo in ship tracks, Atmos. Chem. Phys., 12, 8223-8235

Christensen, M. W., and G. L. Stephens, 2011, Microphysical and macrophysical responses of marine stratocumulus polluted by underlying ships: Evidence of cloud deepening, J. Geophys. Res., 116, D03201

Cole-Dai, J., Volcanoes and climate, Wiley Interdisciplinary Reviews: Climate Change, 1, 824-839

Collins, M., S. F. B. Tett, and C. Cooper, 2001, The internal climate variability of HadCM3, a version of the Hadley Centre coupled model without flux adjustments, Climate Dynamics, 17, 61–81

Collins, W. J., et al., 2011, Development and evaluation of an Earth-System model - HadGEM2, Geoscientific Model Development, 4(4), 1051–1075

Collins, M., Knutti, R., Arblaster, J., J. L. Dufresne, T. F., Friedlingstein, P., X. Gao, W. G., Johns, T., Krinner, G., Shongwe, M., Tebaldi, C., Weaver, A., Wehner, M., 2013, Long-term climate change: projections, commitments and irreversibility, in: Climate Change 2013: The Physical Science Basis. Contribution of Working Group I to the Fifth Assessment Report of the Intergovernmental Panel on Climate Change, edited by: Stocker, T., Qin, D., Plattner, G.-K., Tignor, M., Allen, S., Boschung, J., Nauels, A., Xia, Y., Bex, V., and Midgley, P., Cambridge University Press, Cambridge, UK and New York, NY, USA.

Compo, G. P., et al., 2011, The twentieth century reanalysis project, Q. J. R. Meteorol. Soc., 137(654), 1–28

Cordero, E. and P. M. Forster, 2006: Stratospheric Variability and Trends in Models used for the IPCC AR4. Atmospheric Chemistry and Physics, 6, 5369-5380.

Couce, E., P. J. Irvine, L. J. Gregoire, A. Ridgwell, and E. J. Hendy, 2013, Tropical coral reef habitat in a geoengineered, high-CO2 world, Geophys. Res. Lett., 40, 17991804

Crowley, T., 2000, "Causes of Climate Change Over the Past 1000 Years". Science 289: 270-277

Crumpler, L.S., Aubele, J.C., Senske, D.A., Keddie, S.T., Magee, K.P., Head, J.W., 1997. Volcanoes and centers of volcanism on Venus. In: Bougher, S.W., Hunten, D.M., Phillips, R.J. (Eds.), Venus II: Geology Geophysics, Atmosphere, and Solar Environment. University of Arizona Press, Tucson, pp. 697756.

Crutzen, P. J., 2006, Albedo enhancement by stratospheric sulfur injections: a contribution to resolve a policy dilemma? Clim. Change 77, 211220

Daag, A. S., Bella S. Tubianosa, Christopher G. Newhall, Norman M. Tugol, Dindo Javier, Michael T. Dolan, Perla J. Delos Reyes, Ronaldo A. Arboleda, Ma. Mylene L. Martinez, and Ma. Theresa M. Regalado, 1996, Monitoring sulphur dioxide emission at Mount Pinatubo, Fire and Mud, edited by C. G. Newhall and R. S. Punongbayan. Quezon City: Philippine Institute of Volcanology and Seismology; Seattle: University of Washington Press.

DallAmico, M., Gray, L. J., Rosenlof, K. H., Scaife, A. A., Shine, K. P., and Stott, P. A.: Stratospheric temperature trends: impact of ozone variability and the QBO, Clim. Dynam., 34(23), 381398

Davidson, P., Burgoyne, C., Hunt, H. and Causier, M. 2012 Lifting options for stratospheric aerosol geoengineering: advantages of tethered balloon systems. Phil. Trans. R. Soc. A 370, 42634300

Delworth, T. L., and K. W. Dixon, 2000, Implications of the Recent Trend in the Arctic/North Atlantic Oscillation for the North Atlantic Thermohaline Circulation, Journal of Climate, 13 (21), 3721–3727

Dobson, G. M. B., D. N. Harrison and J. Lawrence, Measurements of the amount of ozone in the earth's atmosphere and its relation to other geophysical conditions, Proc. Roy. Soc., Series A, 122, 456-486, 1929.

Doney, S., Fabry, V.J., Feely, R.A., Kleypas, J.A., 2009, Ocean acidification: the other CO2 problem. Annual Review of Marine Science 1, 169192.

Donner, L. J., et al., 2011, The Dynamical Core, Physical Parameterizations, and Basic Simulation Characteristics of the Atmospheric Component AM3 of the GFDL Global Coupled Model CM3, Journal of Climate, 24 (13), 3484–3519

Driscoll, S., V. Lucarini, Discrepancies in Angular Momentum Conservation and Transfer in Reanalysis Observation Datasets and Couple Model Intercomparison Project 5 (CMIP5) Models. *In advanced state of preparation*

Driscoll, S., A. Bozzo, L. J. Gray, A. Robock, and G. Stenchikov, 2012, Coupled Model Intercomparison Project 5 (CMIP5) simulations of climate following volcanic eruptions. J. Geophys. Res., 117, D17105

Dunkerton, T. J., 1978, On the mean meridional mass motions of the stratosphere and mesosphere, J. Atmos. Sci., 35, 23252333.

Dunkerton, T.J., C.-P.F. Hsu and M.E. McIntyre, 1981, Some Eulerian and Lagrangian diagnostics for a model stratospheric warming. J. Atmos. Sci., 38, 819-843.

Dutton, E. G., and J. R. Christy, 1992, Solar radiative forcing at selected locations and evidence for global lower tropospheric cooling following the eruptions of El Chicho n and Pinatubo, Geophys. Res. Lett., 19, 23132316.

Dutton, E., Greddy, P., Ryan, S. and Deluisi, J.J., 1994, Features and effects of aerosol optical depth observed at Mauna-Loa, Hawaii19821992. Journal of Geophysical ResearchAtmospheres, 99, pp. 82958306.

Efron, B., and R. Tibshirani, 1986, Bootstrap methods for standard errors, confidence intervals, and other measures of statistical accuracy., Stat Sci, 1, 54–75.

Elanskii, N. F., S. G. Zvenigorodskii and S. P. Smyshlyaev, 1987, Dokl. Acad. Nauk SSSR,294, 1077

Ferraro, A. J., Highwood, E. J., Charlton-Perez, A. J., 2014, Weakened tropical circulation and reduced precipitation in response to geoengineering Environ. Res. Lett. 9 014001

Fiedler, G., and L. Wilson, 1975, Volcanoes of the Earth, Moon, and Mars, Elek Sci., London

Fischer, E. M., J. Luterbacher, E. Zorita, S. F. B. Tett, C. Casty, and H. Wanner, 2007, European climate response to tropical volcanic eruptions over the last half millennium, Geophys. Res. Lett., 34, L05707

Forster, P., et al., 2007, Changes in atmospheric constituents and in radiative forcing, in Climate Change 2007: The Physical Science Basis. Contribution of Working Group I to the Fourth Assessment Report of the Intergovernmental Panel on Climate Change, edited by S. Solomon, D. Qin, M. Manning, Z. Chen, M. Marquis, K. Averyt, M. Tignor, and H. Miller, ISBN 978-0-521-88009-1 (pb: 978-0-521-70596-7), Cambridge University Press, Cambridge, United Kingdom and New York, NY, USA.

Fowler, H.J., R.L. Wilby, 2010, Detecting changes in seasonal precipitation extremes using regional climate model projections: implications for managing fluvial flood risk, Water Resources Research, 46, p. W03525

Fujiwara, M., T. Shibata, and M. Hirono, 1982, Lidar observation of a sudden increase of aerosols in the stratosphere caused by volcanic injections, II, Sierra Negra event, J. Atmos. Terr. Phys., 44, 811-818

Fyfe, J.C., K. Von Salzen, J.N.S. Cole and N.P. Gillett, 2013, Surface response to background stratospheric aerosol changes in a coupled atmosphere-ocean model. Geophys. Res. Lett., 40

Gao, C., A. Robock, C. Ammann, 2008, Volcanic forcing of climate over the past 1500 years: An improved ice-core-based index for climate models. J. Geophys. Res., 113, D23111

Gadian, A., 2011, Geoengineering. Atmospheric Science Letters, 12: 161

Garcia-Herrera, R., N. Calvo, R. R. Garcia, and M. A. Giorgetta, 2006, Propagation of ENSO temperature signals into the middle atmosphere: A comparison of two general circulation models and ERA-40 reanalysis data, J. Geophys. Res., 111 (D6)

Garfinkel, C.I., and D.L. Hartmann, 2008, Different ENSO Teleconnections and Their Effects on the Stratospheric Polar Vortex, J. Geophys. Res. Atmos, 113, D18114

Genin, A., B. Lazar, and S. Brenner, 1995, Vertical mixing and coral death in the Red Sea following the eruption of Mount Pinatubo, Nature, 377, 507-510

Gent, P. R., et al., 2011, The Community Climate System Model Version 4, Journal of Climate, 24 (19), 4973–4991

Gerlach, T. M., Henry R. Westrich, and Robert B. Symonds, 1996, Preeruption vapor in magma of the climactic Mount Pinatubo eruption: Source of the giant stratospheric sulphur dioxide cloud, Fire and Mud, edited by C. G. Newhall and R. S. Punongbayan. Quezon City: Philippine Institute of Volcanology and Seismology; Seattle: University of Washington Press. Edition available online, at: http://pubs.usgs.gov/pinatubo/index.html

Gill A. E., 1982, Atmosphere-Ocean Dynamics. Academic Press, 1st edition.

Gleckler, P. J., et al., 2006, Krakatoa lives: The effect of volcanic eruptions on ocean heat content and thermal expansion, Geophys. Res. Lett., 33, L17702

Graf. H.-F., 2011, Two El Nino Types and their Teleconnections with Europe, Geophysical Research Abstracts, Vol. 13, EGU2011-5923

Graf, H.-F., Q. Li, and M. A. Giorgetta, 2007, Volcanic effects on climate: revisiting the mechanisms, Atmospheric Chemistry and Physics, 7 (17), 4503–4511

Graf H-F, D. Zanchettin, 2012, Central Pacific El Nino, the "subtropical bridge" and Eurasian Climate, JGR Atmospheres, 117, (D1)

Grant, J., Fishman, J., Browell, E.V., and others, 1992, Observations of reduced ozone concentrations in the tropical stratosphere after the eruption of Mt. Pinatubo: Geophysical Research Letters, v. 19, p. 1109-1112.

Gray, L. J., Beer, J., Geller, M., Haigh, J. D., Lockwood, M., Matthes, K., Cubasch, U., Fleitmann, D., Harrison, R. G., Hood, L., Luterbacher, J., Meehl, G. A., Shindell, D. T., van Geel, B., White, W., 2010, Solar Influences on Climate. Reiews In Geophysics, 48

Gillett, N. P., Thompson, D. W. J., 2003, Simulation of recent southern hemisphere climate change. Science 302, 273275

Gillett, N. P., J. C. Fyfe, 2013, Annular mode changes in the CMIP5 simulations, Geophysical Research Letters, 40, 6

Gleason, J. F., et al., 1993, Record low global ozone in 1992, Science, 260, 523526.

Goes, M., Keller, K.,Tuana, N., 2011, The economics (or lack thereof) of aerosol geoengineering. Climatic Change 109: 719744.

Gordon, C., C. Cooper, C. A. Senior, H. Banks, J.M. Gregory, T.C. Johns, J.F.B. Mitchell, and R.A.Wood, 2000, The simulation of SST, sea ice extents and ocean heat transports in a version of the Hadley Centre coupled model without flux adjustments, Climate Dynamics, 16, 147-168.

Gornitz, V., S. Lebedeff, and J. Hansen, 1982, Global sea level trend in the past century. Science, 215, 1611-1614

Govindasamy, B., S. Thompson, P. B. Duffy, K. Caldeira, and C. Delire, 2002, Impact of geoengineering schemes on the terrestrial biosphere, Geophys. Res. Lett., 29(22), 2061

Graf, H. F., Q. Li, and M.A. Giorgetta, 2007, Volcanic effects on climate: Revisiting the mechanisms. Atmos. Chem. Phys., 7, 4503-4511

Grant, W. B., Browell, E. V., Long, C. S., Stowe, L. L., Grainger, R. G., and Lambert, A., Use of volcanic aerosols to study the tropical stratospheric reservoir, J. Geophys. Res., 101, 3973 3988, 1996.

Guilyardi, E., 2006, El Niño–mean state–seasonal cycle interactions in a multi-model ensemble, Climate Dynamics, 26, 329–348

Halmer, M. M., 2005, Have volcanoes already passed their zenith influencing the ozone layer? Terra Nova, 17: 500502

Hamilton, C., 2013, Ethical anxieties about geoengineering, in Sandler, Ronald L., (editor), 2013, Ethics and Emerging Technologies, Palgrave Macmillan.

Hansell, A.L., Horwell, C.J., Oppenheimer, C., 2006, The health hazards of volcanoes and geothermal areas, Occupational Environmental Medicine, 63: 149-156.

Hansell, A., Oppenheimer, C., 2004, Health hazards from volcanic gases: a systematic literature review, Archives of Environmental Health, 59(12): 628-639.

Hansell, A.L., 2003, Respiratory effects of volcanic emissions (letter), Occupational and Environmental Medicine, 60, 529-530.

Hansell, A.L., Oppenheimer, C., 2002, Review of health hazards from volcanic gases, Epidemiology, 13(4), Suppl:S188.

Hansen, J., D. Johnson, A. Lacis, S. Lebedeff, P. Lee, D. Rind, and G. Russell, 1981, Climate impact of increasing atmospheric carbon dioxide. Science, 213, 957-966

Hansen, J., M. Sato, R. Ruedy, K. Lo, D. W. Lea, and M. Medina-Elizade, 2006, Global temperature change, Proc. Natl. Acad. Sci. U. S. A., 103, 14,28814,293

Hardiman, S. C., N. Butchart, S. M. Osprey, L. J. Gray, A. C. Bushell, and T. J. Hinton, 2010, The Climatology of the Middle Atmosphere in a Vertically Extended Version of the Met Offices Climate Model. Part I: Mean State. J. Atmos. Sci., 67, 15091525.

Haywood, J. M., et al., 2010, Observations of the eruption of the Sarychev volcano and simulations using the HadGEM2 climate model, J. Geophys. Res., 115, D21212

Haywood, J., Jones, A., Bellouin, N and Stephenson, D., 2013, Asymmetric forcing from stratospheric aerosols impacts Sahelian rainfall, Nature Climate Change

Heckendorn, P. et al., 2009, Impact of geoengineering aerosols on stratospheric temperature and ozone, Environ. Res. Lett., 4, 045108.

Held, I. M., T. L. Delworth, J. Lu, K. Findell, and T. R. Knutson, 2005, Simulation of Sahel drought in the 20th and 21st centuries. Proc. Natl Acad. Sci., 102, 17891-17896

Hess, M., P. Koepke, and I. Schult, 1998, Optical Properties of Aerosols and Clouds: The software package OPAC, Bull. Am. Met. Soc., 79, 831–844.

Hewitt, H. T. et al., 2011, Design and implementation of the infrastructure of HadGEM3: The next-generation Met Office climate modelling system. Geosci. Model Dev. 4, 223 253

Heyward, C., 2013, Situating and Abandoning Geoengineering: A Typology of Five Responses to Dangerous Climate Change, PS: Political Science and Politics, 23-27.

Hines, C. O., 1974, Possible mechanism for production of sun-weather correlations, J. Atmos. Sci., 31(2), 589591.

Hofmann, D. J., S. J. Oltmans, J. M. Harriss, S. Solomon, T. Deshler, and B. J. Johnson, 1992, Observation and possible causes of new ozone depletion in Antarctica in 1991. Nature 359: 283-87.

Holasek, R. E., Self, S., and Woods, A. W., 1996, Satellite observations and interpretation of the 1991 Mount Pinatubo eruption plumes. Journal of Geophysical Research, 100, 8469-8487.

Holton, James R., and Hsiu-Chi Tan, 1980, The Influence of the Equatorial Quasi-Biennial Oscillation on the Global Circulation at 50 mb. J. Atmos. Sci., 37, 22002208.

Holton, J. R., and H. C. Tan, 1982, The quasi-biennial oscillation in the Northern Hemisphere lower stratosphere, J. Meteorol. Soc. Jpn., 60, 140148.

Horwell, C.J. and Baxter, P.J., 2006, The respiratory health hazards of volcanic ash: a review for volcanic risk mitigation. Bulletin of Volcanology 69: 1-24.

Huang J.P., Higuchi K. and Shabbar A., 1998, The relationship between the North Atlantic Oscillation and El-Nino Southern Oscillation, Geophys.Res. Let., 25, 2707-2710.

Hurrell, J. W., and C. Deser, 2009, North Atlantic climate variability: The role of the North Atlantic Oscillation, Journal of Marine Systems, 78(1), 28 – 41

Ineson, S., A. A. Scaife, J. R. Knight, J. C. Manner, N. J. Dunstone, L. J. Gray and J. D. Haigh, 2011, Solar forcing of winter climate variability in the Northern Hemisphere. Nature Geosci., 4, 753757.

IPCC Core Writing Team, R. Pachauri, and A. Reisinger (Eds.), 2007, Climate Change 2007: Synthesis Report. Contribution of Working Groups I, II and III to the Fourth Assessment Report of the Intergovernmental Panel on Climate Change, Cambridge Univ. Press, 104 pp.

IPCC, 2013, Climate Change 2013: The Physical Science Basis. Contribution of Working Group I to the Fifth Assessment Report of the Intergovernmental Panel on Climate Change [Stocker, T.F., D. Qin, G.-K. Plattner, M. Tignor, S.K. Allen, J. Boschung, A. Nauels, Y. Xia, V. Bex and P.M. Midgley (eds.)]. Cambridge University Press, Cambridge, United Kingdom and New York, NY, USA.

IPCC, 2013: Summary for Policymakers. In: Climate Change 2013: The Physical Science Basis. Contribution of Working Group I to the Fifth Assessment Report of the Intergovernmental Panel on Climate Change [Stocker, T.F., D. Qin, G.-K. Plattner, M. Tignor, S.K. Allen, J. Boschung, A. Nauels, Y. Xia, V. Bex and P.M. Midgley (eds.)]. Cambridge University Press, Cambridge, United Kingdom and New York, NY, USA.

Irvine, P.J., D.J. Lunt, E.J. Stone, A. Ridgewell, 2009, The fate of the Greenland Ice Sheet in a geoengineered, high CO2 world, Environ. Res. Lett. 4 045109

Irvine, P. J., A. Ridgwell, and D. J. Lunt, 2010, Assessing the regional disparities in geoengineering impacts, Geophys. Res. Lett., 37, L18702

Irvine, P. J., A. Ridgwell, and D. J. Lunt, 2011, Climatic effects of surface albedo geoengineering, J. Geophys. Res., 116, D24112

Irvine, P. J., R. L. Sriver, and K. Keller, 2012, Tension between reducing sea-level rise and global warming through solar-radiation management, Nature Clim. Change, 2, 97100

Jamieson, D., 2013, Some whats, whys and worries of geoengineering, Climatic Change, Volume 121, Issue 3, pp 527-537

Jones A, Haywood J, Boucher O, Kravitz B, Robock A., 2010, Geoengineering by stratospheric SO2 injection: results from the Met Office HadGEM2 climate model and comparison with the Goddard Institute for Space Studies ModelE. Atmospheric Chemistry and Physics 10: 59996006.

Jones, Andy, Jim Haywood, Olivier Boucher, Ben Kravitz, and Alan Robock, 2010, Geoengineering by stratospheric SO2 injection: Results from the Met Office HadGEM2 climate model and comparison with the Goddard Institute for Space Studies ModelE. Atmos. Chem. Phys., 10, 5999-6006

Jones, A., J. M. Haywood, K. Alterskjr, O. Boucher, J. N. S. Cole, C. L. Curry, P. J. Irvine, D. Ji, B. Kravitz, J. E. Kristjnsson, J. C. Moore, U. Niemeier, A. Robock, H. Schmidt, B. Singh, S. Tilmes, S. Watanabe, and J.-H. Yoon, 2013, The termination effect in experiment G2 of the Geoengineering Model Intercomparison Project (GeoMIP), J. Geophys. Res., doi:10.1029/2013JD020112.

Jones, C., L. M. V. Carvalho, 2002: Active and Break Phases in the South American Monsoon System. J. Climate, 15, 905914

Jones, G. S., J. M. Gregory, P. A. Stott, S. F. B. Tett, R. B. Thorpe, 2005, An AOGCM simulation of the climate response to a volcanic super-eruption, Clim. Dyn., 25, 725738.

Jones, R. G., M. Noguer, D. Hassell, D. Hudson, S. Wilson, G.Jenkins, and J.Mitchell, 2004, Generating high resolution climate change scenarios using PRECIS, Met Office Hadley Centre, Exeter, UK.

Joshi, M.M. and Shine, K.P., 2003, A GCM study of volcanic eruptions as a cause of increased stratospheric water vapor. Journal Of Climate, 16. pp. 3525-3534. ISSN 1520-0442

Karoly, D. J., and B. J. Hoskins, 1982, Three dimensional propagation of planetary waves. J. Meteor. Soc. Japan, 60, 109123.

Karpechko, A. Y., N. P. Gillett, M. DallAmico, and L. J. Gray, 2010, Southern Hemisphere atmospheric circulation response to the El Chichón and Pinatubo eruptions in coupled climate models, Quarterly Journal of the Royal Meteorological Society, 136(652).

Keith, D. W., 2013, A Case for Climate Engineering, A Boston Review Book, MIT Press.

Kent, G. S., M.P. McCormick, 1984, SAGE and SAM II measurements of global stratosphericaerosol optical depth and mass loading, J. Geophys.Res., 89, 5303-5314

Kent, G.S., M.P. McCormick, 1988, Remote sensing of stratospheric aerosol following the eruption of El Chichon, J. Opt. News, 42, 11-19

Kerr, R. A., 1993, Ozone Takes a Nose Dive After the Eruption of Mt. Pinatubo. Science, 260, 490-491.

Kintisch, Eli, 2013, A Sea Change for U.S. Oceanography, Science, Vol. 339 no. 6124 pp. 1138-1143

Kirchner, Ingo, Georgiy L. Stenchikov, Hans-F. Graf, Alan Robock and Juan Carlos Antua, 1999, Climate model simulation of winter warming and summer cooling following the 1991 Mount Pinatubo volcanic eruption. J. Geophys. Res., 104, 19,039-19,055.

Kirkevåg, A., T. Iversen, Ø. Seland, J. B. Debernard, T. Storelvmo, and J. E. Kristjànsson, 2008, Aerosol-cloud-climate interactions in the climate model cam-oslo, Tellus A, 60(3), 492–512

Kirkevåg, A., T. Iversen, Ø. Seland, C. Hoose, J. E. Kristjànsson, H. Struthers, A. Ekman, S. Ghan, J. Griesfeller, D. Nilsson and M. Schulz, 2012, Aerosol-climate interactions in the Norwegian Earth System Model - NorESM

Kistler, R., et al., 2001, The NCEP–NCAR 50–Year Reanalysis: Monthly Means CD–ROM and Documentation, Bulletin of the American Meteorological Society, 82(2), 247–267

Klepper, G. and W. Rickels, forthcoming, Climate Engineering: Fighting Fire with Fire? Review of Environmental Economics and Policy.

Kodera, K., and Y. Kuroda, 2002, Dynamical response to the solar cycle, J. Geophys. Res., 107(D24), 4749

Kodera, K., 1995, On the origin and nature of the interannual variability of the winter stratospheric circulation in the Northern Hemisphere, J. Geophys. Res., 100, 14,07714,087

Kolstad, E., and A. Charlton-Perez, 2010, Observed and simulated precursors of stratospheric polar vortex anomalies in the Northern Hemisphere, Climate Dynamics, 37 (7), 1443–1456.

Kravitz, Ben, Alan Robock, Luke Oman, Georgiy Stenchikov, and Allison B. Marquardt, 2009, Sulfuric acid deposition from stratospheric geoengineering with sulfate aerosols. J. Geophys. Res., 114, D14109

Kravitz, Ben, Alan Robock, and Adam Bourassa, 2010, Negligible climatic effects from the 2008 Okmok and Kasatochi volcanic eruptions. J. Geophys. Res., 115, D00L05

Kravitz, Ben, and Alan Robock, 2011, The climate effects of high latitude volcanic eruptions: The role of the time of year. J. Geophys. Res., 116, D01105

Kravitz, B., A. Robock, O. Boucher, H. Schmidt, K. E. Taylor, G. Stenchikov, and M. Schulz, 2011, The geoengineering model intercomparison project (GeoMIP), Atmospheric Science Letters, 12, 162-167

Kravitz, Ben, Alan Robock, Adam Bourassa, Terry Deshler, Decheng Wu, Ina Mattis, Fanny Finger, Anne Hoffmann, Christoph Ritter, Lubna Bitar, Thomas J. Duck, and John E. Barnes, 2011, Simulation and observations of stratospheric aerosols from the 2009 Sarychev volcanic eruption. J. Geophys. Res., 116, D18211

Kravitz B, MacMartin DG, Caldeira K, 2012, Geoengineering: whiter skies? Geophys Res Lett 39(L11801)

Kravitz, Ben, Alan Robock, Drew T. Shindell, and Mark A. Miller, 2012, Sensitivity of stratospheric geoengineering with black carbon to aerosol size and altitude of injection. J. Geophys. Res., 117, D09203

Kravitz, B., K. Caldeira, O. Boucher, A. Robock, P. J. Rasch, K. Alterskjr, D. Bou Karam, J. N. S. Cole, C. L. Curry, J. M. Haywood, P. J. Irvine, D. Ji, A. Jones, J. E. Kristjnsson, D. J. Lunt, J. Moore, U. Niemeier, H. Schmidt, M. Schulz, B. Singh, S. Tilmes, S. Watanabe, S. Yang, and J.-H. Yoon, 2013, Climate model response from the Geoengineering Model Intercomparison Project (GeoMIP), Journal of Geophysical Research, 118(15), 8320-8332

Kravitz, Ben, Douglas G. MacMartin, Alan Robock, Philip J. Rasch, Katharine L. Ricke, Jason N. S. Cole, Charles L. Curry, Peter J. Irvine, Duoying Ji, David Keith, Jn Egill Kristjnsson, John C. Moore, Helene Muri, Balwinder Singh, Simone Tilmes, Shingo Watanabe, Shuting Yang, and Jin-Ho Yoon, 2014, A multi-model assessment of regional climate disparities caused by solar geoengineering. Env. Res. Lett., 9, 074013

Kuebbeler M, Lohmann U, Feichter J, 2012, Effects of stratospheric sulfate aerosol geo-engineering on cirrus clouds. Geophys Res Lett 39:L23803

Lambert, A., R. G. Grainger, J. J. Remedios, C. D. Rodgers, M. Corney, and F. W. Taylor, 1993, Measurements of the evolution of the Mt. Pinatubo aerosol cloud by ISAMS, Geophys. Res. Lett., 20 (12), 1287–1290

Lane, C.S., Chorn, B.T., and Johnson, T.C., 2013, Ash from the Toba supereruption in Lake Malawi shows no volcanic winter in East Africa at 75 ka. Proceedings of the National Academy of Sciences, 110(20), 80258029.

Lashof, D. A., and D. R. Ahuja, 1990, Relative contributions of greenhous gas emissions to global warrning Nature 344:529-531.

Latham, J., Parkes, B., Gadian, A. and Salter, S., 2012, Weakening of hurricanes via marine cloud brightening (MCB). Atmosph. Sci. Lett., 13: 231237

Latham, J., Bower, K., Choularton, T., Coe, H., Connoly, P., Cooper, G., Craft, T., Foster, J., Gadian, A., Galbraith, L., Ia- covides, H., Johnston, D., Launder, B., Leslie, B., Meyer, J., Neukermans, A., Ormond, B., Parkes, B., Rasch, P., Rush, J., Salter, S., Stevenson, T., Wang, H., Wang, Q., and Wood, R., 2012, Marine cloud brightening, Phil. Trans. R. Soc. A, 370, 42174262

Leavitt, S.W., 1982, Annual volcanic CO2 emission: an estimate from eruption chronologies. Environmental Geology 4:15-21.

Lenton, T.M., 2013, Can Emergency Geoengineering Really Prevent Climate Tipping Points? (Opinion Article), in Geoengineering Our Climate? A Working Paper Series on the Ethics, Politics and Governance of Climate Engineering, available online at geoengineeringourclimate.com

Lenton, T.M., H. Held, E. Kriegler, J. Hall, W. Lucht, S. Rahmstorf, and H.J. Schellnhuber, 2008, Tipping Elements in the Earths Climate System. Proceedings of the National Academy of Sciences of the United States of America 105: 17861793.

Li, C., D. S. Battisti, D. P. Schrag, and E. Tziperman, 2005, Abrupt climate shifts in greeland due to displacements of the sea ice edge. Geophys. Res. Lett., 32, L19 702

Li, Q., H.-F., Graf, Giorgetta, M.: Stationary planetary wave propagation in Northern Hemisphere winter climatological analysis of the refractive index, Atmos. Chem. Phys., 7, 183200, 2006

Li, F., Austin, J., and Wilson, J., 2008, The strength of the Brewer-Dobson circulation in a changing climate: a coupled chemistry model simulation, J. Climate, 21, 4057

Li, Ying and Ngar-Cheung Lau, 2012, Impact of ENSO on the Atmospheric Variability over the North Atlantic in Late WinterRole of Transient Eddies. J. Climate, 25, 320342.

Lobell, David and Field, Christopher, 2007, Global scale climatecrop yield relationships and the impacts of recent warming, Public Health Resources. Paper 152.

Longo BM, Rossignol A, Green JB, 2008, Cardiorespiratory health effects associated with sulphurous volcanic air pollution, Public Health, 122(8):809820

Longo BM, Yang W, Green JB, Crosby FL, Crosby VL, 2010, Acute health effects associated with exposure to volcanic air pollution (vog) from increased activity at Kilauea Volcano in 2008. J Toxicol Environmental Health-Part a-Current Issues 73(20):13701381

Lucarini, V., 2012, Modeling complexity: the case of climate science. arXiv:1106.1265v1 [physics.hist-ph], Proceedings of the Conference "Models, Simulation and the Reduction of Complexity", De Gruyter Verlag, Hamburg

Lucarini, V, 2013, Modeling Complexity: the case of climate science, in "Models, Simulations, and the Reduction of Complexity", Edited by U. Ghde, S. Hartmann, and J. H. Wolf, De Gruyter, pp 229-254.

Lunt, D. J., Ridgwell, S., Valdes, P. J., and Seale, A., 2008, Sunshade world: A fully coupled gcm evaluation of the climatic impacts of geoengineering, Geophys. Res. Lett., 35:L12710.

MacMartin, D.G., Keith, D. W., Kravitz, B., and Caldeira, K., 2013, Management of tradeoffs in geoengineering through optimal choice of non-uniform radiative forcing, Nature Climate Change

MacMynowski, D. G., Keith, D., Caldeira, K., and Shin, H.-J., 2011, Can we test geoengineering? Energy and Environmental Science, 4(12), pp 5044-5052.

Mackie, S., and M. Watson, 2014, Probabilistic detection of volcanic ash using a Bayesian approach, J. Geophys. Res. Atmos., 119, 24092428

Manzini, E., M. A. Giorgetta, M. Esch, L. Kornblueh, and E. Roeckner, 2006, The Influence of Sea Surface Temperatures on the Northern Winter Stratosphere: Ensemble Simulations with the MAECHAM5 Model, Journal of Climate, 19 (16), 3863–3881

Marshall, A. G., A. A. Scaife, and S. Ineson, 2009, Enhanced seasonal prediction of european winter warming following volcanic eruptions, Journal of Climate, 22 (23), 6168–6180

Marsland, S., H. Haak, J. Jungclaus, M. Latif, and F. Roeske, 2003, The Max-Planck-Institute global ocean/sea ice model with orthogonal curvilinear coordinates, Ocean Modell, 5, 91–127.

Maslanik, J. A., C. Fowler, J. Stroeve, S. Drobot, J. Zwally, D. Yi, and W. Emery, 2007, A younger, thinner Arctic ice cover: Increased potential for rapid, extensive sea-ice loss, Geophys. Res. Lett., 34, L24501

McCarthy, J.J., et al., ed., 2001, Climate Change 2001: Impacts, Adaptation and Vulnerability. Contribution of Working Group II to the Third Assessment Report of the Integovernmental Panel on Climate Change. Print version: Cambridge University Press, Cambridge, UK, and New York, N.Y., US.

McClellan, Justin, James Sisco, Brandon Suarez, Greg Keogh, 2011, Geoengineering Cost Analysis, Aurora Flight Sciences, Geoengineering Final Report UC01-001; AR10-182

McClellan, J., D. Keith, J. Apt, 2012, Cost Analysis of Stratospheric Albedo Modification Delivery Systems, Environmental Research Letters 7 034019

McCormick, M.P., and Veiga, R.E., 1992, SAGE II measurements of early Pinatubo aerosols: Geophysical Research Letters, v. 19, p. 155-158.

McCormick, M.P., Thomason, L.W., and Trepte, C.R., 1995, Atmospheric effects of the Mt. Pinatubo eruption: Nature, v. 373, p. 399404

McCusker, K. E., D. S. Battisti, and C. M. Bitz, 2012, The Climate Response to Stratospheric Sulfate Injections and Implications for Addressing Climate Emergencies. J. Climate, 25, 30963116.

Mcintyre, M. E., 1982, How well do we understand the dynamics of stratospheric warmings?, J. Meteorol. Soc. Jpn., 60, 3765

Meehl, G., C. Covey, T. Delworth, M. Latif, B. McAvaney, J. Mitchell, R. Stouffer, and K. Taylor, 2007, The WCRP CMIP3 multi-model dataset: a new era in climate change research, Bulletin of the American Meteorological Society, 88, 1383–1394.

Mercado, R. A., Jay Bertram T. Lacsamana, and Greg L. Pineda, 1996, Socioeconomic impacts of the Mount Pinatubo eruption, Fire and Mud, edited by C. G. Newhall and R. S. Punongbayan. Quezon City: Philippine Institute of Volcanology and Seismology; Seattle: University of Washington Press. Edition available online, at: http://pubs.usgs.gov/pinatubo/index.html

Mercer, A. M., D. W. Keith, and J. D. Sharp., 2011, Public understanding of Solar Radiation Management. Environmental Research Letters, 6: 044006 (9pp)

Miller, G. H., et al., 2012, Abrupt onset of the Little Ice Age triggered by volcanism and sustained by sea-ice/ocean feedbacks, Geophys. Res. Lett., 39, L02708

Mitchell, D., L. Gray, J. Anstey, M. Baldwin, and J. Charlton-Perez, 2012, The influence of Stratospheric Vortex Displacements and Splits on Surface Climate, J. Clim.

Mitchell, D. M., L. J. Gray, and A. J. Charlton-Perez, 2011, The structure and evolution of the stratospheric vortex in response to natural forcings, J. Geophys. Res., 116 (D15)

Mizuta, R., et al., 2012, Climate simulations using MRI-AGCM3.2 with 20-km grid, J. Meteor. Soc. Japan

Mohanakumar, K., 2008, Stratosphere Troposphere Interactions: An Introduction, Springer Science

Moore, J. C., Jevrejeva, S., and Grinsted, A., 2010, Efficacy of geoengineering to limit 21st century sea-level rise, Proc. Natl. Acad. Sci.

Moore, John C., Annette Rinke, Xiaoyong Yu, Duoying Ji, Xuefeng Cui, Yan Li, Kari Alterskjr, Jn Egill Kristjnsson, Helene Muri, Olivier Boucher, Nicolas Huneeus, Ben Kravitz, Alan Robock, Ulrike Niemeier, Michael Schulz, Simone Tilmes, Shingo Watanabe, and Shuting Wang, 2014, Arctic sea ice and atmospheric circulation under the GeoMIP G1 scenario. J. Geophys. Res. Atmos., 119, 567-583

NASA, 1992, The atmospheric effects of stratospheric aircraft: A first program report, M.J. Prather et al. (eds.), NASA Ref. Publ. 1272, pp. 6491.

Naujokat, B., 1986, An update of the observed quasi-biennial oscillation of the stratospheric winds over the tropics, J. Atmos. Sci., 43, 18731877.

Newhall, C. G., Arturo S. Daag, F.G. Delfin, Jr., Richard P. Hoblitt, John McGeehin, John S. Pallister, Ma. Theresa M. Regalado, Meyer Rubin, Bella S. Tubianosa, Rodolfo A. Tamayo, Jr., and Jesse V. Umbal, 1996, Eruptive history of Mount Pinatubo, Fire and Mud, edited by C. G. Newhall and R. S. Punongbayan. Quezon City: Philippine Institute of Volcanology and Seismology; Seattle: University of Washington Press. Edition available online, at: http://pubs.usgs.gov/pinatubo/index.html

Nicoll and Delaney (eds), 2012, Geoengineering: Rules Needed for Climate-Altering Science, IISS Strategic Comments, Vol. 18, Iss. 10, p. 1-5

Niemeier U, Schmidt H, Timmreck C., 2010, The dependency of geoengineered sulfate aerosol on the emission strategy, Atmos. Sci. Let.

Oman, L., A. Robock, G. Stenchikov, G. A. Schmidt, and R. Ruedy, 2005, Climatic response to high-latitude volcanic eruptions, J. Geophys. Res., 110 (D13)

Oppenheimer, C., 2002, Limited global change due to the largest known Quaternary eruption, Toba $\approx$ 74 kyr BP? Quat. Sci. Rev. 81, 15931609.

Oppenheimer M., O'Neill B.C., Webster M., 2008, Negative learning. Clim Change 89:155172.

Orr J. C., V. J. Fabry, O. Aumont, L. Bopp, S.C. Doney, R. A. Feely, A. Gnanadesikan, N. Gruber, A. Ishida, F. Joos, R. M. Key, K. Lindsay, E. Maier-Reimer, R. Matear, P. Monfray, A. Mouchet, R. G. Najjar, G.-K. Plattner, K. B. Rodgers, C. L. Sabine, J. L. Sarmiento, R. Schlitzer, R. D. Slater, I. J. Totterdell, M.-F. Weirig, Y.

Yamanaka, Andrew Yool, 2005, Anthropogenic ocean acidification over the twenty-first century and its impact on calcifying organisms. Nature 437:68186

Osprey, S. M., Lesley J. Gray, Steven C. Hardiman, Neal Butchart, Andrew C. Bushell, and Tim J. Hinton, 2010, The Climatology of the Middle Atmosphere in a Vertically Extended Version of the Met Offices Climate Model. Part II: Variability. J. Atmos. Sci., 67, 36373651.

Otterå, O., 2008, Simulating the effects of the 1991 Mount Pinatubo volcanic eruption using the ARPEGE atmosphere general circulation model, Advances in Atmospheric Sciences, 25, 213–226

Pall P, T. Aina, D. A. Stone, P. A. Stott, T. Nozawa, A. G. J. Hilberts, D. Lohmann, M. R. Allen, 2011, Anthropogenic greenhouse gas contribution to flood risk in England and Wales in autumn 2000. Nature 470:382385.

Palmer, T. N., F. J. Doblas-Reyes, R. Hagedorn, A. Alessandri, S. Gualdi, U. Andersen, H. Feddersen, P. Cantelaube, J-M. Terres, M. Davey, R. Graham, P. Dlcluse, A. Lazar, M. Dqu,J-F. Gurmy, E. Dez, B. Orfila, M. Hoshen, A. P. Morse, N. Keenlyside, M. Latif, E. Maisonnave, P. Rogel, V. Marletto, and M. C. Thomson, 2004, Development of a European Multimodel Ensemble System for Seasonal-to-Interannual Prediction (DEMETER). Bull. Amer. Meteor. Soc., 85, 853872

Palmer, T. N., F. J. Doblas-Reyes, A. Weisheimer, and M. J. Rodwell, 2008, Toward Seamless Prediction: Calibration of Climate Change Projections Using Seasonal Forecasts. Bull. Amer. Meteor. Soc., 89, 459470.

Palmer, T. N., and Coauthors, 2004, Development of a European Multimodel Ensemble System for Seasonal-to-Interannual Prediction (DEMETER). Bull. Amer. Meteor. Soc., 85, 853872.

Palmer, W. C., 1965, Meteorological Drought. Res. Paper No. 45, Weather Bureau, Washington, D.C., 58 pp.

Parson E., Keith D., 2013, End the deadlock on governance of geoengineering research. Science 339:1278 1279

Peixoto, J. P., and A. H. Oort, 1992, Physics of Climate. American Institute of Physics, 520 pp.

Pierce, J. R., D. K. Weisenstein, P. Heckendorn, T. Peter, and D. W. Keith, 2010, Efficient formation of stratospheric aerosol for climate engineering by emission of condensible vapor from aircraft, Geophys. Res. Lett., 37, L18805

Pierrehumbert, R. T., 2010, Principles of Planetary Climate Cambridge University Press, 652 pp.

Pinto, J.P., R.P. Turco, and O.B. Toon, 1989, Self-limiting physical and chemical effects in volcanic eruption clouds, J. Geophy's. Res., 94, 11,165-11,174

Pitari, G., and E. Mancini, 2002, Short-term climatic impact of the 1991 volcanic eruption of Mt. Pinatubo and effects on atmospheric tracers, Nat. Hazards Earth Syst. Sci., 2, 91108.

Pongratz, J., Lobell, D. B., Cao L. and Caldeira, K., 2012, Crop yields in a geoengineered climate. Nature Climate Change

Pope, V. D., M. L. Gallani, P. R. Rowntree, and R. A. Stratton, 2000, The impact of new physical parametrizations in the Hadley Centre model: HadAM3, Climate Dynamics,16, 123-146.

Pope, F. P., Braesicke, P., Grainger, R. G., Kalberer, M., Watson, I. M., Davidson, P. J. and Cox, R. A., 2012, Stratospheric aerosol particles and solar-radiation management. Nature

Prather, M., Catastrophic loss of stratospheric ozone in dense volcanic clouds, 1992, J. Geophys. Res., 97, 1018710191

Punongbayan, R. S., Christopher G. Newhall, Ma. Leonila P. Bautista, Delfin Garcia, David H. Harlow, Richard P. Hoblitt, Julio P. Sabit, and Renato U. Solidum, 1996, Eruption hazard assessments and warnings, Fire and Mud, edited by C. G. Newhall and R. S. Punongbayan. Quezon City: Philippine Institute of Volcanology and Seismology; Seattle: University of Washington Press. Edition available online, at: http://pubs.usgs.gov/pinatubo/index.html

Raddatz, T., C. Reick, W. Knorr, J. Kattge, E. Roeckner, R. Schnur, K.-G. Schnitzler, P. Wetzel, and J. Jungclaus, 2007, Will the tropical land biosphere dominate the climate–carbon cycle feedback during the twenty-first century?, Climate Dynamics, 29, 565–574

Rahmstorf, S., 2007: A semi-empirical approach to projecting future sea-level rise. Science, 315, 368-370.

Ramachandran, S., V. Ramaswamy, G. L. Stenchikov, and A. Robock, 2000, Radiative impact of the Mount Pinatubo volcanic eruption: Lower stratospheric response, J. Geophys. Res., 105 (D19), 24,409–24,429.

Rasch, P. J., S. Tilmes, R. P. Turco, A. Robock, L. Oman, C.-C. J. Chen, G. L. Stenchikov, and R. R. Garcia, 2008, An overview of geoengineering of climate using stratospheric sulphate aerosols, Philosophical Transactions of the Royal Society A: Mathematical, Physical and Engineering Sciences, 366 (1882), 40074037

Ricke, Katharine L. and Morgan, M. Granger and Allen, Myles R., 2010, Regional climate response to solar-radiation management, Nature Geosci

Ricke, K.L., M.R. Allen, and M.G. Morgan, 2010, Regional climate response to solar-radiation management. Nature Geoscience 3:537-541.

Ricke, K.L., D. J. Rowlands, W.J. Ingram, D.W. Keith, and M.G. Morgan, 2012, Effectiveness of stratospheric solar-radiation management as a function of climate sensitivity. Nature Climate Change 2:9296.

Ricke K L, Moreno-Cruz J B, Caldeira K, 2013, Strategic incentives for climate geoengineering coalitions to exclude broad participation Environ. Res. Lett. 8 014021

Robock, A., 2000, Volcanic eruptions and climate, Rev. Geophys., 38(2), 191–219.

Robock, A., J. Mao, 1992, Winter warming from large volcanic eruptions, Geophys. Res. Lett., 19 (24), 2405–2408

Robock, A., J. Mao, 1995, The volcanic signal in surface temperature observations, J. Clim., 8, 1086–1103.

Robock, Alan, 2003, Introduction: Mount Pinatubo as a test of climate feedback mechanisms, in Volcanism and the Earths Atmosphere, Alan Robock and Clive Oppenheimer, Eds. (American Geophysical Union, Washington, DC), 1-8.

Robock, Alan, Tyler Adams, Mary Moore, Luke Oman, Georgiy Stenchikov, 2007: Southern Hemisphere atmospheric circulation effects of the 1991 Mount Pinatubo eruption. Geophys. Res. Lett., 34, L23710

Robock, Alan, 2008, 20 reasons why geoengineering may be a bad idea. Bull. Atomic Scientists, 64, No. 2, 14-18, 59

Robock, Alan, Luke Oman, Georgiy Stenchikov, 2008, Regional climate responses to geoengineering with tropical and Arctic SO2 injections. J. Geophys. Res., 113, D16101

Robock, Alan, Allison B. Marquardt, Ben Kravitz, Georgiy Stenchikov, 2009, The benefits, risks, and costs of stratospheric geoengineering. Geophys. Res. Lett., 36, L19703

Robock, Alan, Martin Bunzl, Ben Kravitz, Georgiy Stenchikov, 2010, A test for geoengineering? Science, 327, 530-531

Robock, Alan, 2012, Will geoengineering with solar radiation management ever be used? Ethics, Policy and Environment, 15, 202-205.

Robock, Alan, 2012, Is geoengineering research ethical? Peace and Security, 4, 226-229.

Robock, Alan, Douglas G. MacMartin, Riley Duren, Matthew W. Christensen, 2013, Studying geoengineering with natural and anthropogenic analogs. Climatic Change, 121, 445-458

Rodwell, M. J., D. P. Rowell, C. K. Folland, 1999, Oceanic forcing of the wintertime North Atlantic Oscillation and European climate, Nature, 398, (6725), 320–323.

Rogelj, J., Hare, W., Chen, C., Meinshausen, M., 2011, Discrepancies in historical emissions point to a wider 2020 gap between 2 °C benchmarks and aggregated national mitigation pledges. Environ. Res. Lett. 6, 19

Rogelj, Hare, B., Nabel, J., Macey, K., Schaeffer, M., Markmann, K., Meinshausen, M., 2009, Halfway to Copenhagen, no way to 2 °C, Nature Reports Climate Change

Roscoe, H. K., 2004, A review of stratospheric H2O and NO2, Adv. Space Res., 34, 17471754

Rosenzweig, C., 2000, Potential impacts of climate change on agriculture. In A Spectrum of Achievement in Agronomy: Women Fellows of the Tri-Societies, ASA

Special Pub. 62. American Society of Agronomy, Crop Science Society of America, and Soil Science Society of America, 73-88.

Rosenzweig, C.E., A. Iglesias, X.B. Yang, P.R. Epstein, E. Chivian, 2001, Climate change and extreme weather events: Implications for food production, plant diseases, and pests. Global Change Human Health, 2, 90-104

Rotman, 2013, A Cheap and Easy Plan to Stop Global Warming, online article, available at http://www.technologyreview.com/featuredstory/511016/a-cheap-and-easy-plan-to-stop-global-warming/, accessed 9 Dec 2014

Rotstayn, L. D., M. A. Collier, M. R. Dix, Y. Feng, H. B. Gordon, S. P., O'Farrell, I. N. Smith, J. Syktus, 2010, Improved simulation of australian climate and enso-related rainfall variability in a global climate model with an interactive aerosol treatment, International Journal of Climatology, 30 (7), 1067–1088

Russel, P.B., Livingston, J.M., Durron, E.G., Pueschel, R.F., Reagan, J.A., Defoor, T.E., Box, M.A., Allen, D., Pilewskie, P., Herman, B.M., Kinne, S.A., Hofmann, D.J., 1993, Pinatubo and pre-Pinatubo optical-depth spectra: Mauna Loa measurements, comparisons, inferred particle size distributions, radiative effects, and relationships to lidar data. Journal of Geophysical Research, 98, pp. 2296922985.

Russell, L. M., Bahadur, R., Ziemann, P. J., 2011, Identifying organic aerosol sources by comparing functional group composition in chamber and atmospheric particles, Proc. Natl. Acad. Sci. USA, 108, 35163521

Salby, M., 2008, Involvement of the BrewerDobson circulation in changes of Northern Hemisphere ozone, Dyn. Atmos. Oceans, 44, 143164

Sato, M., J. Hansen, M. McCormick, J. Pollack, 1993, Stratospheric aerosol optical depths, J. Geophys. Res., 98, 22,987–22,994

Scaife, A. A., Butchart, N., Warner, C. D., Stainforth, D., Norton, W., Austin, J., 2000, Realistic Quasi-Biennial Oscillations in a simulation of the global climate, Geophys. Res. Lett., 27 (1), 3481-3484

Schmidt, G. A., et al., 2006, Present-Day Atmospheric Simulations Using GISS ModelE: Comparison to In Situ, Satellite, and Reanalysis Data, Journal of Climate, 19 (2), 153–192

Shindell, D. T., G. A. Schmidt, M. E. Mann, G. Faluvegi, 2004, Dynamic winter climate response to large tropical volcanic eruptions since 1600, J. Geophys. Res., 109 (D5)

Stothers, R. B., 1996, Major optical depth perturbations to the stratosphere from volcanic eruptions: Pyrheliometric period, 1881 1960, J. Geophys. Res., 101(D2), 3901–3920

Stothers, R. B., 2001, Major optical depth perturbations to the stratosphere from volcanic eruptions: Stellar extinction period, 1961 1978, J. Geophys. Res., 106(D3), 2993–3003

Salby, M., Sassi, F., Callaghan, P., Read, W., Pumphrey, H.: Fluctuations of cloud, humidity and thermal structure near tropical tropopause, J. Climate, 16, 34283446, 2003.

Santer, Benjamin D., Cline Bonfils, Jeffrey F. Painter, Mark D. Zelinka, Carl Mears, Susan Solomon, Gavin A. Schmidt, John C. Fyfe, Jason N. S. Cole, Larissa Nazarenko, Karl E. Taylor, Frank J. Wentz, 2014, Volcanic contribution to decadal changes in tropospheric temperature. Nature Geoscience

Sarewitz, D., R. A. Pielke, Jr., 2000, Prediction in Science and Policy, in Sarewitz, D., R. A. Pielke, Jr., R. Byerly, (editors), 2000, Prediction: Science, Decision Making and the Future of Nature., Washington, DC: Island Press.

Sato, M., J. Hansen, M. McCormick, J. Pollack, 1993, Stratospheric aerosol optical depths, J. Geophys. Res., 98, 22,987–22,994

Schmidt, G. A., et al., 2006, Present-Day Atmospheric Simulations Using GISS ModelE: Comparison to In Situ, Satellite, and Reanalysis Data, Journal of Climate, 19(2), 153–192

Schmidt, H., K. Alterskjr, D. Bou Karam, O. Boucher, A. Jones, J. E. Kristjnsson, U. Niemeier, M. Schulz, A. Aaheim, F. Benduhn, M. Lawrence, C. Timmreck, 2012, Solar irradiance reduction to counteract radiative forcing from a quadrupling of CO2: Climate responses simulated by four Earth system models, Earth System Dynamics, 3, 63-78

Schafer, S., Irvine, P. J., Hubert, A.-M., Reichwein, D., Low, S., Stelzer, H., Maas, A., Lawrence, M. G., 2013, Field tests of solar climate engineering. - Nature Climate Change, 3, 9, p. 766-766

Schaller, N., J. Sedlacek, R. Knutti, 2014, The asymmetry of the climate system's response to solar forcing changes and its implications for geoengineering scenarios, Journal of Geophysical Research - Atmospheres, 119, 2014, 5171-5184

Shindell, D. T., G. A. Schmidt, M. E. Mann, G. Faluvegi, 2004, Dynamic winter climate response to large tropical volcanic eruptions since 1600, J. Geophys. Res., 109 (D5), DOI: 10.1029/2003JD004151

Science and Policy, in Sarewitz, D., R. A. Pielke, Jr., and R. Byerly, (editors), 2000, Prediction: Science, Decision Making and the Future of Nature., Washington, DC: Island Press.

Scott, W.E., Hoblitt, R.P., Torres, R.C., Self, S., Martinez, M.M.L., Timoteo, N., Jr., 1996, Pyroclastic flows of the June 15, 1991, climactic eruption of Mount Pinatubo, in Newhall, C.G., and Punongbayan, R.S., eds., Fire and mud, eruptions and lahars of Mount Pinatubo, Philippines: Philippine Institute of Volcanology and Seismology and University of Washington, p. 545570.

Seager, R., Y. Kushnir, J. Nakamura, M. Ting, N. Naik, 2010, Northern Hemisphere winter snow anomalies: ENSO, NAO and the winter of 2009/10, Geophys. Res. Lett., 37, L14703

Self, S., 1996, The effects and consequences of very large explosive volcanic eruptions, Phil. Trans. R. Soc. A, 2006, 364, 20732097

Self, S., Jing-Xia Zhao, Rick E. Holasek, Ronnie C. Torres, Alan J. King, 1996, The atmospheric impact of the 1991 Mount Pinatubo eruption, Fire and Mud, edited by C. G. Newhall, R. S. Punongbayan. Quezon City: Philippine Institute of Volcanology and Seismology; Seattle: University of Washington Press. Edition available at: http://pubs.usgs.gov/pinatubo/index.html

Seol, D.-I., K. Yamazaki, 1998, QBO and Pinatubo signals in the mass flux at 100 hPa and stratospheric circulation, Geophys. Res. Left., 25, 1641-1644

Serreze, M.C., M.M. Holland, J. Stroeve, 2007, Perspectives on the Arctic's Shrinking Sea-Ice Cover, Science, 315 (5818), 1533-1536

Shepherd, J., K. Caldeira, P. Cox, J. Haigh, D. Keith, B. Launder, G. Mace, G. MacKerron, et al. 2009. Geoengineering the climate. The Royal Society.

Shepherd, Andrew, Tom Mitchell, Kirsty Lewis, Amanda Lenhardt, Lindsey Jones, Lucy Scott, Robert Muir-Wood, 2013, The geography of poverty, disasters and climate extremes in 2030

Shindell, D. T., G. A. Schmidt, R. L. Miller, D. Rind, 2001, Northern Hemisphere winter climate response to greenhouse gas, ozone, solar, and volcanic forcing, J. Geophys. Res., 106, 7193 7210

Shindell, D.T., G.A. Schmidt, M.E. Mann, G. Faluvegi, 2004: Dynamic winter climate response to large tropical volcanic eruptions since 1600. J. Geophys. Res., 109, D05104

Solomon, S., R. W. Sanders, R. R. Garcia, J. G. Keys, 1993, Increased chlorine dioxide over Antarctica caused by volcanic aerosols from Mount Pinatubo, Nature, 363, 245248

Solomon, S., R. W. Portmann, R. R. Garcia, L. W. Thomason, L. R. Poole, M. P. McCormick, 1996, The role of aerosol variations in anthropogenic ozone depletion at northern midlat tudes, J. Geophys. Res., 101, 6713 6727

Solomon, S., Plattner, G.-K., Knutti, R., Friedlingstein, P., 2009, Irreversible climate change due to carbon dioxide emissions. Proc. Natl Acad. Sci. USA

Steil, B., C. Bruhl, M.Giorgetta, E.Manzini, V.Grewe, F.Mager, 2004, The impact of CFCs, greenhouse gases, solar cycle, QBO, ENSO and major volcanoes on stratospheric ozone; transient simulation with the middle atmosphere coupled chemistry climate model ECHAM for the last 40 years

Steinhaeuser, K., A. A. Tsonis, 2014, A Climate Model Intercomparison at the Dynamics Level. Climate Dynamics, 42, 1665-1670.

Stenchikov, G., A. Robock, V. Ramaswamy, M. D. Schwarzkopf, K. Hamilton, and S. Ramachandran, 2002, Arctic Oscillation response to the 1991 Mount Pinatubo

eruption: Effects of volcanic aerosols and ozone depletion, J. Geophys. Res., 107 (D24)

Stenchikov, G., K. Hamilton, A. Robock, V. Ramaswamy, and M. D. Schwarzkopf, 2004, Arctic oscillation response to the 1991 Pinatubo eruption in the SKYHI general circulation model with a realistic quasi-biennial oscillation, J. Geophys. Res., 109 (D3)

Stenchikov, G., K. Hamilton, R. J. Stouffer, A. Robock, V. Ramaswamy, B. Santer, and H.-F. Graf, 2006, Arctic Oscillation response to volcanic eruptions in the IPCC AR4 climate models, J. Geophys. Res., 111 (D7)

Stenchikov, G. L., I. Kirchner, A. Robock, H.-F. Graf, J. C. Antuña, R. G. Grainger, A. Lambert, and L. Thomason, 1998, Radiative forcing from the 1991 mount pinatubo volcanic eruption, J. Geophys. Res., 103 (D12), 13,837–13,857

Stenchikov, G., T. L. Delworth, V. Ramaswamy, R. J. Stouffer, A. Wittenberg, and F. Zeng, 2009, Volcanic signals in oceans, J. Geophys. Res., 114, D16104

Stothers, R. B., 1996, Major optical depth perturbations to the stratosphere from volcanic eruptions: Pyrheliometric period, 1881 1960, J. Geophys. Res., 101(D2), 39013920

Stothers, R. B., 2001, Major optical depth perturbations to the stratosphere from volcanic eruptions: Stellar extinction period, 1961 1978, J. Geophys. Res., 106 (D3), 29933003

Stirling, I., 1997, The importance of polynyas, ice edges, and leads to marine mammals and birds, J. Marine Systems, 10, 9-21

Tabazadeh, A., and Turco, R.P., 1993, Stratospheric chlorine injection by volcanic eruptions: HCl scavenging and implications for ozone: Science, v. 260, p. 10821086

Takahashi, K., A. Montecinos, K. Goubanova, and B. Dewitte, 2011, ENSO regimes: Reinterpreting the canonical and Modoki El Niño, Geophys. Res. Lett., 38(10)

Tanaka, T. Y., K. Orito, T. T. Sekiyama, K. Shibata, M. Chiba, and H. Tanaka, 2003, MASINGAR, a global tropospheric aerosol chemical transport model coupled with MRI/JMA98 GCM: Model description, Meteor. Geophys., 53 (4), 119–138.

Taylor, K. E., R. J. Stouffer, and G. A. Meehl, 2011, An Overview of CMIP5 and the Experiment Design, Bull. Am. Met. Soc., 93(4), 485–498

Telford, P., Braesicke, P., Morgenstern, O., and Pyle, J., 2009, Reassessment of Causes of Ozone Column Variability following the Eruption of Mount Pinatubo using a nudged CCM, Atmos. Chem. Phys., 9, 42514260

The HadGEM2 Development Team: G. M. Martin, Bellouin, N., Collins, W. J., Culverwell, I. D., Halloran, P. R., Hardiman, S. C., Hinton, T. J., Jones, C. D., McDonald, R. E., McLaren, A. J., O'Connor, F. M., Roberts, M. J., Rodriguez, J. M., Woodward, S., Best, M. J., Brooks, M. E., Brown, A. R., Butchart, N., Dearden, C., Derbyshire, S. H., Dharssi, I., Doutriaux-Boucher, M., Edwards, J. M., Falloon, P. D., Gedney, N., Gray, L. J., Hewitt, H. T., Hobson, M., Huddleston, M. R., Hughes, J., Ineson, S., Ingram, W. J., James, P. M., Johns, T. C., Johnson, C. E., Jones, A., Jones, C. P., Joshi, M. M., Keen, A. B., Liddicoat, S., Lock, A. P., Maidens, A. V., Manners, J. C., Milton, S. F., Rae, J. G. L., Ridley, J. K., Sellar, A., Senior, C. A., Totterdell, I. J., Verhoef, A., Vidale, P. L., and Wiltshire, A.: The HadGEM2 family of Met Office Unified Model climate configurations, Geosci. Model Dev., 4, 723-757

Thomas, M. A., C. Timmreck, M. Giorgetta, H. Graf, and G. Stenchikov, 2009a, Simulation of the climate impact of Mt. Pinatubo eruption using ECHAM5 Part 1: Sensitivity to the modes of atmospheric circulation and boundary conditions, Atmos. Chem. Phys., 9, 757-769

Thomas, M. A., M. Giorgetta, C. Timmreck, H. Graf, and G. Stenchikov, 2009b, Simulation of the climate impact of Mt. Pinatubo eruption using ECHAM5 Part 2: Sensitivity to the phase of the QBO and ENSO, Atmos. Chem. Phys., 9, 3001-3009

Thomason, L. W.M. T. Osborn, 1992, Lidar conversion parameters derived from SAGE II extinction measurements, Geophys. Res. Lett., 12, 16551658

Thompson, D. W. J., and J. M. Wallace, 1998, The Arctic oscillation signature in the wintertime geopotential height and temperature fields, Geophys. Res. Lett., 25(9), 1297–1300

Thompson, D. W. J., and J. M. Wallace, 2001, Regional Climate Impacts of the Northern Hemisphere Annular Model, Science, 293 (5527), 85–89

Thompson, D. W. J., M. P. Baldwin, and J. M. Wallace, 2002, Stratospheric Connection to Northern Hemisphere Wintertime Weather: Implications for Prediction, Journal of Climate, 15 (12), 1421–1428

Tilmes, S., R. Moller, and R. Salawitch, 2008, The sensitivity of polar ozone depletion to proposed geoengineering schemes, Science, doi:10.1126/science.1153966.

Timmreck, C., Graf, H. F., 2006, The initial dispersal and radiative forcing of a Northern Hemisphere mid-latitude super volcano: a model study, Atmos. Chem. Phys., 6, 3549, 2006

Timmreck, C., S. J. Lorenz, T. J. Crowley, S. Kinne, T. J. Raddatz, M. A. Thomas, and J. H. Jungclaus, 2009, Limited temperature response to the very large AD 1258 volcanic eruption, Geophys. Res. Lett., 36 (21)

Timmreck, C., H.-F. Graf, S. J. Lorenz, U. Niemeier, D. Zanchettin, D. Matei, J. H. Jungclaus, and T. J. Crowley, 2010, Aerosol size confines climate response to volcanic super-eruptions, Geophys. Res. Lett., 37, L24705

Timmreck, C., 2012, Modeling the climatic effects of large explosive volcanic eruptions. WIREs Clim Change, 3: 545564

Timmreck C, Graf HF, Zanchettin D, Hagemann S, Kleinen T, Kruger K., 2012, Climate response to the Toba eruption: regional changes. Quat Int, 258:3044

Tollefson, J., 2012, Air sampling reveals high emissions from gas field, Nature 482, 139140

Tollefson, J., 2012, Ocean-fertilization project off Canada sparks furore, Nature, 490, 458-459

Trenberth, K. E. and A. Dai, 2007, Effects of Mount Pinatubo volcanic eruption on the hydrological cycle as an analog of geoengineering. Geophys. Res. Lett., 34, L15702

Trenberth, K.E., Fasullo, J.T., Kiehl, J., 2009, Earths Global Energy Budget, Bull. Amer. Meteor. Soc., 311-324

Trepte, C.R., and Hitchman, M.H., 1992, Tropical stratospheric deduced from satellite aerosol data: Nature, v. 355, p. 626-628

Trepte, C.R., Viega, R.E., and McCormick, M.P., 1993, The poleward dispersal of Mount Pinatubo aerosol: Journal of Geophysical Research, v. 98, p. 18563-18573.

Tung, K.-K., and J. Zhou, 2010, The Pacific's Response to Surface Heating in 130 Yr of SST: La Niña–like or El Niño–like?, Journal of the Atmospheric Sciences, 67(8), 2649–2657

Turner, J. , J. C. Comiso, G. J. Marshall, T. A. LachlanCope, T. Bracegirdle, T. Maksym, M. P. Meredith, Z. Wang, A. Orr., 2009, Nonannular atmospheric circulation change induced by stratospheric ozone depletion and its role in the recent increase of Antarctic sea ice extent. Geophysical Research Letters 36:8.

Uppala, S. M., et al., 2005, The ERA-40 re-analysis, Quarterly Journal of the Royal Meteorological Society, 131 (612), 2961–3012

Vaks, A., et al., 2013, Speleothems Reveal 500,000-Year History of Siberian Permafrost. Science. Vol. 340 no. 6129 pp. 183-186

Vallis, G. K., 2006. Atmospheric and Oceanic Fluid Dynamics. Cambridge University Press, 745 pp.

Valero, F. P. J., and P. Pilewskie, 1992, Latitudinal survey of spectral optical depths of the Pinatubo volcanic cloudderived particle sizes, columnar mass loadings, and effects on planetary albedo, Geophys. Res. Lett., 19, 3968

Vance, A., A. J. S. McGonigle, A. Aiuppa, J. L. Stith, K. Turnbull, and R. von Glasow, 2010, Ozone depletion in tropospheric volcanic plumes, Geophys. Res. Lett., 37, L22802

Victor, D. G., M. Granger Morgan, J. Apt, J. Steinbruner, K. Ricke, 2013, The Truth About Geoengineering - Science Fiction and Science Fact, Foreign Affairs

Voldoire, A., and coauthors, 2011, The CNRM-CM5.1 global climate model: Description and basic evaluation, technical doc, CNRM-CM, available at http://www.cnrm.meteo.fr/c

Volodin, E. M., S. V. Kostrykin, and A. G. Ryaboshapko, 2011, Simulation of climate change induced by injection of sulfur compounds into the stratosphere, Izv. Atmos. Oceanic Phys., 47(4), 430438.

Walter, K., H.-F. Graf, 2005, The North Atlantic variability structure, storm tracks, and precipitation depending on the polar vortex strength, Atmos Chem Physics, 5, 239-248, SRef-ID:1680-7324/acp/2005-5-239

Walter, K. M., S. A. Zimov, J. P. Chanton, D. Verbyla, and F. S. Chapin, 2006, Methane bubbling from Siberian thaw lakes as a positive feedback to climate warming. Nature 443: 7175.

Weisenstein, D. K., G. K. Yue, M. K. W. Ko, N. D. Sze, J. M. Rodriguez, and C. J. Scott, 1997, A 2-D model of sulfur species and aerosol, J. Geophys. Res., 102, 13019-13035

Wigley, T. M. L., 2006, A Combined Mitigation/Geoengineering Approach to Climate Stabilization. Science, 314 (5798), 452-454.2006

Williams, S. N., Schaefer, S. J., Calveche, V. M. L., Lopez, D., 1992, Global carbon dioxide emission to the atmosphere by volcanoes: Geochimica et Cosmochimica Acta, v. 56, p. 17651770.

Winker, D. M., and M. T. Osborn, 1992, Preliminary analysis of observations of the Pinatubo volcanic plume with a polarization-sensitive lidar. Geophys. Res. Lett., 19, 171174.

Wolfe, E. W., and Richard P. Hoblitt, 1996, Overview of the eruptions, Fire and Mud, edited by C. G. Newhall and R. S. Punongbayan. Quezon City: Philippine Institute of Volcanology and Seismology; Seattle: University of Washington Press. Edition available online, at: http://pubs.usgs.gov/pinatubo/index.html

Wu, T., R. Yu, and F. Zhang, 2008, A modified dynamic framework for the atmospheric spectral model and its application, Journal of the Atmospheric Sciences, 65 (7), 2235–2253

Wu, T., et al., 2012, The 20th century global carbon cycle from the Beijing Climate Center Climate System Model (BCC_CSM), J. Clim., submitted.

Wunsch, C., Schmitt, R.W., Baker, D.J., 2013, Climate change as an inter-generational problem. Proc. Natl. Acad. Sci. U.S.A. 110 (12), 44354436

Yukimoto, S., and coauthors, 2011, Meteorological Research Institute-Earth System Model v1 (MRI-ESM1) – Model Description, Tech. Rep. Meteor. Res. Inst. 64, 88pp., The Meteorological Research Institute.

Zhang, Jinlun, 2007, Increasing Antarctic Sea Ice under Warming Atmospheric and Oceanic Conditions. J. Climate, 20, 25152529